Physico-Chemical Engineering and Evaluation of Microstructures and Coatings for Solid-State Battery Composite Cathodes

Dem Fachbereich Biologie und Chemie
der Justus-Liebig-Universität Gießen
vorgelegte Dissertation zur Erlangung des akademischen Grades

Doktor der Naturwissenschaften

— Dr. rer. nat. —

Maximilian Kissel, M.Sc.

Gießen, Oktober 2025

Dekan / Dean	Prof. Dr. Holger Zorn
1. Gutachter / 1st Reviewer	Prof. Dr. Dr. h.c. Jürgen Janek (Justus-Liebig-Universität Gießen)
2. Gutachter / 2nd Reviewer	Prof. Dr.-Ing. Arno Kwade (Technische Universität Braunschweig)
Eingereicht / Submitted	02.10.2025
Disputation / Disputation	19.12.2025

Eidesstattliche Erklärung

Die vorliegende Arbeit wurde im Zeitraum vom 03.01.2022 bis 30.09.2025 am Physikalisch-Chemischen Institut der Justus-Liebig-Universität Gießen unter Betreuung von Prof. Dr. Dr. h.c. Jürgen Janek angefertigt. Ich erkläre:

Ich habe die vorgelegte Dissertation selbstständig und ohne unerlaubte fremde Hilfe und nur mit den Hilfen angefertigt, die ich in der Dissertation angegeben habe. Alle Textstellen, die wörtlich oder sinngemäß aus veröffentlichten Schriften entnommen sind, und alle Angaben, die auf mündlichen Auskünften beruhen, sind als solche kenntlich gemacht. Ich stimme einer evtl. Überprüfung meiner Dissertation durch eine Antiplagiat-Software zu. Bei den von mir durchgeführten und in der Dissertation erwähnten Untersuchungen habe ich die Grundsätze guter wissenschaftlicher Praxis, wie sie in der „Satzung der Justus-Liebig-Universität Gießen zur Sicherung guter wissenschaftlicher Praxis“ niedergelegt sind, eingehalten.

Angaben zu auf künstlicher Intelligenz (KI) basierender Hilfen zur Erstellung meiner Dissertation:
Ich habe das KI-Tool ChatGPT (OpenAI) eingesetzt, um von mir verfasste Textpassagen sprachlich zu optimieren und dadurch die Lesbarkeit der Dissertation zu verbessern. Darüber hinaus wurde das Tool zur Ausformulierung von mir vorgegebenen Stichpunkten in vollständige Sätze verwendet. Die zugrundeliegenden inhaltlichen Aspekte der Passagen stammen dabei ausschließlich von mir.
Für diese Zwecke wurde ChatGPT in den individuellen Voreinstellungen wie folgt konfiguriert: „Ändere nicht den Sinn von Textpassagen, sondern verbessere sie nur sprachlich, um die Lesbarkeit zu verbessern.“ Alle generierten Textpassagen wurden anschließend von mir editiert und auf inhaltliche Richtigkeit mit der ursprünglichen Textstelle abgeglichen und gegebenenfalls angepasst.

Gießen, den 02.10.2025

Maximilian Kissel

Abstract

Solid-state batteries are widely regarded as a key technology for next-generation energy storage, promising improved safety and higher energy densities. However, their widespread adoption remains hindered by fundamental challenges in materials development, interface stability, and cell processing. This dissertation addresses the often overlooked interplay between physico–electrochemical understanding and process engineering, with a focus on composite cathodes and cathode active material coatings.

Unlike conventional lithium-ion batteries, where a liquid electrolyte infiltrates a porous electrode structure, solid-state batteries require the solid electrolyte to be directly integrated into the cathode composite during its fabrication. As a result, the mixing of the composite components becomes critical. Using a representative model system comprising a nickel-rich active material, a sulfide solid electrolyte, and a carbon additive, this thesis demonstrates that the quality of the mixing process has a direct impact on the electrochemical performance and reproducibility. Specifically, a method is validated and evaluated to quantify the static active material utilization in the composite as a microstructural descriptor, enabling a clear distinction between static and kinetic capacity losses. This allows for the quantification of mixing quality during process development and helps to avoid misinterpretation of capacity data in early-stage research. Based on this, a scalable mechanofusion process is investigated to create mixed-conducting matrix coatings as cathode microstructures. These coatings enable microstructural control and enhance electrochemical performance by facilitating both ionic and electronic transport across interfaces with intimate contact.

In a complementary study, protective coatings on nickel-rich cathode active material particles using the model coating precursor Li_3PS_4 are investigated. A single annealing parameter is shown to significantly influence the coating's composition, morphology, and ultimately the performance of the entire cell. These findings underscore how variations in processing conditions have major consequences on interphase properties and interfacial stability. To address this parameter space, a practical and efficient benchmarking protocol is developed that combines surface characterization and targeted electrochemical testing, focusing on impedance analysis. This reliable approach enables a systematic screening and an accelerated optimization of cathode coating strategies.

The physico-chemical concepts and process strategies developed in this dissertation are broadly transferable to other material systems. They provide a robust framework for accelerated development and reliable evaluation of composite cathodes and coatings for solid-state batteries — on a fundamental level of materials research as well as toward industrial research.

Zusammenfassung

Festkörperbatterien gelten als Schlüsseltechnologie für die nächste Generation der Energiespeicherung, da sie sowohl eine verbesserte Sicherheit als auch höhere Energiedichten versprechen. Ihre breite industrielle Anwendung wird jedoch noch durch grundlegende Herausforderungen in der Materialentwicklung, der Stabilität an Grenzflächen und der Zellprozessierung eingeschränkt. Diese Dissertation widmet sich der häufig vernachlässigten Schnittstelle zwischen physikalisch-elektrochemischem Verständnis und prozesstechnischer Umsetzung mit einem besonderen Fokus auf die Herstellung von Kompositkathoden und Schutzbeschichtungen für Kathodenaktivmaterialien.

Im Gegensatz zu herkömmlichen Lithium-Ionen-Batterien, bei denen ein flüssiger Elektrolyt eine poröse Elektrodenstruktur infiltriert, muss bei Festkörperbatterien der feste Elektrolyt bereits während der Herstellung des Kathodenkomposits in diesen gezielt integriert werden. Daher ist das Mischen der Kompositbestandteile von entscheidender Bedeutung. Am Beispiel eines repräsentativen Modellsystems mit Nickel-reichem Aktivmaterial, sulfidischem Festelektrolyten und Kohlenstoffadditiv wird gezeigt, dass die Qualität des Mischprozesses einen direkten Einfluss auf die elektrochemische Performance und Reproduzierbarkeit hat. Es wird insbesondere eine Methode validiert und evaluiert, mit der der elektrochemisch inaktive Anteil des Komposits als ein mikrostruktureller Deskriptor quantifiziert werden kann, was eine klare Unterscheidung zwischen statischen (mikrostrukturellen) und kinetischen Kapazitätsverlusten ermöglicht. Diese Methode erlaubt zum einen, die Mischqualität während der Prozessentwicklung zu bewerten, und zum anderen, Fehlinterpretationen elektrochemischer Ergebnisse in frühen Forschungsphasen zu vermeiden. Aufbauend darauf wird ein skalierbarer Mechanofusionsprozess untersucht, mit dem leitfähige Matrixbeschichtungen als Kathodenmikrostrukturen erzeugt werden. Dieser Beschichtungsansatz ermöglicht eine kontrollierte Mikrostrukturherstellung und verbessert die elektrochemische Leistungsfähigkeit durch erleichterten Ionen- und Elektronentransport über Grenzflächen mit engem Kontakt.

In einer komplementären Studie werden Schutzbeschichtungen auf Nickel-reichen Kathodenaktivmaterialpartikeln anhand des Modellbeschichtungsmaterials Li_3PS_4 untersucht. Es wird gezeigt, dass ein einzelner Parameter im Temperprozess die Zusammensetzung, Morphologie und letztlich die Leistung der gesamten Zelle erheblich beeinflussen kann. Die Ergebnisse unterstreichen, wie scheinbar geringe Änderungen der Prozessbedingungen erhebliche Auswirkungen auf die Eigenschaften der Beschichtung und die Grenzflächenstabilität

haben. Zur Untersuchung dieses Parameterraums wird ein praxisnahes und effizientes Benchmarking-Protokoll entwickelt, das Oberflächenanalytik und gezielte elektrochemische Tests mit einem Fokus auf Impedanzspektroskopie kombiniert. Durch diesen zuverlässigen Ansatz wird eine systematische Bewertung und schnellere Optimierung von Schutzbeschichtungen für Kathodenaktivmaterialien ermöglicht.
Die in dieser Dissertation entwickelten physikochemischen Konzepte und Prozessstrategien sind weitgehend auf andere Materialsysteme übertragbar. Sie bieten ein robustes Fundament für die beschleunigte Entwicklung und zuverlässige Bewertung von Kompositkathoden und Beschichtungen für Festkörperbatterien – sowohl im Bereich der Grundlagenforschung als auch im industriellen Kontext.

Contents

PART I

Bridging Science and Engineering in Solid-State Battery Research

1 Introduction

1.1. Background and Motivation

The electrification of our society and industry began years ago and has continuously gained momentum as part of the renewable energy transition. Various energy storage solutions are becoming increasingly important, with rechargeable batteries playing a key role.[1] Batteries are developed, constructed, and used to efficiently store and deliver electrical energy in a controlled, safe, and application-specific manner. All battery systems rely on the conversion of chemical energy into electrical energy via redox reactions in the electrode materials.[2,3] They have found their way into a growing number of applications, including portable consumer electronics, electric vehicles, and grid storage systems. This widespread adoption is mainly due to the success of lithium-ion batteries (LIBs), which were first commercialized in 1991.[4,5] Material and process innovations have steadily increased the practically achievable energy and power density of the cells. At the cell pack level, further performance improvements can be expected due to advanced process and cell engineering.[6–8] However, from a physico-chemical perspective, conventional LIB cells will soon reach their energy density limit.[9] Implementing a lithium metal anode (LMA) instead of a graphite anode would lead to a significant increase in energy density.[5,9] Yet, LIBs with an LMA and a liquid electrolyte (LE) face severe issues such as degradation of the LE and dendrite formation, which also pose safety risks.[10,11]

Replacing the LE with a solid electrolyte (SE) is expected to enable the LMA along with higher energy and power density as well as improved safety.[9,12–14] This is the main driving force behind research on solid-state batteries (SSBs). However, the path from laboratory-scale proof-of-concept cells with low technology readiness level (TRL)[6,15] to practical, scalable, and long-term stable devices remains challenging.[16] While the stable integration of an LMA in SSBs is still unresolved[16–18], the cathode in SSBs is also a critical component since it defines the maximum energy density of the cell and faces various challenges.[16,19,20]

SSB cathodes are usually realized as composites, which are complex multi-phase systems involving a cathode active material (CAM), SE, conductive additive, and possibly a binder.[20–22] The performance of these composites relies on the efficient interplay between the different phases, which requires intimate contact[23–25], stable interfaces[26–28], and a tailored microstructure[20,22,29] to ensure efficient ionic and electronic transport and stable long-term performance. The formation of microstructure and interfaces is defined by particle processing, specifically, in the case of composites, the mixing process. While mixing becomes especially important and challenging toward scale-up, systematic research in this field is limited.[30,31] Moreover, particle processing is crucial in the development of protective CAM coatings, which are necessary to mitigate degradation at the CAM | SE interface.[32,33] Although there have been advancements in material and interface understanding, cathode composites still face problems with respect to electro-chemo-mechanical degradation at interfaces, reproducibility of results, and scale-up, which hinders full exploitation of material properties and slows down development.[16,34]

Research on SSBs often takes place at low TRLs[6,15], focusing on fundamental materials discovery and mechanistic understanding of interfacial phenomena. Toward the expected commercialization of SSBs, process engineering is becoming increasingly important, since it forms the bridge between electrochemistry and the properties of the final product. However, transforming fundamental insights, theoretical concepts, and intrinsic material properties into functional cathode architectures and protective CAM coatings remains a major bottleneck. This doctoral thesis addresses this challenge by aiming to bridge the gap between laboratory proof-of-principle tests and the scale-up of cathode composite and CAM coatings development. It was carried out in the context of a collaborative project with the Institute for Particle Technology (iPAT) from TU Braunschweig, as part of the DFG Priority Programme 2289 "Hetero-Aggregates". The collaboration provided access to complementary expertise and approaches, shaping the focus on particle processing. The key question for this dissertation was how particle processing affects physico-chemical material properties and how physico-chemical concepts can be efficiently applied to particle process engineering. This resulted in the following guiding questions:

- Which physico-chemical concepts and descriptors can be used to quantify the mixing quality of composites resulting from various mixing processes?
- How does the mixing process of cathode composites affect the performance and reproducibility of SSB cells?
- How can cathode composites be rationally designed and mixed in a scalable way?
- What impact do processing parameters have on protective CAM coatings?
- How can a benchmarking be designed to efficiently, effectively, and quantitatively compare different CAM coatings to accelerate their development?

1.2. Outline of the Thesis

Part I of this dissertation provides the scientific and contextual background that is relevant to this doctoral thesis. For reference, all abbreviations and symbols used throughout this thesis are summarized in Section 1.3. Chapter 2 introduces the essential components of SSBs, with a focus on the selection and properties of inorganic SEs as well as anode and cathode materials. Chapter 3 addresses composite cathodes as the central focus of this thesis, which represent the structurally and functionally most complex component in many SSB architectures. Key topics include the cathode microstructure, mechanisms of degradation, and strategies to mitigate performance deterioration through material and processing innovations. Chapter 4 covers general considerations related to SSB testing and benchmarking. This includes the role of model systems, challenges for comparative performance analysis, and an outlook on the translation of laboratory-scale findings to industrially relevant formats. Together, these chapters serve as the conceptual framework that supports the five original publications compiled in Part II.

Publication I of this doctoral thesis, titled *Quantifying static capacity losses in solid-state battery composites via coulometric titration comparison*, presents an in situ electrochemical method to quantify the static CAM utilization in the form of a methodology article. The static CAM utilization describes how many CAM particles are actually electrochemically active in the composite cathode. By discussing pitfalls and limitations, this work serves as a practical guide for researchers aiming to separate fundamental material properties from microstructural, *i.e.*, process engineering shortcomings.

Publication II, titled *Quantifying the Impact of Cathode Composite Mixing Quality on Active Mass Utilization and Reproducibility of Solid-State Battery Cells*, builds on this methodology and applies it to a representative model system. The study highlights, based on a statistical analysis of multiple cells, that performance variations can originate from different mixing processes, even when using identical materials. Furthermore, a quantitative framework is provided for interpreting specific capacity values and for benchmarking processing quality by distinguishing between static and kinetic capacity losses.

Publication III, titled *Mechanofusion-derived cathode composite microstructures with scalable mixed conducting matrix coatings for solid state batteries*, is embedded in the framework of the first two publications, but moves from laboratory-scale mixing to a more scalable process, by investigating a mechanofusion-based fabrication method for cathode composites. Here, SE coatings on a single-crystalline Ni-rich CAM are created via high-intensity mixing, enabling the formation of thin protective coatings and thick matrix coatings. The matrix coating approach was further tailored by adding a carbon additive resulting in mixed conduction behavior. Process–structure–performance relationships were established using both simulation and experimental tools, offering pathways for advanced scalable fabrication of SSB composite cathodes.

Publication IV, titled *Engineering the Artificial Cathode-Electrolyte Interphase Coating for Solid-State Batteries via Tailored Annealing*, focuses on interfacial engineering of SE coatings on a poly-crystalline Ni-rich CAM. Through tailored oxidative annealing of Li_3PS_4 (LPS) based coatings, the morphology and composition of the coating were tuned. A broad characterization approach within a benchmarking framework linked process parameters to coating properties, emphasizing that coating quality is not only material-dependent but also highly process-sensitive.

The results stressed the need for an efficient benchmarking of protective CAM coatings to cover a broader process parameter space. Publication V, titled *Toward efficient development and reliable benchmarking of novel CAM coatings for solid state batteries*, builds upon the previous findings and proposes an improved benchmarking protocol for protective CAM coatings. By combining X-ray photoelectron spectroscopy (XPS) as a surface analytical method with a compact electrochemical testing scheme, a time- and resource-efficient strategy is provided to assess and compare coatings. This methodology accelerates coating development by

providing a practical evaluation framework. Moreover, it contributes to a more reliable interpretation of impedance spectra of cathode composites by discussing pitfalls during quantitative impedance analysis.

Together, these studies advance the physico-chemical understanding of SSB cathode composite behavior, aiming to close the gap between material properties, processing strategies, and realistic cell performance assessment. While focusing on lithium-based SSBs, many discussed concepts and challenges are applicable to other SSB systems. The dissertation provides a framework connecting material-specific insights with the broader challenges of process, performance comparison, and the gap between expected and real-world performance in SSB research.

1.3. Abbreviations and Symbols

In the hype surrounding *the* solid-state battery, it should be noted that there is no standardized definition or nomenclature in this field.[35,36] In literature, terms such as 'quasi-SSB'[37,38], 'pseudo-SSB'[39], 'almost-SSBs'[40], 'hybrid-SSB'[41,42] or 'gel-polymer SSBs'[43] are often encountered, which represent different cell concepts. Sen and Richter[36] proposed a typology based on the principal ion conduction mechanism of the electrolyte. Their classification differentiates between liquid electrolyte batteries (LEB), gel electrolyte batteries (GEB), dry polymer electrolyte batteries (DPEB), plasticized polymer electrolyte batteries (PPEB), hybrid electrolyte batteries (HEB), and solid electrolyte batteries (SEB). In this doctoral thesis, the term SSB is used exclusively for an SEB, *i.e.*, an all-solid-state battery, which consists solely of solid and inorganic components.

List of Abbreviations

Abbreviation	Full Form
2E	2-electrode
3E	3-electrode
CAM	Cathode active material
CB	Carbon black

Abbreviation	Full Form
CC	Constant-current
CCCV	Constant-current-constant-voltage
CEI	Cathode-electrolyte interphase
CNF	Carbon nano fiber
CTC	Coulometric titration comparison
DEM	Discrete element method
EDX	Energy dispersive X-ray spectroscopy
EIS	Electrochemical impedance spectroscopy
ESW	Electrochemical stability window
LCO	Lithium cobalt oxide ($LiCoO_2$)
LE	Liquid electrolyte
LEIS	Low-energy ion scattering
LFP	$LiFePO_4$
LIB	Lithium-ion battery (with liquid electrolyte)
LIC	Li_3InCl_6
LMA	Lithium metal anode
LNMO	$LiNi_{0.5}Mn_{1.5}O_4$
LNO	Lithium nickel oxide ($LiNiO_2$)
LPS	Li_3PS_4
LPSCl	Li_6PS_5Cl
NCM	Lithium nickel manganese cobalt oxide ($Li_xNi_yCo_zMn_{1-y-z}O_2$)
NCM622	$LiNi_{0.6}Co_{0.2}Mn_{0.2}O_2$
NCM82	$LiNi_{0.82}Co_{0.11}Mn_{0.07}O_2$
NCM85	$LiNi_{0.85}Co_{0.10}Mn_{0.05}O_2$
PSD	Particle size distribution
SE	Solid electrolyte
SEI	Solid electrolyte interphase
SEM	Scanning electron microscope
SHE	Standard hydrogen electrode
SoC	State of charge

Abbreviation	Full Form
SSB	Solid-state battery
STEM	Scanning transmission electron microscope
TM	Transition metal
TRL	Technology readiness level
ToF-SIMS	Time-of-flight secondary ion mass spectrometry
VGCF	Vapor grown carbon nano fibers
XPS	X-ray photoelectron spectroscopy
XRD	X-ray diffraction

List of Symbols

Symbol	Unit	Description
η	V	Overpotential
E_{H}	V	Standard redox potential
E_{m}	Wh/kg	Specific energy
$E_{\mathrm{m(Cat)}}$	Wh/kg	Specific energy of the cathode
$E_{\mathrm{m,mix}}$	Wh/kg	Specific energy input
μ_{Li}	J/mol	Chemical potential of lithium
P_{m}	W/kg	Specific power
$P_{\mathrm{m(Cat)}}$	W/kg	Specific power of the cathode
τ	-	Tortuosity factor
l_{eff}	m	Effective pathway length
$l_{\mathrm{electrode}}$	m	Electrode length
Q_{A}	mAh/cm²	Areal capacity
q	mAh/g	Specific capacity
q_{CAM}	mAh/g	Specific capacity referred to CAM mass
R_i	Ω	Resistance of i=cell, anode, separator, cathode
R_{ct}	Ω	Charge transfer resistance

Symbol	Unit	Description
R_{diff}	Ω	Diffusion resistance
R_{ohm}	Ω	Charge transport resistance
SE	J	Stress energy
SF	s^{-1}	Stress frequency
SI	J/kg	Stress intensity
SN	-	Stress number
R_{diff}	Ω	Diffusion resistance
V_{cell}	V	Cell voltage
V_{cutoff}	V	Cutoff voltage
V_{eq}	V	Equilibrium voltage

2 Solid-State Battery Materials

SSBs rely on a complex interplay of electrochemically active materials and solid electrolytes. Understanding their fundamental properties is essential for developing functional and eventually scalable systems. This chapter provides an overview of the key material components, beginning with a general outline of the SSB architecture. The properties and challenges associated with various classes of SEs are discussed, followed by a brief look at commonly used electrode active materials in SSBs.

2.1. General Design of an SSB

SSBs differ from conventional LIBs mainly by replacing the LE with an SE, potentially enabling the use of an LMA.[9] Figure 1 illustrates a simplified SSB architecture composed of anode, cathode, SE separator, and two current collectors. The cathode is usually realized as a composite consisting of CAM and SE particles, also referred to as catholyte. It may also contain conductive carbon additives and a polymer binder. Composites are sometimes also encountered on the anode side; in this case, the SE can be referred to as anolyte.[44]

The basic operating principle of SSBs is identical to that of LIBs. The terms cathode and anode refer to the electrodes during the discharge process, during which oxidation occurs at the negative electrode (anode) and reduction takes place at the positive electrode (cathode). Li-ions migrate from the anode to the cathode through the electrolyte, driven by the chemical potential difference $\Delta\mu_{\mathrm{Li}}$ of lithium between the electrodes, while electrons flow through an external circuit in the same direction. The profile of μ_{Li} across the cell is schematically shown in the bottom part of Figure 1. During charging, the directions are reversed: Li-ions and electrons move from the cathode back to the anode. Despite this reversal, the terms anode and cathode are typically retained for the negative and positive electrodes, respectively—a convention that is also followed throughout this thesis.

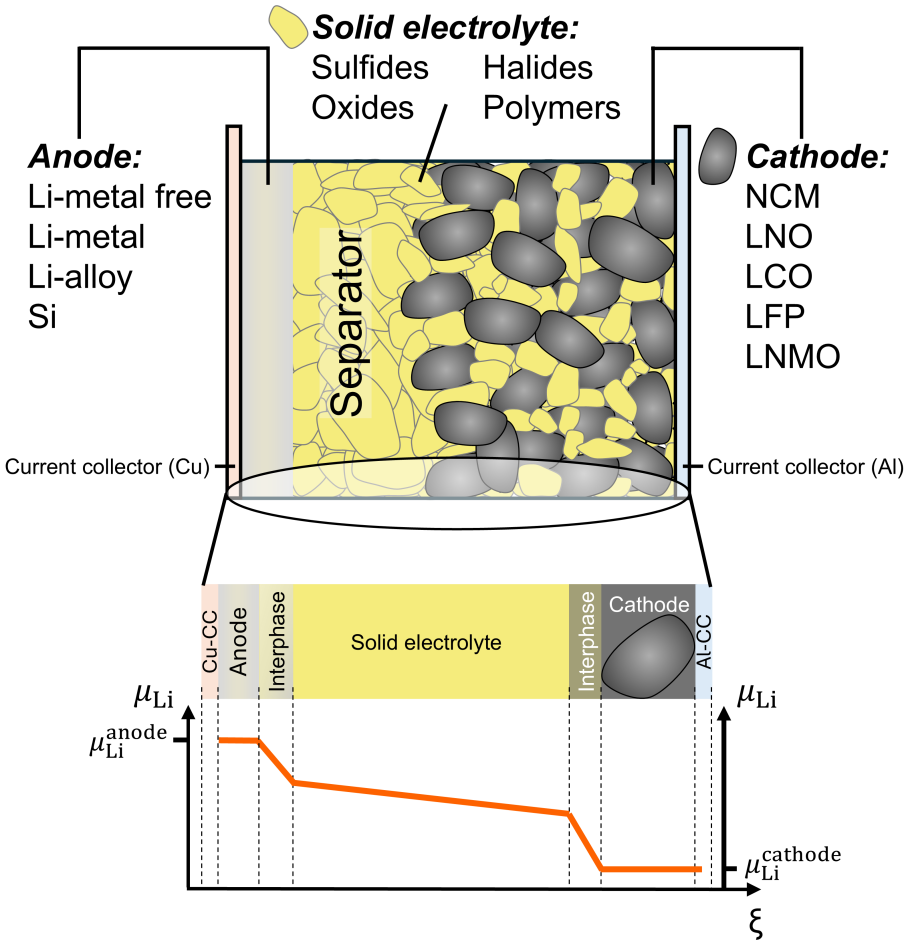

Figure 1. Schematic cell design of a lithium SSB (inspired by references [16, 32, 45]). Top: SSB cell with potentially attractive materials for use as anode, SE, and intercalation CAM. For clarity, common additives such as binders or carbon are excluded. Bottom: Chemical potential profile of lithium, μ_{Li}.

2.2. Finding the Best Inorganic Solid Electrolyte

SEs are the key component of SSBs and represent the fundamental difference compared to conventional LIBs. Different types of inorganic SEs exist, which can be divided into three main classes: sulfides[28,46,47], oxides[28,47,48] and halides[49,50]. This section concisely discusses five key properties that need to be considered in the search for *the best* inorganic SE.

The SE needs to be highly conductive Fast ion conduction is a central requirement for electrolytes. While LEs exhibit a total ionic conductivity of around 10 mS/cm, their effective Li^+ conductivity is typically lower, *e.g.*, 5 mS/cm with a transference number of 0.5.[51,52] In contrast, SEs are single-ion conductors with a Li^+ transference number near unity.

The field experienced a breakthrough in 2011 with the report of a room-temperature conductivity of 12 mS/cm for $Li_{10}GeP_2S_{12}$.[53] Subsequently, other sulfide SEs achieved similar values, eventually surpassing the Li^+ conductivity of LEs by a factor of two.[54–56] Recent advancements with high-entropy compositions, such as $Li_{9.54}(Si_{0.6}Ge_{0.4})_{1.74}P_{1.44}S_{11.1}Br_{0.3}O_{0.6}$, have pushed conductivities to 32 mS/cm.[57–59] For a long time, other SE classes did not exceed 1 mS/cm.[16,28,49] However, the discovery of lithium-metal-oxy-halide electrolytes, such as $LiNbOCl_4$, in 2023 brought a notable change, reporting conductivities exceeding 12 mS/cm and theoretical predictions up to 100 mS/cm.[60] Despite these advancements, most oxide and other halide SEs still lack sufficiently high conductivities to be used as catholytes.

While a conductivity of only about 1 mS/cm may be sufficient to be used as a separator, electrochemical simulations suggest a bulk ionic conductivity of at least 10 mS/cm for catholytes to achieve competitive cell performance, especially at high charging rates.[61] Machine-learning approaches[37,62] are emerging to accelerate the identification of new SEs meeting this requirement, which need to be followed by practical synthesis and evaluation.

Lastly, it should be noted that the electronic conductivity of SEs is generally by orders of magnitude lower but never zero.[63,64] In storage scenarios, *e.g.*, when the battery is charged and not under constant use, this might lead to non-negligible self-discharge. However, the impact of electronic conductivity in SEs under storage conditions is poorly understood, and experimental studies quantifying self-discharge effects are currently lacking.

The SE needs to be stable Beyond high ionic conductivity, SEs must exhibit chemical and electrochemical stability during cell production and operation. Any decomposition of the SE may lead to highly resistive (inter)phases which are detrimental to the cell kinetics.[65–68]

Chemical stability is, on the one hand, important for the processing and handling of the materials. Air- and moisture-sensitive SEs, such as most sulfide SEs, require the use of dry rooms or even inert atmospheres to avoid degradation.[28,69–73] On the other hand, chemical stability is relevant when CAM and SE particles come into mere contact. Theoretical calculations of reaction energies[74–76] show that sulfide, as well as halide SEs, are chemically incompatible with NCM, which could also be confirmed experimentally.[77,78]

Electrochemical stability is critical during cell operation and is usually quantified by the electrochemical stability window (ESW). The ESW describes the potential range in which the SE is stable against oxidation and reduction. Experimentally, the ESW is probed via

cyclic voltammetry—a method that was critically discussed by Dewald *et al*.[79] It was found that practical (kinetic) ESWs are larger than theoretically predicted by thermodynamic calculations. At the same time, they are much smaller than initially reported.[53,80] In this context, Schwietert *et al.*[81,82] stressed the importance of considering indirect decomposition pathways for the accurate prediction of ESWs.

From a stability perspective, sulfide SEs are generally least attractive due to their air and moisture sensitivity and narrow ESW, which causes detrimental interfacial reactions (cf. Section 3.3).[28,81] Halide SEs show higher oxidative stability but are prone to reductive processes and moisture sensitivity.[78,83] In contrast, oxide SEs are chemically robust and possess the broadest ESW, particularly toward reduction.[28]

The SE needs to be safe in and outside the cell SEs are often considered non-flammable, promising intrinsic safety advantages over flammable LEs for applications like electric vehicles.[11,14] However, the safety of SEs depends not only on their inherent properties but also on their behavior within the full cell, where thermal runaway can still occur as demonstrated for sulfide-based SSBs.[12,84,85] Furthermore, sulfide SEs react with water to produce toxic H_2S, posing an additional safety concern.[73,86] Due to limited systematic and quantitative research, comprehensive safety analyses of SSBs, considering both material- and cell-level aspects, are still needed.[12]

The SE needs to possess good processability and mechanical properties The suitability of SEs for SSBs heavily depends on their processability. Recently, viscoelastic inorganic glass SEs have shown promising mechanical properties similar to polymer SEs.[87–89] In contrast, oxides require costly high-temperature sintering for densification[68], which can negatively impact interfacial properties as exemplary shown by Demuth *et al.*[90] for cathode composites. Sulfide SEs are considered rather advantageous in this regard because they can be densified via cold-pressing and processed at room temperature.[28,72,91] In the literature, this is usually attributed to their "softness" or "malleability".[92–95]

From a materials science perspective, such descriptions are lacking in quantitative information on the mechanical properties. Values for the Young's modulus, bulk modulus, shear modulus, and fracture toughness are standard in materials science to compare the mechanical properties of different materials. However, the determination and reporting of these

quantities is less common for SE materials.[96] While standard methods like indentation[97–99], ultrasound spectroscopy[100–104], and DFT calculations[105,106] have been reported, they are not routinely applied to SE materials.

Oxide SEs are comparable to engineering ceramics, enabling the straightforward transfer and application of characterization methods. Consequently, their mechanical properties are well documented in the literature.[101] The situation differs for sulfides, as they are both air-sensitive and typically not processed into dense, sintered pellets. Thus, the mechanical properties of novel sulfide SEs are often not experimentally determined, but only theoretically calculated.[105,106] It is commonly assumed that they are deformable and sufficiently soft. Mechanical properties of halide SEs have, as far as the literature suggests, only been reported in the context of a single theoretical study.[107] Although the quantification of mechanical properties for new SEs is challenging, such data would be highly beneficial, especially for more accurate simulations of production or cell operation processes[108], and understanding chemo-mechanical phenomena[109]. Therefore, establishing standardized experimental measurement setups, also suitable for chemically sensitive SEs, is desired to acquire reliable and comparable data on intrinsic mechanical properties.[96]

The SE needs to be economically viable Toward the commercialization of SSBs, scalable synthesis methods are required to produce SEs cost-effectively, in large quantities, and with sufficient purity.[110–114] Generally, it must be considered that inorganic SEs have higher charge carrier, *i.e.*, lithium ion, densities compared to LEs and polymer electrolytes, which can be a cost issue.[16,88] Additionally, halide SEs of the type Li_3MCl_6(M= In, Er, Sc)[112] depend on critical or rare-earth metals, raising concerns about their economic viability as catholytes for large-scale commercialization. Consequently, research efforts focus on the development of more cost- and resource-efficient halide SEs.[115,116] For sulfide SEs like lithium argyrodites (Li_6PS_5X with X=Cl, Br, I) not only the SE itself but also the required precursor Li_2S needs to be produced in high purity, at low cost, and on large scale.[117,118]

In summary, no single SE type currently fulfills all requirements to be used as both anolyte/separator and catholyte in an SSB. This necessitates future discovery and development of new SEs with improved properties, ideally accelerated by machine-learning

approaches.[37,62] Publication II highlights how to avoid misleading conclusions when experimentally assessing the electrochemical performance as catholyte at the early stage of laboratory research, *e.g.*, upon initial synthesis.

2.3. Anode and Cathode Materials

Electrode active materials are responsible for the storage of Li ions, and in principle, the same active materials as for LIBs can be used in SSBs. While this doctoral thesis focuses on composite cathodes, not only CAMs but also the role of different anode active materials are summarized in this section.

Anode Active Materials From an application-oriented perspective, the promised and necessary boost in energy density of SSBs compared to LIBs is directly coupled to the successful implementation of an LMA, offering the highest specific capacity (3860 mAh/g) and lowest potential ($E_H = -3.04$ V vs. SHE).[9,13,16] Anode- or reservoir-free concepts aim to further increase energy density by avoiding excess lithium.[18,119] However, interface instability, solid electrolyte interphase (SEI) formation, low critical current densities, and dendrite penetration still hinder practical LMA application.[17]

Closely related to LMAs are Li-alloy anodes.[120,121] Among them, Si-based anodes recently gained increasing attention due to the very high specific capacity of 3950 mAh/g.[13,122] Si-anodes are often composite anodes and while being promising, several issues such as ionic and electronic transport for high rates as well as chemo-mechanics require further investigations to be eventually solved.[44,122]

In academic research, the In-Li alloy anode is widely used.[64,123,124] The two-phase eutectic $In/(InLi)_x$ of this system provides a stable potential of $E_H = 0.62$ V vs. Li^+/Li over a wide stoichiometric range and is considered less prone to dendrite and SEI formation.[123–125] The high cost of indium limits the application of this anode type to research on a laboratory scale, including all cells investigated in this doctoral thesis.

Generally, reliable cathode investigations require an anode with a well-defined and stable standard redox potential E_H, a stable interface against the separator, and kinetics that are not rate-limiting.[64]

Cathode Active Materials The pursuit for high-energy density batteries requires the integration of high-energy CAMs in SSBs.[19]

In practice, this puts established materials like $LiCoO_2$ (LCO), delivering a practical capacity of only ~140 mAh/g, out of the focus in SSB research during the recent years.[80,126,127] Also, for the state-of-the-art material in LIBs, $LiFePO_4$ (LFP), research in SSBs with inorganic SEs is limited, and contradicting literature exists.[30,85,128,129] While Kim *et al.*[85] demonstrate an extremely well-performing LFP-based SSB depending on the particle size of the sulfide SE, Cronk *et al.*[128] showed that detrimental oxidative decomposition reactions prevent the use of LFP with sulfide SEs in the cathode. In general, LFP is less attractive for high-performance SSBs because it is a comparatively low-energy density material with an achievable capacity of ~160 mAh/g and a mean operating voltage of only 3.4 V vs. Li^+/Li.

Alternative CAMs for SSBs include spinel-type $LiNi_{0.5}Mn_{1.5}O_4$ (LNMO), which offers high energy density due to its high operating voltage.[130–132] Even high capacity of more than 200 mAh/g can be achieved if the Mn redox ($Mn^{3+} \rightleftharpoons Mn^{4+}$) is used in addition to the Ni redox ($Ni^{2+} \rightleftharpoons Ni^{4+}$) in the so-called wide voltage range (2.3 - 4.9 V vs. Li^+/Li).[133] This is currently prevented in LIBs due to detrimental dissolution of Mn^{2+}, which makes SSBs an attractive use case for LNMO, as transition metal dissolution is expected to be less severe.[134]

Current research on SSBs focuses on high-energy transition metal oxides with the general formula $Li_xNi_yCo_zMn_{1-y-z}O_2$ (NCM) in the cathode.[16,135,136] Ni-rich compounds, with $LiNiO_2$ (LNO) being the end member of this family[137,138], are attractive to achieve higher capacities in the range of ~200 mAh/g since Ni is the main active redox species .[139,140] In this doctoral thesis, polycrystalline $LiNi_{0.85}Co_{0.10}Mn_{0.05}O_2$ (NCM85) and single-crystalline $LiNi_{0.82}Co_{0.10}Mn_{0.07}O_2$ (NCM82) were investigated.

These intercalation materials undergo different phase transitions during charge and discharge, which appear as peaks in the differential capacity plots, as exemplarily shown for NCM85 in Figure 2.[141,142] Their phase transitions are usually denoted as transition from the H1 (1st hexagonal) phase to M (monoclinic) phase, from the M phase to H2 (2nd hexagonal), and from the H2 phase to H3 (3rd hexagonal). The peak heights and positions of the phase transitions change with applied charging rate (C-rate). At low C-rates (Figure 2a), all phase transitions are usually clearly visible and relatively well separated. With increasing C-rate (Figure 2b), the peak intensities can decrease and their positions shift to higher and lower

cell voltages during charge and discharge, respectively, due to the increased overpotential and limiting kinetics. For the example in Figure 2b, the H2→H3 peak is barely visible when charging at 1C, indicating that most particles do not undergo this phase transition.

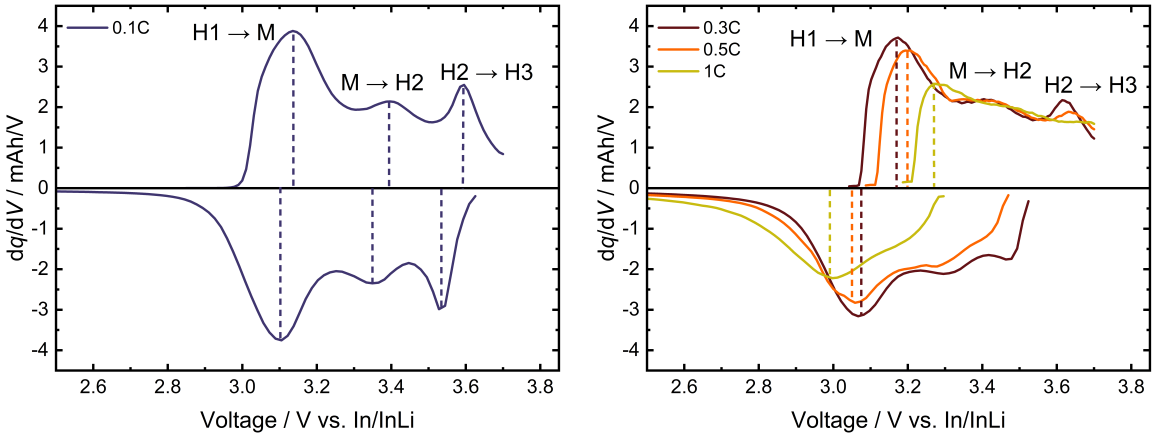

(a) dQ/dV plot for NCM85 at low C-rate. **(b)** dQ/dV plot for NCM85 at higher C-rates.

Figure 2. Differential capacity (dQ/dV) plots for NCM85 at different C-rates indicating the characteristic peaks corresponding to the phase transitions. The underlying data stems from Publication V, while this material and cell system was also used in Publication IV.

The phase transitions have also been investigated in numerous studies via X-ray diffraction (XRD).[140–145] The charging process, *i.e.*, deintercalation of lithium, is reflected in changing lattice parameters. The crystal lattice can be viewed as an alternating stacking of transition metal (TM), oxygen, lithium, and oxygen layers. The lattice parameter a reflects the TM-TM distance within the layer and decreases with increasing state of charge (SoC) since the ionic radii of the TM also decrease due to oxidation. The lattice parameter c represents the distance between the layers and first increases with delithiation due to electrostatic repulsion of the adjacent oxygen layers, which are less screened when not all lithium sites are occupied. At the H2→H3 transition, *i.e.*, at a high degree of delithiation, an abrupt decrease of the lattice parameter c and the unit cell volume is observed.[144,146] In the literature, this severe shrinkage of the interlayer spacing is also referred to as collapse of the layered structure[143,145] and is explained by two effects. On the one hand, there is a transfer of negative charge from oxygen to nickel, which decreases the average charge at the oxygen ions and thus the repulsion of the layers.[145] On the other hand, the absence of lithium ions between the oxygen layers prevents the widening of the interspace.[147]

3 Cathode Composites: From Theory to Reality

While many materials for SSB cathodes show promising intrinsic or theoretically predicted properties, the extent to which these can be exploited in a full cell strongly depends on the interplay between these materials. Full exploitation is challenging due to electrochemical instabilities and the complex interplay between microstructure and processing conditions. Evaluating the performance during cell operation requires integrating and testing the materials in functional cathode composites.

Cathodes in SSBs are usually realized as composites of at least two phases — CAM and SE.[148] Electron conducting additives, such as carbon black (CB) or carbon nano fibers (CNF), are also common.[19,66,93,149] Continuous large-scale production additionally requires a polymer binder, which is usually electrically isolating.[29,72,91] Within this doctoral thesis, no binder was used to reduce the complexity of the system. The use of conductive additives depends on the particular publication.

In this chapter, the role of microstructure as well as degradation mechanisms in composite cathodes is discussed. Hereby, built-in microstructural capacity losses, originating from challenges during particle processing, is differentiated from interfacial degradation occurring during cell operation. Different mitigation strategies addressing both types of degradation are further elaborated. Understanding and controlling these aspects is essential for bridging the gap between idealized theoretical models and real composite cathodes.

3.1. Microstructure of Composite Cathodes

This section covers how the microstructure influences the electrochemical performance of composite cathodes, introducing concepts such as tortuosity and percolation.

In an ideal cathode microstructure, all CAM particles are electrically, *i.e.*, electronically and ionically, connected within percolating networks, thereby enabling full theoretical CAM utilization.[22,150] Percolating networks are those that offer a continuous pathway from the current collector to the separator, *i.e.*, through the whole electrode. The percolation behavior depends on several parameters, such as phase fractions[22,93], particle size distributions (PSDs) and ratios[29,151], and mixing strategies[126,152].

Charge transport along these pathways for electrons and ions needs to be as fast as possible, which requires pathways of short length. In real composite cathodes, the pathways are not straight lines through the electrode with length $l_{\text{electrode}}$ but possess an elongated and tortuous effective length l_{eff}. The ratio $l_{\text{eff}}/l_{\text{electrode}}$ is defined as geometric tortuosity τ and allows for calculating effective partial conductivities for electrons and ions.[29] Tortuosity factors and corresponding effective partial conductivities, which are always lower in composites than the bulk conductivities, have been determined experimentally[65,93,153–158] and via electrochemical modeling[29,159,160] in numerous studies. They stress the importance of minimizing the tortuosity to mitigate charge transport limitations in composite cathodes.[93,159]

At first glance, the percolation and tortuosity of electronic and ionic pathways depend on the phase fractions in the composite cathode. With increasing CAM content, the effective electronic conductivity and electronic percolation increase, while the effective ionic conductivity and percolation decrease. Similar considerations are valid for an increased SE phase content. Previous studies suggest that balancing of electronic and ionic transport pathways is beneficial for the cell performance.[93,157] For high-energy SSB cells (cf. Section 4.2), the CAM fraction in SSB cathodes needs to be maximized, while maintaining sufficiently fast ionic pathways, *i.e.*, avoiding ionic transport limitations. Theoretical microstructure simulations for cathode composites can identify suitable phase compositions and PSDs to achieve microstructures with fully percolating networks.[22,151] However, realizing these microstructures in practice remains challenging since the SE, with its mechanical and morphological properties, must already be considered during electrode manufacturing. This marks a key difference compared to LIBs, where the porous network of CAM, conductive additive, and binder can be easily infiltrated by the LE. For SSB cathode composites, the processing, particularly the mixing, ultimately dictates the final electrode microstructure, including percolation and tortuosity behavior, performance, and reproducibility.[126,152] These aspects are discussed in Publication II.

3.2. Built-in Capacity Limitations and the Role of Particle Processing

In practice, microstructures of SSB composite cathodes deviate from theory and pose several challenges, which are already present before any cell operation, referred to here as built-it capacity limitations. Figure 3 displays an image obtained by scanning electron microscopy (SEM) coupled with energy-dispersive X-ray spectroscopy (EDX) of a real and representative microstructure with NCM82 as CAM and Li_6PS_5Cl (LPSCl) as SE. This example serves as the basis for discussing typical microstructural challenges in the following.

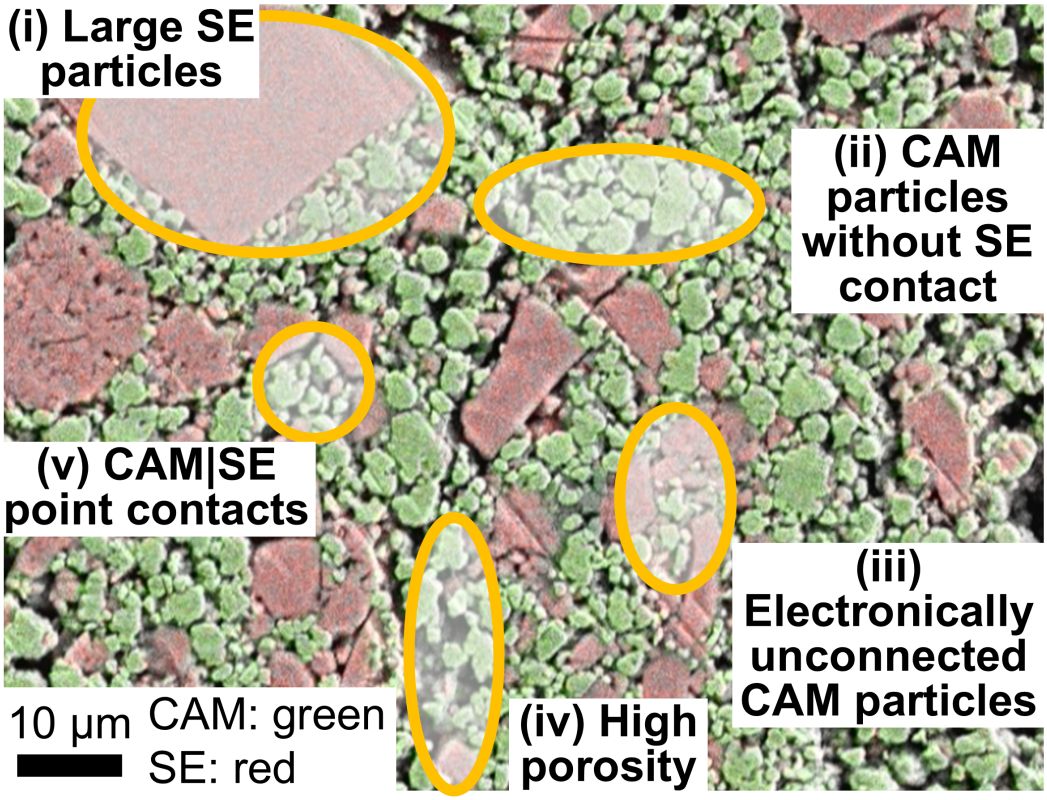

Figure 3. Exemplary SEM-EDX image of an SSB composite cathode microstructure highlighting origins of built-in capacity limitations.

First, the practical realization of tailored particle size distributions is extremely challenging. Typically, CAM particle sizes are predefined, as these materials are generally obtained in commercial quality. As a consequence, the PSD of the SE phase needs to be adapted for achieving high-performance SSB composite cathodes, which requires comminution after synthesis, *e.g.*, via ball milling.[20,148,151,155,159] Often too large SE particles or agglomerates remain, which need to be removed by sieving or are left in the batch and end up in the

composite (see (i) in Figure 3). Such large particles bind unnecessarily large volumes of SE in the composite cathode, which is not available in other regions of the microstructure.[30] In these regions (see (ii) in Figure 3) CAM particles are not in direct ionic contact with the SE. This requires Li-ions to diffuse into neighboring CAM particles, which is a comparatively slow process.[161]

CAM particles may also have no electronic contact via a percolating network to the current collector (see (iii) in Figure 3). These electronically isolated particles are electrochemically inactive and lower the static CAM utilization—a property which is investigated in detail in Publications I, II, and III.

A further often encountered problem in SSB cathodes is a large remaining porosity (see (iv) in Figure 3), which is considered as detrimental.[22,29,159] Reducing porosity goes in line with a better contact between CAM and SE particles. As seen in region (v) of Figure 3, these are usually point contacts, which reduces the active interface area.

The Role of Particle Processing The impact of built-in microstructural capacity limitations can be mitigated primarily by appropriate particle processing.

Ionically or electronically isolated particles are the result of inadequate particle size distributions or insufficient mixing. Previous publications consider "homogeneous" mixing as successful without further quantification. Publication II reveals the importance of the mixing process for accurate data acquisition, evaluation, and interpretation, and discusses an approach to quantify the mixing quality. Particle processing in terms of composite mixing is key for well-performing SSB cathodes. At the same time, it is challenging due to the vast parameter space, such as mixing time and speed, that needs to be explored. Noh *et al.*[126] demonstrated that not only the mixing method but also the order in which the components are mixed can have a significant influence on the electrochemical performance. Also, during mixing, additional effects such as comminution and (de)agglomeration of particles may occur, further complicating the procedure. Since optimizing the mixing process on laboratory scale is usually not the goal during fundamental investigations with a physico-chemical focus, a method is needed to compensate for variations in the mixing process, which is the topic of Publications I and II.

To improve the CAM | SE interfacial contact area, two main processing strategies exist. The first involves infiltration methods, where the SE is wet-chemically synthesized and directly deposited onto the CAM particles.[162–165] The second approach is based on dry coating of SEs on CAM particles, which can be economically favorable since no solvents are required.[23,154,166–168] Publication III systematically investigates such an approach.

Optimizing the particle processing is crucial for large-scale production of SSB composites and can be accelerated using process simulations. In this context, discrete element method (DEM) simulations have proven to be a valuable tool for modeling the mechanical stressing of particles during processing.[30,169,170] A corresponding theoretical framework, originally developed for grinding processes, is provided by the stressing model of Kwade[171]. It considers individual stress events i during which energy, referred to as stress energy SE_i, is transferred to the particles. In general, SE is not constant but follows a frequency distribution. When SE is related to a mass, for instance, that of the stressed particle $m_{\text{particle},i}$, the stress intensity SI is obtained. The mean specific energy input $E_{\text{m,mix}}$ can then be calculated by relating the total energy transferred to the particles to their total mass m_{total} (Equation 1). The total energy is determined by the total number of stress events SN, which is the product of stress frequency SF and process time t_{process}.

$$E_{\text{m,mix}} = \frac{\sum_{i=1}^{SN} SE_i}{m_{\text{total}}} = \frac{\sum_{i=1}^{SF \cdot t_{\text{process}}} SI_i \cdot m_{\text{particle},i}}{m_{\text{total}}} \tag{1}$$

By calculating and comparing $E_{\text{m,mix}}$, the influence of different process parameters, such as mixing time, rotational speed, or grinding media size, can be quantitatively assessed and, as shown in Publication III, eventually linked to experimental observations.

3.3. Interfacial Degradation in Composite Cathodes

During cell operation, further interfacial degradation phenomena in the composite cathode lead to performance deterioration of the SSB, either by increasing the cell resistance or by a loss of active material. Interfacial degradation can be of chemical, electrochemical, or (chemo-)mechanical nature as depicted in Figure 4 and complexly interrelated, thus challenging to deconvolute.[28,67,172–174] The exact degradation pathways and their importance

depend strongly on the material combination used in the cathode composite. In the following, degradation in SSB cathode composites with sulfide SEs, Ni-rich NCM, and CNFs as conductive additive is discussed, since this material combination is promising from an energy and power density perspective but also most challenging with respect to the mitigation of degradation.[16] Moreover, the presented concepts are relevant for Publications IV and V.

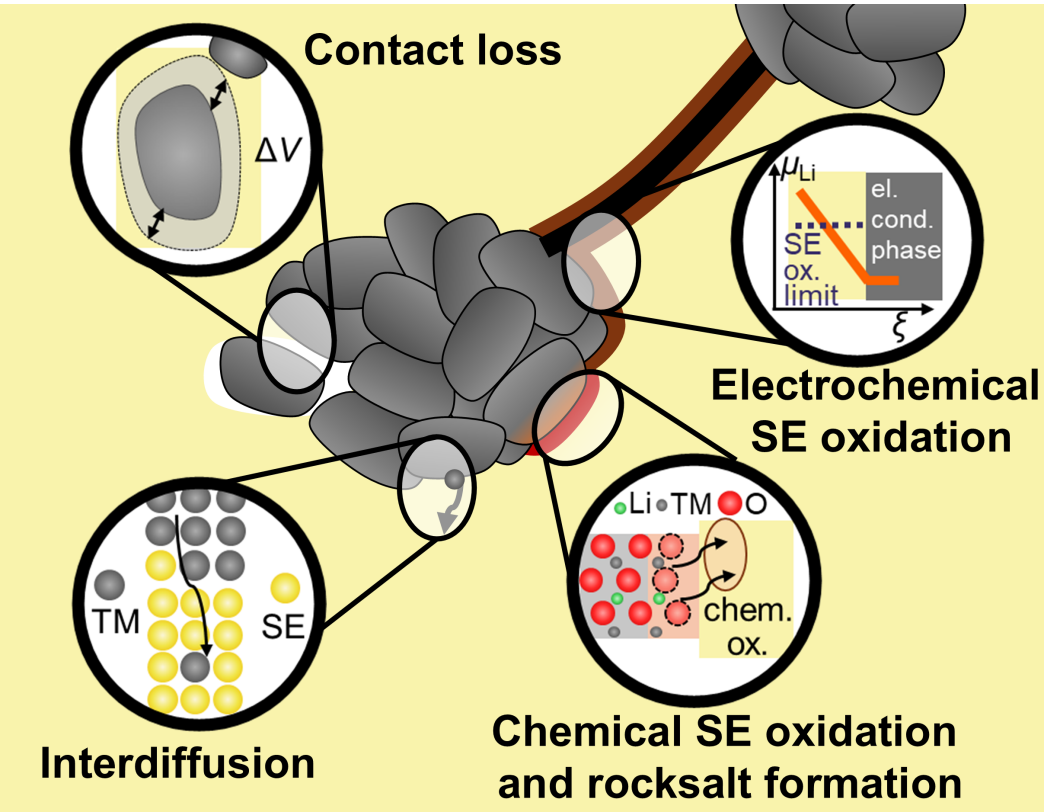

Figure 4. Schematic illustration of interfacial degradation mechanisms in SSB composite cathodes with polycrystalline NCM (dimensions are not accurate).

Electrochemical Degradation of the SE As mentioned in Section 2.2, each SE has an ESW, *i.e.*, a potential range, in which it is electrochemically stable.[81] When in contact with a surface having a potential above or below the ESW limits, the SE is oxidized or reduced, respectively.

In the case of the argyrodite-type sulfide SE LPSCl, possessing a narrow stability window with a practical upper limit of 3.1 V vs. Li^+/Li, this electrochemical oxidation results in the SE losing lithium.[79,82] In the cathode composite, these oxidation reactions occur at three

different interface types, namely at the current collector | SE[175], NCM | SE[176], and CNF | SE[77] interface. The electrochemical decomposition mechanism of LPSCl can be simplified by the following equation, which is not written in a strictly stoichiometric form:

$$\mathrm{Li_6PS_5Cl} \rightleftharpoons \mathrm{Li}_x\mathrm{P}_y\mathrm{S}_z + \mathrm{LiCl(inactive)} \rightleftharpoons \mathrm{S^0} + \mathrm{P_2S_5(inactive)} + \mathrm{LiCl(inactive)} \tag{2}$$

It needs to be noted that P_2S_5 and S^0-like species, often referred to as polysulfides, should be considered as "ideal" oxidation products.[177] Toward their formation, different oxidized intermediate compounds of type $Li_xP_yS_z$ are conceivable, making the exact decomposition mechanism complex.[77,82,175–178]

As indicated in Equation 2, the reactions are partially reversible.[79,82,175,177–179] However, the corresponding reduction reactions require potentials below 2 V vs. Li^+/Li, which are not feasible in NCM-based SSBs.[79,82] Thus, the formed oxidative degradation products persist and increase the resistance due to their low ionic conductivity, leading to performance deterioration.[65,175]

Chemical Degradation of the SE At the SE | NCM interface, additional chemical oxidation of the SE by oxygen takes place. Corresponding reactions can already happen due to mere contact of the SE with NCM.[75,176] More pronounced at high SoC, NCM materials are known to release oxygen[180–182], which reacts with the sulfide SE forming sulfites/sulfates, phosphites/phosphates, and thiophosphites/thiophosphates[173,176,183] as indicated in Equation 3. The equation shown is for illustrative purposes and is not strictly stoichiometric.

$$\mathrm{Li_6PS_5Cl} + \mathrm{O_2(NCM\ lattice)} \rightarrow \mathrm{Li}_x\mathrm{PO}_y + \mathrm{Li}_x\mathrm{SO}_y + \mathrm{Li}_x\mathrm{P}_y\mathrm{S}_z\mathrm{O}_u \tag{3}$$

These chemical decomposition products possess low ionic conductivities[184], leading to an increase in resistance and hindering charge-transfer kinetics.[67,185] The degradation reaction was found to increase with the SoC of the NCM and temperature.[186,187]

Reaction products stemming from electrochemical and chemical oxidation are usually referred to as cathode-electrolyte interphase (CEI).[27,186,188]

Transition Metal Interdiffusion TM interdiffusion out of the lattice structure into the electrolyte is a well-known phenomenon in LIBs.[189] For SSB systems, interfacial diffusion of transition metals has already been reported in 2010 for LCO and a sulfide SE.[190] Zhang *et al.*[134] more recently confirmed via cryo-TEM that dissolution of transition metals from a high-Ni NCM into LPSCl also occurs. Walther *et al.*[77,176,191] assume that interdiffusion of TMs leads to the formation of TM sulfides, which are intermediate products and difficult to detect with analytical ex situ methods.

In general, this topic has received little attention in the SSB community so far. Systematic studies are required to clarify the mechanism of dissolution/interdiffusion and to what extent it has a detrimental effect on the performance in SSBs.

Degradation of the CAM The above-mentioned oxygen release from the NCM at high SoC is accompanied by an irreversible structural transformation. By removing oxygen, the layered structure (TM-O_2) transforms into a cubic rocksalt-type (TM-O) layer.[141,192] This highly resistive phase in the surface region of the particles impedes Li-ion transport by increasing the charge transfer resistance, and it is thus seen as detrimental.[140,180,188]

These and other degradation mechanisms within CAM particles, such as cation mixing, can occur and lead to capacity fading. They are not unique to SSBs, but are inherent challenges for NCM-based cathodes in both SSBs and LIBs. Details can be found and a lot can be learned from respective works on layered oxide materials in LE systems.[141,144,193,194]

Chemo-Mechanical Degradation Chemo-mechanical effects are an interplay between CAM and SE particles and originate from volume changes and the release of gaseous species.

The aforementioned oxidative degradation reactions of the SE lead to decomposition products with smaller molar volumes.[195] Consequently, the partial volume of the catholyte shrinks, and pores form at the interface. Also, the chemically oxidized products show an increased brittleness and stiffness, which hinders them from maintaining proper contact with the CAM particles.[136,195] Oxygen from the NCM not only oxidizes the SE, but can also be released as gaseous species[196], causing additional pore formation and contact loss.

CAM particles further undergo volume changes of up to $\sim$6 % during de-/lithiation processes, which are, in the case of NCM, proportional to the Ni-content and SoC of the material.[140,144,145,197,198] Especially at a high degree of delithiation during the H2$\rightarrow$H3 phase

transition, the unit cell volume of NCM shrinks strongly (cf. Section 2.3). If the surrounding SE is not capable of following these volume changes, further partial or complete contact loss occurs. Thereby, the mechanical properties of the catholyte play a key role, which is demonstrated in Publication III. Additionally, the volume changes can result in interparticle cracking if polycrystalline materials are used. While LEs can penetrate into these cracks and increase the active surface area[199], cracking is a severe problem in SSBs since the SE is not able to fill the occurring cracks, leading to slow kinetics.[161]

All these effects can lead to partial or complete contact loss of NCM particles to the SE or to other NCM particles, which increases the lithium diffusion pathways or reduces the amount of cyclable NCM.[161,200,201]

3.4. Strategies to Mitigate Interfacial Degradation

To mitigate interfacial degradation in composite cathodes, different approaches have been developed, which are discussed in this section. These include modified CAM particles, protective CAM coatings, and adapted cycling conditions.

CAM Particle Level The development of single-crystalline CAMs is considered a promising approach to mitigate interparticle cracking.[135,136] Conforto *et al.*[200] have shown that single-crystalline NCM significantly reduce the detrimental impact of chemo-mechanical degradation in SSB cathodes compared to poly-crystalline NCM. However, according to Minnmann and Strauss *et al.*[20], the problem of volume change persists and might be even more severe along certain facets. This requires a controlled tailoring of the particle shape.[202]

A further strategy involves the development and use of zero- or low-strain materials[198] or blending CAMs with opposite volume changes[197]. However, these approaches have so far relied on low-Ni containing, *i.e.*, low capacity, materials.

Doping, either in the bulk or in the surface of the NCM, is another investigated strategy.[203] The idea is to prevent deleterious phase transformations via crystal lattice stabilization.[204]

Protective CAM Coatings An intensively researched approach to mitigate interfacial degradation is the use of protective CAM coatings.[32,45,173,203] In SSB composite cathodes, an ideal coating protects in three ways: First, it has a low electronic conductivity which shields

the SE from the high potential, mitigating electrochemical oxidation.[45,205] Second, it should reduce chemo-mechanical degradation.[201] Third, it needs to serve as a chemical barrier to prevent chemical reaction with the SE.[32]

Various coating chemistries have been investigated, ranging from binary and ternary oxides[206,207], polymers[201,208] or other SEs with higher stability[209]. At this point, it needs to be noted that usually residual lithium compounds such as LiOH and Li_2CO_3 remain present on the CAM surface after synthesis, which can be regarded as a "natural" or "unintentional" coating.[210,211] Thus, any further intentional coating will rather result in a hybrid coating.[212] An impression of the variety of reported coatings can be found in corresponding review articles and will not be discussed further here.[32,33]

Within this variety, lithium niobate ($LiNbO_3$) can be considered as a standard CAM coating layer. However, it should be noted that *the* $LiNbO_3$ coating does not exist. The final morphology and performance of this, as well as all other coatings, is affected by many process parameters such as coating thickness, annealing temperature or atmosphere, coating process, or additives.[207,213,214] Typical publications on protective coatings, however, basically rely on comparing the performances of cells using coated and uncoated CAM to demonstrate the superior performance of the reported coating. This leads to very unspecific statements and only a limited number of studies investigate multiple processing parameters.[207,214–216] Furthermore, coatings are usually tested with different CAMs and SEs. Given the general difficulties related to benchmarking as discussed in Section 4.2, a comparison across different publications is basically impossible. This hinders the development of optimal coatings.

A first attempt toward systematic benchmarking of CAM coatings was proposed by Hertle *et al.*[173]. Their approach, based on time-of-flight secondary ion mass spectrometry (ToF-SIMS), allowed differentiation between different pathways of degradation, potentially enabling a better mechanistic understanding. This benchmarking framework was employed in Publication IV and further developed in Publication V.

Adapted Cycling Conditions The interfacial degradation phenomena and thereby the cycle life of SSBs can also be tailored by adapting the cycling conditions. Hereby, the key is to avoid the H2→H3 phase transition, which comes along with severe chemo-mechanical degradation as discussed.

This can be realized either by fast charging, so that the cut-off voltage is reached due to the higher overpotential while the NCM has not undergone the phase transition (cf. Section 2.3). However, this only works if the cell is charged in constant-current (CC) mode and not in constant-current-constant-voltage (CCCV) mode.

Another way is to reduce the upper cut-off voltage below the phase transition. Independent of the charging profile, *i.e.*, CC or CCCV, the NCM particles never undergo the H2→H3 phase transition with associated volume changes.[217] This could also reduce the effect of oxygen release and corresponding CEI as well as rocksalt layer formation. However, these advantages come at the expense of reduced achievable capacity, which might be reasonable depending on the specific application scenario.

4 Holistic and Realistic Considerations on SSB Testing

Evaluating the performance and advancing fundamental understanding of SSB materials and composite cathodes requires tailored experimental setups. While research on the laboratory-scale typically operates at low TRLs (TRL 1-4), the omnipresent final battery product demands TRL 9.[6] This significant gap between expectations and reality has already been discussed by Frith *et al.*[6] from a non-academic perspective.

This chapter assesses the role and limitations of model cells, as used in this doctoral thesis, and addresses fundamental challenges in performance benchmarking, standardization, and comparability within SSB research. Finally, an outlook is provided on how natural and engineering sciences can synergistically work together to bridge the TRL gap.

4.1. Laboratory-Scale Testing with Model Cells

Laboratory tests in academic research are often carried out in pelletized press cells (Figure 5), which have been developed in different research groups at early stages of SSB research.[34] Press cells are also used in all works of this doctoral thesis and are basically unchanged for more than eight years.[127]

Press cells are reasonable for laboratory-scale testing for two main reasons. First, only small amounts of materials are needed, typically less than 100 mg per cell. This is important at low TRLs, since novel SEs are often not available in large quantities or are still expensive. Secondly, the impact of engineering factors is considered relatively small, partly because the process chain is short and involves only a few steps, allowing a better focus on material and interface properties. In simplified terms, building a pelletized press cell "only" involves

mixing powders, typically with a mortar and pestle, filling them into a die, and compacting them uniaxially. This approach can be seen as a modular setup that is relatively easy to adapt, in principle allowing one component to be varied while keeping the others constant.

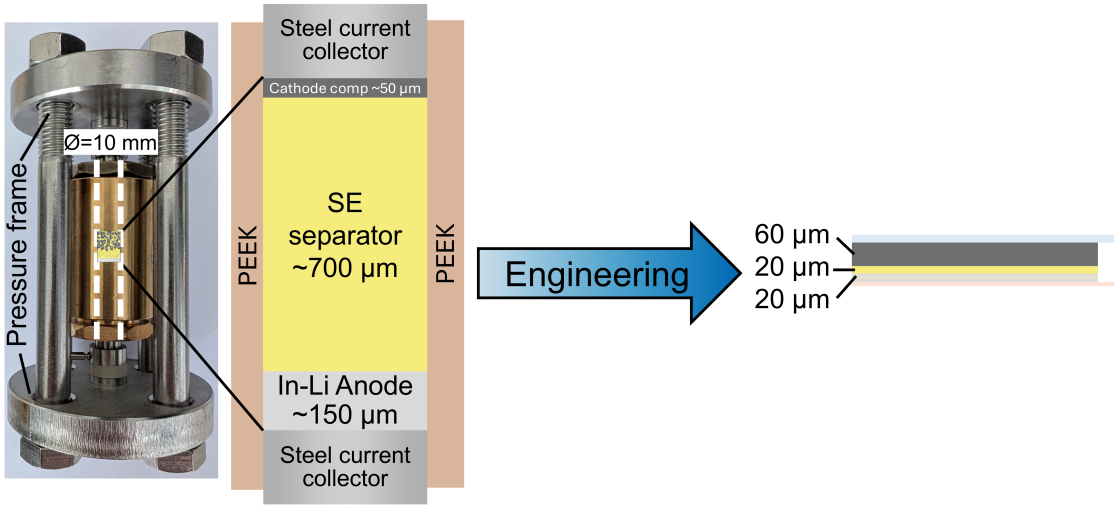

Figure 5. Comparison of the dimensions for a pelletized press cell and a cell designed for practical application. The latter's dimensions are based on ref.[218].

When comparing typical dimensions of such cells with application-relevant cell dimension values, a clear gap becomes apparent (Figure 5). Most notably, a significantly thicker separator and, instead of an LMA, a thick In-Li alloy anode are used. The main reason is to prevent negative effects originating from these parts of the cell, such as dendrite formation and excessive SEI formation, allowing focus solely on cathode-related phenomena. Bridging these gaps, *e.g.*, by fabricating thin separator sheets, involves a lot of advanced engineering science, which can easily distract from the actual, often fundamentally scientific, research question. Thus, the press cells, which are used for cathode-related investigations in this doctoral thesis, should be considered as model cells.

Challenges of Standardization Tests with these model cells are expected to yield reliable and comparable results. However, in 2024 Puls *et al.*[34] demonstrated in an interlaboratory round robin study that the opposite seems to be the case. Their study revealed that a lack of standardization resulted in varying cell assembly parameters across different groups, each using their own custom-made cell setups. These setups differ in current collector diameters, sealing methods, and ways to apply stack pressure.[219]

In the round robin study, large performance variations of full cells were also observed, despite using the same materials.[34] Due to the complexity of the datasets, the exact origins of these discrepancies remained largely unexplained. Nevertheless, the authors emphasized the need for more rigorous reporting of cell assembly parameters and recommended performing measurements in triplicate to improve comparability and reproducibility. Publication II of this thesis implemented this practice, demonstrated a satisfying intralaboratory reproducibility, and proposed guidelines to enhance overall data reliability when investigating SSB cathodes.

The issue of standardization and reporting in SSB testing has been addressed in several comment articles over the past two years.[220] N. Vargas-Barbosa[221] discussed that the reproducibility and comparability of electrochemical data are general problems in the scientific community. As a first step toward improvement, more detailed and transparent reporting of synthesis, handling, processing, assembly, and electrochemical testing conditions was recommended. C. Villevieille[222] highlighted that better reporting is equally important when studying battery materials with advanced characterization techniques. J. Drnec and S. Lyonnard[223] specifically pointed out the need for more reliable and reproducible synchrotron-based characterization methods in battery research. In addition, a perspective article by Wu *et al.*[218] also raised awareness of the importance of reliable SSB testing.

4.2. Issues in Performance Benchmarking

This section highlights the difficulties of benchmarking the electrochemical performances of batteries across different studies.

In simple terms, the ultimate goal of a battery is to store and deliver as much energy as possible, in the shortest possible time, and as many times as possible. This is reflected in a high specific energy E_m (Equation 4) and a high specific power P_m (Equation 5), which depend on the cell voltage V_cell, accumulated charge Q and the current I:

$$E_\mathrm{m} = \frac{V_\mathrm{cell} \cdot Q}{m_\mathrm{cell}} \tag{4}$$

$$P_\mathrm{m} = \frac{V_\mathrm{cell} \cdot I}{m_\mathrm{cell}} \tag{5}$$

In a commercial product (TRL 9), E_m and P_m need to be referred to the total mass of the cell m_{cell}, including materials, current collectors, and the cell casing. In SSB research, however, cell-specific energy or power values are rarely reported in fundamental studies (TRL 1-4).[19] Instead, specific capacities, q, or areal capacities, Q_A, depending on the current, are taken as a figure of merit. In studies focusing on cathodes, the charge is often referred to the CAM mass in the composite. The resulting specific capacity values, q_{CAM}, and corresponding capacity losses are used to compare different modifications and draw conclusions on the material properties. In the following discussion, the focus lies on CAM-specific capacities and the discharge process. Analogous considerations apply to the volumetric capacity, *i.e.*, accumulated charge per volume, and the charging process.

During cell discharge, the measured V_{cell} decreases until a pre-defined cutoff voltage V_{cutoff} is reached. According to Equation 6, V_{cell} differs from the equilibrium voltage V_{eq} by the overpotential η when a current I is drawn, which lowers the achievable capacity. The overpotential depends on the cell resistance, R_{cell}, which contains different resistance contributions from anode, separator, and cathode (Equation 7). Thereby, the cathode resistance contains three main components (Equation 8) originating from charge transport (R_{ohm}), charge transfer (R_{ct}), and diffusion (R_{diff}).[2] The resistance values are not constant, but can evolve over SoC of the CAM and cycling time.[24,161]

$$V_{ch/dis} = V_{eq} \pm \eta = V_{eq} \pm I \cdot R_{cell} \tag{6}$$

$$R_{cell} = R_{anode} + R_{separator} + R_{cathode} \tag{7}$$

$$R_{cathode} = R_{ohm} + R_{ct} + R_{diff} \tag{8}$$

For a theoretical discharge curve under quasi-equilibrium conditions, the overpotential is almost zero (Figure 6) and the achieved capacity sets an upper limit. In practice, the discharge curve differs from the ideal curve, and capacity losses are observed. Publications I, II, and III discuss how these capacity losses can be divided into static and kinetic losses and how to separate them quantitatively. While kinetic losses depend on factors which increase the overpotential, static capacity losses originate from electrochemically inactive CAM particles

and are initially caused by the processing before cell operation (cf. Section 3.2). They can increase further due to chemo-mechanical degradation. Both contributions can lead to a discrepancy between capacities achieved in LIBs and SSBs with the same CAM.[140,150,161,200]

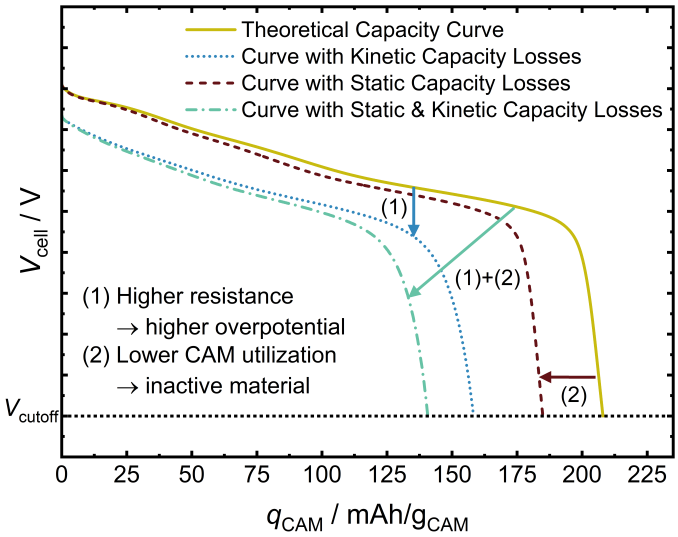

Figure 6. Discharge curves illustrating static and kinetic capacity losses compared to the theoretical capacity equilibrium curve. All curves are calculated from experimental data of cells with NCM85 as CAM.

Another figure of merit is the rate capability, *i.e.*, how much charge can be stored and extracted at a certain C-rate. When using this kinetic quantity, attention needs to be paid to the different resistance contributions (Equation 7) which all affect the overpotential, *i.e.*, how fast the cutoff voltage is reached, and thus the attainable specific capacity. Hence, q_{CAM} is not only affected by cathode-related resistances (Equation 8) but also by contributions of the separator and the anode. As experimentally shown by Alt *et al.*[64], the anode can be kinetically limiting already at relatively low current densities, leading to a non-negligible overpotential. Similarly, a thick separator with a higher resistance will affect the capacity, which is in the end attributed to the cathode.

To properly assess individual cathode kinetics, 3-electrode (3E) setups are required. However, the press cells used in SSB research (cf. Section 4.1) are typically 2-electrode (2E) cells. Several custom-designed 3E SSB cell setups have been reported[224–227], but these are often difficult to prepare or fail to provide a sufficiently stable reference potential for long-term testing. Overall, a widely applicable and easily implementable standard approach across research groups is still lacking.

As stated in a benchmarking study by Randau *et al.*[19], "the interdependence of cell performance measures and the lack of a basic reference system make it difficult to evaluate overall ASSB performance across different cell chemistries". SSB reports usually focus on specific aspects such as modifications of the catholyte or CAM coatings. As mentioned, the investigations are carried out in model cells that have certain dimensions. Since different studies use different thicknesses for the separator and the anode, corresponding values for E_{m} and P_{m} are hardly comparable and significantly lower than if an optimized separator and anode were used.

In addition to different cell setups with varying geometries, the parameters during electrochemical testing also hinder proper benchmarking and comparison. For example, increasing the stack pressure leads to better capacity retention, although it has limited relevance for practical applications.[219,228] Furthermore, the experimental temperature has two effects: it improves transport kinetics while simultaneously accelerating interfacial degradation kinetics.[187] The latter is also dependent on the cycling protocol, in particular on how long the CAM remains in the delithiated, *i.e.*, more reactive state. Consequently, the mode of charging and discharging affects the cell behavior, depending on whether CC or CCCV mode is used. Also, the rest time at high SoC matters. To mitigate degradation, it is beneficial to discharge the cell directly after charging. However, this is far from application since batteries remain in the charged state for most of the time.[229] On the other hand, the exact operating profile is hardly predictable, and a study by Geslin *et al.*[230] showed that dynamic cycling enhances battery lifetime compared to constant current discharge.

Overall, every individual testing and cell parameter affects the electrochemical results of an SSB. To enable meaningful and fair benchmarking, all of these parameters would need to be identical. However, no standardized testing protocols or norms currently exist for SSBs, and different applications often require different performance metrics. Considering that even for a mature technology like LIBs, standards typically exist only on a national level rather than globally, the development of universally accepted testing and evaluation criteria for SSBs appears highly challenging, if not unrealistic. In fact, the definition and application of appropriate metrics and methods remain a fundamental and unresolved issue across many areas of scientific research, far beyond the field of batteries.[231]

Evaluating Cathode Performance in Model Cells Given that the final product, *i.e.*, a battery, is already on the market with existing applications, SSB research at low TRLs is often expected to reflect practical applicability.[218] In the following paragraphs, the performance of cells investigated in this doctoral thesis are evaluated with respect to their relevance for practical applications. For this purpose, they are compared to performance targets adopted from the study by Randau *et al.*[19].

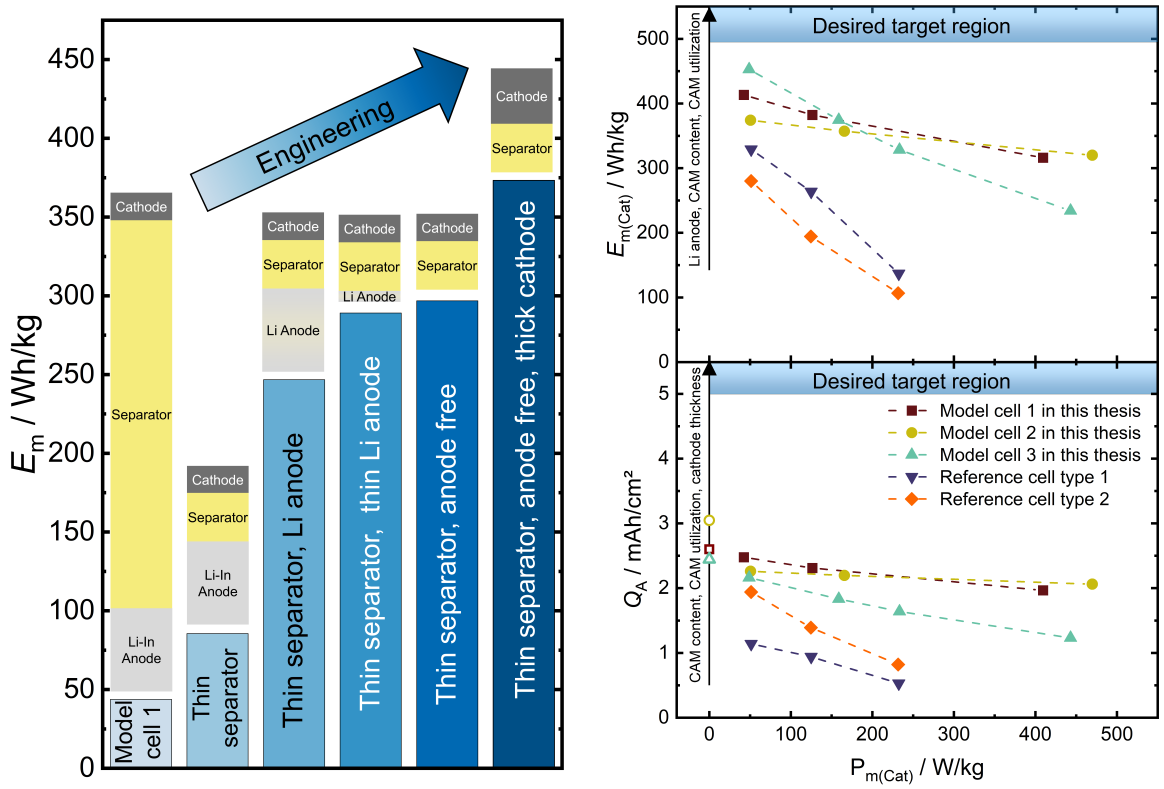

(a) The impact of cell component choices on the cell specific energy E_m. The calculations do not include current collectors and cell casings, which reduce E_m.

(b) Cathode specific energy ($E_{m(Cat)}$, top) and areal capacity Q_A (bottom) as a function of cathode specific power $P_{m(Cat)}$. Empty symbols indicate the nominal Q_A.

Figure 7. Specific energies and performance benchmarking of SSB model cells toward application-relevant properties. The values for the model cells investigated in this thesis are described in the main text and in Table 1. The reference cells and target regions are adopted from ref.[19].

As shown in Figure 7a, E_m with respect to the cell mass, excluding the weight of current collectors and cell casing for SSBs, is only about 40 Wh/kg for a typical laboratory model press cell and thus significantly lower than the minimum requirement for application of

more than 250 Wh/kg. This model cell, used in Publication II, consists of a ∼150 µm thick In-Li anode (48 mg), a ∼700 µm thick (80 mg) Li_6PS_5Cl separator, and a composite cathode of ∼50 µm thickness (15 mg) with 70 wt% NCM82.

The following values need to be considered as hypothetical and assume that an optimized cell engineering is enabling thin separators and anodes. By decreasing the separator down to ∼85 µm (10 mg), E_m roughly doubles to 86 Wh/kg. At this point, it should be noted that separators in this thickness range have already been reported.[232,233] Replacing the In-Li alloy anode by an LMA (100 µm, 3.4 mg), significantly increases the energy density up to ∼261 Wh/kg. In a final cell, careful balancing of cathode and anode is necessary, and, in general, an anode thickness of 20 µm seems to be required and feasible.[18,218] By correspondingly reducing the weight of the LMA, the energy density reaches ∼289 Wh/kg. Realization of zero excess lithium, *i.e.*, anode-free concepts[18,119] would increase the energy density by about 8 Wh/kg to ∼297 Wh/kg. Further increasing the cell-specific energy requires thicker cathodes.[57] Doubling the cathode composite mass in the presented scenario would lead to E_m > 370 Wh/kg, under the assumption that the achievable capacity scales linearly with the composite mass. Overall, main improvements in cell-specific energy can be expected from minimized separator layer thickness[19,57] and a Li anode with minimized excess lithium[18], which requires advanced engineering.

The cell performance is governed by the complex interactions between the anode, separator, and cathode. All components need to be optimized to achieve a low R_{cell} and high E_m and P_m, which is theoretically limited by the specific energy of the cathode composite. As proposed by Randau *et al.*[19], the hypothetical specific energy of the cathode composite, $E_{m(Cat)}$, which considers only the cathode composite mass, can serve as a useful metric to compare the cathode performance in model cell systems. In the following, this metric is used to benchmark the model cell configurations experimentally investigated in this doctoral thesis. Specifically, *Model cell 1* was used in Publication II, *Model cell 2* in Publication III and *Model cell 3* in Publications IV and V. These are compared to two reference cells of the study by Randau *et al.*[19], published in 2020, which employed $LiNi_{0.6}Co_{0.2}Mn_{0.2}O_2$ (NCM622) as CAM with Li_3PS_4 (LPS) as catholyte. Details for all cells are summarized in Table 1.

The top part of of Figure 7b displays a Ragone plot for the five different cells. A clear improvement over the older reference cells is observed, particularly at higher P_{m}. However, the desired target region exceeding 500 Wh/kg for $E_{\mathrm{m(Cat)}}$ is still not reached.[19] This will require an increased CAM content, a higher CAM utilization, and the successful incorporation of a stable LMA.

Table 1. Overview of model cells used in this doctoral thesis and reference cells, showing the compositions of the cathodes for which metrics are shown in Figure 7b.

Cell	Composition (CAM:SE:Additive)	CAM Type	SE Type	Additive	Anode
Model cell 1	70:30:1 (15 mg)	NCM82	LPSCl	CNF	In-Li
Model cell 2	80:20:x (15 mg)	NCM82	Li_3InCl_6	CB	In-Li
Model cell 3	80:20:0 (12 mg)	NCM85	LPSCl	–	In-Li
Reference cell 1	70:30:0 (10 mg)	NCM622	LPS	–	Li
Reference cell 2	70:30:0 (20 mg)	NCM622	LPS	–	Li

In addition to $E_{\mathrm{m(Cat)}}$, a high Q_{A} is essential to achieve cells of sufficient size. The most straightforward way to increase Q_{A} is simply by increasing the amount of cathode composite. As shown in the bottom part of Figure 7b, all model cells presented in this thesis already exceed 2 mAh/cm², thereby surpassing Q_{A} of the reference cells. Nonetheless, the desired target region of more than 5 mAh/cm² has not been reached.[18,19] Such high loading cathodes, even exceeding 20 mAh/cm², have been successfully demonstrated by Li *et al.*[57]. In their work, the authors used an SE with an ionic conductivity of more than 30 mS/cm in a thick battery electrode.

According to a recent perspective by Wu *et al.*[218], areal loadings of >3 mAh/cm² already provide a more realistic reflection of practical applications. In this context, the model cells of this thesis, which need to be considered as reproducible standard cells for cathode-related investigations, not being explicitly optimized for high energy or power density, are relatively close to this requirement. The improvements relative to the earlier reference cells can primarily be attributed to the use of higher-Ni CAMs and a more conductive SE, which together contribute significantly to the enhanced performance. Approaching application-relevant cathode metrics for model cells in the near future appears to be well within reach, highlighting the practical potential of these model systems

4.3. From Laboratory Toward Commercialization

Publications in the field of SSBs should be critically evaluated since often big claims are made from small batteries (adapted from ref.[234]). Rather than overhyping laboratory-scale findings[35], results should be rationally assessed with regard to their relevance and practical applicability. It is important to emphasize that studies using pelletized press cells represent model systems tested under idealized conditions. These may include, for instance, low cathode loadings, thick separators, or high stack pressures. All of these conditions deviate from practical requirements and ultimately demand engineering solutions.[6] In general, significant performance improvements can be expected from advanced and optimized process and cell engineering, as currently demonstrated for LIBs, with the dry battery electrode technology[7,8] being one prominent example.[235]

Toward the commercialization of SSBs, cathode composites must be manufactured in sheet-type form to produce large-format pouch cells. While small pouch cells are certainly closer to real-world applications than press cells, they already pose significant challenges on the laboratory scale: They require large amounts of materials, which in practice are simply not available or too expensive. In addition, their production involves long process chains with numerous engineering variables, such as electrode casting and drying, and subsequent calendering.[72,91] These parameters must be carefully optimized for each material system, which can easily divert focus from fundamental scientific questions. Furthermore, a binder that is typically electrically isolating[29], but can also be ionically conducting[236–238], needs to be incorporated, adding further complexity to the mixing process.

As illustrated in Figure 8, laboratory-scale results can vary considerably, often providing only a rough estimate, since each measurement represents a single data point within a vast process parameter space.[6] This stresses the importance of developing efficient benchmarking approaches, for instance, as proposed in Publication V for protective CAM coatings, to move beyond proof-of-principle studies and to better capture process influences already at an early stage of research.[173,214] At the same time, research at low TRL should critically assess results to avoid over- or underestimating the performance and drawing misleading conclusions. This risk becomes apparent when underestimated processing factors, such as cathode composite mixing, dominate the observed behavior as discussed in Publication II.

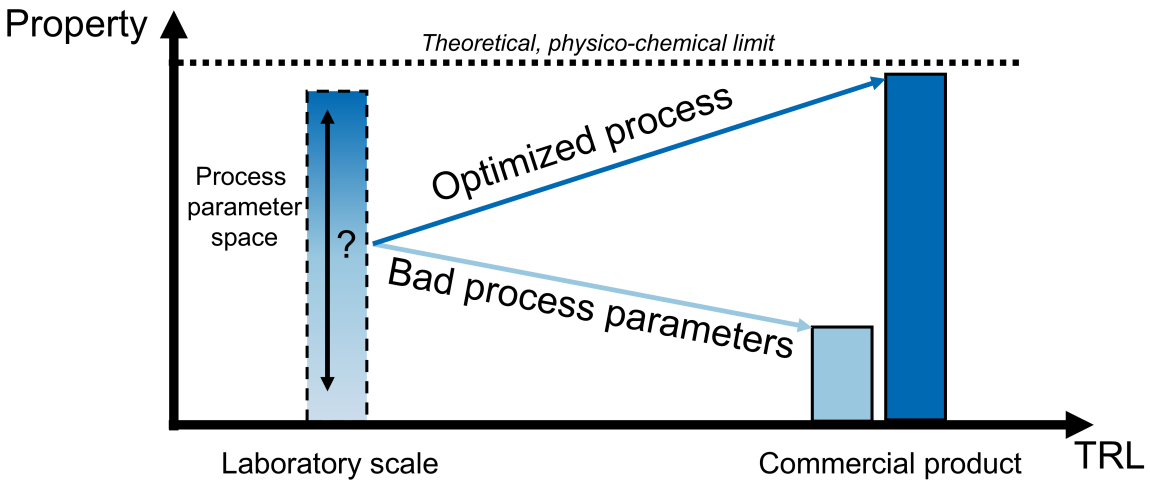

Figure 8. Bridging the gap from laboratory to commercial scale. Process optimization is crucial to reliably and reproducibly approach the theoretical performance limit of a material in a commercial product, moving beyond the broad process parameter space explored at laboratory scale.

In the final product, the electrochemical properties may be significantly better or worse compared to laboratory-scale results, depending on the specific processing conditions. Scaling up processes, aiming at reliably approaching theoretical limits, involves significant engineering and technological efforts, and represents a critical aspect of scientific advancement. Natural sciences play a key role in uncovering theoretical and physico-chemical limits, and in understanding fundamental mechanisms and processes that are generally valid and independent of TRL and scale. Bridging the TRL gap therefore requires a deep understanding of the process–structure–property–performance relationship. Regardless of scale, laboratory or industrial, the process ultimately defines the product.

PART II

Results and Discussion (Publications)

5 Mixing Matters

At the start of this thesis project in January 2022, cathode composites were commonly prepared on a laboratory scale by manual mixing using a mortar and pestle. The resulting composite cathodes were often simply described as "homogeneously mixed" without providing further quantification. At that time, it was unclear whether hand mortaring could be performed reproducibly, even though it was widely used due to its simplicity and accessibility. It was already known that SSB performance depends not only on intrinsic material properties but also on the microstructure in the cathode composite, *i.e.*, the arrangement of particles.[22,29] However, systematic studies focusing on the mixing process and its impact on microstructure and reproducibility were missing.

The following two publications address this gap, providing a detailed assessment of composite microstructures resulting from different mixing procedures. They demonstrate that the mixing process plays a decisive role in determining both electrochemical performance and reproducibility, as it directly determines how many CAM particles are in fact incorporated within the electronic and ionic networks. This property is shown to be quantifiable in terms of the static CAM utilization and needs to be differentiated from kinetic limitations.

The findings underscore that the mixing process, *i.e.*, how particles are processed and integrated into functional composites, is equally important as the material selection itself. Even at a laboratory scale, it must be rigorously controlled and properly reported to avoid misinterpretations of experimental data. In short: mixing matters.

5.1. Publication I: *Quantifying static capacity losses in solid-state battery composites via coulometric titration comparison*

An in situ electrochemical method to quantify the amount of electrochemically active mass, *i.e.*, the static CAM utilization, in the cathode composite was originally reported in 2021 by Conforto *et al.*[200] to track active mass loss during extended cycling. Also, a previous study by Bartsch *et al.*[239] from 2019 used XRD to estimate the CAM utilization. However, a direct comparison between the two approaches was missing.

This work addresses that gap in the form of a methodology paper, critically evaluating both methods. Advantages, disadvantages, underlying assumptions, as well as limitations are comprehensively summarized. The study concludes that XRD is not suitable as a standard approach to determine the static CAM utilization. Without specialized equipment, such as specific cell housings and X-ray sources, it can only be applied ex situ, and its data evaluation is error-prone. By contrast, the in situ electrochemical method, called coulometric titration comparison (CTC), is straightforward and can be easily integrated into standard electrochemical testing programs. Thereby, the paper provides detailed guidance on the proper application of the CTC method for quantifying the static CAM utilization. This microstructural descriptor allows a distinction between static and kinetic capacity losses.

The study was designed by M. Kissel and K. Vettori under the supervision of J. Janek. The first authorship is shared between M. Kissel and K. Vettori as they contributed equally to this work. M. Kissel investigated the SSB cells and carried out the XRD measurements with the help of D. Wagner. K. Vettori provided the LIB reference data, refined the procedure to evaluate the CAM utilization, and implemented it in a Python program. D. Wagner performed the XRD analysis and S. Schröder contributed to the discussion. The manuscript was written by M. Kissel and K. Vettori and edited by all co-authors.

Reproduced from: Kilian Vettori, Maximilian Kissel, Daniel Wagner, Steffen Schröder, Jürgen Janek. Quantifying Static Capacity Losses in Solid-State Battery Composites via Coulometric Titration Comparison. *Chem. Commun.*, 2026, 62, 5241, DOI: 10.1039/D5CC07213A,

ChemComm

ROYAL SOCIETY OF CHEMISTRY

COMMUNICATION

View Article Online
View Journal | View Issue

Cite this: *Chem. Commun.*, 2026, **62**, 5241

Received 18th December 2025,
Accepted 10th February 2026

DOI: 10.1039/d5cc07213a

rsc.li/chemcomm

Quantifying static capacity losses in solid-state battery composites *via* coulometric titration comparison

Kilian Vettori, †*[a] Maximilian Kissel, †[a] Daniel Wagner,[a] Steffen Schröder[b] and Jürgen Janek *[a]

An electrochemical method is discussed to quantify *in situ* the static CAM utilization, *i.e.*, the fraction of electrochemically active mass in solid-state battery composite cathodes. For that, coulometric titration curves of the same active material in cells with solid and liquid electrolytes are compared. The results are contrasted with an *ex situ* method based on X-ray diffraction.

Solid-state batteries (SSBs) have attracted substantial attention in recent years due to their potential to deliver higher energy and power density, along with expected improved safety compared to conventional lithium-ion batteries (LIBs) that use liquid electrolytes (LE).[1,2] Despite the potential benefits, several challenges must be overcome before SSBs can be widely commercialized.[3] This includes issues such as interfacial instability between the electrodes and the solid electrolyte (SE), as well as chemo-mechanical degradation, which currently limits performance and long-term stability.[4] While the goal for the negative side is a reservoir-free lithium metal electrode, the energy density of the cell is limited by the positive electrode, which is designed as a composite of cathode active material (CAM), SE and conductive additives.[5]

As a figure of merit, CAM-specific capacities and capacity losses are often calculated with respect to the mass of CAM in the cathode, $m_{\mathrm{CAM,tot}}$, and used to compare the performance of different composites or cells.[6] In a recent study, we discussed the importance of differentiating between static and kinetic capacity losses in SSB composite cathodes and revealed that different composite mixing can be a main reason for variations in mass-specific capacities with respect to $m_{\mathrm{CAM,tot}}$.[7] Thereby, a central challenge of SSB composites is to properly connect all CAM particles electronically. If this is not achieved, lower mass-specific capacities are observed in SSBs compared to LIBs. We recommend to consider these as static capacity losses.[7,8] The accurate evaluation of mass-specific capacities accounting for static capacity loss of SSBs is critical to avoid data misinterpretation at an early stage of research and for quality control during scale-up.

In the present work, we discuss a reliable and simple electrochemical method to estimate *in situ* the actual electrochemically active mass, $m_{\mathrm{CAM,act}}$, for a given SSB (half) cell with respect to a reference LIB measurement. The methodology is further called coulometric titration comparison (CTC) and has been successfully employed in several of our previous publications.[7–11] CTC shall be highlighted as well as critically discussed here in depth to be more easily implemented by other scientists testing active materials in different electrolyte systems. First, we sketch the differences between LIB and SSB cathode microstructures and their consequences for the capacities during cycling. Then, we illustrate the working principle and the experimental approach of CTC and discuss underlying assumptions as well as natural limitations of the method, including the numerical uncertainty of the method. Finally, we show the results of CTC from an exemplary measurement with $LiNi_{0.82}Mn_{0.07}Co_{0.11}O_2$ (NCM82) in an SSB composite cathode with Li_6PS_5Cl as the SE, and in a porous cathode in organic LE. The determined active mass $m_{\mathrm{CAM,act}}$ and the resulting CAM utilization $\Theta_{\mathrm{CAM,SSB}}$ are compared with Rietveld-refined *ex situ* XRD measurements on composite cathodes, revealing the fraction of electronically unconnected, inactive CAM.

Let us first picture the difference in connectivity of CAM particles in the cathodes of LIBs and SSBs (Fig. 1). In conventional LIBs a porous, electron-conducting network of CAM particles, binder, and carbon additives is infiltrated by LE.[12,13] In this porous electrode design, it can be assumed that nearly all CAM particles are ionically and electronically connected and thus electrochemically active (Fig. 1a). For discussion of this assumption the reader is referred to SI Section S2.1. Differences

[a] *Institute of Physical Chemistry & Center for Materials Research (ZfM/LaMa), Justus-Liebig-University Giessen, Heinrich-Buff-Ring 17, 35392, Giessen, Germany. E-mail: kilian.vettori@uni-giessen.de, juergen.janek@phys.chemie.uni-giessen.de*
[b] *Institute of Experimental Physics I & Center for Materials Research (ZfM/LaMa), Justus Liebig-University Giessen, Heinrich-Buff-Ring 16, 35392, Giessen, Germany*
† These authors contributed equally.

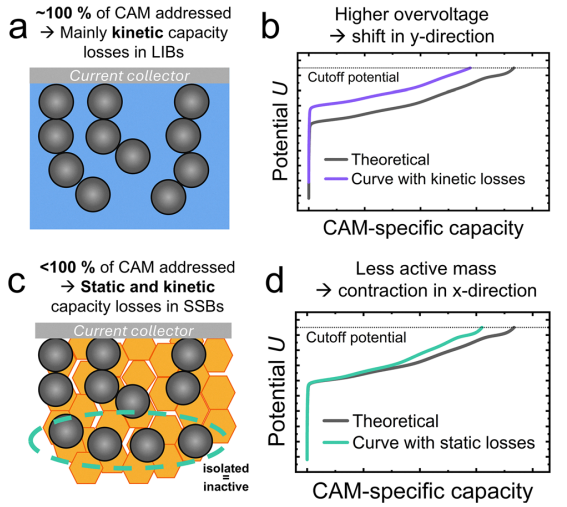

Fig. 1 Cathode designs in LIB and SSB. (a) In LIB, all CAM particles are assumed to be electrochemically active (validated in SI Section S2.1). (b) Thus, different CAM-specific capacities are the result of kinetic losses. (c) In SSB, electronic connection of CAM particles might be incomplete. (d) CAM-specific capacities of SSBs can be lower due to static capacity losses, in addition to kinetic losses. In practice, both processes are intertwined and lead to complex behaviour.

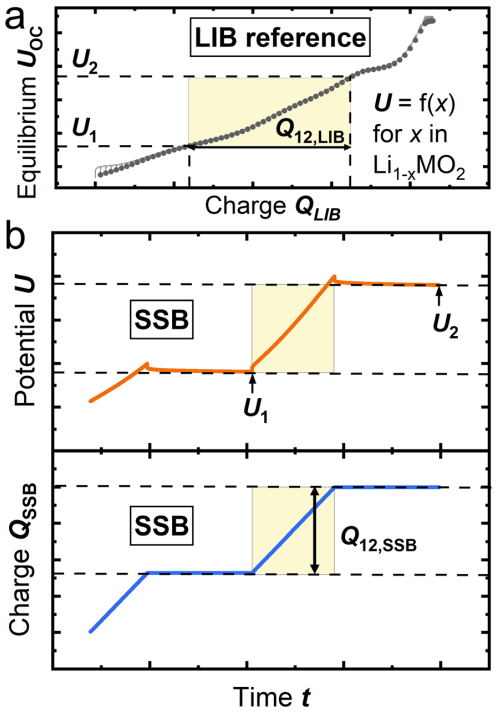

Fig. 2 Working principle of the CTC. (a) Coulometric titration data in LIB serving as reference, (b) potential and accumulated charge of SSB during charge and relaxation steps.

in measurable specific capacity q during the first cycles can then be mainly attributed to kinetic effects, which increase the overpotential (Fig. 1b), so that the cutoff potential is reached earlier.

The situation is different in composite cathodes in SSB cells (Fig. 1c). In this case, the CAM particles need to be mixed with a SE, which comprises particles with a specific size distribution, morphology, and mechanical properties that should be adapted to the properties of the CAM.[14,15] As shown in previous studies also by our group,[7,16] it can happen that a substantial amount of CAM particles is already from the beginning not incorporated in the electronic network, *e.g.* due to poor mixing. In both, LIB and SSB, carbon additives are used to electronically connect the CAM particles. For LIBs more porous carbons are used, whereas SSBs often employ carbon nanofibers (CNF) for long range connection.

The unconnected CAM particles do not take part in charging/discharging, and must be considered as electrochemically inactive, lowering $m_{CAM,act}$. Thus, in addition to kinetic capacity losses, substantial static capacity losses[7] need to be considered, which are visible by a horizontal compression of the charging curve (Fig. 1d). To accurately evaluate the specific capacity and avoid data misinterpretation, precise knowledge of the actual electrochemically active mass $m_{CAM,act}$ in SSB composite cathodes is required.[7]

Here, CTC represents a straightforward approach to quantify $m_{CAM,act}$ and $\Theta_{CAM,SSB}$. The corresponding procedure is sketched in Fig. 2 and will be elaborated in the following for NCM82. Experimental details are given in the SI Section S1.

First, a LIB cell is built as reference, and a coulometric titration curve, *e.g.* based on the galvanostatic intermittent titration technique (GITT),[17] is recorded (Fig. 2a). The open circuit potential (OCP) follows a characteristic function *vs.* the lithium content x in $Li_{1-x}NCMO_2$, which can also be expressed as state-of-charge (SoC) or mass specific capacity q.[18,19] These thermodynamic data serve as the reference curve. Coulometric titration measurements contain inherent errors which are discussed below and estimated in detail in SI Section S2.

To calculate $m_{CAM,act}$ in the SSB composite cathode, two equilibrated potentials U_1 and U_2, and the charge $Q_{12,SSB}$ that was accumulated to reach U_2 need to be known (Fig. 2b). $Q_{12,SSB}$ is then compared to the corresponding $Q_{12,LIB}$ from LIB data.

Together with $m_{CAM,LIB}$, *i.e.*, the total mass of CAM in the LIB cathode, the actual electrochemically active mass of the SSB cathode can be calculated with eqn (1):

$$m_{CAM,act} = m_{CAM,LIB}\frac{Q_{12,SSB}}{Q_{12,LIB}} \quad (1)$$

If less CAM is statically active, after reaching U_2 (or the corresponding SoC), the SSB has accumulated less charge $Q_{12,SSB}$ compared to the LIB. The fraction of active CAM in the SSB, *i.e.* the CAM utilization $\Theta_{CAM,SSB}$, can then be calculated *via* eqn (2):

$$\theta_{CAM,SSB} = m_{CAM,act}/m_{CAM,tot} \quad (2)$$

The following fundamental assumptions need to be considered when calculating the active mass *via* CTC:

View Article Online
ChemComm Communication

First, it is assumed that in the LIB reference cell, 100% of the CAM is electrochemically active and thus all particles contribute to the coulometric titration curve (See SI Section S2.1). Furthermore, CAM utilization is understood as constant during the experiment.

Second, the potentials obtained for LIB and SSB need to be in equilibrium and follow the same titration curve of the pristine CAM. OCP values need to be in a region, where the titration curve is a well-defined and monotonically increasing function *vs.* the lithium content x.

Third, the capacity/charge measured is purely from de-/lithiation of the CAM, meaning a faradaic efficiency FE of 1 without contributions from other reactions, as *e.g.*, electrolyte decomposition.

Furthermore, to ensure a meaningful result for $m_{CAM,act}$, the parameters entering eqn (1) have to be carefully extracted, leading to the following experimental considerations:

The mass of CAM, which is used during the preparation of electrodes (LIB and SSB) is essential for a reliable application of CTC. This means that both $m_{CAM,tot}$ and $m_{CAM,LIB}$ enter the CAM utilization $\Theta_{CAM,SSB}$ with the weighing error. Furthermore, it is known that the CAM utilization in SSBs can be dynamic within the SoC, especially due to interparticle contact issues after volume contraction of NCM-type layered oxides above $\approx$4.2 V.[20] CTC is recommended at potentials where negligible chemo-mechanical changes in utilization occur in SSBs.[21,22]

The potentials need to be equilibrated. Thus, it is recommended to measure at potentials/SoCs where electrode kinetics is fast. For NCM, this is again at medium potentials/SoCs,[23–25] where diffusion of lithium is fast, allowing shorter relaxation times and avoiding concentration gradients.[26,27]

Obviously, SSB and LIB potentials need to be compared against the same reference potential. Since SSBs often employ other counter electrodes, their potentials need to be known and stable, as the In-InLi anode, with +620 mV *vs.* Li^+/Li (SI Section S3.1).[28]

Another consideration regards the OCP fading due to parasitic reactions, *e.g.* electrolyte decomposition re-lithiating the NCM. To quantify this, dU/dt at the end of relaxation, often called "OCV fading" or "self-discharge", at different potentials can be extracted and should be minimized experimentally.[29] The SI Section S2.3.1.2 shows such evaluation for the LIB reference cell. In general, it can be useful to use low loadings to reduce lithium concentration gradients in the cathode, coming with the cost of less precision for $m_{CAM,LIB}$. SI Section S2 provides data and recommendations on optimal experimental design. Potentials should be unique for a specific charge, meaning that two-phase regions/potential plateaus should be avoided, posing challenges for two-phase materials like $LiFePO_4$ (SI Section S2.2).[30] Finally the potential curve should be as close as possible to the pristine CAM, since extended processing is known to change the titration curve.[31]

The charge: We further recommend applying formation cycles to the cells to obtain stable titration curves for the active material, where the faradaic Efficiency (FE) of CAM de-/lithiation is close to 1 and no other processes like CEI formation are expected. Of course, cycling induced changes should be minimized. To identify voltage regions dominated by CAM de-/lithiation, we suggest comparing titration curves in both electrolytes.

We applied the CTC to two SSB cathode composite batches, which are expected to exhibit varying degrees of CAM utilization due to different electrode compositions.[16] One batch with a CAM:SE:CNF ratio of 70 : 30 : 1 (further called "good SSB" and shown in blue) and one with CAM:SE of 60 : 40 ("bad SSB", shown in orange).

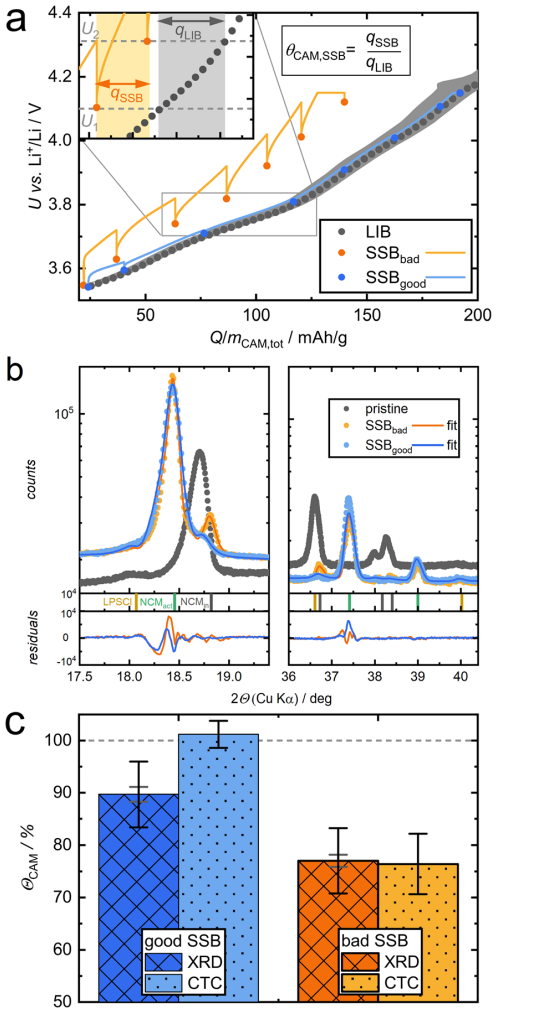

Fig. 3 Experimental results on good and bad SSB cathode composites. (a) Electrochemical data during application of CTC with LIB reference. The inlet shows an exemplary calculation of $\Theta_{CAM,SSB}$ for two OCPs of the bad SSB. (b) XRD spectra and Rietveld refinements with indicated reflex positions. (c) Resulting CAM utilization (eqn (2)) from XRD and CTC method. Grey error bars for XRD are from Rietveld refinement and black from an estimated error of 5 wt% per phase. Error bars for CTC are from application to multiple potential steps (SI Section S3.2).

We obtained multiple relaxed potentials for both SSBs by repeating a simple charge and relaxation protocol, shown by highlighted points in Fig. 3a. The SSB charge procedures (orange, blue data points) deviate from the coulometric titration data of the LIB reference (grey). The inlet showcases how a CAM utilization is calculated for two OCP values of the ''bad'' SSB. This procedure (eqn (2)) was applied for all neighboring OCPs and both cells as shown in SI Section S3.2 *via* a Python script.[32] From the obtained CAM utilizations we calculated a selected average (SI section S3.2), resulting in $\Theta_{CAM,SSB}$ of 76.4 ± 5.8% and 101.2 ± 2.6% for bad and good SSB, respectively.

Additionally, we performed XRD on the ''good'' and ''bad'' SSB composites after extracting them in the U_2 state after holding U = 4.15 V for 12 h. While the major part of the signal corresponds to active, delithiated NCM (NCM_{act}, green indicator) in H2 phase, distinct reflexes of inactive NCM (NCM_{inact}, grey indicator) in H1 phase are observed for both SSBs (Fig. 3b).[33] For comparison, also a pristine composite, containing only NCM_{inact}, is shown in grey. Full diffractograms are given in SI section S4. Shifting of reflexes due to changes in lattice parameters is well understood for NCM and can be compared for the used NCM82 with an *in situ* XRD in a liquid cell reference (SI Section S4). Following the approach by Bartsch *et al.*[34] and Strauss *et al.*[35] the XRD data were refined by the Rietveld method with two NCM phases and the SE phase, allowing an estimation of $\Theta_{CAM,SSB}$. The results of both methods, CTC and XRD, are compared in Fig. 3c. The XRD data validate the CTC method, delivering 89.7% CAM utilization for the good SSB in contrast to only 77.0% for the bad SSB. In SI Section S5 the charge curves of good and bad SSB are compared when being normalized to $m_{CAM,act}$ instead of $m_{CAM,tot}$.

We observe a systematically lower CAM utilization when quantified by XRD for SSBs that perform very well (as measured by CTC). This could be due to a LIB reference that suffers from similar capacity losses as the SSBs, thus overestimating $\Theta_{CAM,SSB}$. Another reason could be LPSCl contributing to capacity while the actual $m_{CAM,act}$ is lower. Most plausible is that Rietveld refinement of a phase with a minor volume fraction and correspondingly small signal in XRD data inherently leads to error-prone results, *e.g.* overinterpretation of device-related shoulders of reflexes.

We believe CTC offers multiple advantages over the approach based on XRD while allowing comparable accuracy. First, it requires no additional equipment and enables an *in situ* determination of $m_{CAM,act}$ instead of *ex situ* and *post mortem* measurements, which is typically done for XRD on SSBs. Furthermore, XRD data refinement as quantification of small mass fractions is inherently inaccurate.

In contrast, coulometric titration comparison (CTC) allows reliable *in situ* access to $m_{CAM,act}$. The procedure is simple to implement and allows an estimation of errors, providing a useful tool. We have applied it successfully to SSB composite cathodes and verified the results with an *ex situ* XRD method, but the procedure can be used for any suitable active material under the assumptions discussed in this work. Furthermore, best-practice is described regarding experimental design and the evaluation *via* Python script facilitates the implementation of CTC. In general, coulometric titration has proven to be highly useful within our working group as multiple publications employing CTC show.[7–11] Applied to SSBs, the possibility to uncover the presence of electrochemically inactive electrode material, may help to develop and optimize advanced cathode composites for next-generation applications.

Author contributions

Kilian Vettori: investigation, writing – original draft, software. Maximilian Kissel: investigation, writing – original draft. Daniel Wagner: formal analysis (XRD Rietveld refinements). Steffen Schröder: writing – review & editing. Jürgen Janek: supervision, writing – review & editing.

Conflicts of interest

There are no conflicts to declare.

Data availability

Coulometric titration data and measurements and the Python code used for evaluation are available in the CTC-data-analysis repository at https://doi.org/10.5281/zenodo.17967963.

Supplementary information (SI) is available. See DOI: https://doi.org/10.1039/d5cc07213a.

Acknowledgements

This work has been funded by the Federal Ministry of Research, Technology and Space under the project HIPOBAT (FKZ: 03XP0611E) and by Deutsche Forschungsgemeinschaft (DFG, German Research Foundation) through the Priority Program 2289 (Project 462470125).

References

1 A. M. Bates, Y. Preger, L. Torres-Castro, K. L. Harrison, S. J. Harris and J. Hewson, *Joule*, 2022, **6**, 742–755.
2 J. Janek and W. G. Zeier, *Nat. Energy*, 2016, **1**, 16141.
3 J. Janek and W. G. Zeier, *Nat. Energy*, 2023, **8**, 230–240.
4 A. Banerjee, X. Wang, C. Fang, E. A. Wu and Y. S. Meng, *Chem. Rev.*, 2020, **120**, 6878–6933.
5 S. Randau, D. A. Weber, O. Kötz, R. Koerver, P. Braun, A. Weber, E. Ivers-Tiffée, T. Adermann, J. Kulisch, W. G. Zeier, F. H. Richter and J. Janek, *Nat. Energy*, 2020, **5**, 259–270.
6 S. Puls, E. Nazmutdinova, F. Kalyk, H. M. Woolley, J. F. Thomsen, Z. Cheng, A. Fauchier-Magnan, A. Gautam, M. Gockeln, S.-Y. Ham, M. T. Hasan, M.-G. Jeong, D. Hiraoka, J. S. Kim, T. Kutsch, B. Lelotte, P. Minnmann, V. Miß, K. Motohashi, D. L. Nelson, F. Ooms, F. Piccolo, C. Plank, M. Rosner, S. E. Sandoval, E. Schlautmann, R. Schuster, D. Spencer-Jolly, Y. Sun, B. S. Vishnugopi, R. Zhang, H. Zheng, P. Adelhelm, T. Brezesinski, P. G. Bruce, M. Danzer, M. El Kazzi, H. Gasteiger, K. B. Hatzell, A. Hayashi, F. Hippauf, J. Janek, Y. S. Jung, M. T. McDowell, Y. S. Meng, P. P. Mukherjee, S. Ohno, B. Roling, A. Sakuda, J. Schwenzel, X. Sun, C. Villevieille, M. Wagemaker, W. G. Zeier and N. M. Vargas-Barbosa, *Nat. Energy*, 2024, **9**, 1310–1320.

7 M. Kissel, M. Schosland, J. Töws, D. Kalita, Y. Schneider, J. Kessler-Kühn, S. Schröder, J. Schubert, F. Frankenberg, A. Kwade, A. Bielefeld, F. H. Richter and J. Janek, *Adv. Energy Mater.*, 2025, **15**, 2405405.
8 G. Conforto, R. Ruess, D. Schröder, E. Trevisanello, R. Fantin, F. H. Richter and J. Janek, *J. Electrochem. Soc.*, 2021, **168**, 70546.
9 P. Minnmann, J. Schubert, S. Kremer, R. Rekers, S. Burkhardt, R. Ruess, A. Bielefeld, F. H. Richter and J. Janek, *J. Electrochem. Soc.*, 2024, **171**, 60514.
10 B.-X. Shi, Y. Yusim, S. Sen, T. Demuth, R. Ruess, K. Volz, A. Henss and F. H. Richter, *Adv. Energy Mater.*, 2023, **13**, 2300310.
11 B.-X. Shi, F. Weber, Y. Yusim, T. Demuth, K. Vettori, A. Münchinger, G. Titvinidze, K. Volz, A. Henss, R. Berger and F. H. Richter, *J. Mater. Chem. A*, 2025, **13**, 2600–2614.
12 A. Kwade, W. Haselrieder, R. Leithoff, A. Modlinger, F. Dietrich and K. Droeder, *Nat. Energy*, 2018, **3**, 290–300.
13 A. Shodiev, F. M. Zanotto, J. Yu, M. Chouchane, J. Li and A. A. Franco, *Energy Storage Mater.*, 2022, **49**, 268–277.
14 P. Minnmann, F. Strauss, A. Bielefeld, R. Ruess, P. Adelhelm, S. Burkhardt, S. L. Dreyer, E. Trevisanello, H. Ehrenberg, T. Brezesinski, F. H. Richter and J. Janek, *Adv. Energy Mater.*, 2022, **12**, 2201425.
15 A. Bielefeld, D. A. Weber and J. Janek, *ACS Appl. Mater. Interfaces*, 2020, **12**, 12821–12833.
16 A. Bielefeld, D. A. Weber and J. Janek, *J. Phys. Chem. C*, 2019, **123**, 1626–1634.
17 W. Weppner and R. A. Huggins, *J. Electrochem. Soc.*, 1977, **124**, 1569–1578.
18 M. Levi and D. Aurbach, *Electrochim. Acta*, 1999, **45**, 167–185.
19 M. D. Radin, S. Hy, M. Sina, C. Fang, H. Liu, J. Vinckeviciute, M. Zhang, M. S. Whittingham, Y. S. Meng and A. van der Ven, *Adv. Energy Mater.*, 2017, **7**, 1602888.
20 R. Koerver, W. Zhang, L. de Biasi, S. Schweidler, A. O. Kondrakov, S. Kolling, T. Brezesinski, P. Hartmann, W. G. Zeier and J. Janek, *Energy Environ. Sci.*, 2018, **11**, 2142–2158.
21 X. Liu, B. Zheng, J. Zhao, W. Zhao, Z. Liang, Y. Su, C. Xie, K. Zhou, Y. Xiang, J. Zhu, H. Wang, G. Zhong, Z. Gong, J. Huang and Y. Yang, *Adv. Energy Mater.*, 2021, **11**, 2003583.
22 S. H. Park, K. G. Naik, B. S. Vishnugopi, X. Xiao, M. Drakopoulos, N. T. Vo, Z. Zhong, P. P. Mukherjee and K. B. Hatzell, *ACS Nano*, 2025, 22262–22269.
23 A. Liu, N. Phattharasupakun, M. M. E. Cormier, E. Zsoldos, N. Zhang, E. Lyle, P. Arab, M. Sawangphruk and J. R. Dahn, *J. Electrochem. Soc.*, 2021, **168**, 70503.
24 R. Weber, A. J. Louli, K. P. Plucknett and J. R. Dahn, *J. Electrochem. Soc.*, 2019, **166**, A1779–A1784.
25 R. Morasch, H. A. Gasteiger and B. Suthar, *J. Electrochem. Soc.*, 2023, **170**, 80522.
26 M. D. Levi, K. Gamolsky, D. Aurbach, U. Heider and R. Oesten, *J. Electroanal. Chem.*, 1999, **477**, 32–40.
27 K. Vettori, S. Schröder, L. Ahrens, R. Wilhelm, S. Kremer, J. K. Eckhardt, T. Brezesinski, A. Kondrakov, J. Mayer, A. Henss and J. Janek, *Adv. Energy Mater.*, 2025, 2502148.
28 A. L. Santhosha, L. Medenbach, J. R. Buchheim and P. Adelhelm, *Batteries Supercaps*, 2019, **2**, 524–529.
29 T. Roth, L. Streck, A. Graule, P. Niehoff and A. Jossen, *J. Electrochem. Soc.*, 2023, **170**, 20502.
30 D. Di Lecce and J. Hassoun, *J. Phys. Chem. C*, 2015, **119**, 20855–20863.
31 L. Zheng, C. Wei, M. D. L. Garayt, J. MacInnis and M. N. Obrovac, *J. Electrochem. Soc.*, 2019, **166**, A2924–A2927.
32 K. Vettori, CTC-data-analysis, 2026, Zenodo10.5281/zenodo. 17967963.
33 C. Ghanty, B. Markovsky, E. M. Erickson, M. Talianker, O. Haik, Y. Tal-Yossef, A. Mor, D. Aurbach, J. Lampert, A. Volkov, J.-Y. Shin, A. Garsuch, F. F. Chesneau and C. Erk, *ChemElectroChem*, 2015, **2**, 1479–1486.
34 T. Bartsch, A.-Y. Kim, F. Strauss, L. de Biasi, J. H. Teo, J. Janek, P. Hartmann and T. Brezesinski, *Chem. Commun.*, 2019, **55**, 11223–11226.
35 F. Strauss, T. Bartsch, L. de Biasi, A.-Y. Kim, J. Janek, P. Hartmann and T. Brezesinski, *ACS Energy Lett.*, 2018, **3**, 992–996.

5.2. Publication II: *Quantifying the Impact of Cathode Composite Mixing Quality on Active Mass Utilization and Reproducibility of Solid-State Battery Cells*

The methodology of Publication I was employed, statistically validated, and further discussed in Publication II. This publication[150] was motivated by an interlaboratory round robin study by Puls *et al.*[34], which revealed large variations in cell performance among different research groups despite using the same materials. However, the underlying reasons remained largely unresolved. The aim of this work was to systematically investigate the intralaboratory reproducibility, with a particular focus on the impact of the cathode composite mixing process on the electrochemical performance. To this end, a model system for composite cathodes was employed, containing NCM82 as CAM, Li_6PS_5Cl as SE, and CNFs as conductive additive. The composites were prepared either manually using a mortar and pestle or machine-made using a mini vibrating mill. A statistically relevant data set was acquired by producing 17 different composite batches, with a minimum of three cells assembled per batch.

The study demonstrates that, even when using identical materials and cell assembly parameters, significant capacity variations up to 40 mAh/g can occur solely due to differences in cathode composite mixing conditions. It shows that hand mortaring is less reproducible than machine-made composites, given that appropriate process parameters are used. A detailed assembly protocol for reproducible performance is reported, and the results can serve as a standardized reference in the future.

Furthermore, the work statistically validates the quantitative framework of Publication I for evaluating the CAM utilization and disentangling static from kinetic capacity losses. This approach encourages rethinking of conventional specific capacity calculations at low TRLs. The findings emphasize the necessity of controlled mixing protocols to achieve reliable and reproducible SSB performances, highlighting a frequently overlooked source of experimental variability. The proposed framework, which differentiates between static and kinetic capacity losses, is directly transferable to other material systems and enables a more precise evaluation of mixing quality. It also contributes to improved data reliability by helping to avoid misinterpretation arising from process issues rather than material limitations.

The study was designed by M. Kissel under the supervision of J. Janek. The experiments were planned and coordinated, and all data were evaluated by M. Kissel. The manuscript was written by M. Kissel and edited by all co-authors.

Reproduced from: Maximilian Kissel, Marie Schosland, Julia Töws, Daizy Kalita, Yannik Schneider, Jill Kessler-Kühn, Steffen Schröder, Johannes Schubert, Finn Frankenberg, Arno Kwade, Anja Bielefeld, Felix H. Richter, Jürgen Janek. Quantifying the Impact of Cathode Composite Mixing Quality on Active Mass Utilization and Reproducibility of Solid-State Battery Cells. *Adv. Energy Mater.*, 2025, 2405405, DOI: 10.1002/aenm.202405405, licensed under CC BY 4.0.

RESEARCH ARTICLE

ADVANCED ENERGY MATERIALS
www.advenergymat.de

Quantifying the Impact of Cathode Composite Mixing Quality on Active Mass Utilization and Reproducibility of Solid-State Battery Cells

*Maximilian Kissel, Marie Schosland, Julia Töws, Daizy Kalita, Yannik Schneider, Jill Kessler-Kühn, Steffen Schröder, Johannes Schubert, Finn Frankenberg, Arno Kwade, Anja Bielefeld, Felix H. Richter, and Jürgen Janek**

Research into the development and understanding of solid-state batteries often relies on pelletized press cells due to their comparative ease of use. However, these model cells are prone to comparability and reproducibility issues. This study examines the extent to which the cathode composite preparation influences the cell performance of a reference system comprising $LiNi_{0.82}Mn_{0.07}Co_{0.11}O_2$ as the cathode active material, Li_6PS_5Cl as the solid electrolyte, carbon nanofibers as the conductive additive, and an indium–lithium foil anode. The cathode composite is prepared either via hand mortaring or in a mini vibrating mill. The mixing process is found to be critical for the reproducibility of cell performance and accounts for many of the discrepancies observed in the capacities of different cells made with identical materials and following the same cell assembly protocol. The open-circuit relaxation method is implemented to quantify active mass utilization in the cathode in situ, which depends on the mixing process and correlates with the cell performance. This approach allows for a quantitative differentiation between static and kinetic capacity losses during the discussion of specific capacity values. The results demonstrate the significance of cathode composite mixing and the necessity of quantifying the mixing quality for reliable electrochemical data acquisition and interpretation.

1. Introduction

Solid-state batteries (SSBs) are heavily investigated in academia and industry driven by their promise of elevated energy and power density as well as higher safety compared to conventional, liquid electrolyte-based, lithium-ion batteries (LIBs). However, toward practical application on a larger scale, different challenges in all parts of the battery cell and at every level of battery cell production need to be overcome.[1–5] To evaluate potential solutions such as protective coatings for active materials, new solid electrolytes, modified cathode active materials and to investigate fundamental physico-chemical phenomena, solid-state battery full cells that consist of an anode, a separator, and a cathode are usually built. These cells are often composed of composites, which are heterogeneous particle mixtures. While such mixtures are less common in the anode [6,7] – where lithium metal or lithium metal alloys are typically used [8–10] – and the separator [11,12], they are particularly prevalent in the cathode.[13–15] Cathode composites frequently comprise particles of cathode active material (CAM), solid electrolyte (SE), and conductive additives. Such composites are employed in various studies investigating, for instance, the kinetics, SE performance, or protective coatings for CAMs.[16–21]

Many investigations on low technology readiness levels (TRL) are conducted using easy-to-prepare pelletized press cells although this cell setup is not commercially relevant.[22] Nevertheless, this approach creates reasonable model cells as the used materials, e.g. coated CAMs, are often not available in large quantities at early state of research. Thus, laboratory-scale composite batches of typically only 100 mg – 300 mg are prepared by mixing of the materials, often carried out only manually with mortar and pestle.[18,21,23–26] The objective of the cathode composite mixing process is to construct well-percolating ion- and electron-conducting networks that possess a sufficiently large active interface area with each other, thereby enabling the participation of all CAM particles in charge and discharge. This is

M. Kissel, M. Schosland, J. Töws, D. Kalita, Y. Schneider, J. Kessler-Kühn, S. Schröder, J. Schubert, A. Bielefeld, F. H. Richter, J. Janek
Institute of Physical Chemistry
Justus-Liebig-University Giessen
Heinrich-Buff-Ring 17, 35392 Giessen, Germany
E-mail: juergen.janek@pc.jlug.de

M. Kissel, M. Schosland, J. Töws, D. Kalita, Y. Schneider, J. Kessler-Kühn, S. Schröder, J. Schubert, A. Bielefeld, F. H. Richter, J. Janek
Center for Materials Research (ZfM/LaMa)
Justus-Liebig-University Giessen
Heinrich-Buff-Ring 16, 35392 Giessen, Germany

F. Frankenberg, A. Kwade
Institute for Particle Technology
Volkmaroder Straße 5, 38104 Braunschweig, Germany

The ORCID identification number(s) for the author(s) of this article can be found under https://doi.org/10.1002/aenm.202405405

DOI: 10.1002/aenm.202405405

ADVANCED SCIENCE NEWS
www.advancedsciencenews.com

ADVANCED ENERGY MATERIALS
www.advenergymat.de

usually self-evident in porous LIB electrodes that are infiltrated by a liquid electrolyte, but, in SSB composite cathodes, the creation of well-percolating networks with 100% electrochemically addressed, i.e., fully utilized, CAM particles is not trivial.[13]

Simulations have shown that the microstructural arrangement of CAM particles and SE particles is crucial for the transport kinetics since it affects the effective conductivities within the composite cathode.[27–29] Experimental studies confirmed the effect of CAM and SE particle sizes as well as pores in the composite cathode on the cell performance.[17,30–32] Despite its expected decisive influence on the microstructure, analyzing the mixing process of cathode composites for SSBs has received comparatively little attention to date.[5,33–35] The mechanical properties of the particles as well as often wide particle size distributions of the SE pose a challenge for a successful mixing process and stress the need for further research and improved processing techniques.[35,36]

As recently commented by Vargas-Barbosa,[37] there is currently no standardized workflow to evaluate the electrochemical performance of an SSB material and to determine the figure of merits for specific battery cells, which makes a comparison between different studies almost impossible.[38,39] Also, a recent wide interlaboratory round-robin study [26] highlighted large discrepancies among different working groups regarding the electrochemical performance of their cells, even when constructed with the same materials. Yet the underlying reasons for the large performance variations remain to be further elucidated, especially with respect to the composite cathode.

In light of these findings, we undertook a critical assessment of our cell construction methodology with respect to reproducibility, conducting an intra-laboratory investigation – complementing the recent round-robin test.[26] Thereby, we show that despite identical assembly parameters, materials, and equipment, significant variations in the specific capacities for nominally identical cells are still possible. These variations can unambiguously be retraced to the microstructure of the composite cathode, which depends solely on the cathode composite mixing process in this study. We propose a cell assembly protocol for pelletized press cells that ensures an improved reproducibility and comparability of the electrochemical performance in this study. We also employ a method for in situ quantification of the mixing quality in terms of active mass utilization, which is found to correlate strongly with cell performance. Based on statistical evaluations, we highlight the significance of this static property for the interpretation of electrochemical capacity data. Furthermore, we discuss the importance of distinguishing between static and kinetic capacity losses, both of which influence the measurable capacity of solid-state cells. Our results highlight the critical role of cathode composite mixing, emphasizing the need for a reproducible composite preparation procedure and its analysis for subsequent electrochemical measurements and data interpretation.

2. Results and Discussion

2.1. Improving the Reproducibility of Pellet-Type Solid-State Battery Cells

Throughout the intra-laboratory benchmarking study, the following parameters were kept constant: the active material batch ($LiNi_{0.82}Mn_{0.07}Co_{0.11}O_2$), the Li_6PS_5Cl solid electrolyte batch, the carbon nanofiber batch with a weight ratio of 70:30:1, the indium-lithium foil couple as the anode, the glovebox handling, pressure setup, and electrochemical benchmarking protocol. This allowed us to focus as much as possible on the composite fabrication employing both manual hand grinding and an automated mechanical mixing process in a mini vibrating mill, which is referred to as "machine-made" in the following. The electrochemical benchmarking protocol (**Figure 1**) deliberately did not include any extended C-Rate tests or long-term cycling to limit the impact of chemo-mechanical effects, which are hard to control.

Following a resting period of 6 h for equilibration of the In–Li anode,[8] the cells underwent an initial formation cycle at 0.1C. As the next step, the amount of active mass, i.e., the CAM utilization, was determined via open circuit potential (OCP) relaxation adapted from the methodology previously reported [40]; its importance is discussed below in detail. At this point, also the full cell impedance was measured at 3.1 V vs. In/InLi, a potential at which the CAM-SE charge transfer resistance is relatively low.[41] Afterwards, the cells were galvanostatically cycled between 1.9 and 3.7 V vs. In/InLi for three cycles at 0.1C, 5 cycles at 0.3C, and 5 cycles at 1.0C before the cell was cycled at 0.1C for one additional cycle. As a last step, the CAM utilization and impedance were again determined, for which no full cycle is required.

This benchmarking program allows us to effectively and efficiently draw conclusions on the reproducibility of the cells. In this study, per batch of cathode composite, either produced by hand grinding or machine-made, three cells were built and electrochemically tested to investigate the variations within each batch, i.e., the intra-batch effects. In theory, all cells should exhibit the same electrochemical performance since the same materials and composition were used. The batches are consecutively numbered and the details including all raw cycling data are openly available (see Data Availability Statement).

2.1.1. Contrasting Hand Mortaring With Machine-made Cathode Composites

In academic lab practice, the mixing of cathode composites is often carried out manually with mortar and pestle as it was also done in the abovementioned round-robin study.[26,42–50] Apart from the inherent limitations of hand grinding in terms of scalability, there is reasonable doubt whether this process is reproducible because the applied forces and movements presumably differ from person to person. To investigate this 'human factor´, we tested three batches of hand-ground composites fabricated by three different persons (batches 1–3). The discharge capacities obtained from the cycling program (Figure 1) are shown in **Figure 2**a for each of the nine cells. Figure 2b displays the mean discharge capacities per batch including the standard deviation for each C-rate.

It is evident that there are considerable discrepancies in the tested cells, with capacities ranging from 162 to 188 mAh g^{-1}. The mean discharge capacity at 0.1C for the composites of batch 1 was (187.0 ± 0.8) mAh g^{-1}, while the composite of batch 2 exhibited a significantly lower capacity of (166.9 ± 3.8) mAh g^{-1}. Also, at 0.3C and 0.1C, the capacities of batch 2 remain lower than those of batch 1. The composite prepared of batch 3 demonstrated capacities intermediate to those of batch 1 and 2, but with

ADVANCED SCIENCE NEWS
www.advancedsciencenews.com

ADVANCED ENERGY MATERIALS
www.advenergymat.de

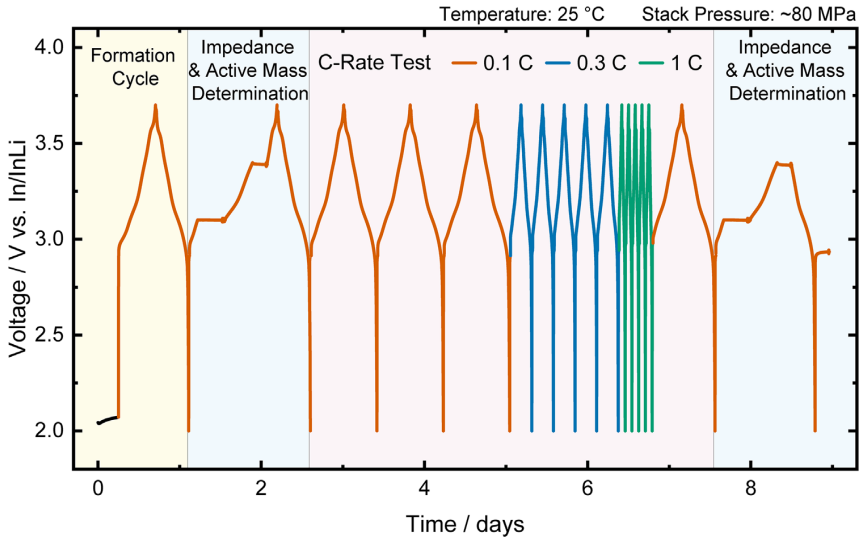

Figure 1. Exemplary voltage profile overtime during the electrochemical benchmarking protocol employed for all cells in this study.

higher variance between 2.2 to 5.9 mAh g^{-1}, depending on the C-rate. Generally, the variance increases with increasing C-rate for the cells of batches 1 and 3, with two outliers of lower capacity. In contrast, the opposite trend is observed for the cells of batch 2, which show very similar, but lower capacities at elevated C-rate. When considering all nine cells, mean discharge capacities of 178.0/162.6/133.3 mAh g^{-1} are achieved at 0.1C/0.3C/1C with a standard deviation of 9.0/9.7/10.8 mAh g^{-1}, respectively. The corresponding coefficients of variation are 5.1/5.6/8.1 %, respectively, indicating a high variation of the data. Overall, the variations in capacities within a single batch and between different batches are unsatisfactorily large.

Furthermore, a machine-made composite preparation with a mini vibrating mill (see Experimental for details) was investigated. This type of cathode composite preparation has been increasingly used in previous studies.[9,17,23,51] Three composite batches were produced in the mill at a frequency of 30 Hz for 30 min using nine ZrO_2 milling balls (5 mm in diameter) for 300 mg of composite.

The discharge capacities for the machine-made composites obtained from the benchmarking cycling program are shown in **Figure** 3a for each of the nine cells, while Figure 3b displays mean discharge capacities per batch including the standard deviation for each C-rate. In the following, the main results will be summarized referring to all nine cells. At 0.1C/0.3C/1C, a mean discharge capacity of 179.5/164.9/138.5 mAh g^{-1} is achieved with a standard deviation of 2.4/3.0/4.3 mAh g^{-1}, respectively. The corresponding coefficients of variation are 1.4/1.8/3.1 %, respectively, which indicate a high reproducibility, i.e., low variation. However, there is a trend of increasing variation with higher C-rate, especially obvious for batches 5 and 6 at 1C, each containing one outlier with lower discharge capacity. Nevertheless,

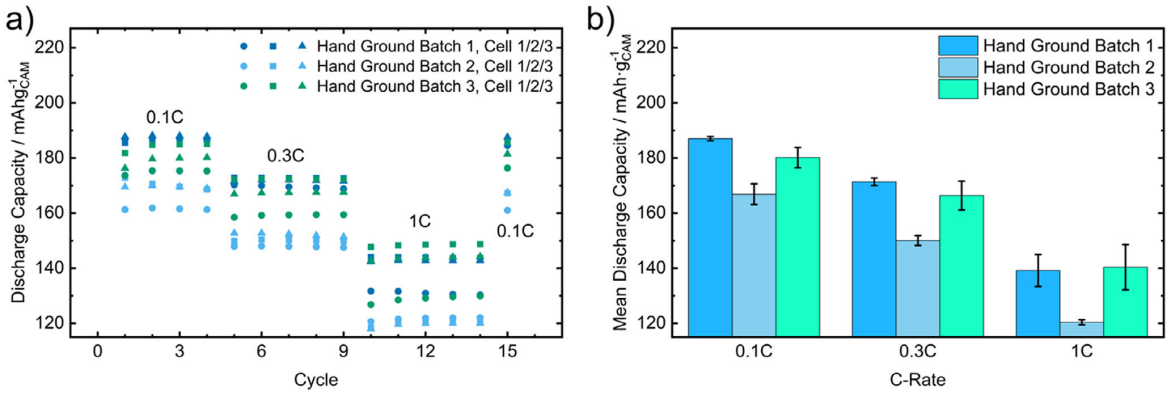

Figure 2. Discharge capacities achieved at different C-rates for a) individual cells and b) average per batch. Each batch was hand-ground for 15 min by a different person.

ADVANCED SCIENCE NEWS
www.advancedsciencenews.com

ADVANCED ENERGY MATERIALS
www.advenergymat.de

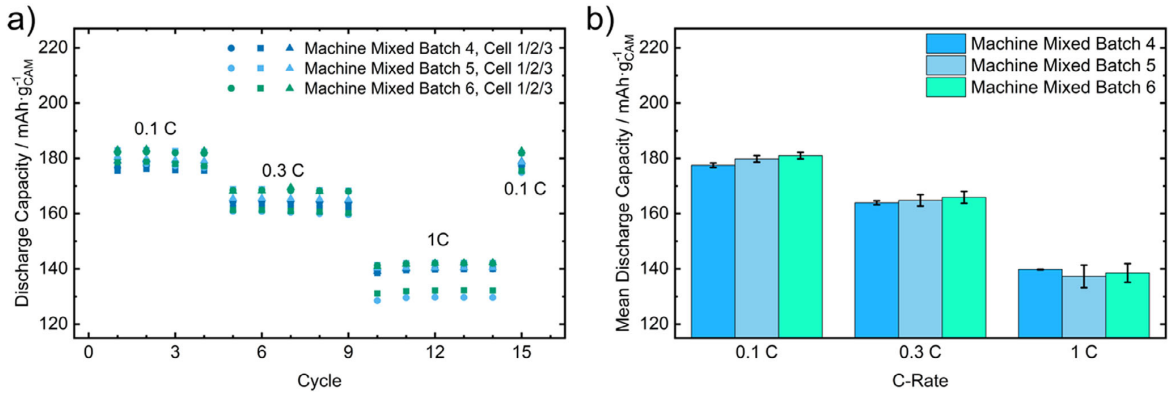

Figure 3. Discharge capacities achieved at different C-rates: a) individual cells and b) average per batch. Each batch was machine-mixed with the same parameters.

compared to the cells with hand-ground composites, we consider the results with machine-made composites to be reproducible. This is even more reasonable when performing a conventional error calculation for specific capacities.

As a standard approach, the specific capacity of the CAM, q_{CAM}, is calculated by referring the measured charge Q to the total mass of active material particles, $m_{CAM,tot}$, which equals the product of composite cathode mass, m_{CC}, and active material mass fraction in the cathode, x_{AM}:

$$q_{CAM} = \frac{Q}{m_{CC} \cdot x_{AM}} \tag{1}$$

In practice, the calculation of q_{CAM} according to Equation 1 is error-prone. Errors in the weighing process and possible loss of composite when filling it into the cell casing should be accounted for with at least $\Delta m_{CC} = 0.1$ mg.[52] Similarly, we assume an error of $\Delta x_{AM} = 0.0005$ resulting from weighing in the powders for the composite preparation. The error in measuring the charge, ΔQ, is assumed to be negligible. Applying the principle of propagation of uncertainty the error for the capacity is

$$\Delta q_{CAM} = \sqrt{\left(\frac{\partial q_{CAM}}{\partial Q} \cdot \Delta Q\right)^2 + \left(\frac{\partial q_{CAM}}{\partial m_{CC}} \cdot \Delta m_{CC}\right)^2 + \left(\frac{\partial q_{CAM}}{\partial x_{AM}} \cdot \Delta x_{AM}\right)^2} \tag{2}$$

with $Q = 1.5$ mAh, $m = 12$ mg and $x = 0.6931$, leading to $\Delta q_{CAM} = 1.5$ mAh g^{-1}. This means that there is always a possible error of at least 1–2 mAh g^{-1} which should be kept in mind when comparing specific capacities of different cells. As a result, the higher intra-batch as well as inter-batch reproducibility of the cell capacities with machine-made composite cathodes is even more evident.

Another potential error source affecting the capacities is the homogeneous distribution of the cathode composite on the separator layer, which should result in a uniform cathode thickness. Since this is more error-prone with the standard amount of 12 mg cathode composite (≈2 mAh cm^{-2} for the used composition in this study), an increased amount of 15 mg (equals ≈2.5 mAh cm^{-2}) cathode composite was tested. Although this leads to a 25% thicker cathode, we found that it has no detrimental effect on cell performance (Figure S1, Supporting Information). Rather, this amount facilitates the homogenous distribution of the composite cathode and is used within the cell assembly protocol introduced in Section 2.1.3.

2.1.2. Effect of Anode Processing on the Resistance

In addition to the cathode preparation, also the anode can have a negative impact on the performance and reproducibility of solid-state cells. The construction of In-Li alloy anodes has been discussed in depth in the literature, as its two-phase character bears the risk of poor kinetics.[7–10] In this work, two ways of anode preparation using an indium and lithium foil couple were used. On the one hand, an individual anode preparation was carried out, which means that the lithium and indium metal foils were stacked on each other, then comparatively little pressure (≈40 MPa) was applied to allow for diffusion and formation of the In/InLi two-phase composite and finally the stack pressure (≈80 MPa) for cycling was applied. As depicted in **Figure 4**, the corresponding anode contributions at the beginning vary between 1.4 and 14.4 Ω•cm^2 with a mean value of (6.3 ± 2.8) Ω•cm^2.

To reduce these variations toward a cell assembly protocol, we investigated on the other hand the effect of pressing the lithium and indium foils together with the separator and composite cathode at 375 MPa. We found that following this approach lowers the absolute impedance contribution as well as the variations to (2.5 ± 1.0) Ω•cm^2. The difference compared to the individual anode preparation is most evident at the beginning of the electrochemical benchmarking protocol (Figure 4). During cycling, the contributions of both ways of anode preparation become more similar but the mean value of the cell assembly protocol anode remains lower. Interestingly, the mean value of the anode resistance decreased to (5.3 ± 3.8) Ω•cm^2 for the individual anode preparation while it slightly increased to (3.9 ± 1.5) Ω•cm^2 for the anodes prepared according to the cell assembly protocol. Nevertheless, more outliers with a much higher impedance contribution are observed for the individual anode preparation.

Overall, compressing the whole cell with 375 MPa leads to a more reproducible cell resistance by controlling the anode contribution, which is especially important for the performance

ADVANCED SCIENCE NEWS
www.advancedsciencenews.com

ADVANCED ENERGY MATERIALS
www.advenergymat.de

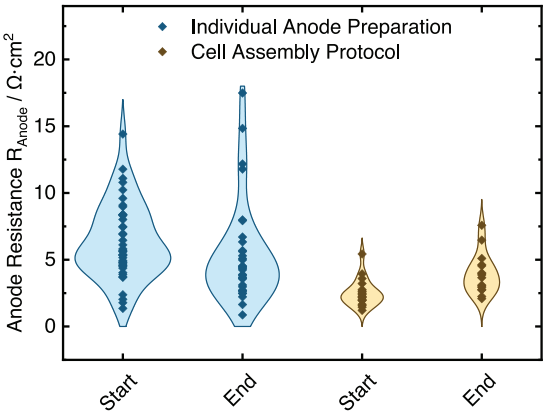

Figure 4. Violin plots of anode contributions to the resistance of all cells investigated in this study (Data File S1, Supporting Information) for which the individual anode preparation or the cell assembly protocol (pressing the whole cell at 375 MPa) was applied. Start and End refer to the beginning and end of the electrochemical benchmarking protocol.

at higher C-rates.[7,8,10] When slightly increasing the separator thickness to ≈700 µm (corresponding to 80 mg Li_6PS_5Cl) and electronically isolating the cell during pressing, there is no risk of short-circuiting the full cell based on our experience. Applying a smaller pressure of ≈60 MPa to allow for diffusion before the densification with 375 MPa did not have an impact (Figure S2, Supporting Information).

As the final layer on the anode side, a 20 µm thick stainless-steel plate is placed on the lithium. The steel plate does not affect the electrochemical measurements but offers two practical advantages. It allows for the reuse of the anode-side steel rods without the need for polishing, since the lithium adheres to the steel plate instead of the rods. Additionally, it allows easy removal of the cell pellet without breakage, which is beneficial for further post-mortem analysis.

2.1.3. A Cell Assembly Protocol for Press Cells

Based on the aspects discussed so far, a detailed cell assembly protocol for the laboratory press cells is defined. On the one hand, this helps to improve reproducibility and comparability, on the other hand, it offers guidelines and a reference system to evaluate cell assemblies using different materials. As shown in **Figure 5**, the cathode composites are first processed in a mini vibrating mill with defined parameters. Depending on the employed materials and weight ratios, it is possible that different parameters for the mini-vibrating mill are required to achieve reproducible results. All cell components are filled in an in-house built cell casing containing a PEEK inlet with an inner diameter of 10 mm.[22] Polished steel rods are used as current collectors on both electrodes. For the full cell, the first 80 mg of the SE separator (corresponding to a thickness of ≈700 µm) are filled in the cell followed by hand pressing. A smooth surface without loose particles should be obtained on which 15 mg of the cathode composite are homogeneously distributed with a flat spatula and again densified via hand pressing. Afterward, indium foil (100 µm thickness, 9 mm diameter) and lithium foil (100 µm thickness, 6 mm diameter), corresponding to an atomic ratio of n(In):n(Li) = 1.86, are placed on the other side of the separator to form the anode, followed by a 20 µm thick stainless-steel plate. A schematic representation of the cell in Figure 5 shows the proportions of the individual components. After cell assembly, the full cell is uniaxially pressed by maintaining 375 MPa for 3 min at room temperature. Thereby, the current collectors need to be electronically isolated to prevent a short circuit. For electrochemical testing, the cells are fixed in a steel frame with four screw bolts of 12 mm diameter. The screw nuts are tightened with a torque of 10 Nm which corresponds to ≈80 MPa stack pressure. Before electrochemical testing in a climate chamber at 25 °C, the cells are left at open circuit voltage for at least 3 h during which the OCV reaches values that depend on the type of CAM and SE in the cathode. In the case of NCM and Li_6PS_5Cl, an OCV between 1.9 and 2.2 V vs. In/InLi is typically observed. Following this cell assembly protocol, working solid-state press cells are achieved that demonstrate sufficiently reproducible performances with capacity variations below 5% in this study.

2.2. On the Importance of Quantifying the Mixing Quality of Composite Cathodes

2.2.1. Quantifying CAM Utilization and Its Correlation with Cell Performance

While the cell assembly protocol provides intra- and inter-batch reproducibility, the low-rate specific capacities of the machine-made composites are all lower than the theoretical capacity provided by the supplier and confirmed by measurement in a LIB coin cell with liquid electrolyte (Figure S3, Supporting Information). Also, even when considering the error due to weighing, the large differences in calculated capacities for the cells with hand-ground composites, for which identical materials were used, are still unexplained.

As stated at the beginning, the microstructure of the composite has a considerable influence on the achievable capacity. In SSB composite cathodes, it may happen that CAM particles are not connected to a percolating ionic and/or electronic conduction network after mixing [31,35] or that they disconnect during cycling [40,43] and thus are inactive during the (dis)charging processes. Whether a CAM particle is electrochemically active or not depends largely on the mixing process, which is not part of the investigation in most studies. Consequently, inadequate mixing of the composite can easily result in data misinterpretation if the resulting microstructure and its effects are not considered. Therefore, a parameter must be identified that quantifies the mixing quality and allows for a comparison between different cells.

As mentioned, usually, the whole mass of the CAM that was weighed in during cell assembly is used for the calculation of specific capacities according to Equation 1. We refer to this in the following as gross specific capacity. As can be surmised from Section 2.1.1, the assumption that all CAM particles are electrochemically connected is overly simplistic and the CAM utilization, i.e., the active-to-gross mass ratio, should be considered when calculating specific capacities. Hence, we suggest distinguishing the gross specific capacity from the active specific capacity, which is

ADVANCED SCIENCE NEWS
www.advancedsciencenews.com

ADVANCED ENERGY MATERIALS
www.advenergymat.de

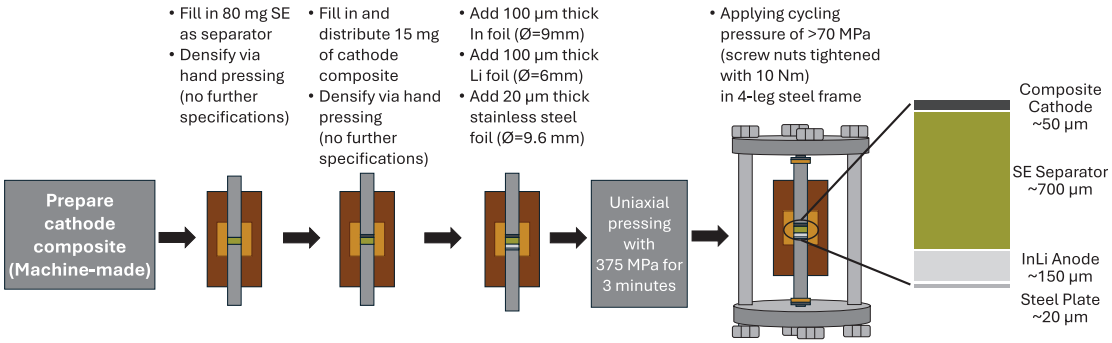

Figure 5. Cell assembly protocol that was established during this study. The success of cathode composite preparation strongly depends on the specific materials, composition, and mixing process parameters.

the specific capacity of electronically and ionically connected, i.e., active CAM particles. The calculation of the active specific capacity, for which the charge only refers to the active mass of CAM, requires that the electrochemically active mass, i.e., the CAM utilization, is quantitatively known.

The determination of the active mass in SSB cells was demonstrated by Bartsch et al.[53] using X-ray diffraction (XRD) measurements, Rietveld refinement, and comparison with reference data. However, this approach is usually only possible ex situ and not feasible as a standard approach for solid-state cells. Conforto et al.[40] employed an in situ electrochemical method, which they called the OCP-relaxation method, for tracking the active mass loss during cycling. In the present study, we employ this approach for in situ and on-the-fly quantification of the initial electrochemically active mass and CAM utilization, which can be related to the microstructure, i.e., the mixing of the cathode composite. The procedure for measuring the required quantities is described in the Experimental Section.

The data was evaluated accordingly to calculate the CAM utilization for the cells shown in Figures 2 and 3, and for additional cells that were prepared with different mixing parameters, as described in Section S1, Supporting Information. **Figure 6** shows that the CAM utilization varies between 74 % and 95 % for the composites all possessing the identical composition. This illustrates that the assumption that all CAM particles in the composite cathode are active is incorrect. Figure 6 depicts two correlation plots in which the mean discharge capacities for each C-rate are plotted against the CAM utilization of the respective cell – as determined from OCP relaxation. Each cell contributes three datapoints, one for each C-rate, to these correlation plots.

In Figure 6a, the gross specific discharge capacity is calculated with respect to the gross mass of CAM particles, $m_{CAM,tot}$, as usually done in the literature. The gross specific capacities show a strong positive correlation with the CAM utilization, i.e., the higher the CAM utilization the higher the discharge capacity. Thereby, the discharge capacities at 0.1C exhibit the strongest correlation with a Pearson correlation coefficient (PCC) of $r = 0.95$ and a coefficient of determination (COD) of $R^2 = 0.90$. At higher C-rates, the PCC remains high but decreases to $r = 0.89$ and $r = 0.73$ for 0.3 and 1C, respectively, while the COD is lowered to $R^2 = 0.80$ and $R^2 = 0.53$, respectively. These results are reasonable: at low C-rates, here 0.1C, the available charge depends mainly on the amount of NCM particles that are electrochemically connected, i.e., the active particles. Thus, a simple linear regression is sufficient to

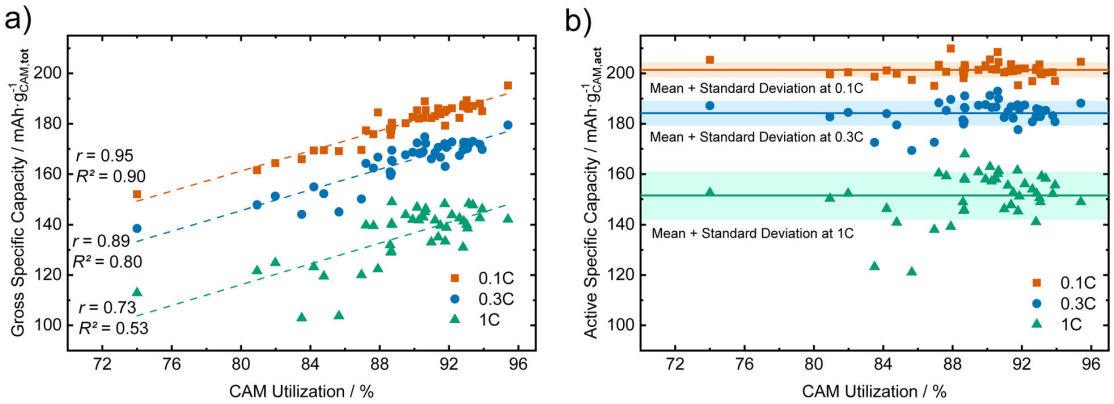

Figure 6. Correlation between capacities and CAM utilization, with the specific capacity calculated a) with respect to the total mass of active material in the cathode, $m_{CAM,tot}$, and b) with respect to the actual electrochemically active mass, $m_{CAM,act}$.

ADVANCED SCIENCE NEWS
www.advancedsciencenews.com

ADVANCED ENERGY MATERIALS
www.advenergymat.de

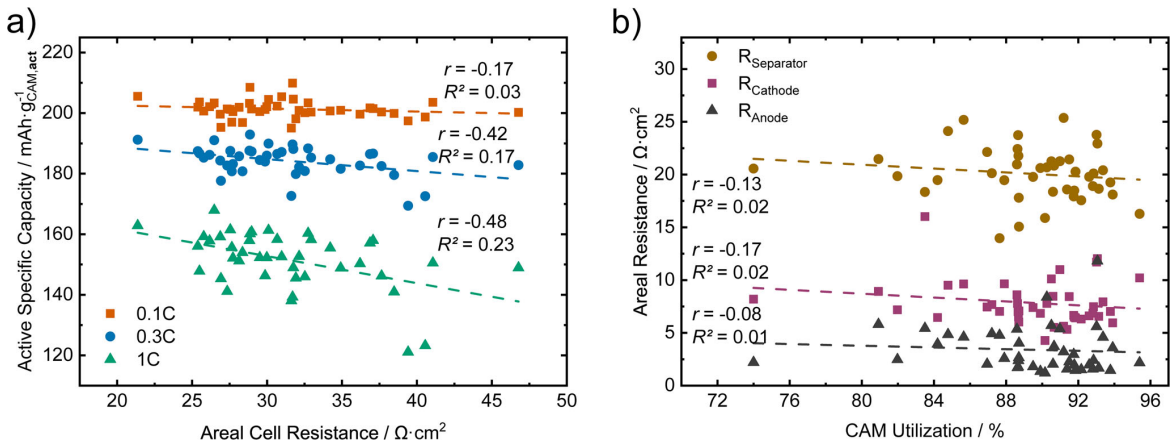

Figure 7. a) Correlation between active specific discharge capacities, calculated with respect to the active mass, and the areal cell resistance extracted from the impedance at 3.1 V vs. In/InLi. b) Individual impedance contributions versus the CAM utilization.

describe 90 % of the variance in capacity at low C-rates (R^2 = 0.90). The correlation between CAM utilization and gross specific capacity is also verified for the last cycle measured at 0.1C at the end of the benchmarking protocol (Figure S5, Supporting Information).

The CAM utilization allows for the normalization of capacities by calculating active specific capacities which are referred to the active mass of CAM particles, $m_{CAM,act}$ (Figure 6b). At 0.1C, this leads to very similar active specific capacities for all cells with a mean value of (201.4 ± 3.0) mAh g^{-1} which is close to the capacity obtained from the LIB cell (Figure S3, Supporting Information). Incidentally, this proves that the OCP relaxation method is suited to determine and compare the CAM utilization quantitatively between different cells. Since the same active material was used for all cells in this study and the cells were cycled identically, also the charge per active CAM particle, calculated via the OCP relaxation method, should be the same and close to the theoretical capacity of the material, as it is the case for the investigated cells. Differences in normalized active specific capacities between different cells result mainly from error propagation in the capacity calculation (cf. Equation 2).

At higher C-rates, the linear model using the CAM utilization as a single parameter can only explain ≈50 % of the gross specific capacity variations measured at 1C (R^2 = 0.53, Figure 6a). Consequently, also the variations in the active specific capacities (Figure 6b) become higher, resulting in mean discharge capacities of (184.2 ± 4.9) mAh g^{-1} at 0.3C and (151.5 ± 9.5) mAh g^{-1} at 1C. This is reasonable since kinetic limitations, i.e. by contributions that lead to an increase in cell resistance and overpotential, become a more prominent factor at higher C-rates and are not fully represented by the CAM utilization. On the one hand, it needs to be considered that depending on the CAM utilization, the active CAM particles experience different effective C-rates than the nominal C-rate.[54] At lower CAM utilization, this results in a comparatively higher overpotential and thus a decrease in the attainable capacity. Correspondingly, an increase of the PCC to r = 0.19 and r = 0.27 for 0.3 and 1C, respectively, for the linear regression of the datapoints of Figure 6b is observed (see Figure S6, Supporting Information). On the other hand, the kinetic limitations in the composite cathode can originate from the transport pathways within its microstructure.

As discussed in previous experimental works and simulations, the cathode microstructure has a strong influence on limiting cell kinetics.[55,56] For example, the effective electronic and ionic conductivities are reduced by the tortuosity of the respective pathways in the composite cathode, which increases the cell resistance.[24,25,30,42] The determination of partial conductivities requires symmetric cell setups,[44,57] three-electrode cells,[58] or transmission line models (TLMs),[40,41,43] which was not possible in this study. The used measurement device sets an upper-frequency limit for the measurement, preventing a suitable fit with a TLM. Nevertheless, we evaluated the cell resistance via electrochemical impedance spectroscopy and fitted the spectra recorded at 3.1 V vs. In/InLi with an R-(RQ)-(RQ)-P equivalent circuit, for simplicity interpreted as a separator-, cathode- and anode-related impedances (Figure S7, Supporting Information), as it is often done in literature.[16,22,41,59] In **Figure 7a**, the active specific discharge capacities for each C-rate are plotted versus the areal cell resistance. It is reasonable to include solely the active CAM in this analysis since only these particles take part in discharging and are susceptible to kinetic effects. In this case, we find a negative correlation, i.e., the capacity decreases with increasing resistance, as expected. While the correlation is generally lower than for the CAM utilization in Figure 6a, it grows with increasing C-rate (r = −0.17 at 0.1C and r = −0.48 at 1C). The same trend is observed when the gross specific capacities are used, but the coefficients of correlation and determination at higher C-rates are lower (Figure S8, Supporting Information).

In addition to the capacities, we expect that the CAM utilization also influences the cathode-related impedance. For a sample that comprises a substantial fraction of electrochemically inactive particles, the effective interface area (= active CAM/SE contact area) is reduced, which should result in elevated cell resistance. To scrutinize this, the separator, cathode, and anode-associated contributions from the impedance are plotted versus the CAM utilization in Figure 7b. As expected, the CAM utilization

ADVANCED SCIENCE NEWS
www.advancedsciencenews.com

ADVANCED ENERGY MATERIALS
www.advenergymat.de

influences neither the separator ($R^2 = 0.02$) nor the anode resistance ($R^2 = 0.01$), i.e., no correlation is found. The linear regression for the cathode resistance yields a slightly higher PCC of $r = -0.17$. However, this value is too low for a correlation, particularly given that the COD is almost zero. We believe that the primary reason for the lack of a substantial observable correlation between cathode resistance and CAM utilization is due to the impedance measurement and corresponding fit. Since the data was fitted with the simplified equivalent circuit R-(RQ)-(RQ)-P, all contributions in the composite are only represented by one (RQ)-element, i.e., by single capacitance and resistance values. As a result, resistance contributions from the active surface area and transport pathways cannot be distinguished. Furthermore, the direct proportionality between the effective interface area and the CAM utilization is probably an oversimplification and not valid in a real microstructure. As we will discuss later, a particle can still be considered active after a partial contact loss. At the same time, the corresponding interface area with the solid electrolyte changes, which leads to an increase in resistance. This means that there is no direct connection between the CAM utilization and the microscopic active interface area.

Overall, the cell performance is strongly affected by the mixing process, during which the actual fraction of electrochemically active mass is defined. This leads to significant variations in the measured gross specific capacities for nominally identical cells. Quantifying the active mass and CAM utilization enables the calculation of active specific capacities, which can compensate for differences in the mixing process. This approach is particularly effective at low C-rates, while at higher C-rates, additional kinetic effects, not fully captured by the CAM utilization as a single parameter, come into play.

2.2.2. The Role of Electrode Design for the Mixing Process and Performance

Successful and reproducible mixing leading to a functional microstructure requires not only a suitable process but also a good electrode design of the composite. The electrode design comprises aspects such as appropriate mass ratios of the electronic and ionic conducting phases, matching particle sizes, and morphologies which all must enable the formation of well percolating networks. For instance, if the amount of SE is chosen too high compared to the electron-conducting phases, no mixing process can build up a microstructure with a well-percolating electronic network and high effective electronic conductivity. This will not only affect the active mass but also the kinetics of the cell. In the following, we illustrate that a poor electrode design impedes a successful mixing process and has a detrimental impact on the kinetic cell performance and reproducibility.

To this end, an identical machine-made composite preparation and cell assembly was carried out using a different product batch of conductive additive (type 2), nominally also carbon nanofibers (CNF). However, the two CNF types possess different morphologies and presumably different dispersing behavior during the composite mixing. While the previously used CNF (type 1) consists of intact fibers, the microstructure of the CNF type 2 is dominated by spherical and agglomerated entities and fibers appear to be disrupted (cf. Figure S9, Supporting Information). The gross

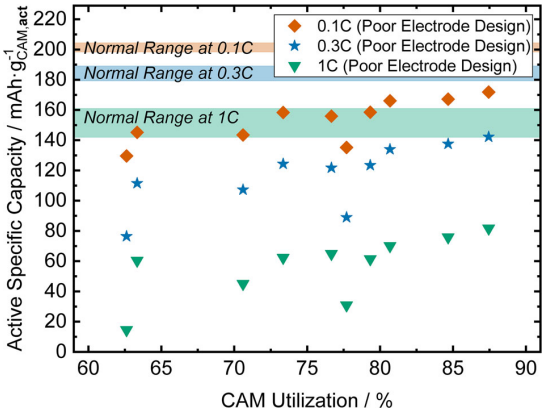

Figure 8. Active specific capacities, calculated with respect to the actual electrochemically active mass, versus CAM utilization for the composites using a different conductive additive (poor electrode design). The shaded areas indicate the mean values and standard deviations (normal range) of capacity variation depicted in Figure 6b.

specific capacities of ten cells using CNF type 2 are depicted in **Figure 8** together with the ranges of active specific capacities observed before (cf. Figure 6b). The CAM utilization for the cells with CNF type 2 is lower than observed with CNF type 1 (75.6 % versus 89.8 % on average). Further, the active specific capacities are significantly reduced by up to 40% at 0.1C and up to 90% at 1C compared to the typical ranges achieved with composites using CNF type 1. Based on the impedance evaluation and differential capacity plots (Figures S10 and S11, Supporting Information), we attribute this weaker performance to a severe kinetic limitation due to the different types of CNF. This leads to significant overpotentials even at 0.1C and thus also the corresponding active specific capacities are lowered. We assume that the CNF type 2 is unable to provide a fine electronically percolating network, which in turn results in a poor electrode design and cell performance with large variations (Figure S12, Supporting Information). At this point, it should be noted that the CAM utilization is a static property and only differentiates between connected and unconnected CAM particles. This parameter does not contain any information on the quality of the connection which is affected by the electrode design.

We further observed that increasing the CAM mass fraction to 80 wt%, while keeping the same CNF type 2, leads to an improvement of the electrochemical properties. The resistances (Figures S10 and S11, Supporting Information) and capacities (Figures S12 and S13, Supporting Information) of the cells come closer to the normal cells with a good electrode design. In this case, we assume that there are already enough electronic pathways because of the higher volume fraction of electronically conducting CAM particles so that the CNF has a less drastic influence on the performance. For the composition of 70:30:1 weight ratio (CAM:SE:CNF) this is not the case and a functional carbon additive is needed to provide an electronically percolating network.

These results stress the importance of the electrode design, which includes the composition as well as the quality of the employed materials for a successful mixing process and good cell

ADVANCED SCIENCE NEWS
www.advancedsciencenews.com

ADVANCED ENERGY MATERIALS
www.advenergymat.de

performance. The presented simple method of evaluating the active mass helps to judge the optimum material choice better by revealing severe kinetic limitations. If the normalized active specific capacities at low C-rates strongly deviate from the theoretical specific capacity, it is a clear indication of significant kinetic limitations, e.g. due to the electrode design.

2.2.3. Assessing the Degree of Mixing to Prevent Data Misinterpretation

In SSB composite cathodes, the achievable capacities strongly depend on the cathode composite microstructure, which, as discussed in the previous sections, is a result of both the electrode design and the composite mixing. To evaluate the mixing quality, we can distinguish two degrees of mixing:

The *primary degree of mixing* quality describes how many particles are actually electrochemically active and is quantified by the CAM utilization as a single parameter. Clearly, this static property defines the achievable capacities at all C-rates by setting the upper limit that can be reached. This limit depends on the electrode design and the success of the mixing process. Another aspect that comes into play at this point is protective CAM coatings. Such coatings are typically electronic insulators [60] and, depending on the coating process, the coating layer might get too thick so that the particles are electronically isolated. This lowers the CAM utilization even further but cannot directly be related to the mixing process itself.

The *secondary degree of mixing* is a measure of how tortuous the transport pathways are which can be quantified by effective conductivities.[44] Here, a good mixing, i.e., a microstructure with low tortuosity, leads to better kinetics, which is especially beneficial at elevated C-rates. However, kinetics are not only microstructure and electrode design dependent but are also affected by interfacial effects such as coating layers, degradation, and poor charge transfer kinetics.

It often remains unclear to which extent a measured gross specific capacity is affected by static or kinetic properties. For low C-rates, it was shown that the corresponding capacities can be normalized, under the condition of a good electrode design, via the electrochemically active mass to calculate the active specific capacity. However, a more accurate normalization method to compensate for microstructural effects at higher C-rates still needs to be developed. A first step toward better comparability is to display rate capability data with respect to effective C-rates in addition to nominal C-rates.[54] In general, absolute specific capacity values measured at higher C-rates might be misleading since the secondary degree of mixing becomes more important.

These considerations on the mixing are highly important for the correct data interpretation in different types of studies. To illustrate why, we propose the following thought experiment: The objective is to conduct a comparative analysis of various SEs and evaluate their performance in a composite cathode comprising the same CAM, same processing, and same composition. The cells are cycled at varying C-rates, and the resulting capacities are evaluated. Remarkable discrepancies between the measured absolute capacities, i.e., gross specific capacities, for different SEs are observed. If we now argue that the SE which leads to the highest specific capacity is 'superior' to the others, we might misinterpret the data. As clearly shown in this study, differences in measured capacities cannot be solely attributed to the SE properties under investigation, such as interfacial degradation, but also depend substantially on the microstructure. The latter is significantly affected by the mixing process as well as the electrode design, the properties of the SEs, and their compatibility with the CAM. For the SE, particularly the mean and width of particle size distribution, particle adhesion forces, and mechanical characteristics influence the quality of mixing and the resulting microstructure. If knowledge of the microstructure, its homogeneity, and the fraction of residual pores is not available, it is not possible to draw well-founded conclusions regarding the performance of the tested SEs. Thus, it remains unclear whether the observed differences in performance originate mainly from the SE itself, for instance, due to varying interfacial degradation, or from the microstructure/mixing, for example, due to particle size issues. A first countermeasure toward more reliable and comparable data would be to determine the active specific capacities by quantifying the CAM utilization and taking these normalized capacities as a reference.

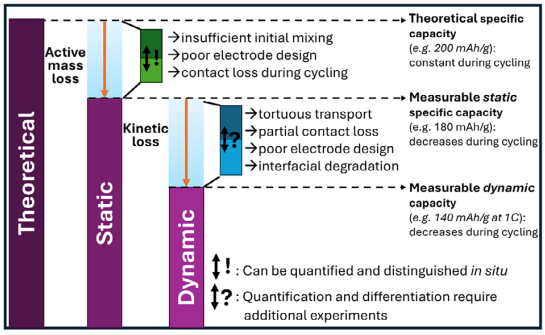

Figure 9. Factors influencing the measurable capacity of solid-state cells. The CAM utilization significantly affects the capacities and needs to be differentiated from other contributions.

2.2.4. Pitfalls and Challenges for the Interpretation of Specific Capacities

Figure 9 gives an overview of possible factors that contribute to a reduced measured (gross) specific capacity and need to be considered when evaluating the performance of solid-state cells. In general, the capacity losses, compared to the theoretical specific capacity, can be divided into two groups: (static) active mass loss and kinetic loss.

The contributions to active mass loss can be quantified and distinguished in situ and define the measurable static specific capacity. On the one hand, initial static active mass loss occurs due to insufficient mixing, which is easily disregarded but cannot be neglected as intensively discussed in this work. Furthermore, poor electrode design leads to an active mass loss since a successful composite mixing requires that the components in principle allow the formation of percolating electronic and ionic networks. Hence, the mass and size ratios of CAM and SE as well as the types and amounts of conductive additives need to be individually adapted to each material system. Also, too high

ADVANCED SCIENCE NEWS
www.advancedsciencenews.com

ADVANCED ENERGY MATERIALS
www.advenergymat.de

porosities must be avoided by sufficient densification and compatible mechanical properties of the particles. We recommend quantifying the initial CAM utilization after a formation cycle at the outset of the electrochemical testing, as presented in this study, to ensure an accurate calculation of the active specific capacities.

On the other hand, solid-state cells are prone to contact loss and cracking, i.e., chemo-mechanical degradation, during cycling because of the volumetric expansion and contraction of active material particles.[40,61,62] The quantification of active mass loss due to contact loss during extended cycling has been demonstrated in previous works.[30,40,43] Hereby, we differentiate between i) complete loss of electronic contact, which results in an inactive CAM particle, and ii) complete loss of ionic contact to the SE, which still allows Li-ions to diffuse into connected CAM particles. Moreover, chemo-mechanical degradation can result in iii) partial ionic contact loss, which leads to less active interfacial area, and iv) partial electronic contact loss. In the latter three cases, the CAM particles are considered as statically active, but their charge contribution is kinetically limited. It has already been shown that their impact on the kinetic losses can be quantified.[40,41,59]

Additionally, kinetic losses have a further microstructural and interfacial degradation component. The microstructure, which is a result of the mixing process and electrode design, defines the effective electronic and ionic conductivities by the tortuosity of the transport pathways. The quantification of their contribution to the resistance and thus kinetic capacity loss requires additional experiments as extensively discussed in the literature.[24,25,42,44,57] Other types of interfacial degradation, e.g. due to oxidation of the SE, lead to a further increase in resistance during cycling.[20,21,60] However, in practice, the differentiation between all kinetic contributions is challenging, but necessary to discuss to which extent a good or poor C-rate performance stems from poor kinetics due to the microstructure, i.e., tortuosity of transport pathways, or due to other effects, such as interfacial degradation.

In evaluating and comparing the performance of cells, three factors are of particular importance regarding the discussion of specific capacities. First, it is essential to clearly indicate the type of calculated specific capacity, namely, to which mass the charge refers. Therefore, we propose to differentiate between the gross specific capacity and the active specific capacity. Second, it is recommended to normalize specific capacities to the active mass, as demonstrated in this study, to enable a more meaningful comparison of the performance of different cells. Thirdly, it is reasonable to indicate the effective C-rates, which depend on the active mass, in addition to the nominal C-rates.

2.2.5. Challenges for the Mixing Process of Cathode Composites for Solid-State Batteries

As intensively discussed, the performance and reproducibility of SSB cells are strongly affected by the composite cathode's microstructure, which is defined during the mixing process. Thereby, even small-scale devices such as the mini vibrating mill used in this study pose a challenge for the mixing process because they allow the variation of many process parameters, such as frequency, time, milling media, or filling level of the milling jar. All these parameters can have an influence on the performance as well as on the reproducibility (see Section S1, Supporting Information) and a complete optimization of the mixing process would require a time-consuming parameter study. Furthermore, it should be noted that optimized mixing parameters for one material combination are not necessarily suitable for other materials or cathode compositions. This is why we believe that a fully optimized lab-scale mixing process, aimed at achieving the highest performance, is not always necessary. Rather the performance reproducibility by a stable mixing process and the consideration of the microstructure for the interpretation are of greater importance in many studies. For this purpose, the cathode composite should be machine-mixed, e.g. in a planetary ball mill or vibrating mill.

A further advantage of such lab-scale mixing devices is that they can serve as useful model systems to simulate the mixing action. These simulations have proven to be helpful tools in quantifying for instance the stressing conditions such as stress intensity distribution and stress number [63] during different mixing processes.[35,64,65] The corresponding simulations of lab-scale devices provide a better understanding and control of the mixing process, which is beneficial for the large-scale production and commercialization of solid-state batteries. In this context, further challenges, such as the incorporation of an electrically insulating binder must be addressed [5,33,34,66,67] Overall, using machine-made cathode composites already at the lab scale not only improves reproducibility but also potentially allows the extraction of mixing parameters to bridge the gap to large-scale mixers, facilitating the optimization of large-scale processing of SSBs.

3. Conclusions

In this work, the intra-laboratory reproducibility of solid-state battery cells in the form of pelletized press cells is investigated. To this end, commercial $LiNi_{0.82}Mn_{0.07}Co_{0.11}O_2$, Li_6PS_5Cl, and CNFs are used in cathode composites, prepared by hand grinding as well as in a mini vibrating mill, to identify possible error sources affecting the reproducibility and overall cell performance. We propose a detailed cell assembly protocol based on machine-made cathode composites that leads to comparable and reproducible solid-state battery cells. Our study demonstrates that significant differences in capacity result from different mixing conditions, which lead to variations in the amount of electrochemically active mass in the composite cathode. The corresponding CAM utilization is shown to be easily electrochemically quantifiable in situ, enabling the normalization of specific capacities to calculate active specific capacities. This proposed approach, readily adaptable to most electrochemical testing protocols, helps to avoid misinterpretation of capacity data. As a result, significant differences in electrochemical performance can now be attributed primarily to the materials or interface modifications being studied, rather than to inhomogeneous mixing. In this context, we illustrate how quantifying the CAM utilization at the beginning of electrochemical cycling experiments allows for a clearer distinction between static and dynamic capacity losses, highlighting its significance when comparing different cell performances. Furthermore, we encourage using machine-made cathode composites, if possible, as they also

ADVANCED SCIENCE NEWS
www.advancedsciencenews.com

ADVANCED ENERGY MATERIALS
www.advenergymat.de

facilitate the acceleration of large-scale processing optimization for SSBs.

4. Experimental Section

Materials and Solid-State Cell Assembly: Single-crystalline NCM82 ($LiNi_{0.82}Mn_{0.07}Co_{0.11}O_2$, with $d_{10}/d_{50}/d_{90}$ = 1.7/3.3/6.1 µm, from MSE Supplies, Tucson, AZ, USA), Li_6PS_5Cl (Argyrodite-CSMP with $d_{10}/d_{50}/d_{90}$ = 0.44/0.79/1.82 µm, from Posco JK Solid Solution, South Korea,) and carbon nanofiber (batch "type 1" with product number 719781 or "type 2" with product number 719811 from Sigma–Aldrich, Saint Louis, MO, USA) was used for the cathode composite with 70:30:1 weight ratio. The composites were either mixed with mortar and pestle or machine-made in a mini vibrating mill (Pulverisette 23 from Fritsch GmbH, Idar-Oberstein, Germany). The parameters for the machine-made mixing process are available in Zenodo at 10.5281/zenodo.14065128. The separator layer consisted of Li_6PS_5Cl (Argyrodite-CMP5 from Posco JK Solid Solution, South Korea). As anode, an indium foil (Alfa Aesar, 99.99%, 9 mm diameter, 100 µm thickness) and a lithium foil (China Energy Lithium, 6 mm diameter, 100 µm thickness) were used. All materials were stored and handled in an argon-filled glovebox to maintain their integrity, with oxygen residues of $p(O_2)/p < 1.0$ ppm and water residues of $p(H_2O)/p < 1.0$ ppm. During this study, no cell was built that was not working at all.

LIB Electrode Preparation: Electrodes were prepared by mixing nickel cobalt manganese oxide ($LiNi_{0.82}Mn_{0.07}Co_{0.11}O_2$ from MSE Supplies), N-methyl-2-pyrrolidone (NMP from Sigma–Aldrich Co.), SuperP carbon (MSE Supplies), and polyvinylidene fluoride (PVDF from MSE Supplies) in a weight ratio of 96:2:2 for the solid components, with a total solid content of 55%. The mixing was performed under argon using a planetary mixer at 2000 rpm for 20 min.

The resulting slurry was cast onto aluminum foil at a rate of 5 mm s^{-1} using a doctor blade with a gap of 120 µm. The foil was heated to 60 °C during the casting. After casting, the cathode sheet was dried under a vacuum at 120 °C for 12 h. The dried electrode was then punched into 12 mm diameter disks and uniaxially compressed with 203 MPa to ensure uniform density. The electrode loading was ≈10 mg cm^{-2}.

LIB Coin Cell Assembly: A general guide for making coin cells can be found elsewhere.[68,69] CR2032 coin cells were assembled using Al-coated cathode cases (MTI Corporation) to prevent degradation of the stainless steel at high potentials. For the anode cases, stainless steel casings were used. In the anode case, a stainless steel spring and stainless steel spacer (16 mm diameter, 100 µm thick) were placed. On top of the spacer a lithium metal chip (MSE Supplies), cleaned by mechanically removing the passivation layer, with a diameter of 14 mm and a thickness of 600 µm was placed. The separator stack consisted of one glass fiber separator (16 mm diameter, GF/D – Whatman) facing the anode and one Celgard separator (16 mm diameter, Celgard) facing the cathode. A total of 70 µL of LP40 electrolyte solution (1 M $LiPF_6$ in 50:50 v/v ethylene carbonate (EC) and diethyl carbonate (DEC), Sigma–Aldrich Co.) was added. The coin cells were sealed using a coin cell crimping press (MTI Corporation) with a force of 0.9 tons. Figure S2 (Supporting Information) depicts the capacity values obtained for a liquid cell at 0.1/0.3/1C.

Electrochemical Measurements: The electrochemical measurements were performed at 25 °C with a BCS-805 Battery Cycling System (Bio-Logic, Seyssinet-Pariset, France). The currents for the galvanostatic cycling were calculated based on a CAM capacity of 190 mAh g^{-1}. The impedance was measured at room temperature with an amplitude of 10 mV. The fitting was done using a serial connection of one resistor, two (R)(Q) elements, and one constant phase element, i.e., R-(R)(Q)-(R)(Q)-P, as equivalent circuit schematically drawn in Figure S7 (Supporting Information). The three resistance values are associated with separator, cathode, and anode contributions. The impedance spectra were fitted using the RelaxIS 3 software package (rhd Instruments, Darmstadt, Germany). Each impedance spectrum was tested for stationarity using the Kramers-Kroning test.

Active Mass Determination: For the active mass determination (adapted from[40]) during the benchmarking program, each SSB cell was charged with 0.1C to 3.1 V, held at that potential for 3 h followed by 4 h of relaxation to determine the potential V_1. Then the cell was charged with 0.05C up to 3.4 V followed by 4 h of relaxation to get the potential V_2. The values of the relaxed potentials for the solid-state cells can be found in Data File S1, Supporting Information. As a quasi-OCP (titration) curve of the CAM, the second charge of a liquid electrolyte cell at 0.02C was taken as a reference (Figure S4, Supporting Information). The liquid cell data was used to assign a reference capacity value q_{actual} to the potential range determined by V_1 and V_2. This value was compared with the measured charge $Q_{measured}$ of the solid-state cell, which can be extracted with the analysis software. The actual electrochemically active mass, $m_{CAM,act}$, was then calculated with:[40,43]

$$m_{CAM,act} = \frac{Q_{measured}}{q_{actual}} \tag{3}$$

The CAM utilization described the ratio between $m_{CAM,act}$, and the total mass of active material that was in the cathode, $m_{CAM,tot}$. While the reference coin cell was not fully optimized and could potentially be improved further, a quantitative comparison among the different SSB cells was possible and valid since all cell data were referred to the same liquid reference cell.

Supporting Information

Supporting Information is available from the Wiley Online Library or from the author.

Acknowledgements

M.K., F.F., A.K. and J.J. acknowledge financial support by Deutsche Forschungsgemeinschaft (DFG, German Research Foundation) through the Priority Program 2289 (Project 462470125) and the Projects 03XP0430A and 03XP0430C (FestBatt Cluster of Competence, FB2-Thio). D.K. and F.H.R. acknowledge the German Federal Ministry of Education and Research (BMBF) for their financial support for the project FLiPS (03XP0261). The language and grammar of the manuscript have partially been improved with the help of DeepL Write and ChatGPT4.0 (by OpenAI).

Open access funding enabled and organized by Projekt DEAL.

Conflict of Interest

The authors declare no conflict of interest.

Data Availability Statement

The data that support the findings of this study are openly available in Zenodo at https://doi.org/10.5281/zenodo.14065128, reference number 14065128.

Keywords

cathode composites, cathode mixing, cell processing, NCM, solid-state battery, sulfide solid electrolytes

Received: November 18, 2024
Revised: March 25, 2025
Published online:

[1] J. Janek, W. G. Zeier, *Nat. Energy* **2023**, *8*, 230.

[2] J. Schnell, T. Günther, T. Knoche, C. Vieider, L. Köhler, A. Just, M. Keller, S. Passerini, G. Reinhart, *J. Power Sources* **2018**, *382*, 160.
[3] Y. Lu, C. Zhao, H. Yuan, J. K. Hu, J. Huang, Q. Zhang, *Matter* **2022**, *5*, 876.
[4] D. Ren, L. Lu, R. Hua, G. Zhu, X. Liu, Y. Mao, X. Rui, S. Wang, B. Zhao, H. Cui, M. Yang, H. Shen, C. Z. Zhao, L. Wang, X. He, S. Liu, Y. Hou, T. Tan, P. Wang, Y. Nitta, M. Ouyang, *eTransportation* **2023**, *18*, 100272.
[5] M. Batzer, C. Heck, P. Michalowski, A. Kwade, *Batteries Supercaps* **2022**, *5*, 202200328.
[6] M. Rana, Y. Rudel, P. Heuer, E. Schlautmann, C. Rosenbach, M. Y. Ali, H. Wiggers, A. Bielefeld, W. G. Zeier, *ACS Energy Lett.* **2023**, *8*, 3196.
[7] Y. J. Nam, K. H. Park, D. Y. Oh, W. H. An, Y. S. Jung, *J. Mater. Chem. A* **2018**, *6*, 14867.
[8] C. D. Alt, S. Keuntje, I. L. Schneider, J. Westphal, P. Minnmann, J. K. Eckhardt, K. Peppler, J. anek, *Adv. Energy Mater.* **2024**, *15*, 2404055.
[9] S. Yanev, C. Heubner, K. Nikolowski, M. Partsch, H. Auer, A. Michaelis, *J. Electrochem. Soc.* **2024**, *171*, 020512.
[10] A. Ikezawa, G. Fukunishi, T. Okajima, F. Kitamura, K. Suzuki, M. Hirayama, R. Kanno, H. Arai, *Electrochem. Commun.* **2020**, *116*, 106743.
[11] L. Xu, J. Li, H. Shuai, Z. Luo, B. Wang, S. Fang, G. Zou, H. Hou, H. Peng, X. Ji, *J. Energy Chem.* **2022**, *67*, 524.
[12] T. Zhang, W. He, W. Zhang, T. Wang, P. Li, Z. Sun, X. Yu, *Chem. Sci.* **2020**, *11*, 8686.
[13] P. Minnmann, F. Strauss, A. Bielefeld, R. Ruess, P. Adelhelm, S. Burkhardt, S. L. Dreyer, E. Trevisanello, H. Ehrenberg, T. Brezesinski, F. H. Richter, J. anek, *Adv. Energy Mater.* **2022**, *12*, 2201425.
[14] Z. Zeng, J. Cheng, Y. Li, H. Zhang, D. Li, H. Liu, F. Ji, Q. Sun, L. Ci, *Mater. Today Phys.* **2023**, *32*, 101009.
[15] Y. Ren, T. Danner, A. Moy, M. Finsterbusch, T. Hamann, J. Dippell, T. Fuchs, M. Müller, R. Hoft, A. Weber, L. A. Curtiss, P. Zapol, M. Klenk, A. T. Ngo, P. Barai, B. C. Wood, R. Shi, L. F. Wan, T. W. Heo, M. Engels, J. Nanda, F. H. Richter, A. Latz, V. Srinivasan, J. Janek, J. Sakamoto, E. D. Wachsman, D. FattakhovaRohlfing, *Adv. Energy Mater.* **2023**, *13*, 2201939.
[16] J. Lin, M. Schaller, G. Cherkashinin, S. Indris, J. Du, C. Ritter, A. Kondrakov, J. Janek, T. Brezesinski, F. Strauss, *Small* **2023**, *20*, 2306832.
[17] E. Schlautmann, A. Weiß, O. Maus, L. Ketter, M. Rana, S. Puls, V. Nickel, C. Gabbey, C. Hartnig, A. Bielefeld, W. G. Zeier, *Adv. Energy Mater.* **2023**, *13*, 2302309.
[18] J. S. Kim, S. Jung, H. Kwak, Y. Han, S. Kim, J. Lim, Y. M. Lee, Y. S. Jung, *Energy Storage Mater.* **2023**, *55*, 193.
[19] J. Lin, M. Schaller, S. Indris, V. Baran, A. Gautam, J. Janek, A. Kondrakov, T. Brezesinski, F. Strauss, *Angew. Chem., Int. Ed.* **2024**, *63*, 202404874.
[20] F. Jin, L. Fadillah, H. Q. Nguyen, T. M. Sandvik, Y. Liu, A. GarcíaMartín, E. Salagre, E. G. Michel, D. Stoian, K. Marshall, W. van Beek, G. Redhammer, M. Mehraj Ud Din, D. Rettenwander, *Chem. Mater.* **2024**, *36*, 6017.
[21] J. Hertle, F. Walther, T. Lombardo, C. Kern, B. Pavlovic, B. Mogwitz, X. Wu, H. Schneider, M. Rohnke, J. Janek, *ACS Appl. Mater. Interfaces* **2024**, *16*, 9400.
[22] W. Zhang, D. A. Weber, H. Weigand, T. Arlt, I. Manke, D. Schröder, R. Koerver, T. Leichtweiss, P. Hartmann, W. G. Zeier, J. Janek, *ACS Appl. Mater. Interfaces* **2017**, *9*, 17835.
[23] O. Maus, M. A. Lange, F. Frankenberg, F. Stainer, V. Faka, E. Schlautmann, C. Rosenbach, A. Jodlbauer, J. Schubert, J. Janek, C. Li, P. Michalowski, H. M. R. Wilkening, A. Kwade, W. G. Zeier, *Adv. Energy Mater.* **2024**, *15*, 2403291.
[24] T. A. Hendriks, M. A. Lange, E. M. Kiens, C. Baeumer, W. G. Zeier, *Batteries Supercaps* **2023**, *6*, 202200544.
[25] H. M. Woolley, M. Lange, E. Nazmutdinova, N. M. Vargas-Barbosa, *ACS Energy Lett.* **2024**, *11*, 3547.
[26] S. Puls, E. Nazmutdinova, F. Kalyk, H. M. Woolley, J. F. Thomsen, Z. Cheng, A. Fauchier-Magnan, A. Gautam, M. Gockeln, S. Y. Ham, M. T. Hasan, M. G. Jeong, D. Hiraoka, J. S. Kim, T. Kutsch, B. Lelotte, P. Minnmann, V. Miß, K. Motohashi, D. L. Nelson, F. Ooms, F. Piccolo, C. Plank, M. Rosner, S. E. Sandoval, E. Schlautmann, R. Schuster, D. Spencer-Jolly, Y. Sun, B. S. Vishnugopi, et al., *Nat. Energy* **2024**, *9*, 1310.
[27] A. Bielefeld, D. A. Weber, J. Janek, *J. Phys. Chem. C* **2019**, *123*, 1626.
[28] A. Bielefeld, D. A. Weber, J. Janek, *ACS App. Mater. Interfaces* **2020**, *12*, 12821.
[29] T. Shi, Q. Tu, Y. Tian, Y. Xiao, L. J. Miara, O. Kononova, G. Ceder, *Adv. Energy Mater.* **2020**, *10*, 1902881.
[30] P. Minnmann, J. Schubert, S. Kremer, R. Rekers, S. Burkhardt, R. Ruess, A. Bielefeld, F. H. Richter, J. Janek, *J. Electrochem. Soc.* **2024**, *171*, 060514.
[31] F. Strauss, T. Bartsch, L. Biasi, A. Y. Kim, J. Janek, P. Hartmann, T. Brezesinski, *ACS Energy Lett.* **2018**, *3*, 992.
[32] D. Hlushkou, A. E. Reising, N. Kaiser, S. Spannenberger, S. Schlabach, Y. Kato, B. Roling, U. Tallarek, *J. Power Sources* **2018**, *396*, 363.
[33] L. Fernandez-Diaz, J. Castillo, E. Sasieta-Barrutia, M. Arnaiz, M. Cabello, X. Judez, A. Terry, L. Otaegui, M. C. Morant-Miñana, A. Villaverde, *Chem. Eng. J.* **2023**, *464*, 142469.
[34] S. Noh, W. T. Nichols, M. Cho, D. Shin, *J. Electroceram.* **2018**, *40*, 293.
[35] F. Frankenberg, M. Kissel, C. F. Burmeister, M. Lippke, J. Janek, A. Kwade, *Powder Technol.* **2024**, *435*, 119403.
[36] A. Sakuda, T. Takeuchi, H. Kobayashi, *Solid State Ionics* **2016**, *285*, 112.
[37] N. M. VargasBarbosa, *Nat. Nanotechnol.* **2024**, *19*, 419.
[38] S. Randau, D. A. Weber, O. Kötz, R. Koerver, P. Braun, A. Weber, E. Ivers-Tiffée, T. Adermann, J. Kulisch, W. G. Zeier, F. H. Richter, J. Janek, *Nat. Energy* **2020**, *5*, 259.
[39] S. Ohno, T. Bernges, J. Buchheim, M. Duchardt, A. K. Hatz, M. A. Kraft, H. Kwak, A. L. Santhosha, Z. Liu, N. Minafra, F. Tsuji, A. Sakuda, R. Schlem, S. Xiong, Z. Zhang, P. Adelhelm, H. Chen, A. Hayashi, Y. S. Jung, B. V. Lotsch, B. Roling, N. M. Vargas-Barbosa, W. G. Zeier, *ACS Energy Lett.* **2020**, *5*, 910.
[40] G. Conforto, R. Ruess, D. Schröder, E. Trevisanello, R. Fantin, F. H. Richter, J. Janek, *J. Electrochem. Soc.* **2021**, *168*, 070546.
[41] R. Ruess, S. Schweidler, H. Hemmelmann, G. Conforto, A. Bielefeld, D. A. Weber, J. Sann, M. T. Elm, J. Janek, *J. Electrochem. Soc.* **2020**, *167*, 100532.
[42] C. König, V. Miß, L. Janin, *ACS Appl. Energy Mater.* **2023**, *6*, 9356.
[43] B. X. Shi, Y. Yusim, S. Sen, T. Demuth, R. Ruess, K. Volz, A. Henss, F. H. Richter, *Adv. Energy Mater.* **2023**, *13*, 2300310.
[44] P. Minnmann, L. Quillman, S. Burkhardt, F. H. Richter, J. Janek, *J. Electrochem. Soc.* **2021**, *168*, 040537.
[45] S. Kim, Y. Lee, K. Kim, B. C. Wood, S. S. Han, S. Yu, *ACS Energy Lett.* **2024**, *9*, 38.
[46] C. König, A. Ramanayagam, J. Kraus, B. Roling, *Batteries Supercaps* **2024**, *7*, 202300578.
[47] D. Lee, Z. Cui, J. B. Goodenough, A. Manthiram, *Small* **2024**, *20*, 2306053.
[48] P. Lu, Y. Wu, D. Wu, F. Song, T. Ma, W. Yan, X. Zhu, F. Guo, J. Lu, J. Peng, L. Chen, H. Li, F. Wu, *Energy Storage Mater.* **2024**, *67*, 103316.
[49] L. Shen, J. L. Li, W. J. Kong, C. X. Bi, P. Xu, X. Y. Huang, W. Z. Huang, F. Fu, Y. C. Le, C. Z. Zhao, H. Yuan, J. Q. Huang, Q. Zhang, *Adv. Funct. Mater.* **2024**, *34*, 2408571.
[50] Y. Wang, H. Hao, K. G. Naik, B. S. Vishnugopi, C. D. Fincher, Q. Yan, V. Raj, H. Celio, G. Yang, H. Fang, Y. M. Chiang, F. A. Perras, P. Jena, J. Watt, P. P. Mukherjee, D. Mitlin, *Adv. Energy Mater.* **2024**, *14*, 2304530.
[51] V. Faka, M. T. Agne, M. A. Lange, D. Daisenberger, B. Wankmiller, S. Schwarzmüller, H. Huppertz, O. Maus, B. Helm, T. Böger, J. Hartel,

ADVANCED SCIENCE NEWS
www.advancedsciencenews.com

ADVANCED ENERGY MATERIALS
www.advenergymat.de

J. M. Gerdes, J. J. Molaison, G. Kieslich, M. R. Hansen, W. G. Zeier, *J. Am. Chem. Soc.* **2024**, *146*, 1710.
[52] D. Alves Dalla Corte, L. Lutz, P. Minnmann, S. Claramunt, A practical guide to building and evaluating lab scale solid-state batteries (white paper), www.hte-company.com.
[53] T. Bartsch, A. Y. Kim, F. Strauss, L. Biasi, J. H. Teo, J. Janek, P. Hartmann, T. Brezesinski, *Chem. Commun.* **2019**, *55*, 11223.
[54] S. Yanev, H. Auer, C. Heubner, S. Höhn, K. Nikolowski, M. Partsch, A. Michaelis, *J. Electrochem. Soc.* **2022**, *169*, 090519.
[55] A. Bielefeld, D. A. Weber, R. Rueß, V. Glavas, J. Janek, *J. Electrochem. Soc.* **2022**, *169*, 020539.
[56] K. G. Naik, B. S. Vishnugopi, P. P. Mukherjee, *ACS App. Mater. Interfaces* **2022**, *14*, 29754.
[57] N. Kaiser, S. Spannenberger, M. Schmitt, M. Cronau, Y. Kato, B. Roling, *J. Power Sources* **2018**, *396*, 175.
[58] E. Quemin, R. Dugas, A. Chaupatnaik, G. Rousse, R. Chometon, B. Hennequart, J. Tarascon, *Adv. Energy Mater.* **2023**, *13*, 2301105.
[59] E. Trevisanello, R. Ruess, G. Conforto, F. H. Richter, J. Janek, *Adv. Energy Mater.* **2021**, *11*, 2003400.
[60] Y. Kimura, T. Fujisaki, T. Shimizu, T. Nakamura, Y. Iriyama, K. Amezawa, *Commun. Mater.* **2024**, *5*, 1.
[61] J. A. Lewis, J. Tippens, F. J. Q. Cortes, M. T. McDowell, *Trends in Chemistry* **2019**, *1*, 845.
[62] F. Strauss, L. Biasi, A. Y. Kim, J. Hertle, S. Schweidler, J. Janek, P. Hartmann, T. Brezesinski, *ACS Mater. Lett.* **2020**, *2*, 84.
[63] A. Kwade, *Chem Eng. Technol.* **2003**, *26*, 199.
[64] C. Welch, K. T. Cho, V. Srinivasan, *Chem. Mater.* **2024**, *36*, 6748.
[65] R. Schlem, C. F. Burmeister, P. Michalowski, S. Ohno, G. F. Dewald, A. Kwade, W. G. Zeier, *Adv. Energy Mater.* **2021**, *11*, 2101022.
[66] Y. J. Nam, D. Y. Oh, S. H. Jung, Y. S. Jung, *J. Power Sources* **2018**, *375*, 93.
[67] M. Batzer, K. Voges, W. Wang, P. Michalowski, A. Kwade, *Mater. Today Commun.* **2022**, *30*, 103189.
[68] T. Marks, S. Trussler, A. J. Smith, D. Xiong, J. R. Dahn, *J. Electrochem. Soc.* **2011**, *158*, A51.
[69] V. Murray, D. S. Hall, J. R. Dahn, *J. Electrochem. Soc.* **2019**, *166*, A329.

6 When Mixing makes Coatings

The scalable creation of tailored cathode composite microstructures via mixing was largely unexplored at the beginning of this thesis project in January 2022. While theoretical studies suggest ideal PSDs or microstructures[20,151], realizing them in a scalable manner remained difficult. Especially employing small CAM particles of a few micrometers or less is demanding since it requires SE particles of even smaller sizes, which is challenging for the comminution and de-agglomeration process of the SE.[30,240] Mixing cathode composites in ball mills, as for instance done in Publication I and II, often results in a rather random arrangement of particles.[159] This raised the question of whether such a "simple" mixing is suitable to create high-performance cathode composites and which alternative scalable approaches are promising.

6.1. Publication III: *Mechanofusion-derived cathode composite microstructures with scalable mixed conducting matrix coatings for solid state batteries*

In this systematic study, a scalable high-intensity ringlayer mixer was used to mix single-crystalline NCM82 with the halide SE Li_3InCl_6 (LIC). LIC has the advantage that it can be synthesized via a simple water-based route and needs to be considered as a model catholyte. A key finding was that the process did not lead to simple mixing but to coating of the NCM particles with LIC, blurring the boundary between “mixing” and “coating”. This approach, based on mechanofusion, was exploited to produce tailored microstructures in the form of a mixed conducting matrix coating. Incorporating CB as an electron-conducting additive enabled the mixed conducting property of the coating. The influence of CB content in the coating was systematically investigated, revealing a trade-off between high CAM utilization, fast cell kinetics, and mechanical stability. In this work, the tools and framework of Publications I and II were successfully applied.

The mixed conducting matrix coating can be regarded as a promising design concept that moves from "random" mixing to a functional engineering of microstructures. Moreover, the approach is scalable and easily adaptable to other material systems, especially to SEs with higher conductivity than LIC, to produce high-performance composite cathodes for SSBs.

This study stresses the importance of the mixing process optimization for high-performance composite cathodes. By linking simulation-based process understanding with morphological and electrochemical analysis, we identify design parameters for efficient mixed-conducting matrices. In addition to the matrix coating, it was also demonstrated that thin covering SE coatings can be achieved with this process, making it attractive for dry-processed protective SE coatings.

The study was designed by M. Kissel and F. Frankenberg under the supervision of J. Janek and A. Kwade. M. Kissel and F. Frankenberg share the first authorship as they contributed equally to this work. F. Frankenberg prepared the samples with the help of N. Laser. T. Demuth carried out the TEM-EDX investigations. D. Wagner analyzed the XRD data. M. Kissel performed the SEM-EDX and XPS measurements and subsequent evaluation. The electrochemical cells were built by A. Lai under the supervision of M. Kissel, who analyzed all electrochemical data. F. Frankenberg carried out the porosity and nanoindentation measurements as well as took care of the DEM simulations. The manuscript was written by M. Kissel and F. Frankenberg and edited by all co-authors.

Reproduced from: Maximilian Kissel, Finn Frankenberg, Thomas Demuth, Anton Lai, Niklas Laser, Daniel Wagner, Ahmed Eisa, Peter Michalowski, Kerstin Volz, Arno Kwade, Jürgen Janek. Mechanofusion-derived cathode composite microstructures with scalable mixed conducting matrix coatings for solid state batteries. *Nat Commun*, 2026, 17, 3215, DOI: 10.1038/s41467-026-71305-2, licensed under CC BY 4.0.

nature communications

Article

https://doi.org/10.1038/s41467-026-71305-2

Mechanofusion-derived cathode composite microstructures with scalable mixed conducting matrix coatings for solid state batteries

Received: 4 June 2025

Accepted: 4 March 2026

Published online: 03 April 2026

Check for updates

Maximilian Kissel[1,4], Finn Frankenberg[2,4], Thomas Demuth[3], Anton Lai[1], Niklas Laser[2], Daniel Wagner[1], Ahmed Eisa[2], Peter Michalowski[2], Kerstin Volz[3], Arno Kwade[2] ✉ & Jürgen Janek[1] ✉

The successful implementation of solid state batteries not only requires the use of high-capacity anodes, but also high-performance composite cathodes. However, the production of solid state battery cathode composites with optimized microstructures remains a significant challenge, especially for large-scale fabrication. Here, we present a scalable high-intensity dry mixing process to create tailored functional coatings on single-crystalline $LiNi_{0.82}Mn_{0.07}Co_{0.11}O_2$ via mechanofusion. We investigate the coating of $LiNi_{0.82}Mn_{0.07}Co_{0.11}O_2$ with the malleable halide solid electrolyte Li_3InCl_6 under various process conditions, linking process parameters obtained from discrete element method simulations with experimentally accessible morphological properties to offer guidelines for further optimization. In this way nanometer-thin covering coatings as well as thick matrix coatings are successfully produced. Incorporating carbon black into the thick matrix coating results in well-performing mixed conducting matrices that can be used directly as composite cathodes without further treatment. The compositions investigated enable stable cycling with a specific capacity of up to $q_{comp} = 100\ mAh\ g^{-1}$ (based on the total mass of the composite cathode) at a C-rate of 1 C (60 min). While higher carbon black content is observed to improve CAM utilization, excessive amounts are detrimental for cell kinetics and chemo-mechanics, emphasizing the importance of the cathode mixing process and composition on overall cell performance.

Solid state batteries (SSBs) have emerged as a promising next-generation energy storage technology, aiming to overcome the safety and energy density limitations of conventional lithium-ion batteries (LIBs) that rely on liquid electrolytes (LEs)[1,2]. Replacing the LE with a solid electrolyte (SE) is expected to enable the implementation of high-energy anode (negative electrode) concepts such as lithium metal anodes[3], "anode-free" configurations[4], or Si-based anodes[5]. To match these expected high-performance anodes, equally high-performing cathodes (positive electrode) are required[6–8].

[1]Institute of Physical Chemistry & Center for Materials Research, Justus-Liebig-Universität Gießen, Gießen, Germany. [2]Institute for Particle Technology, Technische Universität Braunschweig, Braunschweig, Germany. [3]Materials Science Center (WZMW) and Department of Physics, Philipps-University Marburg, Marburg, Germany. [4]These authors contributed equally: Maximilian Kissel, Finn Frankenberg. ✉e-mail: arno.kwade@tu-braunschweig.de; juergen.janek@uni-giessen.de

Article https://doi.org/10.1038/s41467-026-71305-2

SSB cathodes are usually designed as composites of SE, cathode active material (CAM), and additive particles. Towards large-scale commercialization of SSBs, various challenges persist, starting at the material level[9]. Here, research focuses on the one hand on developing advanced SEs with enhanced ionic conductivities[10,11], broader electrochemical stability windows[12,13], or beneficial mechanical properties[14] and on the other hand scaling and sustainable SE production processes[15,16]. Moreover, to mitigate degradation effects at the CAM|SE interface, the use of protective CAM coatings is required[17,18]. As CAM, Ni-rich layered oxides[19–21] are widely used with preference for materials that show beneficial chemo-mechanical properties, i.e., low volume expansion[22–24] and low tendency for cracking[25,26]—as seen in single crystals, which showed improved long-term cycling performance[9,27–30].

Not only the materials in the cathode but especially their arrangement, i.e. the composite microstructure, is crucial for the performance[7,31–33]. The microstructure needs to fulfill three main tasks: First, the CAM particles need to be electronically and ionically connected, i.e., electrochemically active, leading to a high CAM utilization within a percolating network. As recently highlighted by Kissel et al.[34], achieving a complete static CAM utilization is not self-evident in SSBs. Second, the electronic and ionic networks should possess high effective conductivities for an improved kinetic cell performance[35–38]. Lastly, intimate and mechanically as well as (electro)chemically stable solid-solid contacts between the CAM and the SE are crucial to enable fast charge transfer at the interface, while also accommodating the volume expansion of the CAM during charging and discharging[39,40].

The final SSB cathode microstructure is largely defined during the particle mixing process, since, in contrast to LIBs, SSBs usually do not allow infiltration of the cathode with an electrolyte post-assembly. However, despite its importance and challenges toward large-scale implementation[41–43], the actual mixing process has received relatively little attention up to now[44–47]. In academic studies, hand mortaring is common, although this is non-scalable and suffers from reproducibility issues[34,48]. On the other hand, machine-made composites are becoming more prevalent in recent studies[34,43,49,50]. Further processing-related approaches have focused on comminuting SE particles before mixing to achieve a tailored particle size distribution (PSD)[49,51–54]. While this is crucial to match the CAM PSD[7,38,52] it involves additional processing steps that can damage the SEs by solvents[55] or by the milling itself[49,56]. Other approaches are based on solution processes to apply SE coatings on active materials or to infiltrate porous electrodes[57,58]. In general, only a few studies explore scalable composite mixing machines for SSB cathode composites, and in most cases, the corresponding mixing process leads to a more or less "random" ordering of particles[7,43,47].

Recently, employing a combined modeling and experimental approach, Lee et al.[59] introduced the concept of building blocks towards an ideal cathode composite microstructure. Building blocks describe the fundamental units of a composite's microstructure in the form of tailored particle aggregates. By engineering these building blocks, the overall microstructure and thus the resulting material properties can be precisely controlled. Lee et al.[40] highlighted the importance of shear forces, which increase the electrolyte-covered surface area of the active materials. Kawaguchi et al.[60,61] and Hayakawa et al.[62,63] investigated the idea of coating low- and medium-nickel $Li_xNi_yCo_zMn_{1-y-z}O_2$ (NCM) particles with SE in a high-intensity mixer. Kim et al.[39] utilized mechanofusion as a preprocessing step to ensure intimate interfacial contact by coating NCM with Li_6PS_5Cl (LPSCl). This allowed a high CAM loading in the cathode and led to higher specific capacities. However, sole coating with SE is not sufficient since it impedes electron transfer, which would only be possible via CAM-CAM particle contacts after deforming parts of the SE coating layer during densification. To overcome this limitation, the authors added carbon additives to their SE-coated CAM and had to manually mortar the composite once again[39].

Inspired by these recent works, we systematically investigate a dry particle coating approach, based on mechanofusion, in this study to create tailored building blocks for SSB composite cathode microstructures. Going beyond the idea of simple mixing of loose particles and arbitrary (re-)ordering, we employ a scalable high-intensity mixing process to create a defined mixed conducting matrix coating via mechanofusion on single-crystalline Ni-rich $LiNi_{0.82}Mn_{0.07}Co_{0.11}O_2$ (NCM82) without any hand mortaring being involved. In this bottom-up approach, which can also be used to produce protective CAM coatings, we make use of the good deformability of the halide SE Li_3InCl_6 (LIC) as a model catholyte. We investigate the effect of composition and process parameters on the morphology of the coating, coating progress, and possible degradation of the materials, combining scanning electron microscopy (SEM), energy-dispersive X-ray spectroscopy (EDX), (scanning) transmission electron microscopy ((S)TEM), and X-ray photoelectron spectroscopy (XPS). We link experimental results with stressing conditions obtained from discrete element method (DEM) process simulations to describe the coating process on the macroscale. In this way, we establish a basis for future optimization of the mixing process of composite cathodes. We demonstrate that the presented mechanofusion process is suitable to produce thin covering coatings as well as thick matrix coatings. By adding carbon black (CB) into the matrix, the coatings become mixed conducting and are further electrochemically analyzed in detail. Our results show that the mixed conducting matrix coating design approach via mechanofusion is promising as a versatile and scalable production method for SSB composites, while still offering significant potential for further optimization.

Results

Figure 1 illustrates the concept of the mixed conducting matrix coating approach employed in this study. Cathode composites, comprising three components with different PSDs, were fabricated using single-crystalline NCM82, in the following denoted as NCM, with a median particle size of $d_{50} = 3.3\,\mu m$ as CAM, in-house prepared LIC (see "Methods") with particle sizes ranging from 100 nm to 100 μm as SE and CB ($d_{50,aggregates} \approx 250\,nm$) as electron-conducting additive (Fig. 1a).

The particles were mixed in a scalable and commercially available high-intensity mixer (Fig. 1b), which provides high-shear forces within the narrow gap[43], enabling mechanofusion[39,45,64,65]. During this process, the NCM particles act as host particles that are coated with guest particles (here: LIC or premix of LIC and CB, see Table 1 and "Methods"), forming core-shell type heteroaggregates as depicted in Fig. 1c. These aggregates are hereafter referred to as building blocks, following the concept introduced by Lee et al.[59] and are denoted by their composition as NCM:LIC:CB (w/w/w). Process parameters that can be varied during the high-intensity mixing are the rotational speed n, the mixing time t_{mix}, and the filling degree φ. By adjusting these parameters, the properties of the building blocks in this bottom-up approach, and thus the overall microstructure of the cathode composite (Fig. 1d), can be significantly influenced. Towards scalable cathode composite production, all mixtures in this work were prepared in a dry room with a dew point of the supply air of −60 °C without any manual hand mortaring being involved. All mixtures were prepared with a batch size of approximately 20 g, corresponding to a filling degree of 10%. In total, three main investigations (cf. Tables 1 and S1) were conducted and are discussed in the following.

First, the coating thickness of the building blocks was varied by systematically adjusting the ratio of SE (and CB) to NCM, while maintaining constant process time and rotational speed. Secondly, the influence of stress intensity or shear stress, as well as collision number,

Article https://doi.org/10.1038/s41467-026-71305-2

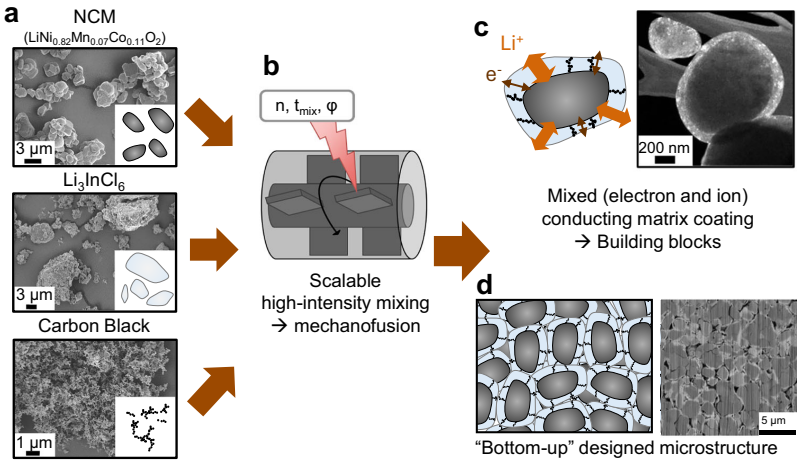

Fig. 1 | Concept of the mixed conducting matrix coating approach. a Starting materials with different particle size distributions are **b** mixed in a high-intensity mixer with varying rotational speed n, mixing times t_{mix}, compositions, and constant filling degree φ, leading to mechanofusion. **c** NCM host particles are coated with an electron and ion conducting matrix, forming building blocks that build up an ordered composite cathode microstructure (**d**).

Table 1 | Overview of samples for the different investigations presented in this study

Type of investigation	Investigated parameters	Constant parameters	Nominal compositions (NCM:LIC:CB, w/w/w)
Coating thickness variation (without CB)	Coating content variation: 1–20 wt%	-Mixing NCM + LIC: 60 min at 10,000 rpm -Filling degree: 10%	99:1:0 98:2:0 95:5:0 90:10:0 80:20:0
Coating thickness variation (with CB)	Coating content variation: 1–20 wt%	-Fixed CB-LIC ratio (20 vol%) -Premixing CB + LIC: 10 min at 5000 rpm -Mixing Premix + NCM: 60 min at 10,000 rpm -Filling degree: 10%	99:1:0.2 98:2:0.3 95:5:0.8 90:10:1.5 80:20:3
Process parameter variation	-Mixing times: 5, 10, 30, 60 min -Rotational speeds: 1000, 2500, 5000, 7500, 10,000 rpm	-Premixing CB + LIC: 10 min at 5000 rpm -Filling degree: 10%	95:5:0.8 80:20:3
Matrix optimization	CB content variation: 0–3 wt%	-Premixing CB + LIC: 10 min at 5000 rpm -Mixing Premix + NCM: 60 min at 10,000 rpm -Filling degree: 10%	80:20:0 80:20:0.2 80:20:0.5 80:20:1 80:20:2 80:20:3

respectively, during mixing was investigated by varying the rotational speed and mixing time for two specific compositions. Third, the mixed conducting matrix coating with a weight ratio of 80:20:x (NCM:LIC:CB) was optimized by altering the CB content x, aiming at achieving a balance between electronic and ionic partial conductivity within the building blocks.

Impact of composition on coating morphology

To investigate the effect of coating material content on the morphology and homogeneity of the coating, different mixtures with coating contents ranging from 1 to 20 wt% were processed at a rotational speed of 10,000 rpm, corresponding to a tip speed of 40 m s^{-1}, for 60 min. As guest particles during the mechanofusion process, pure LIC as well as a LIC-CB mixture with a fixed CB:LIC ratio of 20 vol% CB was used (cf. Table S1). Scanning electron microscopy (SEM) combined with EDX was carried out to visualize the morphology of the coating within the building blocks.

Figure 2a shows that a coating is achieved for all cases, independent of the coating material content. For all EDX acquisitions, the same parameters were used, so that differences in signal intensity can be related to differences in the composition. As expected, the intensity of the chlorine signal, stemming from the coating, decreases with decreasing coating amount. The effect of the coating is further evidenced by the rounding of NCM particle edges, reflected in a decreased aspect ratio and an increased circularity with rising coating material content (Supplementary Fig. S1). This indicates that the coating material fills recessed regions of the NCM particles, leading to a varying thickness across the particle surface (Supplementary Fig. S1e). Intergranular boundaries existing within aggregates of the bare NCM disappear completely for high coating amounts, showing that the coating material is covering these areas (Supplementary Fig. S2). Especially at high coating material contents, an increase in volume-based particle size Q_3 is observed, which is based on the increase in coating thickness (Fig. 2b). However, the coating as such is

Article https://doi.org/10.1038/s41467-026-71305-2

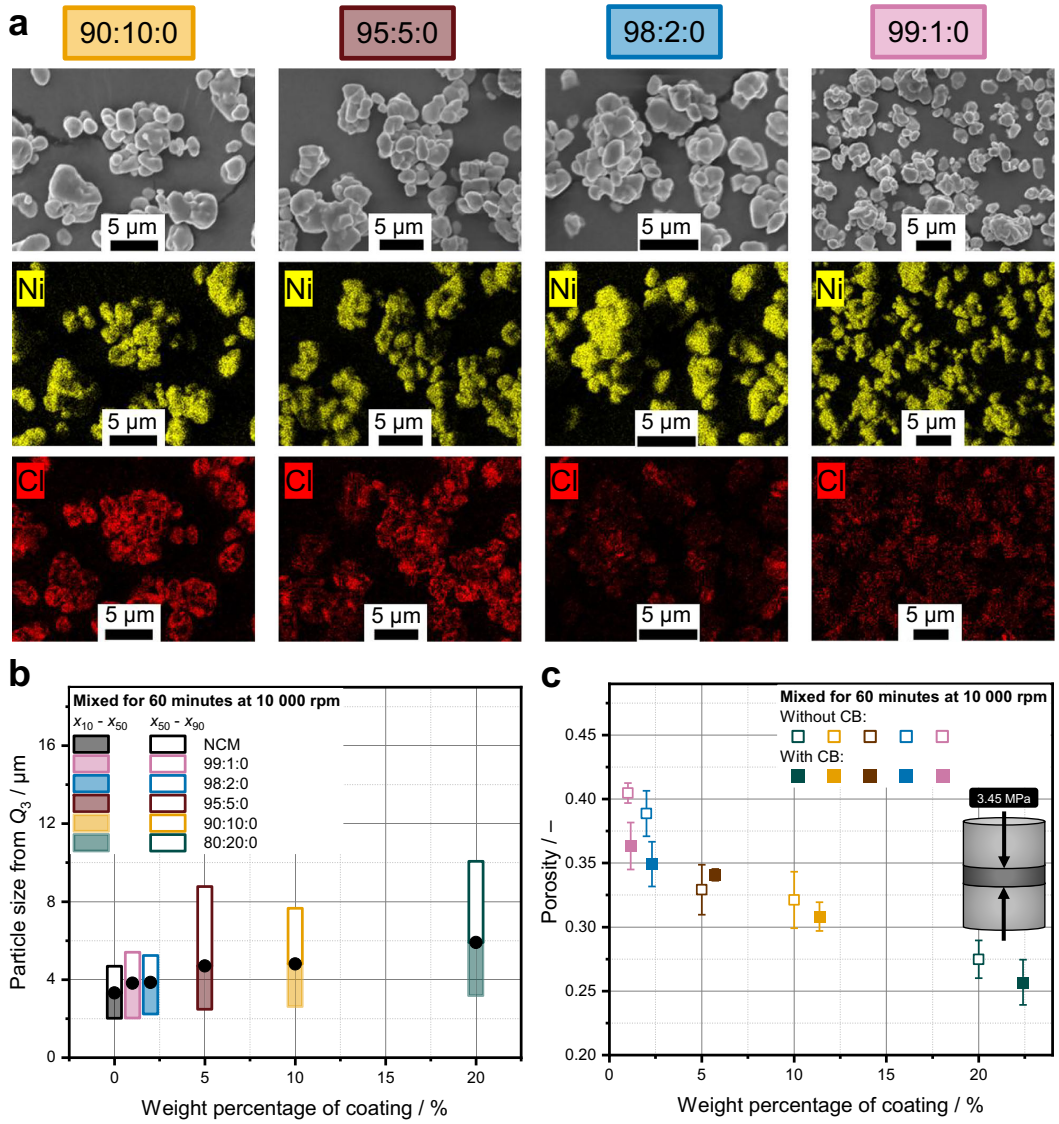

Fig. 2 | Microstructure, PSD, and porosity depending on the coating amount. **a** SEM images and EDX maps of four mixtures with decreasing coating amounts. **b** Corresponding PSDs calculated from SEM images segmentation. **c** Porosity of composite pellets measured at 3.45 MPa. Error bars represent the standard deviation of $n = 3$ porosity measurements.

not the determining factor for this increase, since a theoretical maximum average coating thickness of approximately 150 nm is expected (Supplementary Fig. S3). Rather, multiple agglomerated NCM particles are surrounded by a coating layer, which means that one particle is visible under the SEM and counted in the PSD calculation, but in fact several NCM particles are encapsulated by the coating. Since encapsulation occurs only for some agglomerated NCM clusters, a pronounced broadening of the PSD is observed with increasing coating content. From the broadening of the PSD in combination with the increasing amount of soft coating with increasing coating material content, it can be supposed that the interparticle spaces can be better filled and thus the building blocks can be better packed in the final cathode composite microstructure. This improved packing is indeed reflected in the measured bulk porosity of the cathode composites, which decreases with increasing coating content (Fig. 2c). The porosity of the composite mixtures containing CB is consistently slightly lower than that of the composites without CB. We attribute this to the higher volume fraction of compressible components in the formulations containing CB, which increases from 31.4 to 35.6% for the 80:20 and 80:20:3 compositions, respectively. For the highest coating amount, the porosity measured at a compaction pressure of 3.45 MPa was about 25%. This value corresponds approximately to the porosity of a

Article https://doi.org/10.1038/s41467-026-71305-2

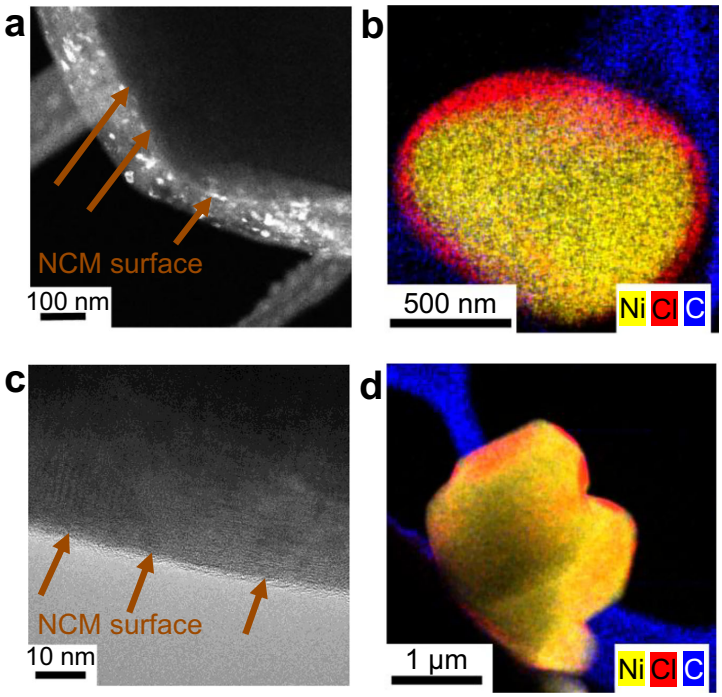

Fig. 3 | TEM images and STEM-EDX maps of coated particles. a, **b** Matrix coating building block with composition 80:20:1. **c**, **d** Thin coating with composition of 99:1:0.

cubic closed packing of spheres. For a higher compaction pressure, we expect more deformation of the coatings and thus a reduced porosity of the composite cathode.

Transmission electron microscopy (TEM) images confirm a homogenous coating layer, exemplarily depicted for a high and low coating amount in Fig. 3. In dark-field imaging of a composition of 80:20:1, some crystals in the coating layer appear bright (Fig. 3a). These bright regions are lattice planes of small crystals (cf. Supplementary Fig. S4a) with random orientations towards the position of the objective lens aperture. X-ray diffractograms (Supplementary Fig. S5) confirm that the crystalline phase of the LIC is preserved, and the mass ratios after Rietveld refinement (Supplementary Table S3) are in line with the expected values, indicating that there is no significant amorphization happening. Corresponding STEM-EDX maps (Fig. 3b and Supplementary Fig. S4b) reveal the presence of carbon in the approximately 100 nm thick coating layer, indicating that the desired mixed conducting matrix coating was achieved. In the case of the 99:1:0 composition, the coating is only approximately 5 nm thick (Fig. 3c, d) and consistently observed along the entire particle surface (Supplementary Fig. S6). Variations in signal intensity across the EDX maps in Fig. 3b, d are attributed to differences in particle orientation relative to the detector, which can influence the intensity of the detected signal.

To further quantify the homogeneity and thickness of the coating, XPS was carried out. Based on the signal intensities of the NCM and coating elements, values for the coverage γ of the building blocks were calculated, which represent the signal intensity ratio of coating to NCM (see "Methods" and ref. 66 for details). The coverage value describes how strongly the signal of the NCM particle is shielded by the coating. It depends on the thickness, the composition (with or without CB), the morphology, and the homogeneity of the coating. A coverage value close to 1 indicates nearly complete surface coverage and the presence of a relatively thick coating layer (cf. Fig. 4a), such that almost no signals from the NCM are detected. This situation corresponds to coating thicknesses of at least ~10 nm, which is approximately the information depth of XPS measurements. While the coverage value itself does not provide information on the morphology or local thickness distribution, it enables assessing whether a continuous coating layer is formed across a broad range of process parameters. For coatings expected to be thinner than ~10 nm (cf. Supplementary Fig. S3), the coverage value derived from XPS no longer reflects the true surface coverage. In this case, even a perfectly covering coating layer will never result in a coverage value of 1, since signals stemming from the NCM can always be detected. Conversely, coatings that are uniformly thicker than at least ~10 nm cannot be distinguished from one another by this method, as all yield coverage values close to 1. As displayed in Fig. 4b, the coverage increases with increasing coating content, which we attribute to the rise in coating thickness. It is also evident that the incorporation of CB in the coating, especially at low coating thicknesses, leads to larger coverage values. Since the weight ratios are kept constant, the coatings that also contain CB occupy a larger volume due to the low (bulk) density of CB. Thus, the signals of the NCM are more strongly shielded, yielding higher coverage values than the CB-free counterparts. At a high coating content corresponding to the ratio 80:20:3, the maximum possible coverage value of 1 is reached, which indicates that the NCM particles are fully covered. This confirms the previously discussed SEM and STEM measurements.

The results demonstrate that high-intensity mixing leading to mechanofusion is a well-suited method for the dry production of core-shell structures with various coating thicknesses. This is particularly attractive for protective coatings employing soft SEs, a promising concept that has recently gained attention to prevent interfacial degradation in SSB cathode composites[65–67].

Article https://doi.org/10.1038/s41467-026-71305-2

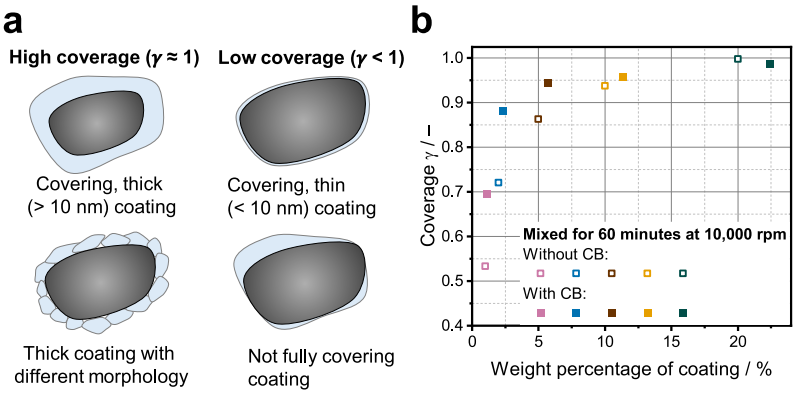

Fig. 4 | Coverage types and coverage dependence on coating content. **a** Schematic illustration of different particle types for which a high and low coverage γ can be calculated. **b** XPS-derived coverage values for samples mixed at 10,000 rpm for 60 min, plotted against the weight percentage of coating. Data is shown for composites with and without CB.

Investigation of process-structure-relations

In the following, we focus on the 80:20:3 composition, which is designed to serve as a matrix coating since it reaches the highest degree of coverage. To investigate the coating progress as a function of process conditions, the composition was produced at different speeds and mixing times.

During high-intensity mixing, mechanical energy is transferred to the particle system through the high relative velocities generated between the rapidly rotating rotor and the surrounding particles. This energy transfer is reflected in the specific energy input $E_{m,\,exp}$, which is significantly influenced by the rotational speed and mixing time. This was estimated experimentally for the different coating experiments from the measured power P, idle power P_0, sample mass m_{total}, and mixing time t_{mix} (cf. Supplementary Fig. S7).

$$E_{m,\,exp} = \frac{\int (P - P_0)dt}{m_{total}} \quad (1)$$

To evaluate the coating progression, the coverage of the 80:20:3 composition is depicted in Fig. 5a as a function of the specific energy input. At lower rotational speeds of 1000 rpm and 2500 rpm, coverage increases with prolonged mixing time and thus specific energy input. In contrast, at higher rotational speeds of $n \geq 5000$ rpm, a maximum coverage of 97–100% (dashed gray region) is reached within just 5–10 min of mixing. Extending the mixing time up to 60 min, results in only marginal changes in coverage values at these higher rotational speeds. A similar trend is observed for a composition of 95:5:0.8 (cf. Supplementary Fig. S8a).

As discussed, similar coverage levels do not necessarily indicate comparable coating morphologies (cf. Fig. 4a). Porosity measurements show a consistent decline in porosity of the cathode composites with increasing specific energy input (Fig. 5b). The reduction in porosity indicates that even when coverage values reach a plateau, the morphology of the building blocks can continue to evolve significantly with varying processing conditions. This is corroborated by SEM images as seen in Fig. 5c for the samples processed at different rotational speeds (see also Supplementary Fig. S9). At 1000 rpm, only an inhomogeneous and particulate deposition of CB and LIC on the NCM particles can be seen, forming cluster-like agglomerates. Moreover, single LIC particles are visible, which have not taken part in the coating process. At 5000 rpm, individual LIC and CB particles remain discernible on the NCM surface, whereas at 10,000 rpm, the NCM particles are uniformly encapsulated by a smooth coating layer. According to mechanofusion theory[68] different coating structures can form at different rotational speeds, ranging from loosely adhered particles to continuous shells. In our case, continuous and smooth shells are observed at high rotational speeds and long mixing times, while lower speeds and reduced energy input tend to result in coatings consisting of loosely adhered particles.

Overall, the coating morphology becomes smoother and less particulate with increasing specific energy input and, at comparable specific energy input, with increasing rotational speed and thus mixer intensity. This leads to an increase in the circularity of the building blocks, as shown for the rotational speeds of 1000 rpm, 5000 rpm and 10,000 rpm mixed for 60 min. Coverage metrics derived from XPS analyses cannot fully resolve these morphological features, which require complementary SEM analysis.

Linking DEM simulations and experiments

To enable a guided optimization of the mechanofusion process for production of SSB cathode composites, we carried out DEM simulations to simulate the stresses acting on the particles in the high-intensity mixer. As elaborated in the "Methods" section and Supplementary Note 3, a coarse-graining approach was applied to handle the extremely high number of real particles. While this approach does not retain information on the original coating progression, it allows for the determination of the mixer's overall stressing conditions. Calibration tests have been carried out to determine the apparent properties of the coarse-grained particles to mimic the original situation. To validate the calibration procedure and calculated coarse-grain density of the coarse-grained particles (Fig. 6b and Supplementary Fig. S10 and Table S2), the mean specific power obtained from the experiments was first compared with the specific power obtained from the DEM simulation in the steady state. Both specific power data show a high degree of agreement, confirming the successful calibration of the particle properties.

In order to quantitatively describe the process and compare process parameters, we applied the stressing model of Kwade[69], which uses the stress energy or stress intensity, respectively, and stress frequency or stress number, respectively, as parameters to calculate the specific energy input E_m based on these model parameters. This allows a quantitative comparison of various process conditions[70,71]. According

Article https://doi.org/10.1038/s41467-026-71305-2

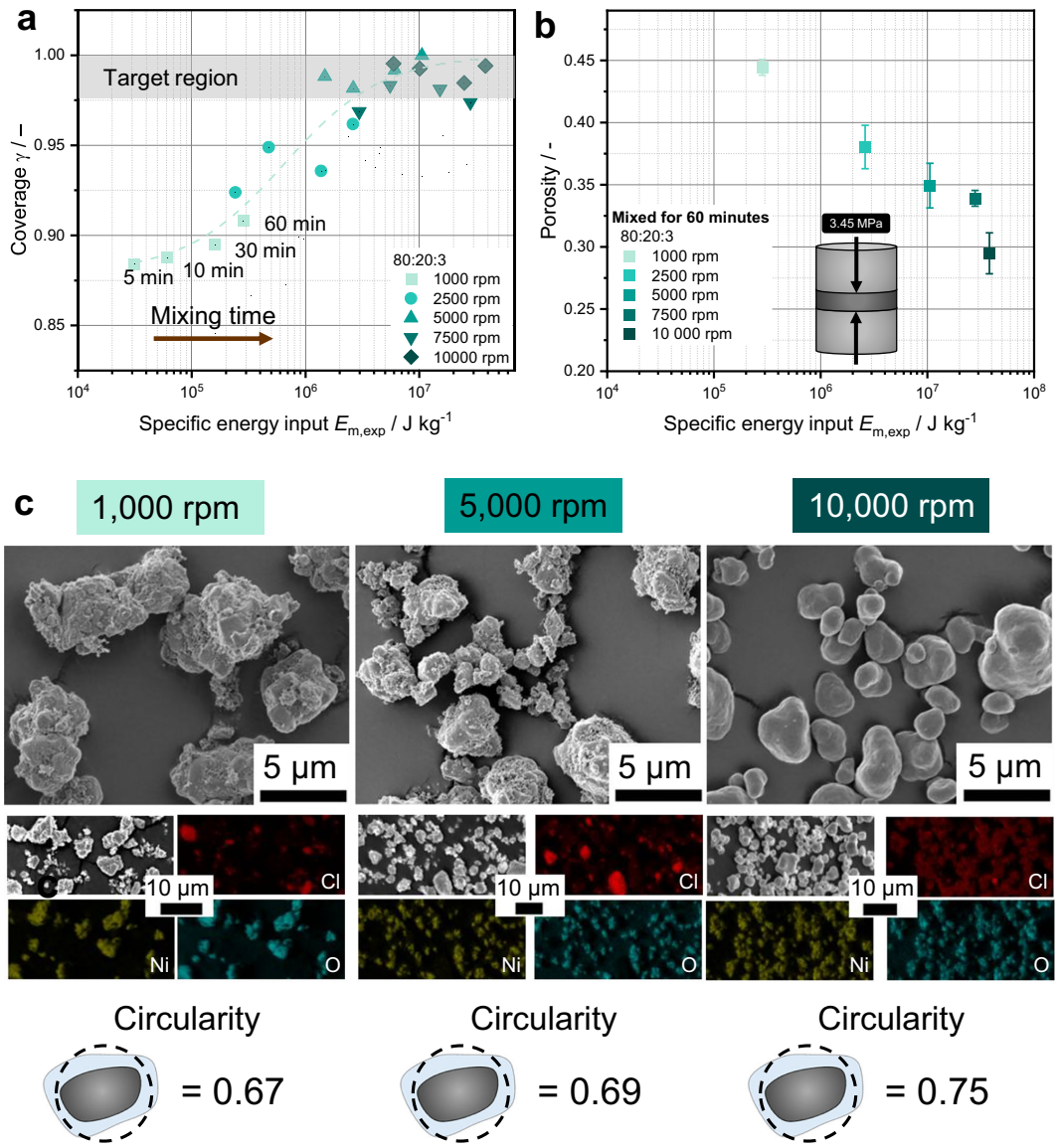

Fig. 5 | Effect of mixing intensity on particle morphology, surface coverage, and porosity for a building block composition of 80:20:3. a Coverage γ as a function of specific energy input. **b** Porosity of composite pellets under 3.45 MPa prepared from mixtures after 60 min, plotted against specific energy input. Error bars represent the standard deviation of $n = 3$ measurements. **c** SEM images and EDX maps of powders mixed at 1000, 5000, and 10,000 rpm for 60 min as well as the obtained mean circularity of the different building blocks.

to Eq. 2, $E_{m,sim}$ is expressed as the product of the mean stress intensity $\overline{SI}_{CG}$ of the particle collisions, corresponding to the mean dissipated energy during coarse-grained particle collisions related to stressed coarse-grain mass, and the mean stress number per particle $\overline{SN}_p$. The $\overline{SN}_p$ can be determined by the frequency of collisions of the coarse-grain particles during mixing SF_{CG} divided by the number of coarse-grains, which is obtained from the ratio of the individua particle mass $m_{particle,CG}$ to total mass m_{total}, and the mixing time t_{mix}. Both parameters $\overline{SI}_{CG}$ and $\overline{SN}_p$ should be approximately scale-invariant (Supplementary Note 3) and are obtained from DEM simulations[43,72] to calculate the simulation-based $E_{m,sim}$.

$$E_{m,sim} = \frac{\overline{SI}_{CG} \cdot m_{particle,CG} \cdot SF_{CG} \cdot t_{mix}}{m_{total}} = \overline{SI}_{CG} \cdot \overline{SN}_p \quad (2)$$

In the following, the parameters $\overline{SI}_{CG}$ and $\overline{SN}_p$ are used to describe the mechanofusion process macroscopically. Both are individually influenced by the rotational speed n and t_{mix}, thus affecting the

Article https://doi.org/10.1038/s41467-026-71305-2

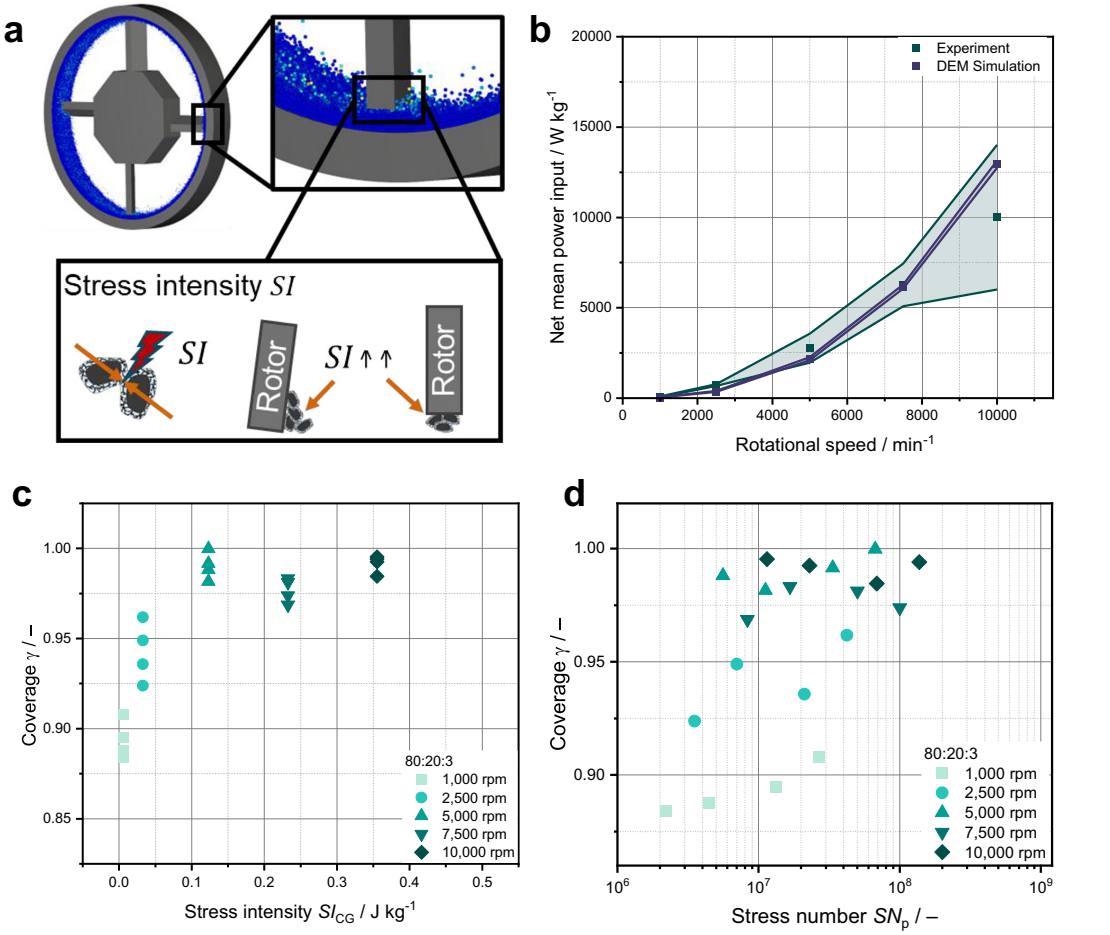

Fig. 6 | DEM simulation of the high-intensity mixing and correlation with experimental coverage. a DEM simulation snapshot and schematic image of the high-intensity mixer indicating the mixing action. **b** Measured and simulated net specific power depending on process time for different rotational speeds and a composition of 80:20:3. Error bars represent the standard deviation of the net power, calculated over 60 min for the experiment and over 0.5 s for the DEM simulations. **c** Calculated Coverage as a function of simulated stress intensity $\overline{SI}_{CG}$. **d** Calculated coverage as a function of simulated stress number $\overline{SN}_p$. Regions 1 and 2 correspond to low and high $\overline{SI}_{CG}$, respectively.

progression and morphology of the coating. $\overline{SI}_{CG}$ is highest near the rotor tip and in the gap between the rotor tip and the mixer wall (Fig. 6a), primarily governed by the rotational speed of the mixer for a constant gap width. An approximate increase of $\overline{SI}_{CG} \propto n^2$ can be expected with increased rotational speed[43], potentially influencing the building block microstructure. In contrast, $\overline{SN}_p$ depends on both the rotational speed and t_{mix}. Therefore, an equivalent energy input can be achieved at lower $\overline{SI}_{CG}$ if compensated by a higher $\overline{SN}_p$ through extended mixing times, although this may result in a different coating morphology.

To understand the individual influence of $\overline{SI}_{CG}$ and $\overline{SN}_p$, stress frequency–stress intensity curves were generated from the recorded particle collisions and served as the basis for determining $\overline{SN}_p$ and $\overline{SI}_{CG}$. The coverage of the 80:20:3 mixtures was plotted against both parameters (Fig. 6c, d). Figure 6c shows that an increasing $\overline{SI}_{CG}$ generally leads to higher coverage values. Notably, at a $\overline{SI}_{CG}$ corresponding to 5000 rpm ($\overline{SI}_{CG}$ = 0.123 J kg^{-1}), nearly complete coverage (>97%) is achieved after only 5 min of mixing. Further increasing $\overline{SI}$ beyond this point results in only slight changes in coverage. However, significant changes in coating morphology that occur at constant mixing time, but varying stress intensities, as already shown in Fig. 5a (see also Supplementary Fig. S9), become visible.

When the coverage is analyzed as a function of $\overline{SN}_p$ (Fig. 6d), it becomes clear that there is no direct proportionality. An equivalent or even higher $\overline{SN}_p$ (region 1) does not achieve the same degree of coverage but depends on the $\overline{SI}_{CG}$. This indicates that elevated $\overline{SI}_{CG}$ (region 2), associated with higher collision energies, is beneficial for forming a uniform coating with higher coverages. Nevertheless, even at lower $\overline{SI}_{CG}$ such as 0.006 J kg^{-1} (1000 rpm) and 0.033 J kg^{-1} (2500 rpm), the coverage gradually increases with $\overline{SN}_p$ due to extended mixing times. However, to achieve more than 97% coverage with a $\overline{SI}_{CG}$ equivalent to 2500 rpm and 1000 rpm, longer mixing times would be required. Even then, the resulting coating morphology is likely to differ significantly, as already observed at higher rotational speeds (5000 rpm and 10,000 rpm), where 97% coverage was also achieved (cf. Fig. 5c). From a process engineering and economic perspective,

Article https://doi.org/10.1038/s41467-026-71305-2

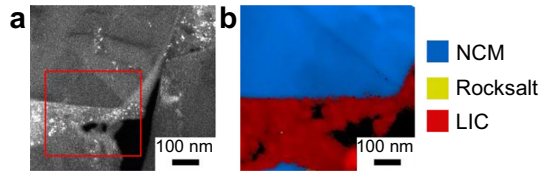

Fig. 7 | Structural damage probed with SPED-TEM. a TEM bright-field image of coated NCM (80:20:3) with the red box indicating the area of the SPED scan. **b** SPED phase map showing only the pristine layered phase and the coating layer. Black points represent mostly amorphous regions or voids.

long mixing times are impractical. Therefore, a higher $\overline{SI}_{CG}$ is preferable to ensure efficient coating formation within reasonable processing times.

To achieve both high coverage and improved homogeneity, the highest $\overline{SI}$ investigated (10,000 rpm) appears to be the most effective choice for the given material system and composition. However, at these high collision energies, potential degradation effects should be monitored, including, for instance, structural damage and strain in the NCM particles as well as elemental interdiffusion at the NCM|coating interface. Structural integrity was probed via scanning precession electron diffraction (SPED) in the TEM. In the dark-field TEM shown in Fig. 7a, the NCM particles appear dark, whereas the coating layer is brighter with distinct bright spots. In the region marked with a red box, a SPED phase map was recorded (Fig. 7b). Thereby, only the pristine layered phase and the coating layer were detected with no evidence of a rock salt-type phase in the NCM surface region, which would be indicative of NCM degradation. This observation was further confirmed by manually inspecting the diffraction patterns at the interface, which did not show any signs of degradation. Additional X-ray diffraction (XRD) measurements and Rietveld refinement likewise revealed no significant changes in lattice parameters or strain (Supplementary Fig. S12 and Table S3). The chemical stability at the interface was probed using STEM-EDX (Supplementary Fig. S13). The element map (Supplementary Fig. S13a) shows the CB-LIC matrix around the NCM particles. To check for elemental interdiffusion, a line scan across the interface was evaluated (Supplementary Fig. S13b). Due to the NCM surface being slightly slanted, the characteristic compositions of NCM and LIC overlap in a small interfacial region (Supplementary Fig. S13c). However, no evidence of elemental diffusion beyond this overlapping region of approximately 10–15 nm width was detected. Based on these observations, we assume that the coating process in the high-intensity mixer does not damage the NCM surface region. Rather, the small single-crystalline particles appear to tolerate the processing conditions. In addition, the softer LIC phase is expected to exert a dampening effect.

It is important to note, however, that this may differ when processing other material systems, such as larger polycrystalline CAM particles or sulfide SEs[73]. Larger particles exhibit a higher defect probability, typically, due to a lower particle strength than for aggregates, according to Rumpf[74], scales as $\sigma \propto \frac{1}{d^2}$, and for primary particles, according to Tavares and King[75], scales as $\sigma \propto \frac{1}{d^{1-z}}$, making fragmentation more likely at similar stress intensities. To corroborate this, we conducted a mixing experiment with larger polycrystalline NCM particles under the same high-stressing conditions applied in this study (10,000 rpm for 60 min). The results show that, although most particles retained their overall structure, a few fragmented particles were observed (Supplementary Fig. S14). Notably, these were consistently among the largest particles, which supports both our considerations. Moreover, applying a mill (e.g., planetary ball mill) for the composite mixing can result in higher stress intensities and might also cause material degradation of the single crystal NCM[71,76].

In these cases, DEM simulations could provide guidance for process optimization, indicating that lower stress intensities, which might be necessary to prevent chemical or structural degradation during processing, can be compensated for by longer mixing times to achieve similar coverages. For example, in the case of coating at 1000 rpm, achieving a target coverage of approximately 97.5% would require extending the mixing time by 200%, i.e., to a total of ~3 h. When combined with further degradation studies, DEM simulations can help identify suitable process parameters for different material systems and mechanofusion processes.

Electrochemical performance of mixed conducting matrix coatings

Based on the investigations discussed above, a maximum stress intensity and maximum stress number, i.e., a rotational speed of 10,000 rpm and a mixing time of 60 min, were selected as fixed process parameters to further study systematically the effect of carbon content in the matrix on the electrochemical performance of the resulting matrix coating. In the following, we refer to the CB-LIC premix as the matrix, and to the NCM–LIC–CB mixture, i.e., the coated NCM particles, as the composite.

Effective charge transport requires fast electronic and ionic pathways between the CAM particles and the current collectors. A matrix coating solely composed of low electron-conducting SE, i.e., a composition of 80:20:0, is expected to limit the electronic transport. In this case, electrons can only be conducted via NCM-NCM point contacts after deformation of the SE coating layer. Thus, the idea is to add an electron-conductive additive to form a mixed conducting matrix. A similar mixture, composed of CB and LPSCl, was already investigated by Reisacher et al.[77] to identify the necessary content of CB to achieve an electronically percolating matrix. Similarly, we evaluated different CB-LIC ratios to identify the percolation threshold p_c for our system.

To this end, we determined the partial electronic conductivities using direct current (DC) polarization in symmetric ion-blocking cells, both for the CB-LIC matrix as well as for the NCM–LIC–CB (80:20:*x*) composites with different compositions. As shown in Fig. 8a, the threshold for electronic percolation, p_c, in the matrix lies between 2 and 5 wt%. Below this range, the partial electronic conductivity of the matrix remains below 0.01 mS cm^{-1}, while at 5 wt%, it increases by four orders of magnitude to almost 200 mS/cm and further rises up to 1000 mS cm^{-1} at 15 wt% CB. The cathode composites exhibit a similar trend for the electronic partial conductivity, which increases from approximately 0.03 mS cm^{-1} at 0% CB to 1.8 mS cm^{-1} at 15% CB in the matrix.

Since the mixed conducting matrix not only needs to provide electronic but also sufficient ionic conduction, we further measured the ionic partial conductivities of the different matrices and composites, respectively. Using DC polarization in symmetric electron-blocking cells, an opposite trend for the ionic conductivity as a function of the CB content is observed (Fig. 8a). With increasing CB content, the ionic conductivity of the matrix decreases from about 0.7 to 0.03 mS cm^{-1}. Similarly, for the composites, the ionic partial conductivity decreases as well. For the highest CB content, the minimum ionic partial conductivity of about 0.006 mS cm^{-1} was measured for the respective composite. The highest ionic partial conductivity of about 0.04 mS cm^{-1} was found for the composite with a CB content in the matrix of 1 wt%.

The differences between maximum and minimum ionic conductivity values are not as large as for the electronic conductivity. Furthermore, not all data points follow a strict monotonic trend with increasing CB content. We attribute this observation to the fact that

Article https://doi.org/10.1038/s41467-026-71305-2

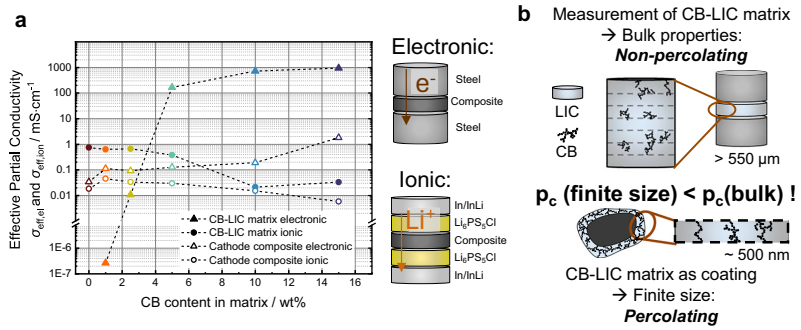

Fig. 8 | Carbon black-dependent electronic and ionic transport properties and size-dependent percolation behavior in composite materials. a Effective partial electronic and ionic conductivities of the matrix and composite as a function of CB content. **b** Schematic showing the impact of sample dimensions on measurable percolation behavior.

the CB is not equally homogeneously distributed in all samples, leading to different microstructures. In general, the differences in conductivities deviating from the trend are rather small, given the general level of uncertainty. Moreover, not only are the materials error-prone, but also the experimental conditions in the dry room might lead to irregularities.

At this point, we would like to highlight that the percolation behavior is not only dependent on the intrinsic material properties but also on the sample size of the considered volume used to determine the percolation threshold. During the measurement of the matrix, bulk properties are assessed, as a relatively large amount of powder is used to produce a thick pellet (Fig. 8b). The values obtained from these bulk-scale measurements are not necessarily representative of the situation when the matrix is applied as a thin coating. In this case, the coating is typically in the nanometer range, representing a finite-size system in which the percolation threshold p_c can be reached earlier, i.e., at lower CB contents. Thus, the macroscopic bulk p_c derived from symmetrical cell setups should rather be viewed as an upper limit for the CB content in the composite.

Additionally, partial conductivities primarily describe charge transport through the bulk composite and offer no insights into the charge transfer kinetics at the CAM/SE interface, particularly since the CAM is typically fully lithiated during such measurements[35]. Therefore, the partial conductivities obtained from symmetrical cells do not necessarily correlate fully with the half-cell performance, as recently also observed by Puls et al.[78].

This assumption is indeed reflected in the cycling performance of the half-cells depicted in Fig. 9a. Here, the cells with CB contents above the determined p_c (80:20:1/2/3) show a significantly worse performance than cells with CB contents below p_c. While the attainable capacities at 0.1 C are still comparable, they rapidly decrease at 0.3 C and 1 C. For example, while providing an initial composite-specific capacity of ~130 mAh g^{-1} at 0.1 C, the 80:20:3 composition can only supply a discharge capacity of less than 10 mAh g^{-1} at 1 C. Interestingly, the composite without any CB in the matrix, i.e., with a negligible electronic conductivity, exhibits a decent performance retaining approximately 85 mAh g^{-1} at 1 C when being charged in constant current constant voltage (CCCV) mode. The electronic transfer across NCM-NCM point contacts seems to be sufficient at the tested stack pressure of about 80 MPa, confirming the previous results of Kim et al.[39]. In the here presented work, we could achieve further improvement in cycling performance when adding some CB into the matrix. Among the tested compositions, the 80:20:0.5 composite delivers the highest composite-specific discharge capacity of q_{comp} = 100 mAh g^{-1} at 1 C after charging in CCCV mode. In the following, the cycling behavior depending on the cathode compositions shall be discussed in more detail.

All capacity values in Fig. 9a refer to the total mass of the composite, since this metric is closer to practically relevant performance indicators than CAM-specific capacities, which are shown together with the Coulombic efficiencies in Supplementary Fig. S15 (see also Supplementary Note 4). As discussed in our previous work[34], not all CAM particles are necessarily electrochemically active in SSB composite cathodes. Depending on the cathode composition and/or the mixing method, a substantial fraction of CAM can remain electronically disconnected and thus inactive, thereby lowering the overall static CAM utilization. Consequently, capacity values based on either the total mass of CAM or the total cathode mass reflect not the intrinsic active material properties but are strongly convoluted with the microstructure of the composite. Thereby, it is possible to differentiate between static and kinetic capacity losses[34]. Static capacity losses consider the issue of incomplete static CAM utilization which is non-negligible for the tested compositions as depicted in Fig. 9b. The highest CAM utilization of about 90% is reached for the highest CB content, while in the low CB (0–0.5%) containing composites only about 65% of the CAM particles are electronically connected. This is reasonable since CB in the matrix is expected to facilitate the formation of electronic connections between the NCM particles. Thus, when more CB is used in the matrix, the probability of electronic connection of a NCM particle increases. For the 80:20:3 composition this leads to the highest achievable capacity of 129 mAh g^{-1} at low C-rates (see also Supplementary Figs. S15a and S16, and Table S4).

On the other hand, we observe that high CB contents are detrimental to the cell kinetics in this study. This is evident from the active specific capacities shown in Fig. 9b which are calculated by referring the measured charge only to the mass of active CAM. Hence, these capacity values describe the kinetics only of the statically active particles. For the 80:20:0.5 composition, an active specific capacity of 180 mAh g^{-1} at 1 C is obtained while for the 80:20:3 composition, only about 10 mAh g^{-1} are reached. The differential capacity curves depicted in Fig. 9c for discharge cycles at 0.3 C and 1 C confirm the differences in kinetic performance depending on the CB content. This is further supported by Supplementary Fig. S16 which shows that more charge is gained from the CV period for the samples with higher CB content, indicating available but kinetically limited capacity.

For an overall assessment, the active specific capacity values, representing a kinetic property, must be considered alongside CAM utilization, which reflects a static property[34]: A high CB content increases the CAM utilization by providing more electronic pathways, leading to higher capacities at low C-rates. However, it simultaneously

Article https://doi.org/10.1038/s41467-026-71305-2

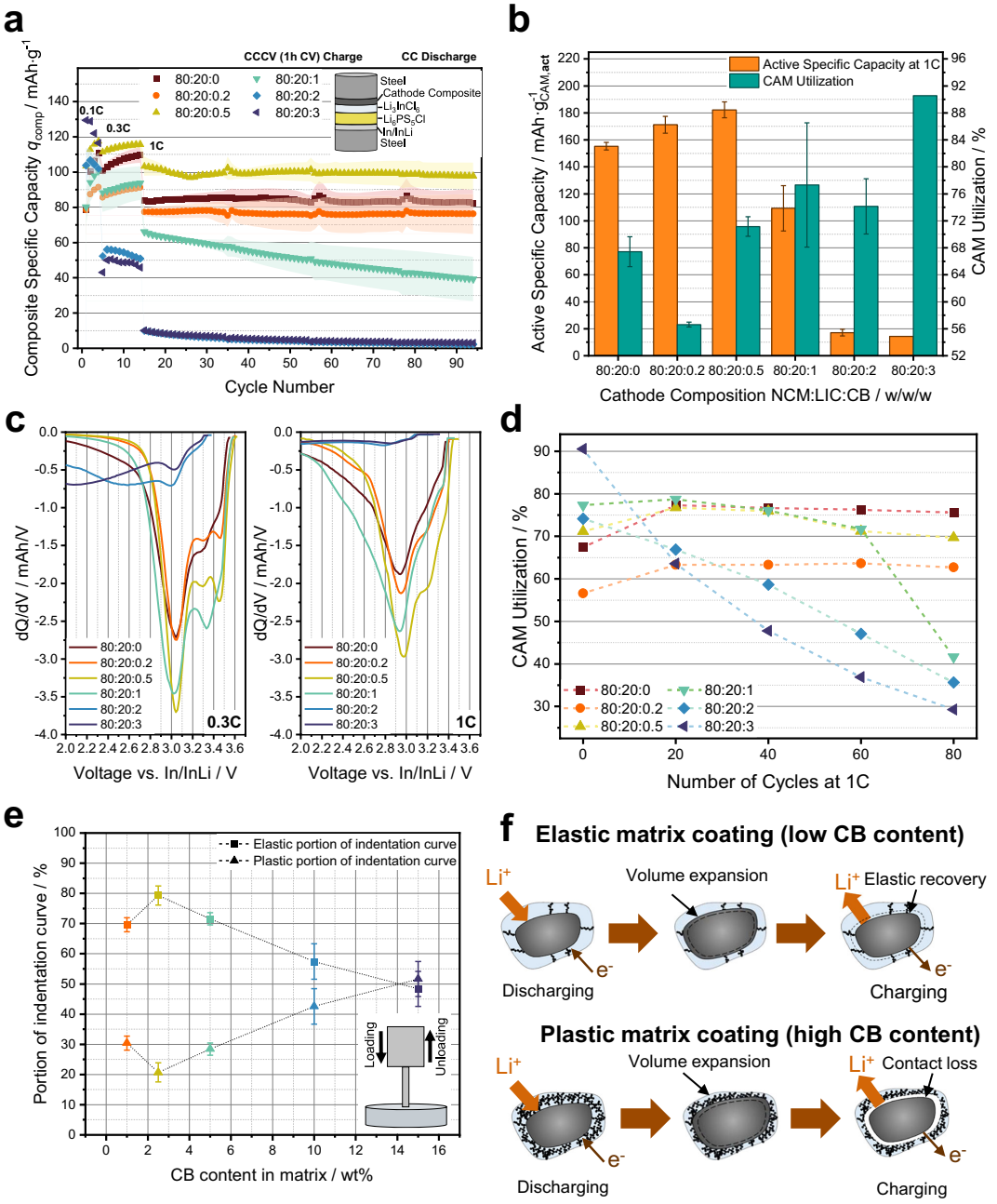

Fig. 9 | Electrochemical performance of half-cells depending on the cathode composite composition (1 C ≈ 200 mA/g ≈ 3 mA/cm²). **a** Cycling performance when cycled in CCCV mode at 25 °C under 80 MPa stack pressure. Error bars represent the standard deviation of at least $n = 2$ cells. **b** Comparison of active specific capacity and CAM utilization. Error bars represent the standard deviation of at least $n = 2$ cells. **c** Differential capacity plots at 0.3 C and 1 C. **d** Evolution of CAM utilization during cycling. **e** Elastic and plastic portions of force–indentation curves obtained from nanoindentation on CB-LIC pellets, which were prepared by compacting the premix at 380 MPa. Error bars represent the standard deviation of $n = 24$ indentations. **f** Schematic illustration of how the mechanical properties of the coating influence microstructure evolution. Elastic coatings enable elastic recovery, preserving interfacial contact, whereas plastic coatings lead to contact loss due to irreversible deformation.

Article https://doi.org/10.1038/s41467-026-71305-2

obstructs the ionic pathways, thereby impairing the kinetic cell performance resulting in low capacities at higher C-rates. Conversely, a low CB content reduces the static CAM utilization, with many CAM particles remaining electronically disconnected and thus electrochemically inactive. At the same time, the remaining electrochemically active particles are found to be kinetically well connected, which is reflected in the high active specific capacities at 1 C (Fig. 9b) and lower overpotentials (Supplementary Fig. S16). The improved kinetic performance during charging and discharging is further underlined by the fact that these particles experience a significantly higher effective C-rate due to the low CAM utilization[34,79]. We do not observe a monotonic trend in capacity as a function of CB content, which we attribute to the fact that the CB distribution within the matrix coating is not yet fully optimized. Consequently, CB agglomeration may lead to reduced electronic connectivity, particularly at CB contents at or below the percolation threshold. This highlights the need to further optimize CB distribution in the matrix, which should be sufficient to ensure high CAM utilization, yet low enough to maintain fast transport kinetics and to prevent excessive electrochemical SE degradation.

In order to quantify the impact of chemo-mechanical degradation, i.e., contact loss[27,33], during cycling at 1 C in CCCV mode, the CAM utilization was determined every 20 cycles. Figure 9d indicates that contact loss, which results in loss of active mass, is more pronounced for the cells with high CB content. We hypothesize that the observed behavior stems from the mechanical properties of the matrix. With increasing CB content, the matrix is much more porous, exhibits reduced elasticity, and shows a greater tendency toward plastic deformation which may hinder its ability to accommodate the volume changes of NCM during continuous cycling. In contrast, a matrix with low CB content is more elastic and maintains contact with the NCM during cycling. For these composites the CAM utilization slightly increases and appears to stabilize during cycling, indicating microstructural changes which lead to new electronic connections.

Nanoindentation measurements on the CB-LIC premix (Supplementary Fig. S17), from which we calculated the elastic and plastic portions of the indentation response (Fig. 9e), corroborate this picture. While there is approximately 20% plastic portion at 2.5 wt% CB in the matrix, it rises to around 50% at 15 wt% CB, highlighting a substantial shift toward plasticity at higher CB concentrations. This behavior is accompanied by a substantial rise in porosity of the CB-LIC matrix with increasing CB content (Supplementary Fig. S17). Notably, at CB contents of 10% and 15% in the matrix, the porosity increases sharply from below 5% (at low CB levels) to approximately 25 and 30%, respectively. The pronounced increase in porosity is directly linked with the observed rise in plasticity and correlates with the sharp decline in CAM utilization during long-term cycling at high CB contents in the coating. As the matrix becomes mechanically less elastic, it loses its ability to accommodate microstructural changes, such as the volume expansion of the CAM, during cycling, leading to significant contact losses and degradation in electrochemical performance (Fig. 9f).

Overall, our results reveal a trade-off between CAM utilization, charge transport kinetics, and mechanical integrity, with a composition of 80:20:0.5 leading to the best performance among the compositions tested in this study. Thereby, no direct correlation between the partial conductivities and half-cell performance is found. The results indicate that the percolation threshold value determined in a macroscopic measurement is rather too high and leads to poor ionic conduction as well as unfavorable mechanical properties which results in a worsened half-cell performance. In general, the concept of partial conductivities appears to have limited meaning in the context of the mixed conducting matrix coating approach introduced in this study. Especially mechanical properties and porosity of the CB-LIC premix as well as the interfacial contact quality are not reflected in these measurements although they were shown to play a significant role. A more relevant assessment can be made by distinguishing between static and kinetic capacity losses in half-cell performances during cycling.

Discussion

Interfacial engineering remains a key challenge for SSBs, as electrochemical, chemical, and especially mechanical instabilities at interfaces strongly affect cycling stability and rate performance. Among various mitigation strategies, solution-based and mechanochemical coating routes have emerged as two complementary approaches to optimize SSB microstructures.

Solution-based routes may enable the formation of SEs around CAM particles in-situ. For the halide SE Li_3InCl_6, such coatings have been demonstrated for $LiCoO_2$ by Wang et al.[80] and Ma et al.[81] using aqueous precursor solutions, followed by (freeze-)drying to crystallize the coating phase. This one-step route is attractive for scalability and energy efficiency, since no separate SE synthesis is required. However, aqueous processing is limited to water-tolerant CAMs like $LiCoO_2$, as Ni-rich CAMs can degrade upon water exposure[82–84]. To date, water-based synthesis has only been reported for Li_3InCl_6[85], while other halide SEs and especially sulfide SEs are chemically unstable in water or alcohols[55,86,87]. Consequently, toxic or highly flammable solvents such as xylene, toluene, or acetonitrile are required[88–91]. This introduces safety risks and higher processing costs due to significant energy demand for solvent evaporation and recovery.

Mechanochemical coatings, as presented in this study, offer a solvent-free alternative, avoiding interactions of the solvent with the CAM. High-shear mixing deposits pre-synthesized SEs directly onto CAMs, ensuring intimate contact and large interfacial area without SE pre-comminution or drying steps[60,61,63,65]. Pre-synthesized SE powders (e.g., LIC or sulfides) are mechanically attached to CAM particles without any intensive SE particle pre-comminution or drying step, eliminating solvent use and associated environmental and safety concerns. Although SE pre-synthesis is still needed, advances in large-scale mechanochemical synthesis have reduced its energy demand[15,92], potentially enabling a fully solvent-free SSB manufacturing chain[76].

As shown in this work, coating formation and homogeneity in dry mechanofusion processes are governed by the interplay between various process parameters, requiring precise process optimization. Excessive collision intensities can induce mechanical degradation of the CAM or SE[76], while insufficient stress intensity and/or number leads to incomplete coatings. The risk of particle defects or breakage increases for large or polycrystalline CAMs due to their higher defect probability. Conversely, small, single-crystalline CAM particles exhibit superior mechanical stability, which explains why no measurable degradation was observed even at the highest stress intensities (10,000 rpm, 60 min) within the mixer used in this study. Further performance improvement is expected by optimizing the homogeneous dispersion of CB in the matrix[93–95]. In particular, preventing agglomeration of the conductive additive should enhance CAM utilization while preserving fast interfacial charge transfer and transport throughout the composite cathode. Since both mechanochemical and solution-based coating strategies have distinct advantages and limitations, their applicability will depend on the specific material system, thereby motivating further process optimization and degradation studies.

In summary, we demonstrate that high-intensity mixing leading to mechanofusion is a promising, well-scalable dry-processing approach to fabricate tailored microstructures. We exploit the plastic deformability of Li_3InCl_6 as a model SE, to create nanometer-thin coatings on the one hand, while also being suitable for building up well-defined thicker mixed conducting matrix coatings around single-crystalline NCM on the other. The process can be broadly applied across different types of SEs. Unlike simple mixing of loose particles and arbitrary (re-) ordering, the mechanofusion process offers a bottom-up pathway to

Article https://doi.org/10.1038/s41467-026-71305-2

engineer cathode building blocks with good interfacial connectivity, eliminating the need for manual mixing or multiple post-processing steps. Through systematic variation of process conditions and compositions, supported by DEM simulations and advanced analytics, we identified key parameters controlling the coating morphology, quantified by XPS-derived coverage values, and electrochemical performance. Notably, cathodes with a composition of 80:20:0.5 (NCM:LIC:CB, w/w/w) exhibited stable cycling at 1 C and a specific capacity of $q_{comp} = 100$ mAh g^{-1}, calculated with respect to the total mass of the composite cathode. We expect considerably higher capacities once SEs with much higher conductivity in the order of 10 mS cm^{-1} will be used. Our findings indicate a clear trade-off between CAM utilization, cell kinetics at higher CB contents, and the mechanical behavior of the matrix coating, underlining the importance of optimizing the composite mixing process. Overall, this work presents a promising and scalable strategy for advancing the manufacturing of high-performance SSB cathodes. While also discussing corresponding challenges of this approach, it motivates further exploration of engineered particle architectures in solid-state energy storage systems.

Methods

Materials

Single-crystalline NCM82 ($LiNi_{0.82}Mn_{0.07}Co_{0.11}O_2$ from MSE Supplies, Tucson, AZ, USA), CB (Super C65 from Imerys, France), and in-house synthesized Li_3InCl_6 (LIC) were used. For the latter one, a water-mediated synthesis was carried out in a dried room with a dew point of −60 °C. The starting components LiCl (99%, Fisher Scientific, Waltham, MA, USA) and $InCl_3$ (99.995%, Fisher Scientific, Waltham, MA, USA) with a mass ratio of 0.365:0.635 (LiCl:$InCl_3$) were mixed in deionized water at 40 °C for 2 h using a stir fish. Then, the mixture was first dried at 80 °C with the vessel open for 24 h and afterwards dried under vacuum for 4 h at 200 °C. From each batch, 32 g of dried in-house synthesized LIC was obtained, and this water-mediated synthesis route could be easily scaled up by employing larger vessels. After drying, the LIC was comminuted using a planetary ball mill (Pulverisette 7, Fritsch GmbH, Idar-Oberstein, Germany) at 600 rpm for 4 min with 5 mm ZrO_2 milling beads, using a 50% milling bead filling ratio.

High-intensity mixing

The building blocks were produced using a Picoline high-intensity mixer equipped with a Nobilta attachment (Hosokawa Alpine AG). Mixing was performed in a dry room maintained at a dew point of −60 °C of the supply air. To mitigate the considerable heat generated during mixing, continuous cooling was applied. The material volume that was filled in was consistently set to 4.91 mL based on the calculated pure mixed density ρ_{mix} across all tests to ensure comparability of stressing conditions (cf. Table S1). In the CB-containing samples, CB and LIC were premixed at 5000 rpm for 10 min to pre-structure the matrix coating. NCM was subsequently added, and mixing was continued for up to 60 min. Sampling during the rotational speed variation tests was performed at 5, 10, 30, and 60 min. All mixtures were stored in sealed bags in an argon atmosphere within the dry room prior to further analysis.

Power data evaluation

The power data P of the high-intensity mixer was continuously recorded at 5 s intervals throughout the entire mixing process. For the evaluation of the experimental specific energy input $E_{m,\,exp}$, only the 60 min mixing phase of all three components was considered. To smooth the power signal, a Savitzky-Golay filter with a span of 50 data points was applied. The idle power P_0 corresponding to each rotational speed was subsequently subtracted from the smoothed data. The resulting net power ΔP was then normalized to the mass of the composite m_{total} used in each experiment (cf. Table S1). Finally, the experimentally derived specific energy input $E_{m,\,exp}$ was calculated with the corresponding mixing time t_{mix} according to Eq. 3.

$$E_{m,\,exp} = \frac{\sum_0^{t_{mix}} \Delta P \cdot \Delta t}{m_{total}} \tag{3}$$

Particle size analysis

To determine the particle size of the building blocks, three SEM images were analyzed using an in-house artificial intelligence tool (particleOS.AI). Details are found in Supplementary Note 1.

DEM simulations

Coarse-grained DEM simulations were conducted to capture the macroscopic processing conditions inside the high-intensity mixing device using Rocky version 2024 R1. To reduce computational cost and enable simulations within a practical timeframe, the particle size was coarse-grained to 300 μm, approximately 100 times larger than the actual experimental particle size.

Calibration experiments and simulations were performed to reproduce the particle dynamics and material behavior. First, compaction experiments were carried out using a ZWICK materials testing machine (ZwickRoell GmbH & Co. KG, Ulm, Germany). In these tests, 1 g of the 80:20:3 composite (processed at different rotational speeds for 60 min) was compacted up to 1000 N, and the corresponding force–displacement curves were recorded. In the DEM simulations, an equivalent 1 g of coarse-grained particles was placed inside a virtual compaction cylinder and compressed until a force of 1000 N and the same average displacement as in the experiments was reached. By adjusting the yield ratio, Young's modulus, and friction parameters, the mechanical response of the simulated particles was calibrated to match the experimental results (cf. Supplementary Fig. S10a).

To further capture the particle flow behavior, the dynamic angle of repose of the 80:20:3 composition was determined using a GranuDrum (Granutools, Awans, Belgium) at a rotational speed of 20 rpm and 51.2 g of powder, during which 60 images were recorded and averaged. In the simulations, a corresponding slice of the drum was modeled and filled with coarse-grained particles rotated at the same speed. As only 15% of the drum length was simulated, only 7.68 g of coarse-grains were used in the simulation to save computation time. The static and dynamic friction coefficients were then iteratively adjusted to reproduce the experimentally observed angle of repose (cf. Supplementary Fig. S10b). The set of calibrated parameters used in the simulation is provided in Supplementary Table S2.

The coarse-grained particles were assumed to possess an internal porosity of 0.39. Based on an experimentally determined bulk density of 1.45 g cm^{-3} and a theoretical mixed density of 3.94 g cm^{-3} for the 80:20:3 composition, a corresponding coarse-grain density of 2.417 g cm^{-3} was calculated (cf. Supplementary Fig. S10c). To validate this value, the filling volume determined from the GranuDrum experiments was compared with the simulated filling volume, showing a high agreement (cf. Supplementary Fig. S10d).

To replicate the 80:20:3 mixing experiment at different rotational speeds, the mixing chamber of the high-intensity mixer was virtually filled with 3.88 g of material (one-fifth of the material) via two particle inlets over a time span of 0 s to 0.1 s., and only one-fifth of the mixer volume was simulated, following the approach by Frankenberg et al.[43]. Following the filling phase, the rotor was set to rotate at varying speeds for 0.4 s until the steady state was reached. The mechanical power acting on the rotor was computed and compared to the experimentally recorded net power, enabling validation of the calibration of the simulation parameters from the compaction and angle of repose experiments. The elasto-plastic Thornton–Ning contact model was employed to account for both the plasticity and elasticity of the particle species.

In addition to the overall power acting on the rotor, particle-based (*i*) mean dissipated power $\overline{P_i}^{\alpha}$ was extracted during the output

Article https://doi.org/10.1038/s41467-026-71305-2

intervals of Δt_{out} = 0.005 s and evaluated following the methodology described by Frankenberg et al.[43]. Therefore, the power values, which are a sum of the work done at one particle $\sum_{c=1}^{N_{c,i}} W_c^{diss}$ during the output interval, was divided by its collision frequency $c_i = \frac{\Delta t_{out}}{N_{c,i}}$ and the mass of one coarse-grain particle $m_{particle,CG}$ to obtain particle-based stress intensities. These stress intensities for each output interval were stored $N_{c,i}$ times to consider that particles undergo $N_{c,i}$ collisions during the output interval. From this data, stress intensity SI–stress frequency relationships were derived, and the overall mean stress intensity $\overline{SI}_{CG}$ of this distribution, as well as the coarse-grain stress frequency SF_{CG} representing the number of all coarse-grain collision events of all particles per second, were derived. The stress number per particle $\overline{SN}_p$, corresponding to the total number of stress events per particle over the process time, was then calculated by integrating the stress frequency over time[43].

$$\overline{SI}_{CG,i}^{diss} = \frac{P_i^{diss}}{c_i \cdot m_{particle,CG}} = \frac{\sum_{c=1}^{N_{c,i}} W_c^{diss}}{\Delta t_{out}} \cdot \frac{\Delta t_{out}}{N_{c,i}} \cdot \frac{1}{m_{particle,CG}} \quad (4)$$

$$\overline{SN}_p = SF_{CG} \cdot t_{mix} \cdot \frac{m_{particle,CG}}{m_{total}} \quad (5)$$

XRD analysis

XRD patterns were recorded using a diffractometer equipped with a Cu Kα monochromatic source (λ= 0.154 nm; Empyrean, Malvern Panalytical, Kassel, Germany). Measurements were performed over an angular range of 5° to 120° 2θ with a step size of 0.053° 2θ. Samples were prepared in an argon atmosphere and sealed with Kapton foil to prevent air exposure during analysis. Background subtraction was applied to all spectra.

Additional XRD measurements to determine the influence of the mixing process on micro-strain were performed using a diffractometer equipped with a Mo K_α source (= 0.071 nm; Empyrean, Malvern Panalytical, Kassel, Germany). Measurements were performed over an angular range of 5° to 40° with a step size of 0.053° using capillaries with 0.6 mm diameter in transmission mode and a divergent beam path. Samples were prepared in an argon atmosphere.

Nanoindentation

Nanoindentation measurements were carried out on pellets made from CB-LIC premixes with varying compositions. The pellets were prepared by compressing 0.69 g of premix at 380 MPa for 3 min using a laboratory press (LaboPress P200S, Vogt Labormaschinen, Germany). Each pellet was then affixed to a glass slide using epoxy resin. To protect the sample from air exposure during transfer, a plastic collar was mounted around the pellet, and a glass cover slip was sealed on top with high-viscosity paste.

Measurements were conducted using a TriboIndenter system (Hysitron Inc., Minneapolis, MN). The sample chamber was purged with argon prior to testing to prevent degradation of the pellet. A 100 μm diameter flat punch indenter was used in displacement-controlled mode. Indentations were performed to a depth of 10 μm at a loading rate of 500 nm s^{-1}. For each pellet, 25 indentations were made, and the average force–displacement curve was determined. From the curves, both the elastic $W_{elastic}$ and plastic $W_{plastic}$ work portions of the total indentation work W_{total} were quantified.

$$W_{total} = \int_0^{s_{max}} F_{loading}(s)ds \quad (6)$$

$$W_{elastic} = \int_{s_0}^{s_{max}} F_{unloading}(s)ds \quad (7)$$

$$W_{plastic} = W_{total} - W_{elastic} \quad (8)$$

Here, s_{max} denotes the maximum indentation depth at the highest applied load, while s_0 corresponds to the residual indentation depth after unloading (i.e., the intersection with the x-axis). $F_{loading}$ and $F_{unloading}$ represent the measured force during the loading and unloading phases, respectively.

Determination of porosity

The porosity of the composites and pure materials was measured in a slightly compacted state using a ZWICK materials testing machine (ZwickRoell GmbH & Co. KG, Ulm, Germany). For each sample, three measurements were performed by filling 1 g of composite powder into the measuring cylinder of the instrument. For the individual raw materials, the following masses were used: 2 g for LIC, 0.25 g for CB, and 1 g for NCM. Compaction was performed up to a force of 395 N (3.45 MPa), and the displacement and applied force were recorded. The bulk density ρ_{bulk} of the composite was determined geometrically in the compacted state, and porosity ε was calculated based on the mixed theoretical solids density ρ_{mix} derived from the known raw material densities, which are ρ_{NCM} = 4.75 g cm^{-3}, ρ_{LIC} = 2.59 g cm^{-3} and ρ_{CB} = 1.96 g cm^{-3} (cf. Table S1).

$$\rho_{mix} = vol.\%_{NCM} \cdot \rho_{NCM} + vol.\%_{LIC} \cdot \rho_{LIC} + vol.\%_{CB} \cdot \rho_{CB} \quad (9)$$

$$\varepsilon = 1 - \frac{\rho_{bulk}}{\rho_{mix}} \quad (10)$$

The porosity of the CB-LIC pellets used for nanoindentation measurements was determined after compaction at 380 MPa.

Scanning electron microscopy (SEM)

The sample preparation was performed in an argon-filled glovebox with oxygen residues of $p(O_2)/p < 1.0$ ppm and water residues of $p(H_2O)/p < 1.0$ ppm. The particles were imaged using a field-emission SEM *GeminiSEM 560* system (Carl Zeiss Microscopy GmbH, Jena, Germany) with 2 kV acceleration voltage and 3 mm working distance. EDX analysis was carried out with the *AzTec* EDX system (Oxford Instruments, United Kingdom). EDX mapping was performed with an acceleration voltage of 10 kV at a working distance of 8.5 mm using the *Ultim Max* detector. Prior to imaging, the particles were sputtered with a 4 nm thin layer of platinum using a LEICA EM ACE600 coater (Leica Microsystems GmbH, Wetzlar, Germany).

(Scanning) transmission electron microscopy ((S)TEM)

The sample preparation of the powder sample was performed in an argon-filled glovebox with oxygen residues of $p(O_2)/p < 1.0$ ppm and water residues of $p(H_2O)/p < 1.0$ ppm. Here, the particles were spread onto carbon film-coated Cu-mesh TEM grids. Moreover, a TEM lamella was prepared by focused ion beam (FIB) milling using a Helios™ 5 Hydra CX DualBeam System (Thermo Fisher Scientific Inc.). The sample was transferred in an argon atmosphere from the glovebox to the FIB system and back using the CleanConnect inert gas transfer system. The TEM grids were then loaded in the glovebox into an inert gas/vacuum transfer TEM holder (from Mel-Build) to avoid reaction of the samples with humidity in the air and transferred to a pumping stand. Here, the argon inside the holder was removed before inserting the holder into the TEM.

High-resolution as well as bright-field and dark-field TEM images were recorded on both a JEOL JEM 3010 (300 kV) and a double Cs-corrected JEOL JEM 2200 FS (200 kV). Both microscopes are equipped with a TVIPS TemCam XF416FS camera, which was used for image acquisition.

Article https://doi.org/10.1038/s41467-026-71305-2

The SPED phase map was measured on the JEOL JEM 3010 equipped with a NanoMEGAS P2000 ASTAR system for scanning and precessing the beam (precession angle 0.6°). The four-dimensional data set was recorded with the TVIPS TemCam XF416FS camera as a video, which was later converted into a rectangular data set (.bloc format) using an in-house written Python code and evaluated using the NanoMEGAS software suite DiffGen 2, Index 2, and MapViewer 2. For phase matching, the crystallographic files (.cif) for NCM82, NiO, and LIC taken from the Inorganic Crystal Structure Database were used as input.

EDX data was recorded on the JEOL JEM 2200 FS using a Bruker Nano XFlash Detector 5060 in scanning TEM mode with a semi-convergence angle of 15.07 mrad. The map data was evaluated using the Esprit 2.3 software.

X-ray photoelectron spectroscopy (XPS)

XPS analysis was performed using a PHI Versa Probe IV system (Physical Electronics Inc., Chanhassen, MN, USA). The powders were filled into Teflon crucibles (inner diameter: 3 mm), pressed to achieve a flat surface, and attached to the sample holder using nonconductive adhesive tape. The sample preparation was performed in an argon-filled glovebox with oxygen residues of $p(O_2)/p < 1.0$ ppm and water residues of $p(H_2O)/p < 1.0$ ppm. All samples were transferred to the XPS machine in an air-tight transfer vessel. Monochromatic Al-K_α radiation (1486.6 eV) was applied for XPS analysis. The X-ray source was operated at a power of 50 W and a voltage of 15 kV, having a beam diameter of 200 µm. A pass energy of 55 eV, a step size of 0.2 eV, a step time of 25 ms, and 20 sweeps were used. The samples were charge-neutralized during measurements. The XPS data were evaluated using CasaXPS (Casa Software Ltd., Teignmouth, UK). The spectra were calibrated in relation to the signal of adventitious carbon C 1*s* at 284.8 eV. For each detail spectrum, a region with the same energy boundaries was defined, and the respective intensities $I_{element}$ (in CPS) were used to calculate the coverage values γ[66]:

$$\gamma = \frac{I_{Cl} + I_{In}}{I_{Cl} + I_{In} + I_{Ni} + I_{Mn}} \tag{11}$$

Equation 11 does not contain the C 1*s* signal intensity because this would include signal intensity stemming from adventitious carbon, which cannot be distinguished from the CB contribution. Moreover, the overall signal intensity, including C 1*s*, depends on several experimental parameters and shows noticeable variations between nominally similar samples. Thus, even the corrected C 1*s* intensity, obtained by subtracting the C 1*s* intensity of a CB-free reference sample, was not used in the coverage calculation. XPS-derived coverage values close to 1 reflect that a covering, >10 nm thick, coating layer was achieved. The values contain no information on the morphology and exact thickness distribution. The coverage values contain averaged information over more than 1000 particles.

Cell building and electrochemical evaluation

All electrochemical cells were built in an argon-filled glovebox with oxygen residues of $p(O_2)/p < 1.0$ ppm and water residues of $p(H_2O)/p < 1.0$ ppm. The cell components were filled in an in-house-built cell casing containing a PEEK die with an inner diameter of 10 mm[34]. The electrochemical measurements were carried out in a controlled environment at $T = 25$ °C. During all electrochemical measurements, the cells were fixed in a steel frame while applying a pressure of approximately 80 MPa (10 Nm torque).

For the determination of the effective partial electronic conductivity, symmetric ion-blocking cells were used with stainless steel rods serving as contacts. 120 mg of the matrix and composite powders were compacted with an uniaxial pressure of 380 MPa for 3 min at room temperature.

For the determination of the effective partial ionic conductivity, symmetric electron-blocking cells were used. For this purpose, 240 mg of composite was hand pressed, and then 60 mg of Li_6PS_5Cl (LPSCl, *Argyrodite-CMP5* from Posco JK Solid Solution, South Korea) was added to each side. The three layers were compacted with a uniaxial pressure of 380 MPa for 3 min at room temperature. Then, indium foil (99.999%, 100 µm thickness, 9 mm diameter, Chempur, Germany) and lithium foil (100 µm thickness, 4 mm diameter, China Energy Lithium) were pressed together on both sides to serve as lithium reservoirs.

For the experimental measurement of effective partial conductivities, chronoamperometry was applied until a stable steady-state current was reached at every voltage step. The voltage-current tuples were fitted linearly, and the resistance and the corresponding conductivity were evaluated according to Ohm´s law. For the symmetric electron-blocking cells, an additional reference measurement using Li-In|LPSCl|In-Li was carried out. The associated resistance was subtracted from the total resistance before calculating the ionic partial conductivity.

For the half-cell testing in a in-house made cell casing[96], the following setups were used: First, 40 mg of LiPSCl powder (*Argyrodite-CMP5* from Posco JK Solid Solution, South Korea) was evenly filled in a PEEK cylinder (10 mm diameter) and pressed by hand. Subsequently, a layer of 40 mg LIC was added and also hand pressed, completing the bilayer separator[97]. Then, approximately 15 mg of the cathode composite was evenly distributed on the LIC layer. On the LPSCl layer of the bilayer separator, an indium foil (99.999%, 100 µm thickness, 9 mm diameter, Chempur, Germany) and a lithium foil (100 µm thickness, 6 mm diameter, China Energy Lithium) were placed to form the In/InLi anode. Afterwards, the cell was uniaxially pressed with approximately 380 MPa for 3 min while being isolated.

The cells were cycled in a cell voltage range between 2.0 and 3.7 V vs. In/InLi at room temperature using a BCS-805 Battery Cycling System (Bio-Logic, Seyssinet-Pariset, France) and a MACCOR electrochemical workstation. Charging was done in CCCV mode by holding the cutoff potential for 1 h. The C-rates were calculated based on a CAM-specific capacity of 200 mAh/g_{NCM}, taking into account the nominal amount of NCM in the cathode (1 C ≈ 200 mA/g ≈ 3 mA/cm²).

The CAM utilization was determined similarly to as described in a previous publication[34]: Each SSB cell was charged with 0.1 C to 3.1 V vs. In/InLi, held at that potential for 3 h, followed by 3 h of relaxation to determine the potential V_1. Then, the cell was charged with 0.05 C up to 3.4 V, followed by 5 h of relaxation to get the potential V_2. The relaxed OCP values are given in the Supplementary Source Data File. As a quasi-OCP (titration) curve of the CAM, the capacity-voltage curve of an LE cell at 0.02 C was taken as a reference (cf. Supplementary Fig. S18) for which the data file is openly available in Zenodo at https://doi.org/10.5281/zenodo.14065128, reference number 14065128. For the LIB reference cell, it was assumed that it possesses a comparable voltage-capacity curve to the SSBs. The validity of this approximation is discussed in Supplementary Fig. S19.

The liquid cell data was used to assign a reference specific capacity value $q_{ref,LIB}$ to the potential range determined by V_1 and V_2. This value was compared with the measured capacity $q_{measured}$ of the solid-state cell, which can be extracted with the analysis software. The CAM utilization was then calculated with Eq. 11:

$$\text{CAM Utilization} = \frac{q_{measured}}{q_{ref,\,LIB}} \tag{12}$$

The active specific capacities are calculated by dividing the measured capacities by the CAM utilization, i.e., the charge is referred only to the actual electrochemically active mass.

Data availability

The source data used for all figures in this study are provided in the Source data File, which has been deposited, together with additional data, in Zenodo at https://doi.org/10.5281/zenodo.18493074.

References

1. Janek, J. & Zeier, W. G. A solid future for battery development. *Nat. Energy* **1**, 16141 (2016).
2. Bates, A. M. et al. Are solid-state batteries safer than lithium-ion batteries? *Joule* **6**, 742–755 (2022).
3. Wang, R., Cui, W., Chu, F. & Wu, F. Lithium metal anodes: present and future. *J. Energy Chem.* **48**, 145–159 (2020).
4. Huang, W.-Z. et al. Anode-free solid-state lithium batteries: a review. *Adv. Energy Mater.* **12**, 2201044 (2022).
5. Song, A. et al. A review on the features and progress of silicon anodes-based solid-state batteries. *Adv. Energy Mater.* **13**, 2301464 (2023).
6. Janek, J. & Zeier, W. G. Challenges in speeding up solid-state battery development. *Nat. Energy* **8**, 230–240 (2023).
7. Minnmann, P. et al. Designing cathodes and cathode active materials for solid-state batteries. *Adv. Energy Mater.* **12**, 2201425 (2022).
8. Dixit, M. B. et al. Understanding implications of cathode architecture on energy density of solid-state batteries. *Energy Storage Mater.* **40**, 239–249 (2021).
9. Han, Y. et al. Single- or poly-crystalline Ni-rich layered cathode, sulfide or halide solid electrolyte: Which will be the winners for all-solid-state batteries? *Adv. Energy Mater.* **11**, 2100126 (2021).
10. Kamaya, N. et al. A lithium superionic conductor. *Nat. Mater.* **10**, 682–686 (2011).
11. Kuhn, A. et al. A new ultrafast superionic Li-conductor: ion dynamics in $Li_{11}Si_2PS_{12}$ and comparison with other tetragonal LGPS-type electrolytes. *Phys. Chem. Chem. Phys.* **16**, 14669–14674 (2014).
12. Wang, Z.-Y. et al. Achieving high-energy and high-safety lithium metal batteries with high-voltage-stable solid electrolytes. *Matter* **6**, 1096–1124 (2023).
13. Liu, J., Wang, S., Qie, Y. & Sun, Q. Identifying lithium fluorides for promising solid-state electrolyte and coating material of high-voltage cathode. *Mater. Today Energy* **21**, 100719 (2021).
14. Dai, T. et al. Inorganic glass electrolytes with polymer-like viscoelasticity. *Nat. Energy* **8**, 1221–1228 (2023).
15. Grube, M. et al. Solvent-free and scalable mechanochemical synthesis of high-performance sulfide solid electrolytes. *J. Energy Storage* **121**, 116593 (2025).
16. Jo, Y.-S. et al. Engineering green and sustainable solvents for scalable wet synthesis of sulfide electrolytes in high-energy-density all-solid-state batteries. *Green. Chem.* **25**, 1473–1487 (2023).
17. Kimura, Y. et al. Coating layer design principles considering lithium chemical potential distribution within solid electrolytes of solid-state batteries. *Commun. Mater.* **5**, 1–13 (2024).
18. Nakamura, T., Amezawa, K., Kulisch, J., Zeier, W. G. & Janek, J. Guidelines for all-solid-state battery design and electrode buffer layers based on chemical potential profile calculation. *ACS Appl. Mater. Interfaces* **11**, 19968–19976 (2019).
19. Ruess, R. et al. Single-Crystalline $LiNiO_2$ as High-Capacity Cathode Active Material for Solid-State Lithium-Ion Batteries. *J. Electrochem. Soc.* **170**, 20533 (2023).
20. Wang, L. et al. High-energy all-solid-state lithium batteries enabled by Co-free $LiNiO_2$ cathodes with robust outside-in structures. *Nat. Nanotechnol.* **19**, 208–218 (2024).
21. Dai, Y. et al. Exploring of the upper limit of nickel content in cathode materials for PEO-based solid-state batteries. *Chin. Chem. Lett.* 111157, https://doi.org/10.1016/j.cclet.2025.111157 (2025).
22. Strauss, F. et al. Rational design of quasi-zero-strain NCM cathode materials for minimizing volume change effects in all-solid-state batteries. *ACS Mater. Lett.* **2**, 84–88 (2020).
23. Liu, C., Roters, F. & Raabe, D. Role of grain-level chemo-mechanics in composite cathode degradation of solid-state lithium batteries. *Nat. Commun.* **15**, 7970 (2024).
24. Koerver, R. et al. Chemo-mechanical expansion of lithium electrode materials—on the route to mechanically optimized all-solid-state batteries. *Energy Environ. Sci.* **11**, 2142–2158 (2018).
25. Ryu, H.-H. et al. Microstrain alleviation in high-energy Ni-rich NCMA cathode for long battery life. *ACS Energy Lett.* **6**, 216–223 (2021).
26. Kondrakov, A. O. et al. Anisotropic lattice strain and mechanical degradation of high- and low-nickel NCM cathode materials for Li-ion batteries. *J. Phys. Chem. C* **121**, 3286–3294 (2017).
27. Conforto, G. et al. Editors' Choice—quantification of the impact of chemo-mechanical degradation on the performance and cycling stability of NCM-based cathodes in solid-state Li-ion batteries. *J. Electrochem. Soc.* **168**, 70546 (2021).
28. Payandeh, S., Goonetilleke, D., Bianchini, M., Janek, J. & Brezesinski, T. Single versus poly-crystalline layered oxide cathode materials for solid-state battery applications—a short review article. *Curr. Opin. Electrochem.* **31**, 100877 (2022).
29. Ruess, R. et al. Influence of NCM particle cracking on kinetics of lithium-ion batteries with liquid or solid electrolyte. *J. Electrochem. Soc.* **167**, 100532 (2020).
30. Trevisanello, E., Ruess, R., Conforto, G., Richter, F. H. & Janek, J. Polycrystalline and single crystalline NCM cathode materials—quantifying particle cracking, active surface area, and lithium diffusion. *Adv. Energy Mater.* **11**, 2003400 (2021).
31. Bielefeld, A., Weber, D. A. & Janek, J. Microstructural modeling of composite cathodes for all-solid-state batteries. *J. Phys. Chem. C* **123**, 1626–1634 (2019).
32. Bielefeld, A., Weber, D. A., Rueß, R., Glavas, V. & Janek, J. Influence of lithium ion kinetics, particle morphology and voids on the electrochemical performance of composite cathodes for all-solid-state batteries. *J. Electrochem. Soc.* **169**, 20539 (2022).
33. Minnmann, P. et al. Editors' Choice—visualizing the impact of the composite cathode microstructure and porosity on solid-state battery performance. *J. Electrochem. Soc.* **171**, 60514 (2024).
34. Kissel, M. et al. Quantifying the impact of cathode composite mixing quality on active mass utilization and reproducibility of solid-state battery cells. *Adv. Energy Mater.* **15**, 2405405 (2025).
35. Minnmann, P., Quillman, L., Burkhardt, S., Richter, F. H. & Janek, J. Editors' Choice—quantifying the impact of charge transport bottlenecks in composite cathodes of all-solid-state batteries. *J. Electrochem. Soc.* **168**, 40537 (2021).
36. Hendriks, T. A., Lange, M. A., Kiens, E. M., Baeumer, C. & Zeier, W. G. Balancing partial ionic and electronic transport for optimized cathode utilization of high-voltage $LiMn_2O_4/Li_3InCl_6$ solid-state batteries. *Batter. Supercaps* **6**, e202200544 (2023).
37. Kaiser, N. et al. Ion transport limitations in all-solid-state lithium battery electrodes containing a sulfide-based electrolyte. *J. Power Sources* **396**, 175–181 (2018).
38. Bielefeld, A., Weber, D. A. & Janek, J. Modeling effective ionic conductivity and binder influence in composite cathodes for all-solid-state batteries. *ACS Appl. Mater. Interfaces* **12**, 12821–12833 (2020).
39. Kim, J. et al. High-performance all-solid-state batteries enabled by intimate interfacial contact between the cathode and sulfide-based solid electrolytes. *Adv. Funct. Mater.* **33**, 2211355 (2023).
40. Lee, D. et al. Shear force effect of the dry process on cathode contact coverage in all-solid-state batteries. *Nat. Commun.* **15**, 4763 (2024).
41. Schnell, J. et al. All-solid-state lithium-ion and lithium metal batteries—paving the way to large-scale production. *J. Power Sources* **382**, 160–175 (2018).
42. Batzer, M., Gundlach, D., Michalowski, P. & Kwade, A. Scalable production of separator and cathode suspensions via extrusion for

sulfidic solid-state batteries. *ChemElectroChem* **10**, e202300452 (2023).
43. Frankenberg, F. et al. Investigating the production of all-solid-state battery composite cathodes by numerical simulation of the stressing conditions in a high-intensity mixer. *Powder Technol.* **435**, 119403 (2024).
44. Noh, S., Nichols, W. T., Cho, M. & Shin, D. Importance of mixing protocol for enhanced performance of composite cathodes in all-solid-state batteries using sulfide solid electrolyte. *J. Electroceram* **40**, 293–299 (2018).
45. Titscher, P., Götz von Olenhusen, A., Arlt, T., Manke, I. & Kwade, A. Evaluation of a high-intensive mixing process in a ring shear mixer and its impact on the properties of composite particles for lithium–sulfur battery cathodes. *Energy Technol.* **7**, 1801059 (2019).
46. Helmers, L. et al. Sustainable solvent-free production and resulting performance of polymer electrolyte-based all-solid-state battery electrodes. *Energy Technol.* **9**, 2000923 (2021).
47. Fernandez-Diaz, L. et al. Mixing methods for solid state electrodes: techniques, fundamentals, recent advances, and perspectives. *Chem. Eng. J.* **464**, 142469 (2023).
48. Puls, S. et al. Benchmarking the reproducibility of all-solid-state battery cell performance. *Nat Energy* **9**, 1310–1320 (2024).
49. Maus, O. et al. Influence of post-synthesis processing on the structure, transport, and performance of the solid electrolyte $Li_{5.5}PS_{4.5}Cl_{1.5}$ in all-solid-state batteries. *Adv. Energy Mater.* **15**, 2403291 (2025).
50. Schlautmann, E. et al. Graded cathode design for enhanced performance of sulfide-based solid-state batteries. *ACS Energy Lett.* **10**, 1664–1670 (2025).
51. Schlautmann, E. et al. Impact of the solid electrolyte particle size distribution in sulfide-based solid-state battery composites. *Adv. Energy Mater.* **13**, 2302309 (2023).
52. Shi, T. et al. High active material loading in all-solid-state battery electrode via particle size optimization. *Adv. Energy Mater.* **10**, 1902881 (2020).
53. König, C., Miß, V., Janin, L. & Roling, B. Mitigating the ion transport tortuosity in composite cathodes of all-solid-state batteries by wet milling of the solid electrolyte particles. *ACS Appl. Energy Mater.* **6**, 9356–9362 (2023).
54. Park, C. et al. Electrochemical properties of composite cathode using bimodal sized electrolyte for all-solid-state batteries. *J. Electrochem. Soc.* **166**, A5318–A5322 (2019).
55. Ruhl, J., Riegger, L. M., Ghidiu, M. & Zeier, W. G. Impact of solvent treatment of the superionic argyrodite Li_6PS_5Cl on solid-state battery performance. *Adv. Energy Sustain. Res.* **2**, 2000077 (2021).
56. Wang, Y. et al. Mechanical milling-induced microstructure changes in argyrodite LPSCl solid-state electrolyte critically affect electrochemical stability. *Adv. Energy Mater.* **14**, 2304530 (2024).
57. Choi, Y. E. et al. Coatable Li_4SnS_4 solid electrolytes prepared from aqueous solutions for all-solid-state lithium-ion batteries. *ChemSusChem* **10**, 2605–2611 (2017).
58. Kim, D. H. et al. Infiltration of solution-processable solid electrolytes into conventional Li-ion-battery electrodes for all-solid-state Li-ion batteries. *Nano Lett.* **17**, 3013–3020 (2017).
59. Lee, W. et al. Advanced parametrization for the production of high-energy solid-state lithium pouch cells containing polymer electrolytes. *Nat. Commun.* **15**, 5860 (2024).
60. Kawaguchi, T., Nakamura, H. & Watano, S. Dry coating of electrode particle with model particle of sulfide solid electrolytes for all-solid-state secondary battery. *Powder Technol.* **323**, 581–587 (2018).
61. Kawaguchi, T., Nakamura, H. & Watano, S. Parametric study of dry coating process of electrode particle with model material of sulfide solid electrolytes for all-solid-state battery. *Powder Technol.* **305**, 241–249 (2017).
62. Hayakawa, E., Nakamura, H., Ohsaki, S. & Watano, S. Dry mixing of cathode composite powder for all-solid-state batteries using a high-shear mixer. *Adv. Powder Technol.* **33**, 103705 (2022).
63. Hayakawa, E., Nakamura, H., Ohsaki, S. & Watano, S. Design of active-material/solid-electrolyte composite particles with conductive additives for all-solid-state lithium-ion batteries. *J. Power Sources* **555**, 232379 (2023).
64. Friebel, J. M., Ditscherlein, R., Ditscherlein, L. & Peuker, U. A. Three-dimensional characterization of dry particle coating structures originating from the mechano-fusion process. *Microsc. Microanal.* **30**, 179–191 (2024).
65. Jin, F. et al. Elucidating the impact of Li_3InCl_6-coated $LiNi_{0.8}Co_{0.15}Al_{0.05}O_2$ on the electro-chemo-mechanics of Li_6PS_5Cl-based solid-state batteries. *Chem. Mater.* **36**, 6017–6026 (2024).
66. Kissel, M. et al. Engineering the artificial cathode-electrolyte interphase coating for solid-state batteries via tailored annealing. *Chem. Mater.* **37**, 2192–2203 (2025).
67. Kim, J. S. et al. Synergistic halide-sulfide hybrid solid electrolytes for Ni-rich cathodes design guided by digital twin for all-solid-State Li batteries. *Energy Storage Mater.* **55**, 193–204 (2023).
68. Tanno, K. Current status of the mechanofusion process for producing composite particles. *KONA Powder Part. J.* **8**, 74–82 (1990).
69. Kwade, A. A stressing model for the description and optimization of grinding processes. *Chem. Eng. Technol.* **26**, 199–205 (2003).
70. Burmeister, C. F. & Kwade, A. Process engineering with planetary ball mills. *Chem. Soc. Rev.* **42**, 7660–7667 (2013).
71. Schlem, R. et al. Energy storage materials for solid-state batteries: design by mechanochemistry. *Adv. Energy Mater.* **11**, 2101022 (2021).
72. Burmeister, C. F., Hofer, M., Molaiyan, P., Michalowski, P. & Kwade, A. Characterization of stressing conditions in a high energy ball mill by discrete element simulations. *Processes* **10**, 692 (2022).
73. Zheng, L., Wei, C., Garayt, M. D. L., MacInnis, J. & Obrovac, M. N. Spherically smooth cathode particles by mechanofusion processing. *J. Electrochem. Soc.* **166**, A2924–A2927 (2019).
74. Rumpf, H. C. H. Zur Theorie der Zugfestigkeit von Agglomeraten bei Kraftübertragung an Kontaktpunkten. *Chem. Ing. Tech.* **42**, 538–540 (1970).
75. Tavares, L. & King, R. Single-particle fracture under impact loading. *Int. J. Miner. Process.* **54**, 1–28 (1998).
76. Frankenberg, F. et al. Tailoring composite microstructure through milling for dry-processed sulfide-based solid-state battery cathodes. *Small* **21**, e07279 (2025).
77. Reisacher, E., Kaya, P. & Knoblauch, V. Percolation behavior of a sulfide electrolyte–carbon additive matrix for composite cathodes in all-solid-state batteries. *Batteries* **9**, 595 (2023).
78. Puls, S., Ketter, L., Zeier, W. G. & Vargas-Barbosa, N. M. Opportunities and limitations of partial transport quantification in all-solid-state composite electrodes. *ACS Electrochem.* **1**, 2432–2447 (2025).
79. Yanev, S. et al. Rapid determination of all-solid-state battery performance via chronoamperometry. *J. Electrochem. Soc.* **169**, 90519 (2022).
80. Wang, C. et al. Interface-assisted in-situ growth of halide electrolytes eliminating interfacial challenges of all-inorganic solid-state batteries. *Nano Energy* **76**, 105015 (2020).
81. Ma, T. et al. In-situ cathode coating for all-solid-state batteries by freeze-drying technology. *Nano Energy* **124**, 109522 (2024).
82. Mayer, J. K. et al. Investigation of moisture content, structural and electrochemical properties of nickel-rich NCM based cathodes processed at ambient atmosphere. *J. Electrochem. Soc.* **169**, 60512 (2022).
83. Lechner, M., Wölfl, S., Kurz, E. & Daub, R. Identification of critical moisture exposure for nickel-rich cathode active materials in lithium-ion battery production. *J. Power Sources* **626**, 235661 (2025).

84. Zhang, L. et al. Elucidating the humidity-induced degradation of Ni-rich layered cathodes for Li-ion batteries. *ACS Appl. Mater. Interfaces* **14**, 13240–13249 (2022).
85. Li, X. et al. Water-mediated synthesis of a superionic halide solid electrolyte. *Angew. Chem.* **131**, 16579–16584 (2019).
86. Zhang, Z. et al. One-step solution process toward formation of Li6PS5Cl argyrodite solid electrolyte for all-solid-state lithium-ion batteries. *J. Alloys Compd.* **812**, 152103 (2020).
87. Nikodimos, Y., Huang, C. J., Taklu, B. W., Su, W. N. & Hwang, B. J. Chemical stability of sulfide solid-state electrolytes: stability toward humid air and compatibility with solvents and binders. *Energy Environ. Sci.* **15**, 991–1033 (2022).
88. Park, K. H. et al. Design strategies, practical considerations, and new solution processes of sulfide solid electrolytes for all-solid-state batteries. *Adv. Energy Mater.* **8**, 1800035 (2018).
89. Emley, B. et al. On the quality of tape-cast thin films of sulfide electrolytes for solid-state batteries. *Mater. Today Phys.* **18**, 100397 (2021).
90. Nikodimos, Y. et al. Unveiling the chemical stability and solvent compatibility of halide solid-state electrolytes: insights from isothermal calorimetric titration and synchrotron spectroscopy. *Chem. Mater.* **37**, 7622–7634 (2025).
91. Wang, C. et al. A universal wet-chemistry synthesis of solid-state halide electrolytes for all-solid-state lithium-metal batteries. *Sci. Adv.* **7**, eabh1896 (2021).
92. Hofer, M. et al. Effective mechanochemical synthesis of sulfide solid electrolyte Li_3PS_4 in a high energy ball mill by process investigation. *Adv. Powder Technol.* **34**, 104004 (2023).
93. Mayer, J. K. et al. Influence of the carbon black dispersing process on the microstructure and performance of Li-ion battery cathodes. *Energy Technol.* **8**, 1900161 (2020).
94. Weber, M., Mayer, J. K. & Kwade, A. The Carbon Black Dispersion Index DI CB: a novel approach describing the dispersion progress of carbon black containing battery slurries. *Energy Technol.* **11**, 2201299 (2023).
95. Bockholt, H., Haselrieder, W. & Kwade, A. Intensive powder mixing for dry dispersing of carbon black and its relevance for lithium-ion battery cathodes. *Powder Technol.* **297**, 266–274 (2016).
96. Zhang, W. et al. Interfacial processes and influence of composite cathode microstructure controlling the performance of all-solid-state lithium batteries. *ACS Appl. Mater. Interfaces* **9**, 17835–17845 (2017).
97. Rosenbach, C. et al. Visualizing the chemical incompatibility of halide and sulfide-based electrolytes in solid-state batteries. *Adv. Energy Mater.* **13**, 2203673 (2022).

Acknowledgements

M.K., F.F., J.J., and A.K. acknowledge financial support by Deutsche Forschungsgemeinschaft (DFG, German Research Foundation) through the priority program 2289 (project 462470125) and by BMFTR through the projects 03XP0430A, 03XP0430C (FestBatt Cluster of Competence, FB2-Thio) and 03XP0590D (FoFeBat). Language and grammar of the manuscript have partially been improved with the help of *DeepL Write* and *ChatGPT4.0* (by OpenAI).

Author contributions

M.K. and F.F. contributed equally to this work. M.K., F.F., A.K., and J.J. conceived the project. M.K. and F.F. designed and coordinated the experiments. F.F. prepared the mixtures with the help of N.L., measured the porosities, carried out DEM simulations of the mixing process and analyzed the data. M.K. carried out the electrochemical investigations with help of A.L., measured and analyzed the EDX-SEM and XPS data. T.D. carried out the STEM-EDX and TEM investigations. D.W. analyzed the XRD data. M.K. and F.F. wrote the first version of the manuscript which was edited by all authors.

Funding

Open Access funding enabled and organized by Projekt DEAL.

Competing interests

The authors declare no competing interests.

Additional information

Supplementary information The online version contains supplementary material available at https://doi.org/10.1038/s41467-026-71305-2.

Correspondence and requests for materials should be addressed to Arno Kwade or Jürgen Janek.

Peer review information *Nature Communications* thanks Bohua Wen and the other, anonymous, reviewer(s) for their contribution to the peer review of this work. A peer review file is available.

7 Coatings in Control

Stabilizing the interface between sulfide-based SEs and high-energy CAMs such as Ni-rich layered oxides is crucial for improved long-term stability. Without modifications, this interface is prone to chemical and electrochemical degradation, leading to impedance growth, poor capacity retention, and ultimately cell failure. Protective CAM coatings are a common strategy to mitigate these effects.

A wide range of coating materials and methods, including the process described in Publication III, has been explored, and in corresponding publications, positive effects compared to a bare reference sample have been demonstrated. However, a lack of comparability and reproducibility across studies makes it difficult to evaluate which coating strategy is superior to others and truly leads to stable CAM | SE interfaces.

The following publications show that the effectiveness of coatings is highly sensitive to processing conditions, opening a large parameter space. Therefore, an efficient benchmarking is required to accelerate the development of protective CAM coatings. Interfacial degradation is addressable but only with well-engineered coatings and meaningful benchmarking.

7.1. Publication IV: *Engineering the Artificial Cathode-Electrolyte Interphase Coating for Solid-State Batteries via Tailored Annealing*

This publication[214] investigates the artificial CEI coating, initially reported in a proof of principle study by Zuo *et al.*[241], within a broader process parameter space. For this purpose, poly-crystalline NCM85 was coated with the sulfide SE LPS and annealed at different temperatures. The morphology and composition of the different coatings were probed via X-ray photoelectron spectroscopy (XPS), scanning transmission electron microscopy (STEM), and low-energy ion scattering (LEIS). The performance of the coatings was examined in composite cathodes with LPSCl as catholyte within a benchmarking framework developed by Hertle *et al.*[173], which is mainly based on ToF-SIMS analysis.

The study advances the understanding of the artificial CEI coating concept by establishing process-structure-performance relations. It is demonstrated that process parameters, in this case the annealing temperature, have a critical impact on the performance and need to be carefully explored. Thereby, the results stress the need to move beyond proof-of-principle coating studies and the importance of considering various process parameters. If these parameters are not tailored, a coating can easily be misleadingly interpreted. Furthermore, it is shown that an effective benchmarking is capable of accelerating the identification of suitable process parameters.

The study was designed by M. Kissel, F. Walther, and J. Hertle under the supervision of J. Janek. The experiments were planned and coordinated by M. Kissel. The XPS and ToF-SIMS measurements were carried out by F. Walther. M. Kissel prepared the samples, performed the electrochemical experiments, and evaluated the data. R. Zhang prepared the cells with tape-casted electrodes. P. Brüner performed the LEIS measurements. T. Demuth carried out the STEM-EDX measurements. The manuscript was written by M. Kissel and edited by all co-authors.

Reproduced from: Maximilian Kissel, Felix Walther, Jonas Hertle, Thomas Demuth, Ruizhuo Zhang, Philipp Brüner, Torsten Brezesinski, Kerstin Volz, Jürgen Janek. Engineering the Artificial Cathode-Electrolyte Interphase Coating for Solid-State Batteries via Tailored Annealing. *Chem. Mater.*, 2025, 37, 6, 2192–2203, DOI: 10.1021/acs.chemmater.4c03086,

CHEMISTRY OF MATERIALS

Open Access

pubs.acs.org/cm

Article

Engineering the Artificial Cathode-Electrolyte Interphase Coating for Solid-State Batteries via Tailored Annealing

Maximilian Kissel, Felix Walther, Jonas Hertle, Thomas Demuth, Ruizhuo Zhang, Philipp Brüner, Torsten Brezesinski, Kerstin Volz, and Jürgen Janek*

Cite This: *Chem. Mater.* 2025, 37, 2192−2203

Read Online

ACCESS | Metrics & More | Article Recommendations | Supporting Information

ABSTRACT: Solid-state batteries with nickel-rich layered oxide cathode active materials (CAMs) and sulfide-based solid electrolytes (SEs) are emerging as promising candidates for next-generation energy-storage systems. However, both active and electrolyte materials suffer from poor (electro)chemical compatibility, leading to severe degradation at the SE|CAM interface which is highly detrimental to the long-term cycling stability. Inspired by the natural cathode-electrolyte interphase (CEI), a novel coating concept involves formation of a protective, artificial CEI coating prior to cell assembly. Here, we investigate the oxidative annealing process after coating Li_3PS_4 as precursor onto polycrystalline $LiNi_{0.85}Co_{0.10}Mn_{0.05}O_2$ (NCM85). A combination of microscopic (scanning transmission electron microscopy, STEM), spectroscopic/spectrometric (X-ray photoelectron spectroscopy, XPS, low energy ion scattering, LEIS, and time-of-flight secondary ion mass spectrometry, ToF-SIMS), and electrochemical methods reveals that the composition, morphology, and performance of the coating can be tailored by controlled annealing in oxidizing atmosphere. The effect on coating quality and its stabilizing effect on the SE|CAM interface are examined. Only a morphologically and compositionally optimized coating can successfully prevent interfacial degradation, highlighting the need for tailored process parameters to fully exploit the coating potential. The optimization is supported by an efficient benchmarking framework combining electrochemical and analytical methods, which can serve as a basis for further systematic coating studies.

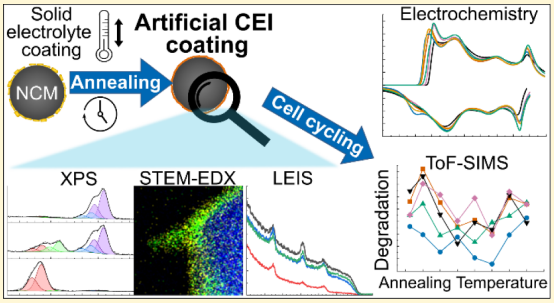

INTRODUCTION

Solid-state batteries (SSBs) are considered promising candidates for next-generation energy storage, mainly due to their potential for higher energy density and potentially improved safety compared to conventional lithium-ion batteries (LIBs).[1−5] Achieving very high energy densities requires the use of a Li-metal anode, which is assumed to be enabled by a solid electrolyte (SE) separator.[6,7] Besides, silicon has recently gained attention as anode material in LIBs and lithium-ion SSBs due to its high specific capacity and low potential of 0.4 V vs Li^+/Li.[8,9] The anode in SSBs is separated by an (ideally) dense and thin SE layer from the cathode to prevent any chemical crossover between the electrodes and to provide electronic insulation. The cathode is typically a composite consisting of SE particles (often called catholyte), cathode active material (CAM) and may also contain an electron-conducting additive and a binder. With regard to materials in the cathode composite, various combinations of CAMs and SEs have been intensely explored.[10] As CAMs, Ni-rich $LiNi_xCo_yMn1_{-x-y}O_2$ (NCM) layered oxides are currently favored, while research on $LiFePO_4$ (LFP)-based SSBs is scarce.[11−14] Ni-rich CAMs are particularly promising, since they offer high theoretical specific capacities and high operating voltages, small volume change upon delithiation/lithiation, as well as being less resource-critical than e.g., $LiCoO_2$ (LCO).[15] Different types of SEs have been tested as catholytes, such as sulfides, oxides, polymers, halides, or composite/hybrid SEs.[16−19] Recently, even the incorporation of a small amount of liquid electrolyte has been regarded as a feasible approach, which may be considered as a route from all-solid to "almost-solid".[20,21] While each SE class has distinct advantages and disadvantages, sulfide SEs are of particular interest as catholytes, since they offer very high ionic conductivities, exceeding 10 mS/cm at room temperature, as recently achieved by high-entropy SEs for example.[22,23] Another advantage is their deformability and processability, eliminating the need for energy-, time-, and cost-intensive

Received: November 7, 2024
Revised: March 5, 2025
Accepted: March 6, 2025
Published: March 11, 2025

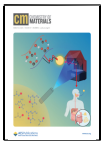

sintering processes, which otherwise can also lead to the formation of unwanted phases.[24]

However, a critical challenge in implementing sulfide SEs and Ni-rich CAMs are interfacial degradation processes caused by the chemical and electrochemical incompatibility of the materials used.[25−28] As previously reported, this interfacial degradation is especially severe at high states of charge,[29] resulting in damage to both the SE and CAM and the formation of unwanted interfacial side products (i.e., an interphase) within a cathode-electrolyte interphase (CEI).[30] The CEI—as well as any structurally degraded near-surface layer in the NCM—impedes Li-ion transport, increases interfacial resistance, and ultimately degrades the cell performance. It is generally composed of two major types of oxidized degradation products: Polysulfides formed by electrochemical oxidation (delithiation) of the SE[31,32] and oxygenated sulfurous and phosphorous species, formed by oxygen-involving oxidation.[33,34] The latter is supposed to be more detrimental to cell degradation.[35] The required oxygen is released from the NCM lattice, reacts with the SE, thereby forming oxygenated sulfurous species (sulfites/sulfates, Li_xSO_y), oxygenated phosphorous species (phosphites/phosphates, Li_xPO_y), and mixed phases of type $Li_xP_yS_zO_u$.[36] In addition, gaseous reaction products like SO_2 have been reported.[37,38] The oxygen loss from the NCM particles causes surface reconstruction with rock-salt-phase formation, which is well-known to block Li-ion transport.[30,36] In addition to the (electro)chemical reactions, the NCM particles undergo morphological and chemo-mechanical degradation. Cycling-induced volume expansion and contraction cause cracking of CAM particles and contact loss between SE/CAM and CAM/CAM, resulting in an increased overpotential and reduced attainable capacity.[39]

In order to prevent the aforementioned degradation phenomena, various CAM coatings have been investigated.[40] The idea is that a thin layer of material on the CAM surface acts as a physical and/or chemical barrier, hindering interfacial reactions between CAM and SE.[41,42] Different approaches have been explored, including the application of ternary lithium oxides, with $LiNbO_3$ being a prominent example,[43] binary oxides (e.g., HfO_2[44,45]) polymers,[46] or halide electrolytes[47] as coatings. While recent advances have shown promising results in improving interfacial stability and enhancing battery performance, long-term stability, scalability, and cost-effectiveness remain major challenges for practical implementation.

As recently reported by our group, the formation of an artificial CEI is a promising approach to prevent interfacial degradation.[48] This approach mimics the natural CEI formation of sulfide SEs during a controlled treatment, aiming to accommodate the driving force of the chemical reaction between sulfide SE and Ni-rich CAM while preventing harmful side reactions. So far, this concept has only been studied within a narrow parameter range, which is typical for most coating investigations reported in literature.

In general, various instrumental analytical techniques can be applied to characterize the coating morphology and composition.[49] However, not all of them are suitable for an efficient and systematic parameter study, due to difficulties in sample preparation or limited statistically relevant information that can be quantified. A possible approach is the combination of a high-throughput method, such as X-ray photoelectron spectroscopy (XPS), and further high-resolution techniques, such as scanning transmission electron microscopy (STEM), for a smaller number of selected samples. With respect to electrochemical performance, long-term cycling tests are usually carried out to prove a positive coating effect compared to a not-intentionally coated sample. However, this only allows for a proof-of-principle without further understanding of the coating mechanism and subsequent optimization of the coating parameters. Hereby, the true potential of the coating might be left undiscovered. Another drawback of long-term cycling experiments is that chemo-mechanical degradation of the full cell and anode-related contributions come into play.[50] They can easily interfere with the effects of cathode-electrolyte interface degradation and impede understanding of the actual effectiveness of the CAM coating in suppressing detrimental interfacial reactions. Chemo-mechanically improved battery cells, on the other hand, often require a slurry fabrication process, including wet processing with suitable solvents and binders, introducing more material combinations and interfaces, making it difficult to relate results directly to the SE|CAM interface.[44] In addition, a larger amount of CAM is needed during composite preparation, compared to lab-scale hand-grinding approaches. Especially during the development of new coating strategies, these larger quantities may not always be available. Thus, new experimental approaches are required to evaluate and benchmark the performance of coatings, such as recently proposed.[51]

One principal aim of this study is to demonstrate that such a systematic CAM coating investigation can be carried out in an efficient and effective way, which facilitates comprehensive understanding of the coating and enables further optimization. Therefore, in this work, we delve into the artificial CEI coating approach, and systematically examine the impact of annealing on CEI formation. We use Li_3PS_4 as sulfide SE and $LiNi_{0.85}Co_{0.10}Mn_{0.05}O_2$ (NCM85) as Ni-rich CAM. The second focus of this work is to gain a better understanding of the coating formation process. To achieve this, the SE was deposited on the CAM surface by a dry-coating approach. The SE-coated CAM was then annealed in synthetic air at various temperatures up to 700 °C. In the following, we employ a combined approach using analytical and electrochemical methods to gain insights into the effect of annealing on the coating properties. We show that the coating morphology as well as composition can be modified by tailored annealing, which has a significant impact on performance. We demonstrate the importance of investigating various process parameters during coating preparation to avoid too general and potentially misleading statements about the coating. Optimal properties of the proposed CEI coating and cell performance are achieved at moderate annealing temperatures, highlighting the versatility of this coating approach and providing guidance for further optimization.

■ EXPERIMENTAL SECTION

Cathode Active Material Coating. The cathode active material ($LiNi_{0.85}Co_{0.10}Mn_{0.05}O_2$, NCM85) was provided by BASF SE and dried under vacuum at 200 °C for 12 h prior to utilization. The coating was applied through dry-coating with mortar and pestle, followed by a heat treatment under synthetic air, similar to previous work by Zuo et al.[48] Accordingly, Li_3PS_4 (NEI Corporation) was added to NCM85 in a weight ratio of 1:99, and the mixture was hand ground for 30 min using an agate mortar. The mixed powder, i.e., SE-coated NCM, was pressed into pellets by a hand press

https://doi.org/10.1021/acs.chemmater.4c03086
Chem. Mater. 2025, 37, 2192−2203

and transferred in a snap cap vial into a tube furnace. The annealing was done in synthetic air (118.5 sccm N_2 and 31.5 sccm O_2 flow). The temperature was increased with a heating rate of 2 K/min, and the final annealing temperature (up to 700 °C) was held for 1 h. After cooling down to room temperature and transferring the sample back to the glovebox, the pellet was hand ground for 5 min to get loose coated CAM powder, which was investigated further. Besides the transfer to and from the oven in a snap cap vial, all samples were treated in an argon-filled glovebox ($p(O_2)/p$ < 0.1 ppm, $p(H_2O)/p$ < 1.0 ppm).

Thermogravimetric Analysis−Mass Spectrometry (TGA-MS). Measurements were performed on a NETZSCH STA-409-PC coupled with a mass spectrometer QMS 403 Aëolos under synthetic air. About 20 mg of the Li_3PS_4 powder was placed in an alumina crucible and heated up to 800 °C.

X-ray Photoelectron Spectroscopy (XPS). XPS analyses were performed using a PHI5000 Versa Probe II system (Physical Electronics Inc.). The powders were filled into Teflon crucibles (inner diameter: 3 mm) and attached to the sample holder using nonconductive adhesive tape. All samples were transferred under argon using a transfer vessel for PTS sample holders by PREVAC. Monochromatic Al−K_α radiation (1486.6 eV) was applied for XPS analysis. The X-ray source was operated at a power of 50 W and a voltage of 17 kV. The analysis spot diameter was set to 200 μm. For charge compensation, a dual beam charge neutralization (ion beam combined with a low-energy electron beam) was used during measurements. The pass energy of the analyzer was 29.35 eV. The XPS data were evaluated using CasaXPS (Casa Software Ltd.). The spectra were calibrated in relation to the signal of adventitious carbon at 284.8 eV. For signal fitting, GL[30] line shapes and Shirley background were applied. Common fitting restrictions (e.g., theoretical signal area ratios depending on the analyzed orbital, fwhm constraints, and published values for spin orbit splitting) were used.

Scanning Transmission Electron Microscopy (STEM). The sample preparation was performed in an argon-filled glovebox with oxygen residues of $p(O_2)/p$ < 1.0 ppm and water residues of $p(H_2O)/p$ < 1.0 ppm. Here, the bare and coated particles were spread onto on carbon film-coated Cu-mesh TEM grids. These grids were then loaded into an inert/vacuum transfer holder (from Mel-Build) and transferred to the TEM under argon atmosphere to avoid reaction of the samples with air. A double Cs-corrected JEOL-JEM2200FS STEM, operating at 200 kV, was used for STEM imaging in the low annular dark-field regime. EDX maps were recorded using a Bruker Nano XFlash Detector 5060.

Low Energy Ion Scattering (LEIS). LEIS measurements were performed at IONTOF GmbH using a Qtac100 low-energy ion scattering spectrometer. Due to its high surface sensitivity, LEIS typically requires in-vacuum cleaning of samples prior to analysis to remove adsorbed species, as the standard method of atomic oxygen cleaning was not applicable for these samples. Spectra were recorded at room temperature, 100 °C, 200 °C, 400 °C, and 600 °C. The instrument is equipped with a double-toroidal analyzer with a fixed scattering angle of 145°. This setup maximizes the measurement sensitivity to keep the ion-beam induced sample damage within the static regime while still obtaining spectra with low noise levels. All samples were analyzed using a 3 keV $^4He^+$ ion beam at normal incidence, with an ion beam current of 2.6 nA scanned over an analysis area of 2 × 2 mm^2. With an acquisition time of 120 s per spectrum, this results in an ion fluence of $5 \cdot 10^{13}$ ions/cm^2, well within the static limit for a 3 keV $^4He^+$ analysis ion beam.

Cell Fabrication and Cycling. For the fabrication of solid-state battery cells, commercially available Li_6PS_5Cl (NEI Corporation) was used without further modification. The Li_6PS_5Cl SE was received and stored in an argon-filled glovebox to maintain its integrity, with oxygen residues of $p(O_2)/p$ < 1.0 ppm and water residues of $p(H_2O)/p$ < 1.0 ppm. The composite cathodes were composed of (un)coated NCM and Li_6PS_5Cl with a mass ratio of 80:20 wt %. No carbon additives or binders were used. The mixture was hand ground in an agate mortar for 15 min.

The basic cell setup used in this study is described in a previous publication.[52] As separator, 60 mg of Li_6PS_5Cl was pressed by hand. About 12 mg cathode composite was added on one side of the separator and distributed evenly. This side of the cell was closed with a modified steel stamp with an Al_2O_3 inlet as current collector to enable advanced post-mortem analysis of the composite cathode as reported by Hertle et al.[51] Afterward, the stacked pellet was pressed at 375 MPa for 3 min. On the other side of the separator, an indium foil (Alfa Aesar, 99.99%, 9 mm diameter, 100 μm thickness) and a lithium foil (China Energy Lithium, 6 mm diameter, 100 μm thickness) were placed to form the In/InLi anode. The complete cell was held in an aluminum frame at a constant pressure of 50 MPa (10 N m torque) during the electrochemical measurements. The cells were cycled at 0.05C (calculated based on a specific capacity of 200 mAh/g) between 1.9 and 3.7 V vs. In/InLi for 1.5 cycles (charge−discharge−charge) and relaxed overnight until the start of the ToF-SIMS measurement.

Time-of-Flight Secondary Ion Mass Spectrometry (ToF-SIMS). ToF-SIMS measurements were performed on a TOF-SIMS 5−100 by IonTOF GmbH Germany, which is equipped with a 25 keV Bi cluster primary ion gun for SIMS analysis. The full cell samples were prepared in an argon-filled glovebox. Insulating adhesive tape was used to attach the composite cathodes to the sample holder. The samples were transferred to the instrument under inert atmosphere using the transfer system Leica EM VCT500 (Leica Microsystems). The analysis area was 150 × 150 μm^2 and rasterized with 256 × 256 pixels (random mode). All measurements were performed in negative ion mode with 25 keV Bi_3^+ primary ions with a dose of $1 \cdot 10^{12}$ ions/cm^2 and a cycle time of 60 μs in spectrometry mode. The data were calibrated with the software SurfaceLab 7.3 (IONTOF GmbH). Pixel-by-pixel normalization (see[51] for details) was used for data analysis in this study. The analysis was performed through an in-house Python code,[53] which performed the pixel-by-pixel analysis on all the peaks identified as relevant. The data are scaled by the total ion count. For each sample, at least 14 different regions were analyzed to obtain statistically relevant information.

Tape-Cast Electrode Preparation. Uncoated and coated NCM85 (annealed at 400 °C) was used for slurry-cast electrode preparation following previous work.[45] Anhydrous o-xylene (97%, Sigma-Aldrich) as solvent, Super C65 carbon additive (TIMCAL Ltd.), and polyisobutylene binder (Oppanol N 150, BASF SE) were used in the preparation of the slurry. A composite cathode was first prepared by ball-milling (FRITSCH GmbH) CAM, SE, and Super C65 in a weight ratio of 69.3:29.7:1.0 at 140 rpm for 30 min. The as-prepared cathode composite was further wetted by o-xylene

https://doi.org/10.1021/acs.chemmater.4c03086
Chem. Mater. 2025, 37, 2192−2203

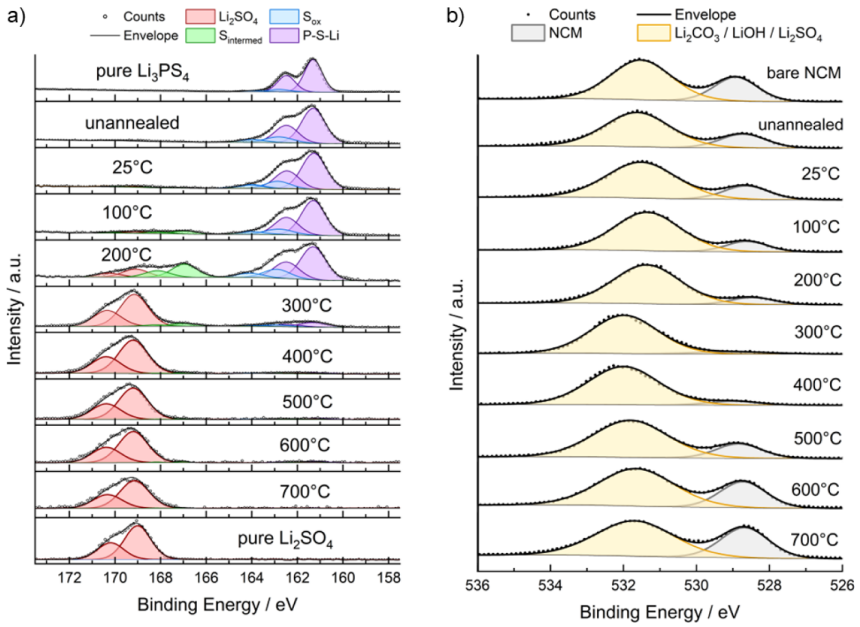

Figure 1. (a) XP detail spectra of the S 2p signal indicating the coating composition depending on the annealing temperature. With increasing temperature, the precursor Li_3PS_4 (E_B = 161.2 eV) transforms into Li_2SO_4-like species (E_B = 169.4 eV). (b) XP detail spectra of the O 1s signal monitoring the evolution of the NCM lattice oxygen signal (gray) and the oxygen signal stemming from surface impurities/coating (yellow). Lower NCM signals suggest increased coating coverage.

with a fixed solid content of 64 wt % and mixed at 600 rpm for 2 min in a centrifugal planetary mixer. The binder solution was then added dropwise to the wetted composite in a weight ratio of 1:99 (binder:cathode composite), followed by further mixing at 2000 rpm for 6 min. Next, the slurry was cast onto Al foil using a mini tape casting device from MTI Corp. All preparation steps were conducted under inert atmosphere either in a sealed container or inside an argon-filled glovebox. The as-prepared cathode sheet was first dried in the glovebox at room temperature for 4 h, then under vacuum for another 12 h. Finally, the cathode tape was punched into discs with a diameter of 9 mm for further electrochemical testing. The assembling procedure was the same as that for the pelletized cells described above, and the cells were cycled between 2.28 and 3.68 V vs. In/InLi.

RESULTS AND DISCUSSION

The sulfide solid electrolyte Li_3PS_4 (LPS) was dry-coated onto polycrystalline NCM85 and then annealed at temperatures between 25 and 700 °C under synthetic air for 1 h to form a coating mimicking the natural CEI. For each artificial CEI coating, both the morphology and the chemical composition were investigated first. In this work, we focused on X-ray photoelectron spectroscopy (XPS) combined with additional scanning transmission electron microscopy (STEM), energy-dispersive X-ray spectroscopy (EDX), and low-energy ion scattering (LEIS) measurements on selected samples. Afterward, all coatings were tested electrochemically in pelletized cells, and the degradation products were analyzed *post mortem* via time-of-flight secondary ion mass spectrometry (ToF-SIMS).

Characterization of Coating Composition and Coverage via XPS and LEIS. XPS analysis as a surface-sensitive technique was performed to monitor compositional changes in the coating, as well as changes in the coating coverage due to the variation in temperature. The aim of the temperature treatment is to oxidize the LPS coating precursor, involving synthetic air as an alternative oxygen source to prevent damage to the CAM. Oxygenated sulfurous- and phosphorous species are formed in these reactions, whereby both (partially lithiated) Li_xSO_y, Li_xPO_y, and mixed phases, such as $Li_xS_yP_zO_v$, are conceivable. Thus, changes in composition were tracked with the S 2p (Figure 1a) and P 2p detail spectra (Figure S1).

The S 2p peak at a binding energy around 161.2 eV corresponds to sulfur in the form of PS_4^{3-} in the LPS precursor, while the S 2p peak around 169.4 eV indicates the formation of sulfates.[33] As seen in Figure 1a, after annealing at 25 °C in synthetic air, the coating precursor has not significantly reacted. The main contributions in the S 2p spectrum match well with the pristine LPS measured as reference. The same accounts for the P 2p spectrum. With increasing annealing temperature, successive transformation of the coating precursor is observed in the S 2p and P 2p spectra. The precursor starts to oxidize to a greater extent between 100 and 200 °C, and the conversion seems to be completed at around 400 °C. The corresponding energy positions indicate the formation of Li_2SO_4- and Li_3PO_4-like species, and thus the intended transformation. With a further rise in temperature above 400 °C, no further changes in the signal shape are observed in the S 2p and P 2p spectra. However, the overall intensity of both decreases, already indicating a removal of coating material.

The compositional evolution is additionally supported by changes in the O 1s signal region (Figure 1b). For the bare NCM, two principal peaks in the O 1s spectrum can be differentiated, which are attributed to the lattice oxygen of the

https://doi.org/10.1021/acs.chemmater.4c03086
Chem. Mater. 2025, 37, 2192−2203

NCM at lower binding energy ($E_B \approx 528.7$ eV) and to Li_2CO_3/LiOH impurities at higher binding energy (~531.4 eV), both of which are typically found on the surface of NCM particles.[54,55] The latter peak can also be seen for the coated samples, but they overlap with contributions originating from Li_2SO_4- and Li_3PO_4-like species, which can be found at slightly higher binding energies of about 532 and 532.5 eV, respectively.[56,57] Accordingly, the signal position of the combined peak shifts to higher binding energies for moderate annealing temperatures (300 and 400 °C), due to the formation of Li_2SO_4- and Li_3PO_4-like species, and shifts back toward the original position for temperatures above 500 °C, also indicating evaporation/sublimation of the coating.

The effect of coating removal can be more clearly seen in the NCM lattice oxygen contribution at around 528.7 eV depending on annealing temperature (Figure 1b). For the unannealed sample, the contribution is reduced compared to the bare NCM, indicating that the precursor covers the NCM surface. With increasing temperature, the intensity of the NCM lattice oxygen contribution is successively decreasing to a minimum for the sample annealed at 300 °C. At this temperature, no NCM lattice oxygen can be detected indicating that the particles are covered with a layer of at least 10 nm. This thickness corresponds approximately to the depth of information in XPS measurements. A further increase of annealing temperature leads again to a rise in lattice oxygen contribution, which indicates that the NCM surface is successively exposed and the coverage decreases. After annealing at 700 °C, the contribution is even higher than for the uncoated reference sample, suggesting that in addition to the removal of coating material, also the common surface impurities (e.g., Li_2CO_3 and LiOH) are partially removed.

A similar trend concerning the coating coverage can be derived from the Ni 2p signal (Figure S2). The decrease in the Ni 2p signal up to an annealing temperature of 300 °C indicates that the transformation of the coating precursor is accompanied by an increasing coverage of the NCM, since XPS is a surface sensitive technique and the NCM:LPS mass ratio was the same in all cases. By comparing the signal intensities of the Ni 2p (CAM) and S 2p/P 2p (coating) detail spectra, the coverage was semiquantitatively evaluated. For this purpose, we used the sum of the relative intensities of the S 2p and P 2p signals for the coating, $I_{coating}$, and the Ni 2p signal for the CAM, I_{CAM}. According to eq 1, the degree of coverage, γ, can reach values between 0 ("not" covered) and 1 ("fully" covered):

$$\gamma = \frac{I_{coating}}{I_{coating} + I_{CAM}} \quad (1)$$

The values for the differently annealed samples are depicted in Figure 2. A maximum coverage for annealing at 300 °C and a decreasing coverage at higher annealing temperatures are found, which confirms the previously discussed observations. It should be noted that the coverage values only serve as an indicator to allow for a comparison among the samples. The calculated values cannot be considered as the real coverage, since the signal intensities are also affected by the coating layer thickness and surface impurities contribute to a lower NCM signal, although they are not part of the intentional coating. Due to the spatial resolution of XPS no single particles are measured but instead statistical information is obtained by analyzing more than 1500 particles simultaneously. Apart from

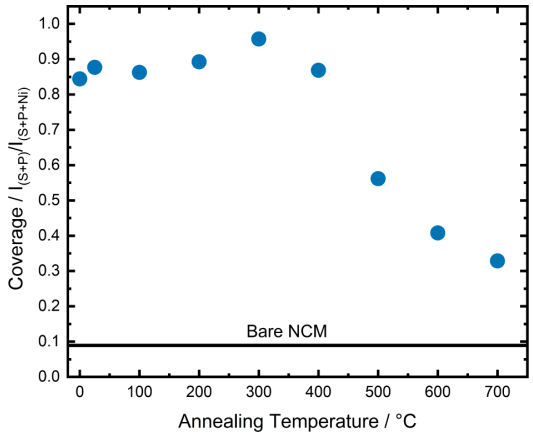

Figure 2. Coating coverage as a function of annealing temperature (hereby 0 °C means unannealed), approximated from relative XPS intensities. Signal intensities (at. %) of coating elements (S, P) are evaluated with respect to the Ni signal stemming from the NCM.

eq 1, other methods of expressing the degree of coverage are feasible. For instance, one could consider the relative Ni signal without any further calculations (Figure S3). All approaches lead to the same trend, allowing for a semiquantitative comparison of the coating coverage by XPS indicating that the annealing temperature affects the coverage and thickness of the coating layer.

The XPS results are supported by thermogravimetric analysis (TGA) combined with mass spectrometry (MS) measurements, carried out under synthetic air on the pure precursor material LPS (Figure S4). After an initial slight weight loss, e.g., due to previous hydrolysis, LPS is stable up to ~180 °C. At an onset temperature of 180 °C, oxidation with mass increase occurs. This ends at about 300 °C, which is consistent with the conclusions on the coating coverage drawn from the XPS analysis. At ~320 °C, oxidation/decomposition begins with a primarily endothermic loss of mass, which is completed at around 380 °C. Especially the second part of the reaction is accompanied by the evolution of SO (m/z = 48) and SO_2 (m/z = 64). We note that also signals with m/z = 50 and m/z = 66 can be detected between 300 and 400 °C, corresponding to POH_3 and PO_2H_3, respectively. However, their intensity is lower, by 1 order of magnitude, than that for the sulfurous species. From 400 °C onward, successive slight weight loss is detected. Accordingly, the main reactions occur between 200 and 400 °C, and the trend in coating coverage derived from XPS correlates well with the TGA data. At higher temperatures, the coating precursor starts to evaporate, which is accompanied by SO, SO_2, POH_3, and PO_2OH_3 evolution. Based on these results, TGA analysis of the SE coating precursor should be considered as a useful precharacterization method for narrowing the range of annealing temperature for coating preparation optimization.

Low energy ion scattering (LEIS) was further carried out to gain more surface sensitive information. Figure 3 depicts the LEIS spectra of three coated NCM samples annealed at different temperatures, along with a bare reference sample, all heated to 200 and 600 °C inside the LEIS device before analysis to remove surface adsorbates. The labeled surface peaks represent the elemental composition of the outer atomic

https://doi.org/10.1021/acs.chemmater.4c03086
Chem. Mater. 2025, 37, 2192−2203

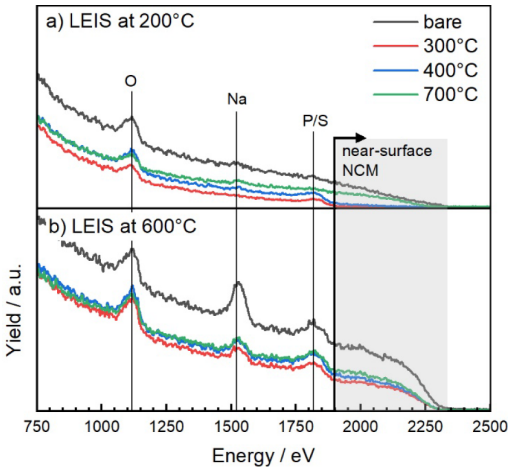

Figure 3. LEIS spectra (taken with 3 keV $^4He^+$) of bare and coated NCM annealed at 300, 400, and 700 °C after heating to (a) 200 °C and (b) 600 °C in the LEIS device.

layer. The absence of a surface peak for Mn/Ni/Co, which were not resolved under these measurement conditions, indicates that no metal atoms from the base material are present in the outer surface layer. However, most of the baseline of the spectrum is due to subsurface NCM atoms, with lower energy values corresponding to greater depth. All signal intensity at energies of 1900 eV and higher originates from NCM atoms in near-surface layers at a depth of 1 to 3 nm. At 200 °C measurement temperature (Figure 3a), these near-surface NCM signals are significantly reduced for the coated samples annealed at 300 and 400 °C, indicating the presence of a coating. Also, for the coated sample annealed at 700 °C a small signal reduction compared to the bare NCM is observed. With increasing temperature in the measurement device, the situation changes. At 600 °C (Figure 3b), the subsurface NCM signal strongly increases for samples annealed at 300 and 400 °C compared to the spectrum shown in Figure 3a. This suggests an increased fraction of NCM just below the surface, meaning that the coating thickness and coverage are decreased. The coated sample annealed at 700 °C shows this behavior from the beginning, presumably because it was already annealed to such a high temperature during the coating process. The reason for the overall higher intensity of the spectra recorded at 600 °C is probably related to some change in surface chemistry, which increases the reionization of He. However, further investigations are required to elucidate this aspect. The occurring sulfur/phosphorus peak for the bare NCM at 600 °C might stem from impurities of the coprecipitation step during the NCM synthesis. Such sulfur residuals were already observed in a previous work by EDX and ToF-SIMS.[58] Sodium is a typical surface contamination, which is often detected in LEIS measurements.[59] Overall, when measuring at 600 °C, the spectra look qualitatively almost identical for all samples, which is probably due to the removal of coating at elevated temperatures. Accordingly, the coated samples become similar to the uncoated NCM, which overall is in agreement with the previously described XPS and TGA-MS results.

Characterization of Coating Morphology via STEM-EDX. LAADF STEM investigations were conducted on selected samples to gain visual information on the coating morphology at the nanoscale (Figure 4). While no coating

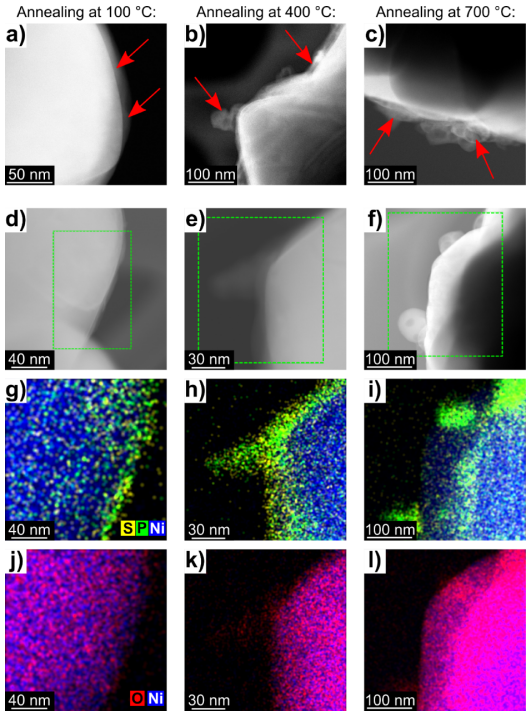

Figure 4. Low-angle annular dark field (LAADF) STEM and STEM-EDX images of LPS-coated NCM85 annealed at 100 °C (a, d, g, j), 400 °C (b, e, h, k), and 700 °C (c, f, i, l). Red arrows indicate the coating and green boxes the area probed using EDX.

layer is visible for the bare NCM (Figure S5), the LPS-coated particles show different coating morphologies depending on the annealing temperature. For the coated sample annealed at 100 °C, a relatively uniform layer of 5 to 20 nm thickness is found (Figure 4a,d), indicating successful dry-coating. However, occasionally we found larger coating particles (Figure S6), which confirms the assumption that the surface layer is not completely homogeneous after the simple coating approach based on hand grinding used in this work. In general, the coating preferably accumulates in notches between the primary particles (Figure S7). The morphology significantly changes with increasing annealing temperature. After annealing at 400 °C, a relatively thick (20 nm−50 nm) and rough coating is found (Figure 4b,e). Additionally, some coagulation is observed, which leads to the formation of medium to large coating particles. The highest annealing temperature of 700 °C results in the formation of even larger particles (50 nm−120 nm) with almost no coating in between (Figure 4c,f). Apparently, the coating underwent a morphological transformation by removal of thin layers and aggregation into larger particles.

STEM-EDX confirmed the previous results with respect to the coating composition. Sulfur and phosphorus were detected in all samples irrespective of the annealing temperature (Figure 4g−i). However, oxygen signals were only detected in the samples annealed at 400 and 700 °C (Figure 4k,l). No oxygen

https://doi.org/10.1021/acs.chemmater.4c03086
Chem. Mater. 2025, 37, 2192−2203

was observed in the coating of the sample annealed at 100 °C (Figure 4j), indicating the coating precursor was not yet oxidized, as expected from the XPS investigations. We like to note that the coating and particles are quite sensitive to the electron beam and degrade under the strong irradiation during EDX measurements. Changes in coating morphology during the EDX measurements are thus unavoidable.

Overall, the characterization results demonstrate that the coating properties are not fully determined during the mechanical dry-coating process, but can be tailored during annealing. Not only the composition, but also the morphology of coating can be adjusted by controlled annealing. With a tailored annealing program, it seems feasible to further optimize the coating with respect to coverage and thickness (see also Section S1).

Electrochemical Performance. To examine the influence of the coating composition and morphology on electrochemical performance and the interfacial processes within the composite cathode, systematic cell cycling with subsequent *post mortem* analysis using ToF-SIMS was performed in accordance with a benchmarking approach reported earlier.[51] The cells consisted of a Li_6PS_5Cl (LPSCl) separator, an In/InLi anode and a cathode composite of NCM and LPSCl. They underwent only 1.5 cycles (charge−discharge−charge) and a relaxing step overnight before the ToF-SIMS measurement, allowing for time-efficient benchmarking of the coating performance.

From the short-term cycling results, various metrics can be extracted and taken into consideration to assess the electrochemical performance of the coatings. First, the initial Coulomb efficiency (ICE) is a good indicator for the interfacial decomposition of SE. In SSBs, the significantly larger first-cycle charge capacity stems from the oxidative decomposition of SE.[31,60] It is therefore often the case that a higher ICE indicates lower initial SE decomposition. As depicted in Figure 5a, the ICE reaches around 85% for the uncoated sample. Interestingly, for the lower annealing temperatures up to 200 °C, the coated samples show even lower ICEs. For annealing temperatures of 300 °C and above, the ICE improves compared to the bare NCM. This already indicates that coating composition and morphology significantly affect interfacial reactions and thus the electrochemical properties and that a coating does not always lead to an improvement. The absolute capacities follow a similar trend, for which the 700 °C sample reaches the highest second-cycle specific charge capacity of 199.5 mAh/g. Here, apart from the 25 °C sample, all coatings lead to an improvement compared to the composite using bare NCM. However, from these results alone, no firm conclusions can be drawn about the quality of coating depending on the annealing temperature.

Since the measurable capacities strongly depend also on the microstructure of the cathode composite which in turn depends on the mixing process, additional parameters, such as overpotential, as measure for the internal resistance were considered. When galvanostatically charging the cell, the upper cutoff voltage, here 3.7 V vs. In/InLi, is reached while the actual state-of-charge (SOC) of the CAM is lower. Analogously, when discharging the cell, the lower cutoff voltage, here 1.9 V vs. In/InLi, is reached while the actual SOC of the CAM is higher. Thus, during a following OCV period in both cases, the potential relaxes toward the actual SOC of the system. A stronger relaxation is the consequence of a higher overpotential during charging/discharging and indicates a

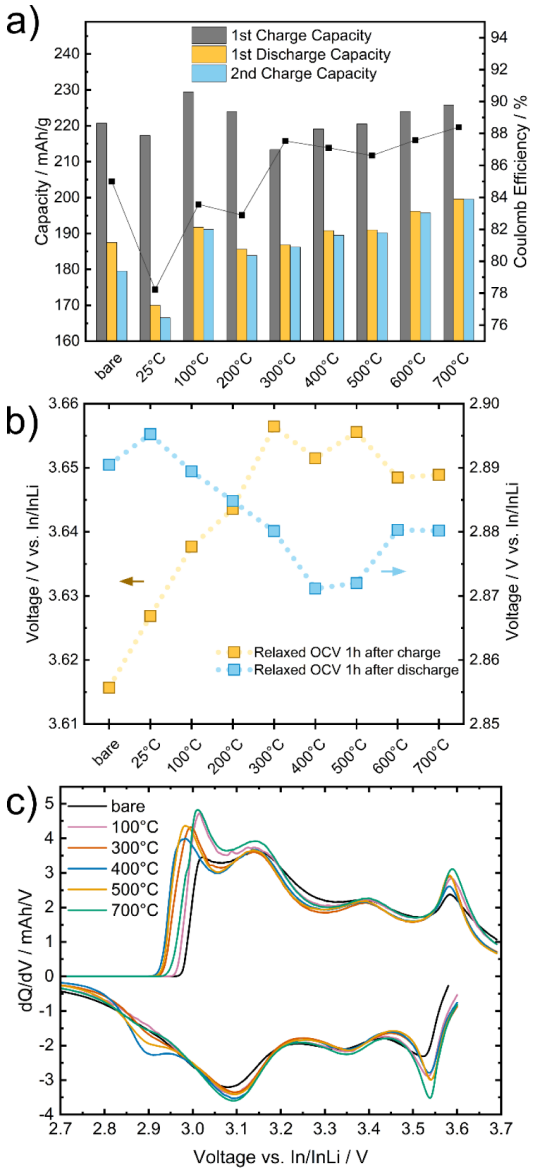

Figure 5. Electrochemical parameters used for comparison of the coating effects including (a) the specific capacities of 1.5 cycles, (b) the relaxed OCV reached after 1 h after galvanostatic charging/discharging to 3.7/1.9 V vs In/InLi, and (c) differential capacity plots of the first discharge and second charge cycles.

larger cell resistance. Since the tested cells were built identically, a difference in cell resistance should be mainly attributed to the CEI degradation layer. Comparing the relaxed potentials 1 h after charging/discharging, as depicted in Figure 5b, allows a ranking of the coating quality. The relaxed potentials are maximal after charge and minimal after discharge for the samples annealed at 300 to 500 °C. Lower annealing temperatures lead to a significantly larger potential relaxation, indicating higher cell resistance. Also, higher annealing temperatures lead to a slightly stronger relaxation. This trend is confirmed by the differential capacity plots of the first

https://doi.org/10.1021/acs.chemmater.4c03086
Chem. Mater. 2025, 37, 2192−2203

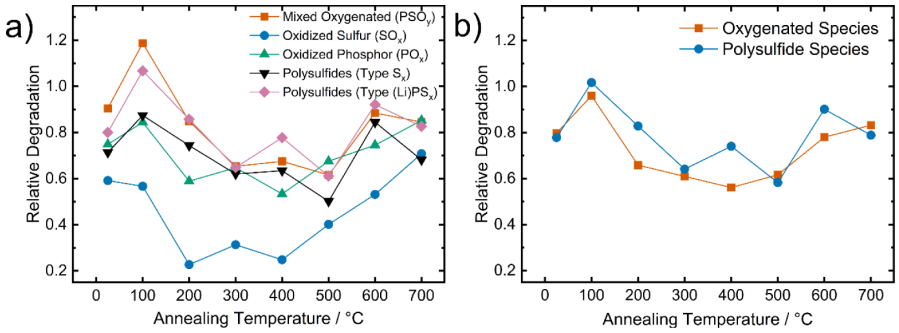

Figure 6. ToF-SIMS surface analysis to determine the relative degradation of composite cathodes with differently annealed LPS-coated NCMs. The signal intensity of each fragment is normalized to the respective total ion signal before calculating the relative degradation, which corresponds to the relative intensity of the signal with respect to the signal of a composite cathode using uncoated NCM.

discharge and second charge cycles (Figure 5c). In general, the overpotential is found to be decreased for all coated samples compared to the bare NCM. However, the samples annealed at medium to high temperatures clearly show a reduced overpotential compared to coated samples treated at lower or higher temperatures. During discharge, the samples annealed at 400 and 500 °C show an additional feature at ~2.9 V vs In/InLi, which is commonly referred to as "kinetic hindrance" region and is considered as a beneficial feature.[61] Overall, the electrochemical results are in accordance with the XPS, TGA-MS, LEIS, and STEM/EDX results: Annealing between 300 and 500 °C leads to an optimized coating, which in turn improves the performance from an electrochemical perspective.

Post-Mortem ToF-SIMS Degradation Analysis. After the short-term cycling, ToF-SIMS measurements were carried out to detect and quantify degradation products. The combination of electrochemical data and *post mortem* analysis is imperative to holistically compare different coatings.[51] Considering the strong correlation between the EC performance and the interfacial degradation, the resulting side products during cycling will be discussed thoroughly in the following section. While the electrochemical performance (in terms of achievable capacity and capacity retention) should be as high as possible, the relative degradation product signals should be as low as possible.

In general, interfacial degradation between NCM and sulfide SEs can be divided into two pathways.[51] One is arising from the SE being in contact with electronically conducting surfaces, i.e., the current collector, CAM surface, or carbon additives, leading to electrochemical oxidation through lithium extraction, e.g., formation of polysulfide species.[31] They do not necessarily have to be regarded as detrimental, since the as-formed compounds can be assumed to be redox active within a certain potential range, but they may increase local resistance.[35,62,63] The other type of degradation is arising from the chemical, oxygen-involving oxidation of the SE being in contact with the CAM particles. Thereby, sulfites/sulfates (Li_xSO_y), phosphites/phosphates (Li_xPO_y), and thiophosphites/thiophosphates ($Li_xS_yP_zO_u$) are generated as parasitic byproducts, as well as gaseous reaction products. Since the oxygen originates from the NCM, the reactions are accompanied by surface reconstruction with rock-salt phase formation, which is known to impede lithium transport.[30,36] Our coating approach intends to minimize the damage to the CAM and the associated more or less "uncontrolled" reactions with the SE.

To investigate the effect of the coatings on interfacial reactions, ToF-SIMS measurements were performed. In the analysis, the ion fragments can be assigned to different groups of degradation products, as depicted in Figure 6a. Herein, the results of principle component analysis (PCA) were used to weight the intensity of the corresponding fragments appropriately (cf. ref 51 for details). The signals were normalized with respect to the uncoated sample to directly see the influence of the coating on the ion fragment intensities. Relative degradation values above 1 indicate that more degradation products were detected for the sample than for the bare reference material, while values below 1 indicate the opposite trend. For better visualization, we further grouped the fragments from Figure 6a into the two main (solid) degradation products (polysulfide-like and oxygenated species) in Figure 6b.

Compared to the bare reference sample, almost all coatings lead to a decrease in degradation products, even though the coating itself consists of oxygenated sulfurous and phosphorous species. However, there are distinct differences for the different annealing temperatures, and a clear trend is apparent. Apart from the sample annealed at 100 °C, the degradation products successively decrease with increasing annealing temperature down to a minimum for the coatings annealed between 300 and 500 °C. At higher annealing temperatures, the trend in coating coverage and electrochemical data is reflected by the increased fraction of degradation products. Higher annealing temperatures lead to partial removal of the coating, resulting in more reactive CAM|SE interfaces, which in turn results in an increase in side products. Accordingly, the less the coverage, the higher the electrochemical performance in terms of initial capacity, but also the fraction of degradation products.

Overall, the coating seems suitable to mitigate interfacial reactions between NCM and SE, resulting in smaller fractions of both oxygenated sulfurous/phosphorous species and polysulfides. Particularly the latter is remarkable, since the coating itself already consists of oxygenated sulfurous/phosphorous species. According to the data shown so far, the best compromise between coating morphology/composition, electrochemical performance, and degradation products can be found for the coated CAMs annealed at 300 and 400 °C. Although the bare NCM surface initially provides a higher

https://doi.org/10.1021/acs.chemmater.4c03086
Chem. Mater. 2025, 37, 2192−2203

capacity in the initial charge cycle, it suffers from significant interfacial degradation and overpotential, which is expected to result in inferior long-term cycling performance compared to the coated samples.

Long-Term Cycling Performance. To verify the predicted improved long-term performance, cells with slurry-cast cathode sheets were cycled over a longer period of time. The aim is to reduce the influence of chemo-mechanical degradation, which is a severe problem in pelletized cells that have been used for short-term cycling.[50] A disadvantage of slurry-cast electrodes is that relatively larger amounts of coated material are required, which are often not easily available for small batch testing in lab scale. Thus, in our case, only the coated sample annealed at 400 °C was chosen for long-term cycling experiments, since it provides a fully oxidized coating, which is not the case for the sample annealed at 300 °C. The corresponding electrochemical performance is shown in Figure 7. The coated sample reaches a significantly higher ICE

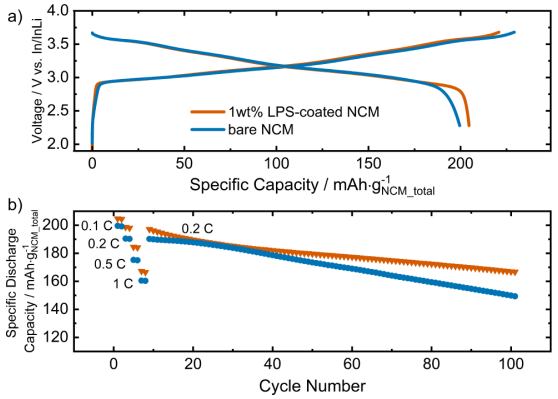

Figure 7. Cycling performance of the uncoated and LPS-coated NCM in a full cell with tape casted electrodes. (a) First-cycle voltage profiles at C/10 and (b) specific discharge capacities calculated with respect to the total mass of NCM in the composite cathode over 100 cycles (at C/5 after initial rate capability testing).

(92.7%) compared to the uncoated NCM (87.1%) and a first-cycle specific discharge capacity of almost 205 mAh/g. The capacities were calculated with respect to the total mass of NCM in the composite cathode. In the following, the C-rate was gradually increased from 0.1 to 1.0C. The SE-coated CAM delivered specific discharge capacities of 204, 198, 184, and 166 mAh/g at 0.1, 0.2, 0.5, and 1.0C, respectively, i.e., about 97, 90, and 81% of the capacity achieved at 0.1C was retained at higher C-rates. In contrast, the specific discharge capacities and their retention were lower for the bare NCM85 (199/190/175/160 mAh/g at 0.1/0.2/0.5/1.0C). Also, during long-term cycling at 0.2C, the coated sample proves its improved long-term performance, retaining 85% (vs 79% for the uncoated counterpart) of the capacity after 90 cycles. It should be noted that practically also the anode can significantly contribute to capacity fading during long-term cycling and its influence is not well controlled in a two-electrode cell configuration. However, based on the statistics, at least two independent cells were measured and presented the same trend, thus corroborating the significantly enhanced performance by the introduced coating and reducing the interference from the anode. During cycling, the SE oxidation and CEI growth continue, leading to a continuously increasing interfacial resistance, which in turn lowers the capacity during galvanostatic cycling. These processes are effectively mitigated by the SE-coated sample, thus leading to improved long-term performance.

Discussion of the Artificial CEI Coating. Cathode active material coatings are frequently not subjected to systematic analysis and optimization in the literature. Consequently, the influence of different process parameters on the microstructure, composition, and performance may remain undiscussed, and the true potential of coatings cannot be accurately assessed. At the same time, results are often referred to the coating material in general, although its properties may vary significantly depending on the process parameters. Rather than making generalized statements about the performance of a particular coating material, it is more prudent to consider the specific process parameters and their impact on the coating's microstructure, composition, and ultimately its performance.

As demonstrated in this work, not every coating leads to an improvement since the annealing temperature, for instance, has a crucial effect by influencing not only the composition, but also the morphology (coverage) of the coating. The highest coverage was obtained for an annealing temperature of 300 °C, while a fully oxidized surface layer required temperatures beyond 300 °C. To achieve both high coating coverage and full SE oxidation, we further investigated the influence of annealing time and gas atmosphere. Details of this investigation are presented in Section S1. It was found that a longer annealing time has a beneficial effect only if the oxidation is not completed after 1 h, that is, for temperatures below 400 °C. Increasing the oxygen partial pressure in the annealing atmosphere can accelerate the precursor oxidation at lower temperatures, allowing for shorter annealing times. The annealing not only affects the coating properties but may also alter the defect chemistry and structure of the cathode material.[24,64] To deconvolute these contributions and to fully elucidate the working principle of the artificial CEI coating, further systematic investigations are required in the future.

While already the annealing process allows for a significant optimization of the artificial CEI by adjusting the annealing temperature, time, and atmosphere, numerous other parameters may further improve the coating properties. The deposition method, with associated parameters, such as precursor amount, may enable a more uniform and thinner coating. Moreover, the precursor type can be varied, since all sulfide SEs are in principle applicable for that purpose, which may require again a reassessment of process parameters. Further optimization of all these parameters has the potential to enhance the performance of the artificial CEI coating approach. Thereby, a systematic benchmarking framework is able to facilitate and accelerate the optimization process. In general, the development and optimization of active material coatings remain an important and challenging task on the path toward stable solid-state batteries.

■ CONCLUSIONS

We have investigated the effect of annealing process on the properties of a CAM coating, which involves creating an artificial CEI prior to cell assembly. After applying the sulfide SE, Li_3PS_4, as coating precursor during a simple dry-coating process on polycrystalline $LiNi_{0.85}Co_{0.10}Mn_{0.05}O_2$, the annealing temperature was systematically varied. The resulting coatings were characterized in detail using XPS, TGA-MS, LEIS and STEM with respect to their morphology and

https://doi.org/10.1021/acs.chemmater.4c03086
Chem. Mater. 2025, 37, 2192−2203

chemical composition. The analyses revealed that both properties are strongly dependent on the annealing temperature. The temperature should be as high as necessary to ensure complete oxidation of the coating precursor and at the same time as low as possible to avoid evaporation or coagulation of coating. Further electrochemical testing and *post mortem* ToF-SIMS analysis showed that only a properly annealed coating leads to the intended mitigation of interfacial degradation. The corresponding temperature range was found to lie between 300 and 400 °C. Preliminary additional tests with respect to annealing time and gas atmosphere indicated that these process parameters can also significantly affect the coating quality. These results emphasize the versatility of the proposed coating approach.

Overall, our work highlights the importance of investigating different process parameters to fully explore the coating potential and to avoid too generalized statements. We have demonstrated that this can be achieved through efficient benchmarking, combining electrochemical tests as well as microscopic and spectroscopic/spectrometric methods.

■ ASSOCIATED CONTENT

Supporting Information

The Supporting Information is available free of charge at https://pubs.acs.org/doi/10.1021/acs.chemmater.4c03086.

XP spectra of the P 2p and Ni 2p signals for the un(coated) NCM, extracted relative Ni fraction as a function of temperature, TGA-MS for Li_3PS_4, additional STEM images of un(coated) NCM, and discussion of the effect of annealing time and atmosphere (PDF)

■ AUTHOR INFORMATION

Corresponding Author

Jürgen Janek − *Institute of Physical Chemistry, Justus Liebig University Giessen, Giessen 35392, Germany; Center for Materials Research (ZfM/LaMa), Justus Liebig University Giessen, Giessen 35392, Germany; Battery and Electrochemistry Laboratory (BELLA), Institute of Nanotechnology, Karlsruhe Institute of Technology (KIT), Karlsruhe 76131, Germany;* orcid.org/0000-0002-9221-4756; Email: juergen.janek@pc.jlug.de

Authors

Maximilian Kissel − *Institute of Physical Chemistry, Justus Liebig University Giessen, Giessen 35392, Germany; Center for Materials Research (ZfM/LaMa), Justus Liebig University Giessen, Giessen 35392, Germany;* orcid.org/0000-0001-9201-0748

Felix Walther − *Institute of Physical Chemistry, Justus Liebig University Giessen, Giessen 35392, Germany; Center for Materials Research (ZfM/LaMa), Justus Liebig University Giessen, Giessen 35392, Germany;* orcid.org/0000-0002-5843-4237

Jonas Hertle − *Institute of Physical Chemistry, Justus Liebig University Giessen, Giessen 35392, Germany; Center for Materials Research (ZfM/LaMa), Justus Liebig University Giessen, Giessen 35392, Germany;* orcid.org/0000-0001-8040-8038

Thomas Demuth − *Materials Science Center (WZMW) and Department of Physics, Philipps-University Marburg, Marburg 35032, Germany;* orcid.org/0009-0002-9796-4959

Ruizhuo Zhang − *Battery and Electrochemistry Laboratory (BELLA), Institute of Nanotechnology, Karlsruhe Institute of Technology (KIT), Karlsruhe 76131, Germany;* orcid.org/0000-0003-0292-5026

Philipp Brüner − *IONTOF GmbH, Münster 48149, Germany*

Torsten Brezesinski − *Battery and Electrochemistry Laboratory (BELLA), Institute of Nanotechnology, Karlsruhe Institute of Technology (KIT), Karlsruhe 76131, Germany;* orcid.org/0000-0002-4336-263X

Kerstin Volz − *Materials Science Center (WZMW) and Department of Physics, Philipps-University Marburg, Marburg 35032, Germany;* orcid.org/0000-0002-4456-5439

Complete contact information is available at: https://pubs.acs.org/10.1021/acs.chemmater.4c03086

Author Contributions

M.K.: conceptualization, formal analysis, investigation, visualization, project administration, writing original draft. F.W.: conceptualization, XPS and SIMS investigation, formal analysis, review and editing. J.H.: conceptualization, review and editing. T.D.: STEM-EDX investigation, review and editing. R.Z.: tape cast electrode investigation, review and editing. P.B.: LEIS investigation, review and editing. T.B.: supervision, review and editing. K.V.: supervision, review and editing. J.J.: conceptualization, supervision, funding acquisition, review and editing.

Notes

The authors declare no competing financial interest.

■ ACKNOWLEDGMENTS

This research was funded by the Deutsche Forschungsgemeinschaft (DFG, German Research Foundation)—within the priority program 2289 (heteroaggregates) under project no. 462470125 and by BASF SE. The authors acknowledge Dr. Alexander Sedykh for performing the TGA-MS measurement. Language and grammar of the manuscript have partially been improved with the help of *DeepL Write*.

■ REFERENCES

(1) Janek, J.; Zeier, W. G. A solid future for battery development. *Nat. Energy* **2016**, *1* (9), 16141.

(2) Sun, Y.-K. Promising All-Solid-State Batteries for Future Electric Vehicles. *ACS Energy Lett.* **2020**, *5* (10), 3221−3223.

(3) Alex, M. B.; Preger, Y.; Torres-Castro, L.; Katharine, L. H.; Stephen, J. H.; John, H. Are solid-state batteries safer than lithium-ion batteries? *Joule* **2022**, *6*, 742−755.

(4) Yu, X.; Chen, R.; Gan, L.; Li, H.; Chen, L. Battery Safety: From Lithium-Ion to Solid-State Batteries. *Engineering* **2023**, *21*, 9−14.

(5) Betz, J.; Bieker, G.; Meister, P.; Placke, T.; Winter, M.; Schmuch, R. Theoretical versus Practical Energy: A Plea for More Transparency in the Energy Calculation of Different Rechargeable Battery Systems. *Adv. Energy Mater.* **2019**, *9* (6), 1803170.

(6) Wang, R.; Cui, W.; Chu, F.; Wu, F. Lithium metal anodes: Present and future. *J. Energy Chem.* **2020**, *48*, 145−159.

(7) Jetybayeva, A.; Aaron, D. S.; Belharouak, I.; Mench, M. M. Critical review on recently developed lithium and non-lithium anode-based solid-state lithium-ion batteries. *J. Power Sources* **2023**, *566*, 232914.

(8) Huo, H.; Janek, J. Silicon as Emerging Anode in Solid-State Batteries. *ACS Energy Lett.* **2022**, *7* (11), 4005−4016.

(9) Franco Gonzalez, A.; Yang, N.-H.; Liu, R.-S. Silicon Anode Design for Lithium-Ion Batteries: Progress and Perspectives. *J. Phys. Chem. C* **2017**, *121* (50), 27775−27787.
(10) Han, Y.; Jung, S. H.; Kwak, H.; Jun, S.; Kwak, H. H.; Lee, J. H.; Hong, S.-T.; Jung, Y. S. Single- or Poly-Crystalline Ni-Rich Layered Cathode, Sulfide or Halide Solid Electrolyte: Which Will be the Winners for All-Solid-State Batteries? *Adv. Energy Mater.* **2021**, *11* (21), 2100126.
(11) Cronk, A.; Chen, Y.-T.; Deysher, G.; Ham, S.-Y.; Yang, H.; Ridley, P.; Sayahpour, B.; Nguyen, L. H. B.; Oh, J. A. S.; Jang, J.; Tan, D. H. S.; Meng, Y. S. Overcoming the Interfacial Challenges of LiFePO 4 in Inorganic All-Solid-State Batteries. *ACS Energy Lett.* **2023**, *8* (1), 827−835.
(12) Kim, T.; Kim, K.; Lee, S.; Song, G.; Jung, M. S.; Lee, K. T. Thermal Runaway Behavior of Li6PS5Cl Solid Electrolytes for LiNi0.8Co0.1Mn0.1O2 and LiFePO4 in All-Solid-State Batteries. *Chem. Mater.* **2022**, *34* (20), 9159−9171.
(13) Frankenberg, F.; Kissel, M.; Burmeister, C. F.; Lippke, M.; Janek, J.; Kwade, A. Investigating the production of all-solid-state battery composite cathodes by numerical simulation of the stressing conditions in a high-intensity mixer. *Powder Technol.* **2024**, *435*, 119403.
(14) Roitzheim, C.; Sohn, Y. J.; Kuo, L.-Y.; Häuschen, G.; Mann, M.; Sebold, D.; Finsterbusch, M.; Kaghazchi, P.; Guillon, O.; Fattakhova-Rohlfing, D. All-Solid-State Li Batteries with NCM−Garnet-Based Composite Cathodes: The Impact of NCM Composition on Material Compatibility. *ACS Appl. Energy Mater.* **2022**, *5* (6), 6913−6926.
(15) Payandeh, S.; Goonetilleke, D.; Bianchini, M.; Janek, J.; Brezesinski, T. Single versus poly-crystalline layered oxide cathode materials for solid-state battery applications - a short review article. *Curr. Opin. Electrochem.* **2022**, *31*, 100877.
(16) Zhao, Q.; Stalin, S.; Zi Zhao, C.; Archer, L. A. Designing solid-state electrolytes for safe, energy-dense batteries. *Nat. Rev. Mater.* **2020**, *5* (3), 229−252.
(17) Mangani, L. R.; Villevieille, C. Mechanical vs. chemical stability of sulphide-based solid-state batteries. Which one is the biggest challenge to tackle? Overview of solid-state batteries and hybrid solid state batteries. *J. Mater. Chem. A* **2020**, *8* (20), 10150−10167.
(18) Laiqiang, X.; Jiayang, L.; Shuai, H.; Luo, Z.; Wang, B.; Fang, S.; Zou, G.; Hou, H.; Peng, H.; Xiaobo, J. Recent advances of composite electrolytes for solid-state Li batteries. *J. Energy Chem.* **2022**, *67*, 524−548.
(19) Kwak, H.; Wang, S.; Park, J.; Liu, Y.; Kim, K. T.; Choi, Y.; Mo, Y.; Jung, Y. S. Emerging Halide Superionic Conductors for All-Solid-State Batteries: Design, Synthesis, and Practical Applications. *ACS Energy Lett.* **2022**, *7* (5), 1776−1805.
(20) Woolley, H. M.; Vargas-Barbosa, N. M. Hybrid solid electrolyte-liquid electrolyte systems for (almost) solid-state batteries: Why, how, and where to? *J. Mater. Chem. A* **2023**, *11* (11), 1083−1097.
(21) Huo, H.; Janek, J. Solid-state batteries: from'all-solid' to'almost-solid'. *Natl. Sci. Rev.* **2023**, *10* (6), 1−3.
(22) Lin, J.; Schaller, M.; Cherkashinin, G.; Indris, S.; Du, J.; Ritter, C.; Kondrakov, A.; Janek, J.; Brezesinski, T.; Strauss, F. Synthetic Tailoring of Ionic Conductivity in Multicationic Substituted, High-Entropy Lithium Argyrodite Solid Electrolytes. *Small* **2024**, *20*, 2306832.
(23) Lin, J.; Cherkashinin, G.; Schäfer, M.; Melinte, G.; Indris, S.; Kondrakov, A.; Janek, J.; Brezesinski, T.; Strauss, F. A High-Entropy Multicationic Substituted Lithium Argyrodite Superionic Solid Electrolyte. *ACS Mater. Lett.* **2022**, *4* (11), 2187−2194.
(24) Demuth, T.; Fuchs, T.; Walther, F.; Pokle, A.; Ahmed, S.; Malaki, M.; Beyer, A.; Janek, J.; Volz, K. Influence of the sintering temperature on LLZO-NCM cathode composites for solid-state batteries studied by transmission electron microscopy. *Matter* **2023**, *6* (7), 2324−2339.
(25) Janek, J.; Zeier, W. G. Challenges in speeding up solid-state battery development. *Nat. Energy* **2023**, *8* (3), 230−240.
(26) Xiao, Y.; Miara, L. J.; Wang, Y.; Ceder, G. Computational Screening of Cathode Coatings for Solid-State Batteries. *Joule* **2019**, *3* (5), 1252−1275.
(27) Lou, S.; Zhang, F.; Fu, C.; Chen, M.; Ma, Y.; Yin, G.; Wang, J. Interface Issues and Challenges in All-Solid-State Batteries: Lithium, Sodium, and Beyond. *Adv. Mater.* **2021**, *33* (6), 2000721.
(28) Liang, Y.; Liu, H.; Wang, G.; Wang, C.; Ni, Y.; Nan, C.-W.; Fan, L.-Z. Challenges, interface engineering, and processing strategies toward practical sulfide-based all-solid-state lithium batteries. *InfoMat* **2022**, *4* (5), No. e12292.
(29) Tong Zuo, T.; Rueß, R.; Pan, R.; Walther, F.; Rohnke, M.; Hori, S.; Kanno, R.; Schröder, D.; Janek, J. A mechanistic investigation of the Li10GeP2S12|LiNi1-x-yCoxMnyO2 interface stability in all-solid-state lithium batteries. *Nat. Commun.* **2021**, *12* (1), 6669.
(30) Li, X.; Ren, Z.; Norouzi Banis, M.; Deng, S.; Zhao, Y.; Sun, Q.; Wang, C.; Yang, X.; Li, W.; Liang, J.; Li, X.; Sun, Y.; Adair, K.; Li, R.; Hu, Y.; Sham, T.-K.; Huang, H.; Zhang, L.; Lu, S.; Luo, J.; Sun, X. Unravelling the Chemistry and Microstructure Evolution of a Cathodic Interface in Sulfide-Based All-Solid-State Li-Ion Batteries. *ACS Energy Lett.* **2019**, *4* (10), 2480−2488.
(31) Walther, F.; Randau, S.; Schneider, Y.; Sann, J.; Rohnke, M.; Richter, F. H.; Zeier, W. G.; Janek, J. Influence of Carbon Additives on the Decomposition Pathways in Cathodes of Lithium Thiophosphate-Based All-Solid-State Batteries. *Chem. Mater.* **2020**, *32* (14), 6123−6136.
(32) Auvergniot, J.; Cassel, A.; Ledeuil, J.-B.; Viallet, V.; Seznec, V.; Dedryvère, R. Interface Stability of Argyrodite Li6PS5Cl toward LiCoO2, LiNi1/3Co1/3Mn1/3O2, and LiMn2O4 in Bulk All-Solid-State Batteries. *Chem. Mater.* **2017**, *29* (9), 3883−3890.
(33) Walther, F.; Koerver, R.; Fuchs, T.; Ohno, S.; Sann, J.; Rohnke, M.; Zeier, W. G.; Janek, J. Visualization of the Interfacial Decomposition of Composite Cathodes in Argyrodite-Based All-Solid-State Batteries Using Time-of-Flight Secondary-Ion Mass Spectrometry. *Chem. Mater.* **2019**, *31* (10), 3745−3755.
(34) Visbal, H.; Aihara, Y.; Ito, S.; Watanabe, T.; Park, Y.; Doo, S. The effect of diamond-like carbon coating on LiNi0.8Co0.15Al0.05O2 particles for all solid-state lithium-ion batteries based on Li2S−P2S5 glass-ceramics. *J. Power Sources* **2016**, *314*, 85−92.
(35) Zuo, T.-T.; Walther, F.; Teo, J. H.; Rueß, R.; Wang, Y.; Rohnke, M.; Schröder, D.; Nazar, L. F.; Janek, J. Impact of the Chlorination of Lithium Argyrodites on the Electrolyte/Cathode Interface in Solid-State Batteries. *Angew. Chem., Int. Ed.* **2023**, *62* (7), No. e202213228.
(36) Kobayashi, S.; Watanabe, H.; Kato, T.; Mizuno, F.; Kuwabara, A. Atomic-Scale Observations of Oxygen Release Degradation in Sulfide-Based All-Solid-State Batteries with Layered Oxide Cathodes. *ACS Appl. Mater. Interfaces* **2022**, *14* (34), 39459−39466.
(37) Bartsch, T.; Strauss, F.; Hatsukade, T.; Schiele, A.; Kim, A.-Y.; Hartmann, P.; Janek, J.; Brezesinski, T. Gas Evolution in All-Solid-State Battery Cells. *ACS Energy Lett.* **2018**, *3* (10), 2539−2543.
(38) Strauss, F.; Teo, J. H.; Schiele, A.; Bartsch, T.; Hatsukade, T.; Hartmann, P.; Janek, J.; Brezesinski, T. Gas Evolution in Lithium-Ion Batteries: Solid versus Liquid Electrolyte. *ACS Appl. Mater. Interfaces* **2020**, *12* (18), 20462−20468.
(39) Conforto, G.; Ruess, R.; Schröder, D.; Trevisanello, E.; Fantin, R.; Richter, F. H.; Janek, J. Editors' Choice—Quantification of the Impact of Chemo-Mechanical Degradation on the Performance and Cycling Stability of NCM-Based Cathodes in Solid-State Li-Ion Batteries. *J. Electrochem. Soc.* **2021**, *168* (7), 70546.
(40) Morchhale, A.; Tang, Z.; Yu, C.; Farahati, R.; Kim, J.-H. Coating materials and processes for cathodes in sulfide-based all solid-state batteries. *Curr. Opin. Electrochem.* **2023**, *39*, 101251.
(41) Culver, S. P.; Koerver, R.; Zeier, W. G.; Janek, J. On the Functionality of Coatings for Cathode Active Materials in Thiophosphate-Based All-Solid-State Batteries. *Adv. Energy Mater.* **2019**, *9*, 1900626.
(42) Nakamura, T.; Amezawa, K.; Kulisch, J.; Zeier, W. G.; Janek, J. Guidelines for All-Solid-State Battery Design and Electrode Buffer

https://doi.org/10.1021/acs.chemmater.4c03086
Chem. Mater. 2025, 37, 2192−2203

Layers Based on Chemical Potential Profile Calculation. *ACS Appl. Mater. Interfaces* **2019**, *11* (22), 19968−19976.
(43) Payandeh, S.; Strauss, F.; Mazilkin, A.; Kondrakov, A.; Brezesinski, T. Tailoring the LiNbO3 coating of Ni-rich cathode materials for stable and high-performance all-solid-state batteries. *Nano Res. Energy* **2022**, *1* (3), No. e9120016.
(44) Ma, Y.; Zhang, R.; Tang, Y.; Ma, Y.; Teo, J. H.; Diemant, T.; Goonetilleke, D.; Janek, J.; Bianchini, M.; Kondrakov, A.; Brezesinski, T. Single- to Few-Layer Nanoparticle Cathode Coating for Thiophosphate-Based All-Solid-State Batteries. *ACS Nano* **2022**, *16* (11), 18682−18694.
(45) Zhang, R.; Ma, Y.; Tang, Y.; Goonetilleke, D.; Diemant, T.; Janek, J.; Kondrakov, A.; Brezesinski, T. Conformal Li2HfO3/HfO2 Nanoparticle Coatings on Layered Ni-Rich Oxide Cathodes for Stabilizing Interfaces in All-Solid-State Batteries. *Chem. Mater.* **2023**, *35* (17), 6835−6844.
(46) Shi, B.-X.; Yusim, Y.; Sen, S.; Demuth, T.; Ruess, R.; Volz, K.; Henss, A.; Richter, F. H. Mitigating Contact Loss in Li6PS5Cl-Based Solid-State Batteries Using a Thin Cationic Polymer Coating on NCM. *Adv. Energy Mater.* **2023**, *13* (24), 2300310.
(47) Wang, J.; Zhao, S.; Zhang, A.; Zhuo, H.; Zhang, G.; Han, F.; Zhang, Y.; Tang, L.; Yang, R.; Wang, L.; et al. Halide-Coated Ni-Rich NCM Improves Cycling Stability in Sulfide All-Solid-State Batteries. *ACS Appl. Energy Mater.* **2023**, *6* (7), 3671−3681.
(48) Zuo, T.-T.; Walther, F.; Ahmed, S.; Rueß, R.; Hertle, J.; Mogwitz, B.; Volz, K.; Janek, J. Formation of an Artificial Cathode−Electrolyte Interphase to Suppress Interfacial Degradation of Ni-Rich Cathode Active Material with Sulfide Electrolytes for Solid-State Batteries. *ACS Energy Lett.* **2023**, *8* (3), 1322−1329.
(49) Moryson, Y.; Walther, F.; Sann, J.; Mogwitz, B.; Ahmed, S.; Burkhardt, S.; Chen, L.; Klar, P. J.; Volz, K.; Fearn, S.; Rohnke, M.; Janek, J. Analyzing Nanometer-Thin Cathode Particle Coatings for Lithium-Ion Batteries—The Example of TiO2 on NCM622. *ACS Appl. Energy Mater.* **2021**, *4* (7), 7168−7181.
(50) Teo, J. H.; Strauss, F.; Walther, F.; Ma, Y.; Payandeh, S.; Scherer, T.; Bianchini, M.; Janek, J.; Brezesinski, T. The interplay between (electro)chemical and (chemo)mechanical effects in the cycling performance of thiophosphate-based solid-state batteries. *Mater. Futures* **2022**, *1* (1), 15102.
(51) Hertle, J.; Walther, F.; Lombardo, T.; Kern, C.; Pavlovic, B.; Mogwitz, B.; Wu, X.; Schneider, H.; Rohnke, M.; Janek, J. Benchmarking of Coatings for Cathode Active Materials in Solid-State Batteries Using Surface Analysis and Reference Electrodes. *ACS Appl. Mater. Interfaces* **2024**, *16*, 9400−9413.
(52) Zhang, W.; Weber, D. A.; Weigand, H.; Arlt, T.; Manke, I.; Schröder, D.; Koerver, R.; Leichtweiss, T.; Hartmann, P.; Zeier, W. G.; Janek, J. Interfacial Processes and Influence of Composite Cathode Microstructure Controlling the Performance of All-Solid-State Lithium Batteries. *ACS Appl. Mater. Interfaces* **2017**, *9* (21), 17835−17845.
(53) Lombardo, T. *User-friendly Scripts for Experimental Battery Researachers*. https://github.com/teolombardo/User-friendly-scripts-for-experimental-battery-researchers. (Accessed 04 March 2025).
(54) Aktekin, B.; Sedykh, A. E.; Müller-Buschbaum, K.; Henss, A.; Janek, J. The Formation of Residual Lithium Compounds on Ni-Rich NCM Oxides: Their Impact on the Electrochemical Performance of Sulfide-Based ASSBs. *Adv. Funct. Mater.* **2024**, *34*, 2313252.
(55) Wood, K. N.; Teeter, G. XPS on Li-Battery-Related Compounds: Analysis of Inorganic SEI Phases and a Methodology for Charge Correction. *ACS Appl. Energy Mater.* **2018**, *1* (9), 4493−4504.
(56) Nagao, K.; Hayashi, A.; Deguchi, M.; Tsukasaki, H.; Mori, S.; Tatsumisago, M. Amorphous LiCoO2-Li2SO4 active materials: Potential positive electrodes for bulk-type all-oxide solid-state lithium batteries with high energy density. *J. Power Sources* **2017**, *348*, 1−8.
(57) Nikam, R. D.; Kwak, M.; Lee, J.; Rajput, K. G.; Banerjee, W.; Hwang, H. Near ideal synaptic functionalities in Li ion synaptic transistor using Li3POxSex electrolyte with high ionic conductivity. *Sci. Rep.* **2019**, *9* (1), 18883.
(58) Ahmed, S.; Pokle, A.; Schweidler, S.; Beyer, A.; Bianchini, M.; Walther, F.; Mazilkin, A.; Hartmann, P.; Brezesinski, T.; Janek, J.; Volz, K. The Role of Intragranular Nanopores in Capacity Fade of Nickel-Rich Layered Li(Ni1-x-yCoxMny)O2 Cathode Materials. *ACS Nano* **2019**, *13* (9), 10694−10704.
(59) Hidde, H. B. Low-Energy Ion Scattering. In *Characterization of Materials*; John Wiley & Sons, 2012, pp. 1−23. DOI: .
(60) Koerver, R.; Walther, F.; Aygün, I.; Sann, J.; Dietrich, C.; Zeier, W. G.; Janek, J. Redox-active cathode interphases in solid-state batteries. *J. Mater. Chem. A* **2017**, *5* (43), 22750−22760.
(61) Karger, L.; Nunes, B. N.; Yusim, Y.; Mazilkin, A.; Zhang, R.; Zhao, W.; Henss, A.; Kondrakov, A.; Janek, J.; Brezesinski, T. Protective Nanosheet Coatings for Thiophosphate-Based All-Solid-State Batteries. *Adv. Mater. Interfaces* **2024**, *11* (14), 2301067.
(62) Wang, S.; Tang, M.; Zhang, Q.; Li, B.; Ohno, S.; Walther, F.; Pan, R.; Xu, X.; Xin, C.; Zhang, W.; Li, L.; Shen, Y.; Richter, F. H.; Janek, J.; Nan, C.-W. Lithium Argyrodite as Solid Electrolyte and Cathode Precursor for Solid-State Batteries with Long Cycle Life. *Adv. Energy Mater.* **2021**, *11* (31), 2101370.
(63) Schwietert, T. K.; Arszelewska, V. A.; Wang, C.; Yu, C.; Vasileiadis, A.; Klerk, N. J. J.; Hageman, J.; Hupfer, T.; Kerkamm, I.; Xu, Y.; et al. Clarifying the relationship between redox activity and electrochemical stability in solid electrolytes. *Nat. Mater.* **2020**, *19* (4), 428−435.
(64) Pokle, A.; Ahmed, S.; Schweidler, S.; Bianchini, M.; Brezesinski, T.; Beyer, A.; Janek, J.; Volz, K. In Situ Monitoring of Thermally Induced Effects in Nickel-Rich Layered Oxide Cathode Materials at the Atomic Level. *ACS Appl. Mater. Interfaces* **2020**, *12* (51), 57047−57054.

https://doi.org/10.1021/acs.chemmater.4c03086
Chem. Mater. 2025, 37, 2192−2203

7.2. Publication V: *Toward efficient benchmarking and development of novel CAM coatings for solid-state batteries*

While the benchmarking approach developed by Hertle *et al.*[173] was successfully applied in Publication IV, it also presents a few drawbacks, making it less attractive for broader adoption. A central disadvantage is the reliance on ToF-SIMS analysis to obtain meaningful results. While this sensitive surface analysis technique is powerful, it is not available in every research group.

This manuscript introduces a more practical benchmarking approach, suitable for both academic and industrial research on protective CAM coatings. It combines an XPS-based pre-characterization with a one-week electrochemical testing program. The study demonstrates that distinct differences between coatings can already be detected using this short-term testing. In doing so, it specifically addresses degradation at high SoC, *i.e.*, aging of the CAM|SE interface, while minimizing the influence of other degradation sources. Thereby, this work highlights pitfalls in electrochemical impedance spectroscopy (EIS) analysis of CAM coatings.Furthermore, it critically discusses the limitations of long-term cycling tests and other extended testing challenges which investigating novel CAM coatings.

Overall, the study provides an efficient and practical benchmarking framework, presenting a clear advancement over the previously reported approach by Hertle *et al.*[173]. While the SIMS-based framework of the latter remains valuable for understanding coating mechanisms and detailed comparisons, the approach presented here allows exploration of a broader parameter space in a reasonable timeframe and addresses wider challenges in achieving reliable benchmarking.

The study was designed by M. Kissel under the supervision of J. Janek. The experiments were planned and coordinated, and all data were evaluated by M. Kissel. F. Schnaubelt, S. L. Benz, and H. Schneider contributed to the discussion of electrochemical and XPS data. J. Kessler-Kühn and A. Lai assisted with cell building. P. Minnmann provided the long-term cycling data. The manuscript was written by M. Kissel and edited by all co-authors.

Reproduced from: Maximilian Kissel, Felix Schnaubelt, Jill Kessler-Kühn, Sebastian L. Benz, Anton Lai, Philip Minnmann, Holger Schneider, Jürgen Janek. Toward Efficient Benchmarking of new CAM Coatings. *J. Electrochem. Soc.*, 2026, 173, 070501, DOI:10.1149/1945-7111/ae55d2, licensed under CC BY 4.0.

Journal of The Electrochemical Society, 2026 **173** 070501

Toward Efficient Development and Reliable Benchmarking of Novel CAM Coatings for Solid State Batteries

Maximilian Kissel,[1,2,z] Felix Schnaubelt,[1,2] Jill Kessler-Kühn,[1,2] Sebastian L. Benz,[1,2] Anton Lai,[1,2] Philip Minnmann,[3] Holger Schneider,[4] and Jürgen Janek[1,2,z]

[1]*Institute of Physical Chemistry, Justus Liebig University Giessen, 35392 Giessen, Germany*
[2]*Center for Materials Research (ZfM/LaMa), Justus Liebig University Giessen, 35392 Giessen, Germany*
[3]*HTE GmbH, 69123 Heidelberg, Germany*
[4]*BASF SE, 67056 Ludwigshafen, Germany*

Electro-chemo-mechanical degradation phenomena at the CAM|solid electrolyte interface lead to both impedance growth and capacity fading in solid state batteries (SSBs). Driven by this, protective coatings on cathode active materials (CAMs) have emerged as a key strategy to mitigate interfacial degradation in SSB composite cathodes. Currently, the development of novel protective CAM coatings is hindered by poor comparability and benchmarking issues, due to non-standardized testing protocols. Moreover, even within a single laboratory, coating optimization remains challenging, as performance strongly depends on processing parameters that cannot be efficiently explored through long-term cycling alone. Here, we present a systematic benchmarking approach to isolate and quantify the coating effect on interfacial stability. Our two-step workflow combines X-ray photoelectron spectroscopy (XPS) for pre-characterization of coating coverage and thickness with a standardized, time-efficient electrochemical testing protocol that delivers quantitative results within one week. We demonstrate that even short-term benchmarking can reveal significant performance differences across coatings and process routes. In addition, we critically discuss challenges associated with long-term testing and impedance analysis, as well as general considerations regarding interlaboratory benchmarking and the comparability of CAM coatings. Overall, the proposed approach provides a framework to guide coating optimization and accelerate the development of stable, high-performance SSBs.
 [DOI: 10.1149/1945-7111/ae55d2]

Manuscript submitted January 22, 2026; revised manuscript received March 5, 2026. Published March 31, 2026.

Supplementary material for this article is available online

Solid state batteries (SSBs), employing solid electrolytes (SEs) instead of liquid ones, have attracted significant attention due to their potentially higher energy densities, improved safety, and longer cycle life, compared to traditional lithium-ion batteries.[1,2] Currently, one of the most promising configurations for SSBs involves the use of high-nickel layered cathode active materials (CAMs) and sulfide SEs. High Ni-CAMs offer high energy densities, while sulfide SEs provide high ionic conductivity at room temperature and favorable mechanical properties. However, their combination in composite cathodes still faces major challenges.[3,4] The primary drawback is interfacial degradation at the CAM|SE interface, caused by chemical and electrochemical incompatibility which leads to increased impedance and capacity fading.[5–7] To address this issue, researchers in academia and industry have explored various strategies, with one of the most promising being the application of protective coatings on the CAM surface.[8] These coatings act as a barrier between the cathode and the SE to mitigate unwanted side reactions, thereby improving overall battery performance. A wide range of coating materials has been investigated, including for instance oxides,[9–11] halides,[12,13] and polymers[14,15]. Numerous studies have demonstrated that coatings can enhance capacity retention, reduce impedance increase as well as degradation products.

Comparing the performance of protective coatings across studies remains challenging, making it difficult to assess the true potential of novel approaches. This can be attributed to several factors. First, the general interlaboratory comparability is notably low, making it difficult to reproduce and validate results obtained in different laboratories.[16] Additionally, no standardized testing program exists for evaluating the performance of protective CAM coatings. This lack of standardization leads to inconsistencies in testing conditions, rendering direct comparisons between studies unreliable and unfair.[17]

Furthermore, as demonstrated in a previous study by our group,[18] a single processing parameter can significantly impact coating performance while many studies remain proof of concepts. This highlights the need to reliably explore a broader range of process parameters already at early levels of development to better assess a coating's potential and avoid drawing premature conclusions.[10,19–21]

Covering more of this process parameter space and accelerating coating development, requires efficient and reliably short-term benchmarking. Hertle et al.[22] proposed a systematic approach combining time-of-flight secondary ion mass spectrometry (ToF-SIMS) and three-electrode tests. While this framework provided valuable insights into the degradation mechanisms and coating performance, it had certain limitations: The electrochemical information obtained was limited to 1.5 cycles, primarily serving as a preparatory step for the ToF-SIMS measurements. Reactive coatings, that form within the initial cycles, may be misinterpreted due to the limited electrochemical data. Also, the results were only meaningful when combined with SIMS data, which requires careful analysis and is not standard equipment in many laboratories.[23]

To overcome these drawbacks and gain more comprehensive information in a straightforward manner, we have developed an alternative benchmarking approach consisting of two stages: X-ray photoelectron spectroscopy (XPS) is used as a pre-characterization method to obtain initial information on coating coverage and thickness, followed by an short-term electrochemical testing protocol designed to provide time-efficient, quantifiable data within approximately one week. Our method enables a straightforward and adaptable framework for academic and industrial researchers to more quickly and reliably identify promising coating approaches and process parameters, as well as those that are not viable. The set of parameters, acquired within approximately one week, can also be used for machine learning or design of experiment studies.[24]

In the following, we will discuss the strategy of our benchmarking approach in detail and present the results obtained from a comparison of six different coatings and an uncoated reference. We demonstrate that our short-term benchmarking delivers a sound set of quantifiable parameters, which allows a reliable ranking. We further discuss pitfalls during impedance analysis and challenges for further tests, which are still needed to evaluate promising coatings in detail.

[z]E-mail: maximilian.kissel@uni-giessen.de; juergen.janek@uni-giessen.de

Journal of The Electrochemical Society, 2026 **173** 070501

Motivation, Workflow and Scope of the Benchmarking Approach

The performance of novel protective CAM coatings for SSBs is typically evaluated based on long-term cycling performance combined with C-rate tests, with specific capacities and respective capacity retention compared to an uncoated reference serving as the figure of merit. This time-consuming approach restricts the investigation of a broader process parameter space although, as demonstrated in a recent study by our group, many coating process parameters influence the resulting coating properties.[18] However, systematic investigations that explore and report a broader parameter space remain scarce.[10,11,25,26] Most published works are rather proof of principle studies comparing a new coating chemistry, processed with certain parameters, to a bare reference, leaving further optimization potential largely unclear. Crucially, coatings or process parameters that fail to improve performance are rarely reported, which limits the knowledge gained for the broader community.

To accelerate the development and enhance the processing understanding of novel protective CAM coatings, a time efficient and reliable benchmarking framework is desired. The workflow of the here proposed approach is depicted in Fig. 1a and will be briefly summarized in the following.

Different CAM coatings processed under various conditions are first characterized with XPS to get information on the coating's composition and coverage. The coated CAM particles are then mixed with solid electrolyte in a mixing machine to ensure comparable interfacial contact. Afterwards, half-cells with the composites are assembled according to a standard operation procedure (SOP), followed by a short-term electrochemical testing program. The electrochemical short-term benchmarking (Fig. 1b) starts with a low C-rate formation cycle to determine the initial Coulomb efficiency (ICE). The second cycle is employed to measure impedance at medium state of charge (SoC) and to quantify the CAM utilization. This microstructural property describes the fraction of CAM particles that are both ionically and electronically connected and thus can be electrochemically active.[27] The degree of CAM utilization depends mainly on the particle size distributions and ratios of the SE and CAM, the weight ratio in the composite, and the composite mixing process.[27–29] If a reproducible mixing process is established, a significantly lower CAM utilization points to a coating, typically electron blocking, that is too thick. Since the focus is on material and particularly CAM|SE interfacial properties, potential variations in the mixing process and microstructures are quantified by calculating active specific capacities.[27] For this calculation, the charge is normalized to the mass of active CAM particles.

With respect to degradation at the CAM|SE interface it needs to be noted that this is both (electro)chemical[30–36] and chemo-mechanical[37–40] in nature. While effective coatings must mitigate both, probing these effects requires different approaches and efforts. Chemo-mechanical degradation becomes evident during extended cycling, whereas (electro)chemical degradation can be detected more quickly and reliably.[36,41] The latter leads to the formation of a resistive cathode–electrolyte interface (CEI), which is particularly pronounced at high SoC—a highly relevant condition, since batteries often remain in the charged state.[42] Thus, the coating's ability to suppress ageing under high SoC is critical.[33,34,36,43] In conventional long-term cycling tests, the actual time cells spend at high SoC often remains unclear. Instead, probing this protection capability can be efficiently done by integrating high-voltage holds as recently shown by Truong et al.[36] That is why the proposed the short-term benchmarking deliberately includes a "short-term aging" step after the fourth charge (Fig. 1b) to trigger (electro)chemical reactions at the CAM|SE interface,[32] while simultaneously monitoring impedance. In the following discharge,

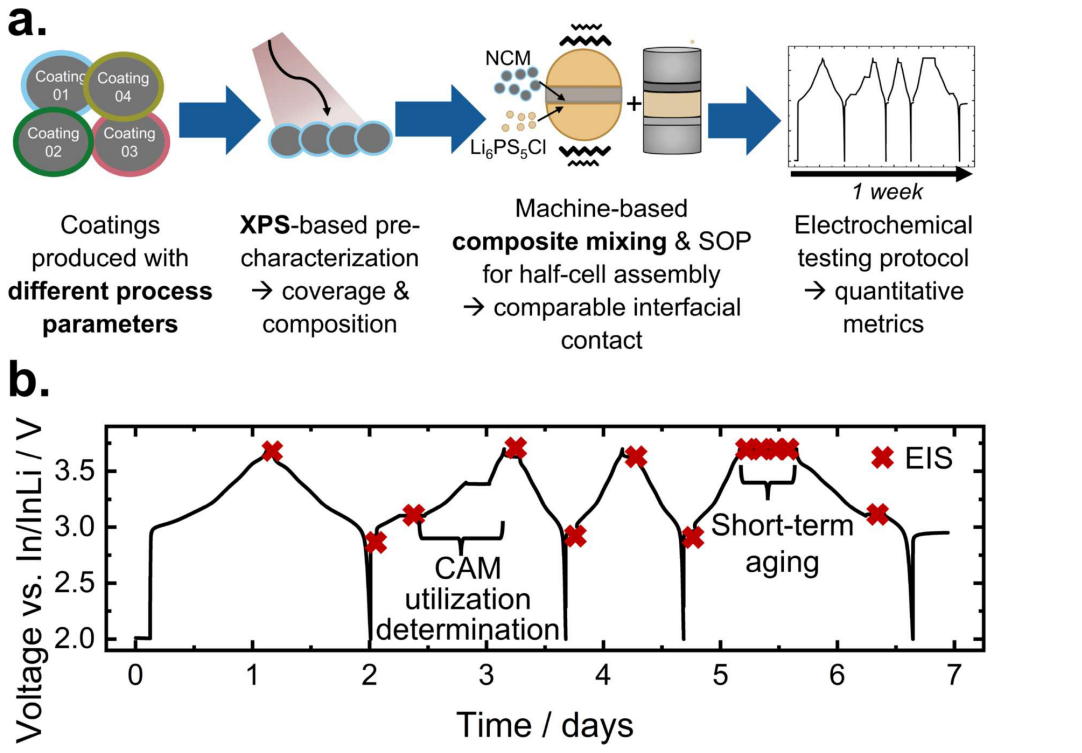

Figure 1. Efficient benchmarking of novel CAM coatings. (a) Workflow with the central elements of this benchmarking approach. (b) Representative voltage profile over time during the electrochemical benchmarking protocol. Important impedance measurement points are indicated with an asterisk.

Journal of The Electrochemical Society, 2026 **173** 070501

impedance is again measured at medium SoC for comparison with the beginning of the protocol.

The goal of the overall workflow is to reliably and efficiently narrow the coating process parameter space, thereby accelerating coating development. It is not intended to replace long-term cycling or complementary tests, but rather to make these tests more efficient.

Experimental

Materials and solid-state cell assembly.—All materials were stored and handled in an argon-filled glovebox, with oxygen residues of $p(O_2)/p < 1.0$ ppm and water residues of $p(H_2O)/p < 1.0$ ppm. The cathode active material ($LiNi_{0.85}Co_{0.10}Mn_{0.05}O_2$, NCM85) was provided by BASF SE and dried under vacuum at 200 °C for 12 h prior to further testing. Seven samples based on the same CAM were tested, whereby *Uncoated-Ref* denotes the uncoated base CAM. Among the six coated CAMs denoted as *Coating*-01 to *Coating*-06, *Coating*-02 represents the artificial CEI coating previously reported by our group.[18,44] It corresponds to Li_3PS_4 (NEI Corporation, Somerset, NJ, USA) coated NCM85 which was annealed at 400 °C as described in our previous publication.[18] All other coated CAMs were provided by BASF SE and used without further treatment.

The composites were machine-made in a mini vibrating mill (Pulverisette 23 from Fritsch GmbH, Idar-Oberstein, Germany) using 6 ZrO_2 balls with 5 mm diameter at 15 Hz for 30 min. Commercially available Li_6PS_5Cl (NEI Corporation, Somerset, NJ, USA) was used as catholyte without further modification. The composite had a mass ratio of 80:20 wt% (CAM:SE) and a total mass of 200 mg. No carbon additive is used, excluding its effect on SE degradation, to put the focus on the CAM|SE interface.[22,45]

For the electrochemical half-cells, an in-house made cell casing[46] was used and the assembly followed a standardized protocol:[27] First, 80 mg of Li_6PS_5Cl (NEI Corporation, Somerset, NJ, USA) were filled in the mold and pressed by hand. 12 mg of the prepared cathode composite were evenly distributed on top of the separator and pressed by hand (corresponding to a total loading of $\sim$15.3 $mg_{composite}\,cm^{-2}$, with 12.2 $mg_{CAM}\,cm^{-2}$). As anode, an indium foil (Alfa Aesar, 99.99%, 9 mm diameter, 100 μm thickness) and a lithium foil (China Energy Lithium, 6 mm diameter, 100 μm thickness) were used. The whole cell was pressed uniaxially at 375 MPa for 3 min.

XPS.—XPS analysis was performed using a PHI Versa Probe IV system (Physical Electronics Inc., Chanhassen, MN, USA). The powders were filled into Teflon crucibles with an inner diameter of 3 mm, pressed to achieve a flat surface and attached to the sample holder using nonconductive adhesive tape. All samples were transferred from the glovebox to the XPS machine in an air-tight transfer vessel. Monochromatic Al-K_α radiation (1486.6 eV) was applied for XPS analysis. The X-ray source was operated at a power of 50 W and a voltage of 15 kV having a beam diameter of 200 μm. A pass energy of 55 eV, a step size of 0.2 eV, a step time of 20 ms and 20 sweeps were used. The samples were charge-neutralized during measurements. The XPS data were evaluated using CasaXPS (Casa Software Ltd, Teignmouth, UK). The spectra were calibrated in relation to the signal of adventitious carbon C 1 s at 284.8 eV. For each detail spectrum, a region and the respective intensities were used to calculate the coverage values γ.

Electrochemical short-term testing.—The electrochemical measurements (cf Fig. 1b) were performed at 25 °C with a VMP-300 potentiostat (Bio-Logic, Seyssinet-Pariset, France). The stack pressure of $\sim$80 MPa was applied via a steel frame. The currents for the galvanostatic cycling between 2.0 and 3.7 V vs In/InLi were calculated based on a CAM-specific capacity of 190 mAh g^{-1}. The impedance was measured with an amplitude of 10 mV from 3 MHz down to 100 mHz. The fitting was done using a serial connection of one resistor, two (R)(Q) elements, and one constant phase element, i.e., *R*-(*R*)(*Q*)-(*R*)(*Q*)-*Q*, as simplified equivalent circuit. The high frequency part ($>10^5$ Hz) is represented by a single resistor associated with the SE separator. The two semicircles at mid-frequency ($\sim10^5-10^1$ Hz) and low-frequency ($\sim10^1-10^{-1}$ Hz) are attributed to cathode and anode contributions similar to previous studies.[30,31,41] The impedance spectra were fitted using the RelaxIS 3 software package (rhd Instruments, Darmstadt, Germany). Each impedance spectrum was tested for stationarity using the Kramers-Kroning test.

After a resting period of 3 h, the cells underwent a formation cycle at 0.05 C. In the second cycle, the CAM utilization was determined via coulometric titration comparison:[47] Each SSB cell was charged with 0.05 C to 3.1 V vs In/InLi, held at that potential until the current dropped below 0.005 C or until reaching 3 h, followed by 3 h of relaxation to determine the potential V_1. An impedance spectrum ("start") was recorded. Then, the cell was charged with 0.05 C up to 3.4 V, followed by 4 h of relaxation to get the potential V_2. As a quasi-OCP (titration) curve of the CAM, the third charge of a liquid electrolyte cell at 0.02 C was taken as a reference (Fig. S1). The liquid cell data was used to assign a reference specific capacity value q_{actual} to the potential range determined by V_1 and V_2. This value was compared with the measured absolute charge $Q_{measured}$ of the solid-state cell, which can be extracted with the analysis software. The actual electrochemically active mass, $m_{CAM,act}$ was then calculated with Eq. 1:

$$m_{CAM,act} = \frac{Q_{measured}}{q_{actual}} \quad [1]$$

The cells were charged to the upper cutoff, followed by a full third cycle at 0.1 C. In the fourth cycle, the cells were charged at 0.1 C to 3.7 V vs In/InLi and this potential was held until the current dropped below 0.01 C or until reaching 3 h. Then, impedance spectra were continuously measured for 10 h while fixing the cells at 3.7 V vs In/InLi. After reaching 3.1 V vs In/InLi in the following discharge, the cells relaxed for 3 h before the last impedance spectrum ("end") was measured.

In an additional experiment, to monitor the evolution of the charge transfer resistance (cf Figs. 5a, 5c and S5), which is contributing to the total cathode resistance, as function of the SoC, a current of 50 μA ($\sim$64 μA cm^{-2}) was applied for 4 h, followed by a relaxation period of 4 h. Then, impedance was measured and these three steps were repeated for charge and discharge.

Long-term cycling.—All components in direct contact with the chemicals were dried at least 12 h under vacuum with 120 °C, all other components were dried at least 24 h at 60 °C. The C65 was dried under dynamic vacuum at 300 °C for 24 h using a Büchi vacuum drying furnace. All process steps were carried out in a glovebox under inert gas atmosphere.

Cathode composites were thoroughly hand ground for 15 min with an NCM:SE:C weight ratio of 65:30:5. Li6PS5Cl (NEI Corporation, Somerset, NJ, USA) and C65 (Timcal Deutschland GmbH, Düsseldorf, Germany) served as SE and carbon additive respectively. Cells were assembled in ASC-A+ cell casings (Sphere Energy, Paris, France) with a diameter of 8 mm made out of PEEK. First, 42 mg of LPSCl were inserted and compressed at 100 MPa for 30 s. Afterwards, 12 mg of composite cathode was inserted, distributed carefully and compressed with the SE separator under 370 MPa for 3 min. Finally, an indium disc (7 mm, 100 μm thickness, 24 mg) and a freshly rolled lithium disc (4 mm, 100 μm, 0.9 mg) were added. An 8 mm stainless steel disc was inserted and the cell was sealed using nylon ferrules (swagelock) and fastening 6 screws with 2 Nm each, resulting in an applied stack pressure of ca. 80 MPa.

Cell cycling was performed at 45 °C in a Binder KB115 climate chamber using an Arbin LBT battery cycler. Before the first charging step, cells were rested for 6 h to allow for (In/InLi)x alloy formation and temperature equilibration. The currents for the galvanostatic cycling between 2.0 and 3.68 V vs In/InLi were calculated based on

Journal of The Electrochemical Society, 2026 **173** 070501

a CAM-specific capacity of 190 mAh g^{-1}. Between charging and discharging in constant current mode the cells rested for 15 min.

Results

XPS-based pre-characterization of coating morphology and composition.—Novel coatings are typically first analyzed with respect to their morphology and composition to assess whether the deposition process was successful. In a previous work, we have already discussed the challenges of characterizing nanometer-thin protective CAM coatings.[48] Common methods include energy-dispersive X-ray spectroscopy (EDS), combined with electron microscopy techniques, such as scanning electron microscopy (SEM) and transmission electron microscopy (TEM). While TEM, for instance, provides valuable morphological information such as coating thickness, it offers poor statistics and often suffers from demanding and time-consuming sample preparation which limits the exploration of a broader coating process parameter space.

In our proposed approach, XPS is employed as a pre-characterization technique for quality control. This method delivers statistical information by simultaneously probing signals from more than 1000 particles (Figs. 2a and S2). Furthermore, sample preparation is comparatively easy, the measurement can be automated, and multiple samples can be analyzed in one session. From the XPS measurements, the coverage γ can be calculated (Eq. 2), serving as a parameter to semi-quantitatively compare different coatings and processing conditions:

$$\gamma = \frac{I_{\text{coating}}}{I_{\text{coating}} + I_{\text{CAM}}} \quad [2]$$

Coverage values range from 0 to 1: A γ value of 1 (or close to 1 above a certain threshold value) indicates that no signals from the underlying CAM are detected, meaning that the particles are conformally covered by a coating layer of at least 5–10 nm thickness, which roughly corresponds to the XPS information depth. It should be noted that coatings of different thicknesses above 10 nm cannot be distinguished by XPS; all yield a coverage of 1. Moreover, γ does not provide information on coating thickness uniformity. Coverage values below 1 indicate that either the coating is thinner than 10 nm, or it is a non-conformal layer (Fig. 2b). A thin but fully covering coating may produce similar γ values as a thicker, but only partially covering coating. Thus, a coverage below 1 does not necessarily indicate a bad coating quality as some coatings are intentionally designed in the single-digit nanometer range.[14,26,49] Especially in this case, coverage values should be interpreted carefully and verified with complementary techniques such as TEM, as demonstrated previously.[18] Additionally, it should be noted that real powder topography, including surface roughness and variations in particle height within the probed area, can influence XPS signal intensities and therefore affect the absolute γ value. While the schematics in Figs. 2a, 2b represent an idealized surface, γ remains useful as a comparative metric across samples measured under

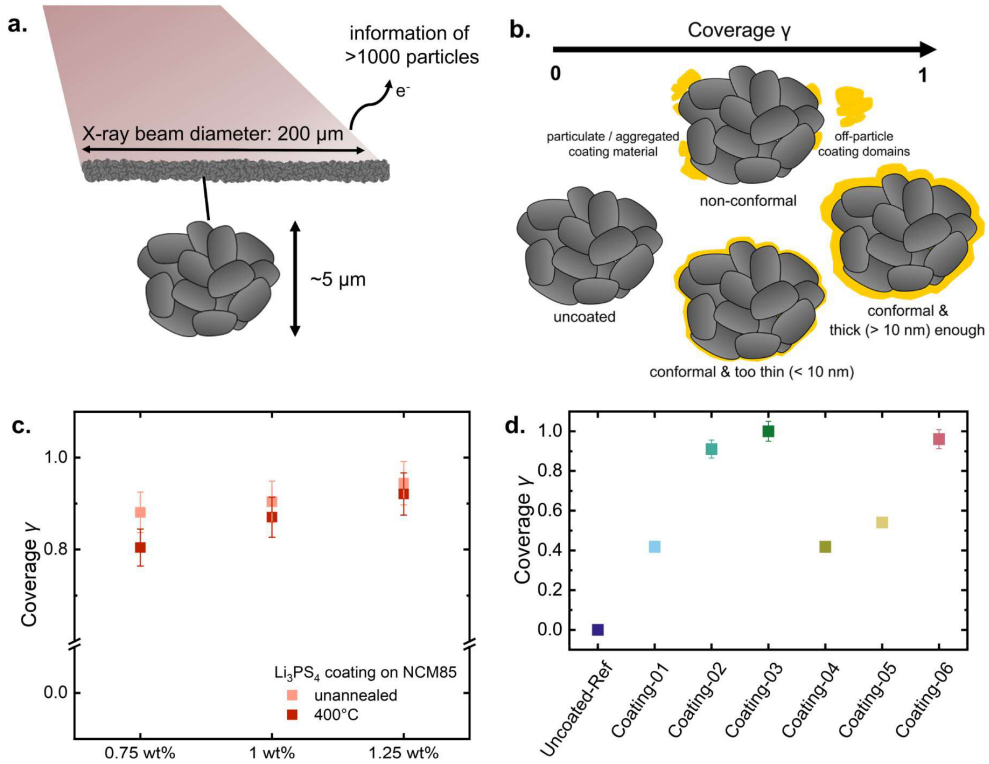

Figure 2. Results from XPS as pre-characterization technique. a) Schematic illustrating the size ratio between incident X-ray beam and investigated particles. (b) Meaning of different coverage values γ for the coating morphology. (c) Proof of concept for Li_3PS_3 coated NCM85, showing that the coverage values reflect the trend in coating amount, respectively thickness. (d) Coverage values determined for the coatings investigated in this study. Error bars represent an estimated uncertainty of 5%.

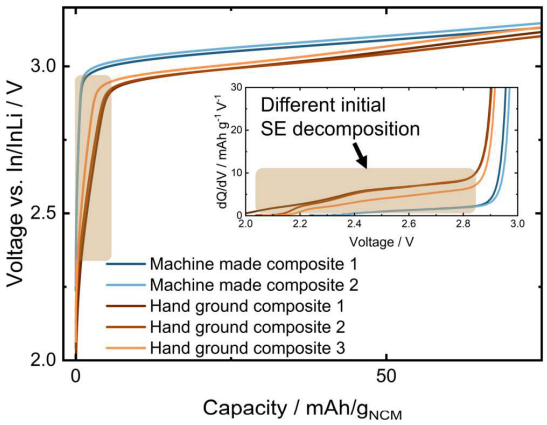

Figure 3. Effect of cathode composite preparation on the initial electrochemical decomposition. While the machine-made composites show comparable and small amounts of initial decomposition charge, the hand ground composites are less reproducible and lead to more electrochemical decomposition.

identical conditions. For many coating chemistries, the XPS information depth of 5–10 nm should be sufficient[12,13,26,50] to assess whether the deposition process was successful. Effects such as aggregated or detached coating particles, forming off-particle coating domains, lead to exposure of bare CAM surfaces, which will lead to coverage values below a certain threshold value for γ, indicating inferior morphological coating quality. Accordingly, this XPS approach is reasonable as a pre-characterization within an efficient benchmarking framework.

Figure 2c depicts the calculated coverage values for samples with different wt% of Li_3PS_4 coating on NCM85, which corresponds to the type of *Coating*-02. The expected trend of increasing coverage with higher coating amounts is clearly reproduced. The reduced coverage observed after annealing is also captured and was attributed in our previous work to partial evaporation and aggregation of the coating.[18] The coverage values of the samples investigated in this study further reveal clear differences (Fig. 2d): While *Coating*-02, *Coating*-03 and *Coating*-06 show a coverage close to 1, the other coatings exhibit lower coverages in the range of 0.4–0.5.

Importance of the composite mixing process.—The performance of coatings can only be reliably compared if a standard operation procedure for the SSB cell assembly is established. This includes the fabrication pressures[16] as well as the preparation of the composites.[27] As shown in a previous study, different mixing procedures can lead to significant performance variations for nominally identical cells.[27] This aspect is particularly critical when investigating interfacial degradation phenomena. As depicted in the differential capacity plots of the first charge for cells employing *Uncoated-Ref* as CAM with the same SE (Fig. 3), the initial SE decomposition charge[15,51] also referred to as "shoulder capacity"[52] and attributed to electrochemical SE oxidation below 3 V vs In/InLi, varies systematically depending on the mixing method. Machine-prepared composites exhibit lower and more reproducible decomposition charges, whereas hand-ground composites show higher and less reproducible values. These findings demonstrate that composite preparation affects the resulting electrode microstructure and interfacial characteristics. Therefore, meaningful comparison of different coating materials requires identical and reproducible mixing conditions. In this study, all composites were prepared using a mini vibrating mill to ensure consistency.

Metrics from electrochemical short-term benchmarking.—Valuable metrics can be extracted already from the first cycles. In the initial formation cycle (Fig. S3a), *Uncoated-Ref* achieves the second highest charge capacity (228 mAh g^{-1}), but only the second lowest discharge capacity of 189.8 mAh g^{-1}. Apart from *Coating*-04, all coatings achieve higher initial discharge capacities with *Coating*-03 and *Coating*-06 reaching up to 206 mAh g^{-1}.

As already discussed, it is essential to account for the static CAM utilization, which describes the fraction of active CAM particles, when comparing capacities. In the tested composites, CAM utilizations above 95% are achieved (Fig. S3b), indicating a reproducible and successful mixing process. If such a reproducible mixing process is established, a significantly lower CAM utilization points to a coating, typically electron blocking, that is too thick.

The active specific discharge capacities of the first three cycles (Fig. 4a) already reveal differences between the coatings. *Coating*-01, −02, −03 and −06 deliver higher discharge capacities than *Uncoated-Ref*. Thereby, the differences between the best three coatings are negligible providing about 205 mAh g^{-1} at 0.05 C and 195 mAh g^{-1} at 0.1 C. The capacity of *Coating*-01 drops by 36% from 202 mAh g^{-1} in the first discharge to 181 mAh g^{-1} in the second discharge, indicating worse kinetics, for instance due to increased degradation, compared to the top performers. Notably, *Coating*-04 and *Coating*-05 deliver lower capacities than the reference.

A similar trend is visible in the initial Coulomb efficiency (ICE) depicted in Fig. 4b. Here, all coatings achieve higher values than the bare NCM, partially exceeding 90%. The ICE contains not only information on the initial decomposition charge and contact loss but also on the NCM relithiation kinetics.[52–55] Kaeli et al.[52] have shown that the first cycle capacity loss in SSBs contains contributions from reversible and irreversible SE oxidation, as well as sluggish NCM redox kinetics. The latter one has already been well known for liquid electrolyte systems.[53,54] The effect of electrochemical oxidation of the SE is mainly visible as charge below 3 V vs In/InLi, most notably in the first cycle.[15,51] However, in the differential capacity plot of the first charge (Fig. S4a), only minor differences are visible among the coatings. It should be noted that at higher potentials, further SE oxidation can occur, and the different coatings may provide varying degrees of protection against this process. Differences in ICE should also be attributable to different relithiation kinetics. This hypothesis is supported by the differential capacity plots of the first discharge seen in Fig. 4c. The kinetic hindrance peak (KH)[53] is most pronounced for *Coating*-03, which also reaches the highest ICE of 92.7%. This feature is also visible for *Coating*-02 and −06 but absent for all other samples. In theory, additional discharge capacity can be harvested by applying and holding a low cut-off voltage[52] to mitigate losses from the reversible SE oxidation and sluggish NCM redox kinetics. However, these cycling conditions are not feasible in practice, and the corresponding losses cannot be circumvented.

The ranking of the coatings based on the differential capacity plots changes over cycles. While the overpotential during the first charge of *Coating*-04 and *Coating*-05 is similarly higher than for the bare reference (Fig. S4b), *Coating*-05 gets worse during cycling as seen in the dQ/dV plot of the fourth cycle (Fig. 4d) indicating that more degradation has happened. While *Coating*-01 shows an overpotential comparable to that of the top three performing coatings in the first cycle, it is significantly worse in the fourth charge. The overpotentials of the best three coatings (*Coating*-02, −03 and −06) are similar during the first four cycles.

Pitfalls during impedance analysis.—Before discussing impedance data for the different coatings, some important general considerations need to be addressed. Electrochemical impedance spectroscopy (EIS) is a powerful technique to decouple and identify resistance contributions and their evolution over time.[56] It has been successfully applied to show that coatings can mitigate the cathode resistance increase compared to uncoated references.[13,44,49] EIS of cells with a coated and uncoated CAM is usually measured after charge/discharge.[31,57]

The top part of Fig. 5a illustrates problems with this approach, when extracting impedance contributions Z_i. The shape of the

Journal of The Electrochemical Society, 2026 **173** 070501

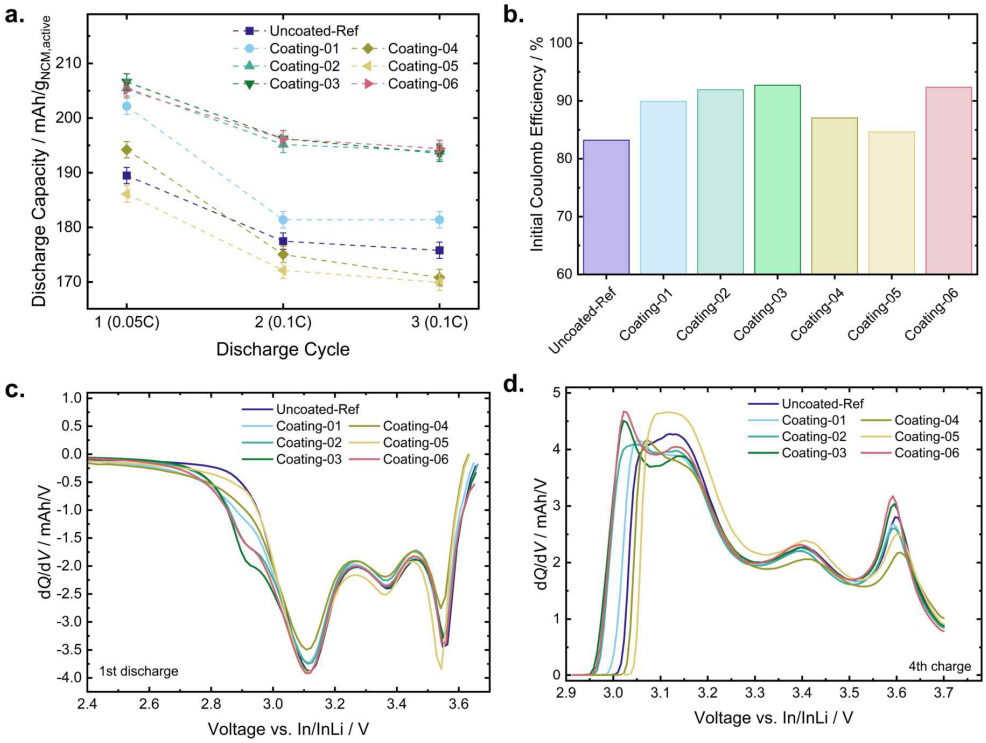

Figure 4. Electrochemical metrics from short-term benchmarking. (a) Specific discharge capacities, normalized by the active mass, for the first three cycles, (b) Initial Coulomb efficiency, (c) differential capacity profiles of the first discharge, (d) differential capacity profiles during the fourth galvanostatic charge.

Nyquist plots varies with SoC, leading to an overlap of time constants of different processes. At high and low SoC, these overlaps prevent clear distinction, and fitting the corresponding spectra becomes more error-prone, if possible at all. This limitation is less critical when simply comparing coated and uncoated samples, as their impedances usually differ strongly ($Z_{bare} \gg Z_{coated}$). Yet, when comparing different effective coatings, a more precise and quantitative impedance analysis is required.

For the fitting of the impedance spectra, an equivalent circuit of the form $R_{separator}$-($R_{cathode}$)(Q)-(R_{anode})(Q)-Q was applied in this work. It must be noted that the cathode-associated resistance $R_{cathode}$ consists of multiple contributions, as expressed in Eq. 3:

$$R_{cathode} = R_{CT} + R_{constriction} + R_{CEI} + R_{rocksalt} \quad [3]$$

The SoC dependence of the charge transfer (CT) resistance R_{ct} is well-known and follows a U-shaped curve as function of SoC.[58–61] R_{ct} can be regarded as an intrinsic property of intercalation CAMs, determined by the lithium concentration in the material.[59] As shown for *Uncoated-Ref* in Figs. 5a and S5, $R_{cathode}$ exhibits the expected U-shaped behavior.

It is important to note that for the tested samples, the OCV relaxes during 3 h after charging to 3.7 V (Fig. S6), leading to different SoCs at which the impedance is measured. The maximum deviation is $\Delta U_{max} =$ 46 mV (Fig. 5b). This seemingly small voltage difference corresponds however to a resistance difference of ~24 Ω·cm^2 in the first and ~57 Ω·cm^2 in the second cycle (Fig. 5c). Since $R_{cathode}$ behaves similarly during charge and discharge after the first cycle (Fig. S5), we attribute this resistance evolution primarily to R_{ct}. This means that, when measuring EIS after charge, an error of 30%–40% can arise solely from variations in SoC. Therefore, conducting EIS at the same SoC is imperative for a quantitative comparison of different coatings.

During the benchmarking program, the impedance evolution is tracked at different SoCs. Exemplary Nyquist plots for *Uncoated-Ref* are depicted in Fig. 6a: the upper panel displays spectra at medium SoC (3.1 V vs In/InLi), the lower panel spectra at high SoC, *i.e.*, after charge and during the 10 h potential hold at 3.7 V vs In/InLi. As expected, the semicircle in the mid-frequency range (~10^5–10^1 Hz), attributed to $R_{cathode}$, evolves over time and is SoC dependent.

Comparing $R_{cathode}$ at 3.1 V vs In/InLi (Fig. S7), differences among all samples emerge (Fig. 6b). For *Uncoated-Ref*, $R_{cathode}$ increases by 68% from 22 to 37 Ω·cm^2. A significant improvement is achieved with *Coating*-02, −03 and −06 which show lower absolute (<8 Ω·cm^2) and relative (<33%) impedance increase, indicating better protection against interfacial degradation. In contrast, the other coatings cannot be considered as promising in this regard: While *Coating*-01 shows a lower relative resistance increase (55%) compared to *Uncoated-Ref*, it starts from a higher absolute resistance. The same applies to *Coating*-04 and *Coating*-05, both even exceeding a final resistance of 50 Ω·cm^2.

Significant (electro)chemical degradation occurs at high SoC,[32] making the holding step at high potential (3.7 V vs In/InLi) particularly relevant. The impedance spectra for all samples are displayed in Fig. S8. Consistent with previous works by Zuo et al.[30] and Witt et al.,[31] $R_{cathode}$ increases linearly with the square root of time during the 3.7 V hold (Fig. 6c), indicating a diffusion-controlled process. The slope of this increase corresponds to the rate constant, which varies significantly among the coatings (Table S1). A similar ranking to that in Fig. 5b emerges: *Coating*-04 and −05 perform worst with slopes of up to 40 Ω·cm^2·h$^{-0.5}$, whereas *Coating*-03 and −06 perform best with only about 3 Ω·cm^2·h$^{-0.5}$, compared to ~15 Ω·cm^2·h$^{-0.5}$ for *Uncoated-Ref*.

In the previous works,[30,31] this impedance increase was assigned purely to CEI growth. However, Fig. 6d challenges this interpretation: Here, the resistance increase during the 3.7 V hold (Fig. 6c),

Journal of The Electrochemical Society, 2026 **173** 070501

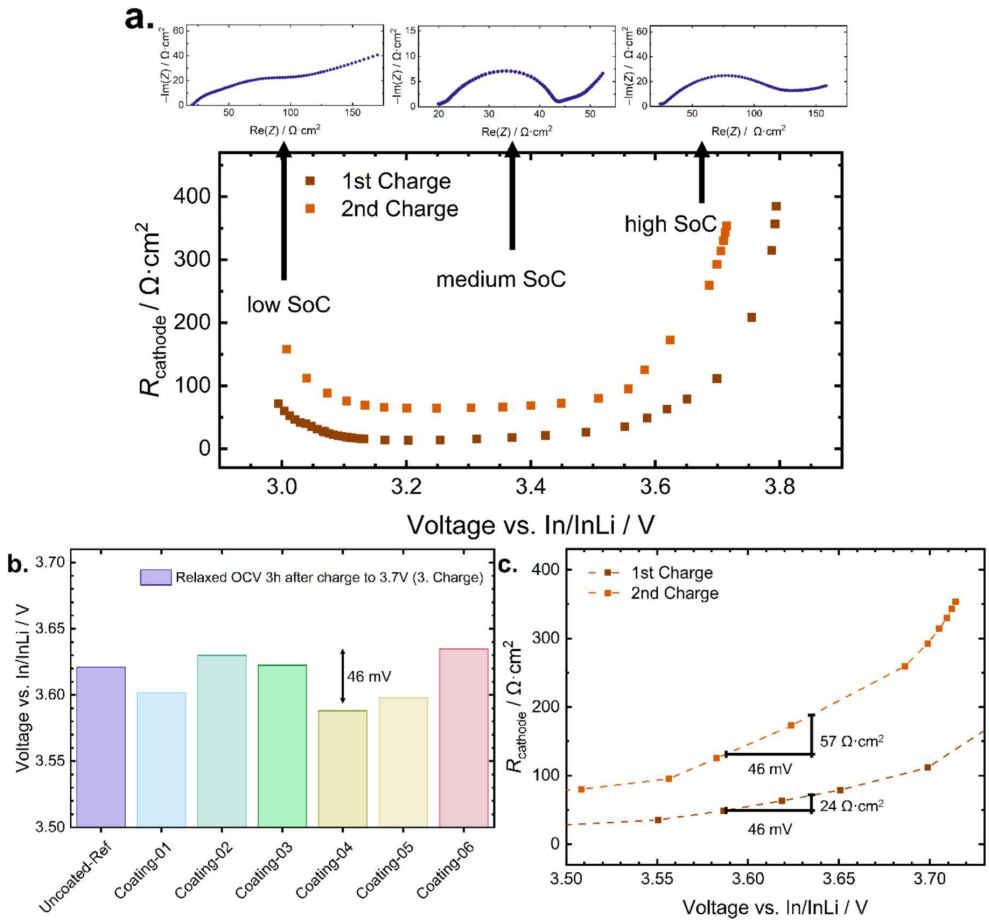

Figure 5. Influence of SoC on impedance measurements. (a) $R_{cathode}$ as function of cell voltage showing the characteristic U-shaped curve and representative Nyquist plots at low, medium and high SoC. (b) Relaxed OCV values during 3 h after galvanostatic charge to 3.7 V vs In/InLi, revealing deviations of up to 46 mV. (c) Corresponding differences in $R_{cathode}$ for Uncoated-Ref, reaching up to 57 Ω cm^2 solely due to differences in SoCs.

$\Delta R_{cathode}$ (@3.7 V), is compared with the increase in cathode resistance measured at 3.1 V, $\Delta R_{cathode}$ (@3.1 V), at the beginning and end of the benchmarking program (Fig. 6b). The data clearly show that $\Delta R_{cathode}$ (@3.7 V) > $\Delta R_{cathode}$ (@3.1 V), thus the CEI growth appears to be significantly overestimated based on the high voltage hold data. Three hypotheses may explain this observation:

1. Redox-active CEI: The CEI formed during the high voltage hold, is partially redox active[62–64] and reduced upon lowering to 3.1 V. However, this conflicts with known reduction potentials, which lie well below 3 V vs In/InLi.[52,65,66]
2. Contact loss: Volume shrinkage of NCM during hold at 3.7 V vs In/InLi[67] could cause contact loss, which leads to an increasing constriction contribution[68] to the resistance.
3. Continuous SoC change: Li-ion extraction from the NCM may continue during the holding step, gradually shifting the SoC. Given the steep U-shaped R_{ct} dependence in this region, even small SoC changes could yield noticeable impedance increases. Supporting this hypothesis, a small but measurable current (15–1.5 μA) is detected during EIS measurement (Fig. S9), although this current could also stem from continuous electrochemical SE oxidation.

Although CEI growth may be overestimated during the high-voltage hold, the measurements reveal clear differences between the coatings, reflecting their protection capability against interfacial degradation and enabling a ranking. Regardless of the exact mechanism, which might also overlap, it remains essential for reliable benchmarking and comparison of CAM coatings, that EIS measurements are always conducted at the same SoC across all samples.

Discussion

Limitations, extensions and future benchmarking challenges.— Based on the presented time efficient short-term benchmarking, the most promising coatings can be identified reliably within one week. In this study, these are *Coating*-02, −03 and −06. *Coating*-02 corresponds to the artificial CEI coating,[44] for which further process optimization can lead to further performance improvement.[18] While this approach should therefore be considered promising, it requires further work before extended testing. The two most promising coatings, *Coating*-02 and −06, show comparable performance and warrant further investigation. Within the proposed benchmarking framework, no clear ranking between these two samples is possible.

Journal of The Electrochemical Society, 2026 **173** 070501

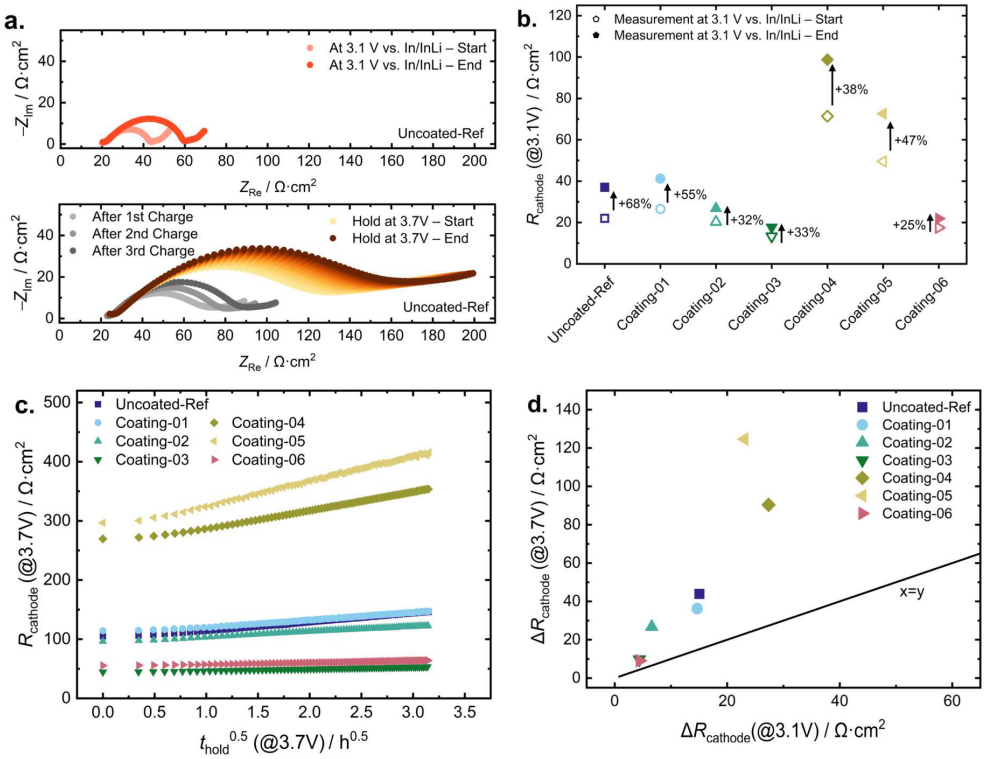

Figure 6. Results from impedance analysis at different SoCs. (a) Representative Nyquist plots for Uncoated-Ref at medium (top) and high (bottom) SoC. (b) Comparison of $R_{cathode}$ measured at 3.1 V vs In/InLi at the start (2nd cycle) and end (4th cycle) of the benchmarking program. (c) Evolution of $R_{cathode}$ during the hold at 3.7 V vs In/InLi as function of $t^{0.5}$. (d) Resistance increase during the hold at 3.7 V vs In/InLi plotted vs the resistance increase measured at 3.1 V vs In/InLi.

Limited insight into coating kinetics and no information on chemo-mechanical degradation over the long term is provided. To reliably rank the best coatings and to better understand their working principle, complementary tests would be needed, including long-term cycling, C-rate tests, and *post-mortem*. In the following, the associated challenges with respect to reliability, comparability and reproducibility will be discussed that will go in hand with such tests.

To evaluate the kinetic properties of the coating in detail, C-rate tests should preferably be performed in a three-electrode (3E) setup.[22,69–71] In a two-electrode (2E) setup, the measured cell kinetics can be limited by anode kinetics at higher rates.[71–74] For the tested cells with *Uncoated-Ref*, *Coating*−03 and *Coating*−06 (Figs. S10) 1 C corresponds to ∼2.3 mA cm^{-2}, which can already induce a non-negligible, unknown anode overpotential that cannot be resolved with 2E. If this overpotential is not reliably reproducible, C-rate results become prone to misinterpretation, especially if the differences between coated samples are small. Even when the cathode kinetic performance is isolated via the 3E setup, the microstructure, defined by the composition of composite, the mixing process as well as the areal loading strongly affect the rate performance,[27,75,76] in addition to the coating and interfacial degradation. In our previous work, we showed that capacity variability increases with C-rate, even for identical materials.[27] Thus, the coating is not necessarily the decisive factor for apparent differences in kinetic performance. Accordingly, the results of promising coatings should be carefully evaluated, preferably based on measurements performed in at least duplicates from independent composite batches, to reduce variance and avoid erroneous conclusions.

Data from multiple cells is also required for a reliable assessment of long-term cycling performance. Long-term cycling tests provide valuable insights into chemo-mechanical degradation, such as contact loss and particle cracking.[15] However, to be meaningful, this approach requires detailed data analysis that goes beyond simple comparison of capacity values, as demonstrated by Conforto et al.[37] It is important to note that the capacity retention is a property which depends on many factors beyond the coating itself. In electrochemical testing, the performance of the entire cell is probed and not just that of the coating. Figure 7a demonstrates that *Coating*-03 and *Coating*-06, identified as most promising by the short-term benchmarking, indeed also deliver sustained improved performance over multiple cycles, providing an initial validation of the pre-screening approach. However, upon extending the cycling to higher cycle numbers (Fig. 7b), cells using *Uncoated-Ref* as CAM, which initially exhibited similar cycling behavior, begin to show increasing divergence in performance. After 500 cycles at 1 C, cell 1 retains only 64% of its initial capacity, while cell 2 reaches 75%. This divergence arises because multiple degradation mechanisms can emerge over time in an uncontrollable way and significantly influence long-term performance. A coating can only enhance the interfacial stability at the CAM|SE interface, potentially mitigating degradation and contact loss, whereas degradation processes at the anode interface[36,71,74] or elsewhere may still dominate long-term stability. Hence, a stable and practical reference electrode is crucial for meaningful long-term evaluation. In general, isolating the effect of the coating and attributing variations in long-term cell performance solely to it remains challenging.

Journal of The Electrochemical Society, 2026 **173** 070501

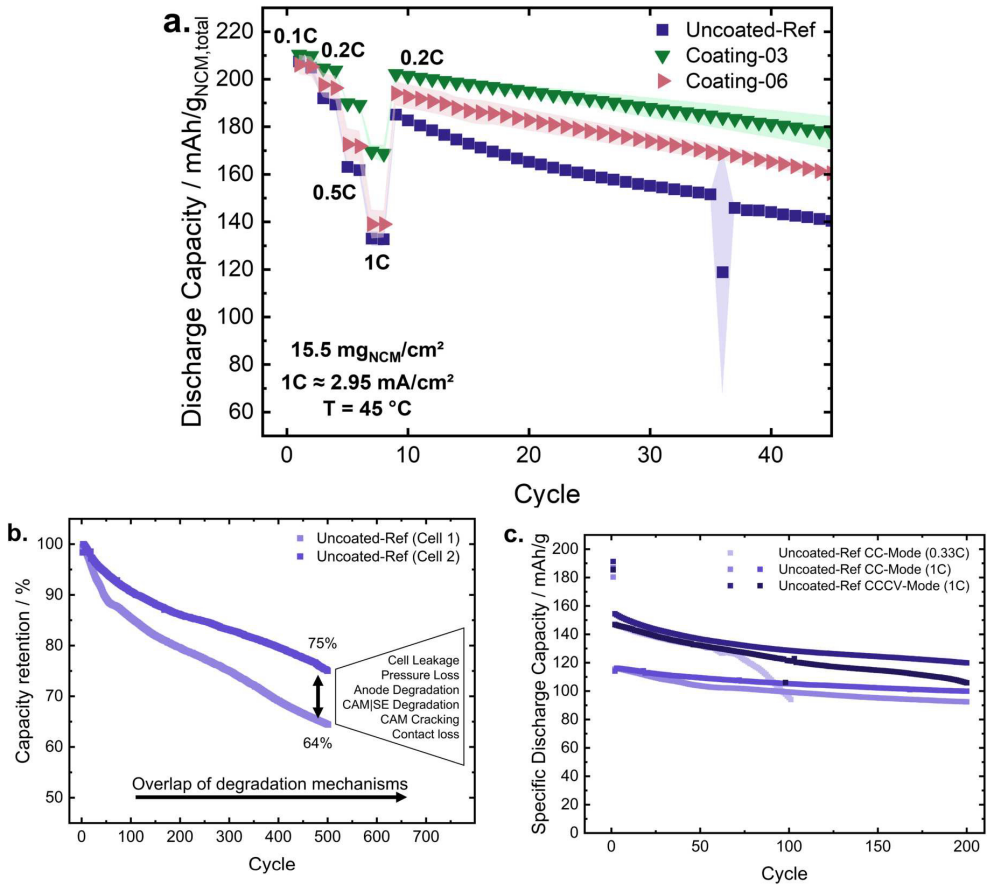

Figure 7. Long-term cycling tests and associated challenges. (a) C-rate test and long-term cycling for *Uncoated-Ref, Coating*-03 and *Coating*-06, represented as average and standard deviation for n = 3 cells. The large standard deviation for *Uncoated-Ref* at cycle 36 is due to a technical problem of the battery cycler. (b) Long-term cycling performance of two cells with *Uncoated-Ref*, indicating different sources of cell performance degradation, most of which are unaffected by CAM coatings. (c) Influence of cycling conditions on the long-term performance of *Uncoated-Ref*, revealing that slower cycling rate leads to faster capacity fading.

While long-term cycling tests remain reasonable and necessary for later stages of coating development, they are inefficient, error-prone, and restrict the parameter space that can be explored in early research. Moreover, long-term cycling data complicate the identification of promising coating strategies across different studies, given the poor reproducibility and comparability of SSB performance in general, as recently demonstrated by Puls et al.[16]. In addition, results from different studies are only comparable if similar cycling conditions are applied. This includes not only the voltage range, but also the duration at high SoC leading to increased calendar aging. Cycling in constant-current (CC) mode, with short resting times after charge, improves stability, but is far from practical conditions. Figure 7c shows that capacity fading depends on both C-rate and charging mode. Stronger fading occurs at 0.33 C compared to 1 C in CC mode. This can be explained by the high overpotential at 1 C, which prevents NCM particles from undergoing the H2→H3 transition (Fig. S11). Since this phase transition is associated with severe volume shrinkage[67] and chemo-mechanical degradation, cells cycled at 1 C appear to retain capacity better. When using constant-current-constant-voltage (CCCV) charging at 1 C, fading is more pronounced. These results highlight that fair comparisons of capacity retention across different studies are only possible under identical cycling conditions. Unfortunately, no standardized electrochemical testing protocol for long-term cycling exists, and developing one is challenging due to the complexity of application scenarios.[77] Nevertheless, we encourage to test coatings under rather harsher conditions, such as longer resting times after charge or CCCV charging protocols, to better reveal degradation effects.

Post mortem analysis of degradation products can provide additional metrics to quantitatively compare coatings and reveal their working principles, *i.e.*, whether more electrochemical or chemical oxidation by oxygenation is prevented.[22] Such analyses need to be (semi-)quantitative and sensitive. A corresponding approach was presented and discussed in depth by Hertle et al.[22] using ToF-SIMS combined with principal component analysis. While ToF-SIMS is a powerful technique, its application to battery materials is challenging, requiring careful sample handling and data analysis. A detailed discussion of SIMS applications in battery research, including pitfalls and best practices, is provided by Lombardo et al.[23]

Interfacial degradation studies can be effectively combined with high-temperature storage experiments, which are application-relevant since coatings must prevent degradation at temperatures above 40 °C.[32,33] As shown in previous publications, the SE does not only degrade via polysulfide formation at the CAM|SE interface but also at the interfaces toward carbon additives and the current collector.[5,45]

To isolate the effects of the CAM|SE interface, carbon additives should be omitted from the composite,[6] and a modified current collector, as proposed by Hertle et al. should be employed.[22]

Final remarks on comparability.—Beyond the discussed aspects, it is important to note that many properties of CAMs in composite cathodes are not governed by the coating alone. Particle size of the CAM, for example, must be similar to allow a fair comparison across different studies, since it affects the diffusion kinetics within the CAM particles. While smaller CAM particles are advantageous in this regard,[53,78] coatings can only marginally influence the CAM-intrinsic diffusion kinetics. Likewise, temperature has a strong impact on degradation processes and cycling performance (cf Figs. 7a and S10) and needs to be constant across studies for a fair comparison. Therefore, meaningful benchmarking requires such variables to be standardized, or at least carefully reported, to enable a certain degree of reliable intra- and inter-laboratory comparability.

Conclusions

The presented short-term benchmarking enables rapid identification of promising and less promising coatings within one week, significantly expanding the accessible process parameter space. By including a short-term aging step, the CAM|SE interface is particularly probed, and degradation is quantified via impedance analysis. Given a reproducible cathode composite mixing process, quantification of the CAM utilization further indicates whether typically electron-blocking coating is too thick. A coating, that performs well in this short-term test, will not necessarily excel in the long term, as limited information on transport kinetics and chemo-mechanical degradation is provided. Nevertheless, it is unlikely that a coating, performing poorly in the short-term benchmarking, will outperform others over longer cycles. Consequently, the ranking obtained from this approach can be used to optimize coating processes in a substantially shorter time. Follow-up experiments are necessary but, as discussed, need to be carefully conducted to avoid misleading conclusions.

This benchmarking framework is broadly applicable and easily adaptable, offering an efficient alternative to long-term cycling tests, particularly in the early stages of CAM coating development. While it does not directly assess capacity retention, it delivers a similar range of metrics as long-term tests, with the advantages of greater reliability and time efficiency (see Table S2 in the Supplementary Information for a concise overview and comparison). This makes the approach especially suitable for integration with machine learning or design-of-experiment studies.

Acknowledgments

The authors acknowledge financial support by BASF SE, by Deutsche Forschungsgemeinschaft (DFG) through the priority program 2289 (project 462470125) and by German Federal Ministry of Education and Research (BMBF) in the project InCa-M (03XP0594A).

Data Availability

The data that support the findings of this study are openly available in Zenodo at https://doi.org/10.5281/zenodo.18775495.

ORCID

Maximilian Kissel https://orcid.org/0000-0001-9201-0748
Felix Schnaubelt https://orcid.org/0009-0006-5619-9102
Jill Kessler-Kühn https://orcid.org/0009-0007-3978-2782
Sebastian L. Benz https://orcid.org/0000-0002-0650-984X
Anton Lai https://orcid.org/0009-0007-2524-3171
Philip Minnmann https://orcid.org/0000-0002-9646-0487
Holger Schneider https://orcid.org/0000-0002-8798-2961
Jürgen Janek https://orcid.org/0000-0002-9221-4756

References

1. J. Janek and W. G. Zeier, "A solid future for battery development." *Nat. Energy*, **1**, 16141 (2016).
2. Y.-K. Sun, "Promising all-solid-state batteries for future electric vehicles." *ACS Energy Lett.*, **5**, 3221 (2020).
3. K. J. Kim, M. Balaish, M. Wadaguchi, L. Kong, and J. L. M. Rupp, "Solid-State Li-Metal batteries: challenges and horizons of oxide and sulfide solid electrolytes and their interfaces." *Adv. Energy Mater.*, **11**, 2002689 (2021).
4. J. Janek and W. G. Zeier, "Challenges in speeding up solid-state battery development." *Nat. Energy*, **8**, 230 (2023).
5. F. Walther, R. Koerver, T. Fuchs, S. Ohno, J. Sann, M. Rohnke, W. G. Zeier, and J. Janek, "Visualization of the interfacial decomposition of composite cathodes in argyrodite-based all-solid-state batteries using time-of-flight secondary-ion mass spectrometry." *Chem. Mater.*, **31**, 3745 (2019).
6. E. Quemin, R. Dugas, T. Koç, B. Hennequart, R. Chometon, and J.-M. Tarascon, "Decoupling parasitic reactions at the positive electrode interfaces in argyrodite-based systems." *ACS Appl. Mater. Interfaces*, **14**, 49284 (2022).
7. A. Banerjee, X. Wang, C. Fang, E. A. Wu, and Y. S. Meng, "Interfaces and interphases in all-solid-state batteries with inorganic solid electrolytes." *Chem. Rev.*, **120**, 6878 (2020).
8. Y. Xiao, L. J. Miara, Y. Wang, and G. Ceder, "Computational screening of cathode coatings for solid-state batteries." *Joule*, **3**, 1252 (2019).
9. C. Liu et al., "Stabilization of single crystal $LiNi_{0.90}Mn_{0.05}Co_{0.05}O_2$ via ZrO_2 dual-functional coating enables superior performance for solid-state lithium battery." *Chem. Eng. J.*, **500**, 156866 (2024).
10. D. Kitsche, Y. Tang, H. Hemmelmann, F. Walther, M. Bianchini, A. Kondrakov, J. Janek, and T. Brezesinski, "Atomic layer deposition derived zirconia coatings on Ni-Rich cathodes in solid-state batteries: Correlation between surface constitution and cycling performance." *Small Science*, **3**, 2200073 (2023).
11. S. Payandeh, F. Strauss, A. Mazilkin, A. Kondrakov, and T. Brezesinski, "Tailoring the $LiNbO_3$ coating of Ni-rich cathode materials for stable and high-performance all-solid-state batteries." *Nano Research Energy*, **1**, e9120016 (2022).
12. F. Jin et al., "Elucidating the impact of Li3InCl6-Coated $LiNi_{0.8}Co_{0.15}Al_{0.05}O_2$ on the electro-chemo-mechanics of Li6PS5Cl-Based solid-state batteries." *Chem. Mater.*, **36**, 6017 (2024).
13. F. Jin et al., "LiBF4 -Derived coating on $LiCoO_2$ for 4.5 V operation of Li 6PS5 Cl-Based solid-state batteries." *Energy & Environ Materials*, **8**, e70047 (2025).
14. B.-X. Shi et al., "Lithiated polymer coating for interface stabilization in Li_6PS_5Cl-based solid-state batteries with high-nickel NCM." *J. Mater. Chem. A*, **13**, 2600 (2025).
15. B.-X. Shi, Y. Yusim, S. Sen, T. Demuth, R. Ruess, K. Volz, A. Henss, and F. H. Richter, "Mitigating contact loss in Li6PS5Cl-Based solid-state batteries using a thin cationic polymer coating on NCM." *Adv. Energy Mater.*, **13**, 2300310 (2023).
16. S. Puls et al., "Benchmarking the reproducibility of all-solid-state battery cell performance." *Nat. Energy*, **9**, 1310 (2024).
17. S. Randau et al., "Benchmarking the performance of all-solid-state lithium batteries." *Nat. Energy*, **5**, 259 (2020).
18. M. Kissel, F. Walther, J. Hertle, T. Demuth, R. Zhang, P. Brüner, T. Brezesinski, K. Volz, and J. Janek, "Engineering the artificial cathode-electrolyte interphase coating for solid-state batteries via tailored annealing." *Chem. Mater.*, **37**, 2192–2203 (2025).
19. J. Y. Lee, S. Noh, J. Y. Seong, S. Lee, and Y. J. Park, "Suppressing unfavorable interfacial reactions using polyanionic oxides as efficient buffer layers: low-cost Li_3PO_4 coatings for sulfide-electrolyte-based all-solid-state batteries." *ACS Appl. Mater. Interfaces*, **15**, 12998 (2023).
20. N. Ohta, K. Takada, I. Sakaguchi, L. Zhang, R. Ma, K. Fukuda, M. Osada, and T. Sasaki, "$LiNbO_3$-coated $LiCoO_2$ as cathode material for all solid-state lithium secondary batteries." *Electrochem. Commun.*, **9**, 1486 (2007).
21. B. Nascimento Nunes, L. Karger, R. Zhang, A. Kondrakov, and T. Brezesinski, "Enhanced cycling performance of the $LiNiO_2$ Cathode in Li-ion batteries enabled by Nb-based surface coating." *ChemSusChem*, **18**, e202402202 (2025).
22. J. Hertle, F. Walther, T. Lombardo, C. Kern, B. Pavlovic, B. Mogwitz, X. Wu, H. Schneider, M. Rohnke, and J. Janek, "Benchmarking of coatings for cathode active materials in solid-state batteries using surface analysis and reference electrodes." *ACS Appl. Mater. Interfaces*, **16**, 9400 (2024).
23. T. Lombardo, F. Walther, C. Kern, Y. Moryson, T. Weintraut, A. Henss, and M. Rohnke, "ToF-SIMS in battery research: Advantages, limitations, and best practices." *J. Vac. Sci. Technol. A*, **41**, 053207 (2023).
24. P. C.V., A. K. Lakshminarayanan, B. Ramasubramanian, and S. Ramakrishna, "Progress of machine learning in materials design for Li-ion battery." *Next Materials*, **2**, 100145 (2024).
25. F. Strauss, J. H. Teo, J. Maibach, A.-Y. Kim, A. Mazilkin, J. Janek, and T. Brezesinski, "Li_2ZrO_3-Coated NCM622 for application in inorganic solid-state batteries: role of surface carbonates in the cycling performance." *ACS Appl. Mater. Interfaces*, **12**, 57146 (2020).
26. W. S. K. Bong, A. Shiota, T. Miwa, Y. Morino, S. Kanada, and K. Kawamoto, "Effect of thickness and uniformity of LiNbO3-coated layer on $LiNi_{0.5}Co_{0.2}Mn_{0.3}O_2$ cathode material on enhancement of cycle performance of full-cell sulfide-based all-solid-state batteries." *J. Power Sources*, **577**, 233259 (2023).
27. M. Kissel et al., "Quantifying the impact of cathode composite mixing quality on active mass utilization and reproducibility of solid-state battery cells." *Adv. Energy Mater.*, **15**, 2405405 (2025).
28. E. Schlautmann et al., "Impact of the solid electrolyte particle size distribution in sulfide-based solid-state battery composites." *Adv. Energy Mater.*, **13**, 2302309 (2023).

29. A. Bielefeld, D. A. Weber, and J. Janek, "Microstructural modeling of composite cathodes for all-solid-state batteries." *J. Phys. Chem. C*, **123**, 1626 (2019).
30. T. T. Zuo, R. Rueß, R. Pan, F. Walther, M. Rohnke, S. Hori, R. Kanno, D. Schröder, and J. Janek, "A mechanistic investigation of the $Li_{10}GeP_2S_{12}$|$LiNi_{1-x-y}Co_xMn_yO_2$ interface stability in all-solid-state lithium batteries." *Nat. Commun.*, **12**, 1 (2021).
31. M. Witt, M. A. Lange, and W. G. Zeier, "Influence of state-of-charge-dependent decomposition kinetics at the Li_6PS_5Cl|$LiNi_{0.83}Co_{0.11}Mn_{0.06}O_2$ interface on solid-state battery performance." *Chem. Electro. Chem.*, **12**, e202500237 (2025).
32. Y. Morino, "Degradation rate at the solid–solid interface of sulfide-based solid electrolyte–cathode active material." *J. Power Sources*, **541**, 231672 (2022).
33. H. Lee, J. Seok, C. Chung, S. Park, J. Kim, and W.-S. Yoon, "Impact of high-temperature storage on capacity fading of Ni-rich cathodes in sulfide-based all-solid-state batteries." *Chem. Eng. J.*, **498**, 154903 (2024).
34. K. Yoon et al., "Detrimental effect of high-temperature storage on sulfide-based all-solid-state batteries." *Appl. Phys. Rev.*, **9**, 031403 (2022).
35. S.-K. Jung, H. Gwon, S.-S. Lee, H. Kim, J. C. Lee, J. G. Chung, S. Y. Park, Y. Aihara, and D. Im, "Understanding the effects of chemical reactions at the cathode–electrolyte interface in sulfide based all-solid-state batteries." *J. Mater. Chem. A*, **7**, 22967 (2019).
36. T. K. Truong, G. Whang, J. Huang, S. E. Sandoval, and W. G. Zeier, "Probing solid-state battery aging: Evaluating calendar vs cycle aging protocols via time-resolved electrochemical impedance spectroscopy." *J. Mater. Chem. A*, **13**, 17261 (2025).
37. G. Conforto, R. Ruess, D. Schröder, E. Trevisanello, R. Fantin, F. H. Richter, and J. Janek, "Editors' Choice—Quantification of the impact of chemo-mechanical degradation on the performance and cycling stability of NCM-Based cathodes in solid-state Li-ion batteries." *J. Electrochem. Soc.*, **168**, 70546 (2021).
38. R. Ruess, S. Schweidler, H. Hemmelmann, G. Conforto, A. Bielefeld, D. A. Weber, J. Sann, M. T. Elm, and J. Janek, "Influence of NCM particle cracking on kinetics of lithium-ion batteries with liquid or solid electrolyte." *J. Electrochem. Soc.*, **167**, 100532 (2020).
39. M. K. Jangid, T. H. Cho, T. Ma, D. W. Liao, H. Kim, Y. Kim, M. Chi, and N. P. Dasgupta, "Eliminating chemo-mechanical degradation of lithium solid-state battery cathodes during 4.5 V cycling using amorphous Nb2O5 coatings." *Nat. Commun.*, **15**, 10233 (2024).
40. A. de Gol, K. B. Dermenci, L. Farkas, and M. Berecibar, "Electro-chemo-mechanical degradation in solid-state batteries: A review of microscale and multiphysics modeling." *Adv. Energy Mater.*, **14**, 2403255 (2024).
41. Y. Morino and S. Kanada, "Electrochemical and material analyses for sulfide-based solid electrolyte–cathode interface under high voltage." *J. Power Sources*, **509**, 230376 (2021).
42. S. Speidel and T. Bräunl, "Driving and charging patterns of electric vehicles for energy usage." *Renew. Sustain. Energy Rev.*, **40**, 97 (2014).
43. Y. Morino, H. Tsukasaki, and S. Mori, "Microscopic degradation mechanism of argyrodite-type sulfide at the solid electrolyte-cathode interface." *ACS Appl. Mater. Interfaces*, **15**, 23051 (2023).
44. T.-T. Zuo, F. Walther, S. Ahmed, R. Rueß, J. Hertle, B. Mogwitz, K. Volz, and J. Janek, "Formation of an artificial cathode–electrolyte interphase to suppress interfacial degradation of Ni-Rich cathode active material with sulfide electrolytes for solid-state batteries." *ACS Energy Lett.*, **8**, 1322 (2023).
45. F. Walther, S. Randau, Y. Schneider, J. Sann, M. Rohnke, F. H. Richter, W. G. Zeier, and J. Janek, "Influence of carbon additives on the decomposition pathways in cathodes of lithium thiophosphate-based all-solid-state batteries." *Chem. Mater.*, **32**, 6123 (2020).
46. W. Zhang et al., "Interfacial processes and influence of composite cathode microstructure controlling the performance of all-solid-state lithium batteries." *ACS Appl. Mater. Interfaces*, **9**, 17835 (2017).
47. K. Vettori, M. Kissel, D. Wagner, S. Schröder, and J. Janek, "Quantifying static capacity losses in solid-state battery composites via coulometric titration comparison." *Chem. Commun.*, **62**, 5241 (2026).
48. Y. Moryson et al., "Analyzing nanometer-thin cathode particle coatings for lithium-ion batteries—the example of TiO_2 on NCM622." *ACS Appl. Energy Mater.*, **4**, 7168 (2021).
49. D. I. Jang, H. Y. Ko, J. Park, J. Y. Lee, and Y. J. Park, "Artificial byproduct coatings through a sublimated sulfur vapor reaction to enhance the stability of cathode/sulfide electrolyte interfaces." *ACS Energy Lett.*, **9**, 5966 (2024).
50. J. Haust et al., "LiNbO3 coatings on NCM622: Structure and performance insights." *Adv. Mater. Interfaces*, **12**, e00590 (2025).
51. S. Randau et al., "On the additive microstructure in composite cathodes and alumina-coated carbon microwires for improved all-solid-state batteries." *Chem. Mater.*, **33**, 1380 (2021).
52. E. Kaeli, Z. Jiang, X. Yang, E. P. K. L. Choy, N. B. Liang, E. Barks, S. Wang, S. D. Kang, and W. C. Chueh, "Decoupling first-cycle capacity loss mechanisms in sulfide solid-state batteries." *Energy Environ. Sci.*, **18**, 1452 (2025).
53. L. Karger, A. Kondrakov, and T. Brezesinski, "On the mechanistic understanding of first-cycle capacity loss in polycrystalline and single-crystal layered Ni-rich oxide cathodes for li-ion batteries." *Chemistry Europe*, **3**, e202500097 (2025).
54. J. Kasnatscheew et al., "The truth about the 1st cycle Coulombic efficiency of $LiNi_{1/3}Co_{1/3}Mn_{1/3}O_2$ (NCM) cathodes." *Phys. Chem. Chem. Phys.*, **18**, 3956 (2016).
55. B. Aktekin, A. E. Sedykh, K. Müller-Buschbaum, A. Henss, and J. Janek, "The formation of residual lithium compounds on Ni-Rich NCM oxides: Their impact on the electrochemical performance of sulfide-based ASSBs." *Adv. Funct. Mater.*, 2313252 (2024).
56. P. Vadhva, J. Hu, M. J. Johnson, R. Stocker, M. Braglia, D. J. L. Brett, and A. J. E. Rettie, "Electrochemical impedance spectroscopy for all-solid-state batteries: Theory, methods and future outlook." *Chem. Electro. Chem.*, **8**, 1930 (2021).
57. R. Zhang, Y. Ma, Y. Tang, D. Goonetilleke, T. Diemant, J. Janek, A. Kondrakov, and T. Brezesinski, "Conformal Li_2HfO_3/HfO_2 nanoparticle coatings on layered Ni-rich oxide cathodes for stabilizing interfaces in all-solid-state batteries." *Chem. Mater.*, **35**, 6835 (2023).
58. K. Vettori et al., "Chemical and structural degradation of single crystalline high-nickel cathode materials during high-voltage holds." *Adv. Energy Mater.*, **15**, 2502148 (2025).
59. R. Morasch, H. A. Gasteiger, and B. Suthar, "Li-ion battery active material impedance analysis I: Comparison of measured NCM 111 kinetics with butler-volmer equation based predictions." *J. Electrochem. Soc.*, **170**, 80522 (2023).
60. R. Weber, A. J. Louli, K. P. Plucknett, and J. R. Dahn, "Resistance growth in lithium-ion pouch cells with $LiNi_{0.80}Co_{0.15}Al_{0.05}O_2$ positive electrodes and proposed mechanism for voltage dependent charge-transfer resistance." *J. Electrochem. Soc.*, **166**, A1779 (2019).
61. R. Koerver, I. Aygün, T. Leichtweiß, C. Dietrich, W. Zhang, J. O. Binder, P. Hartmann, W. G. Zeier, and J. Janek, "Capacity fade in solid-state batteries: interphase formation and chemomechanical processes in nickel-rich layered oxide cathodes and lithium thiophosphate solid electrolytes." *Chem. Mater.*, **29**, 5574 (2017).
62. R. Koerver, F. Walther, I. Aygün, J. Sann, C. Dietrich, W. G. Zeier, and J. Janek, "Redox-active cathode interphases in solid-state batteries." *J. Mater. Chem. A*, **5**, 22750 (2017).
63. J. Auvergniot, A. Cassel, D. Foix, V. Viallet, V. Seznec, and R. Dedryvère, "Redox activity of argyrodite Li6PS5Cl electrolyte in all-solid-state Li-ion battery: An XPS study." *Solid State Ionics*, **300**, 78 (2017).
64. J. Auvergniot, A. Cassel, J.-B. Ledeuil, V. Viallet, V. Seznec, and R. Dedryvère, "Interface stability of argyrodite Li6PS5Cl toward LiCoO2, $LiNi_{1/3}Co_{1/3}Mn_{1/3}O_2$, and $LiMn_2O_4$ in bulk all-solid-state batteries." *Chem. Mater.*, **29**, 3883 (2017).
65. T. K. Schwietert et al., "Clarifying the relationship between redox activity and electrochemical stability in solid electrolytes." *Nat. Mater.*, **19**, 428 (2020).
66. A. Banerjee et al., "Revealing nanoscale solid-solid interfacial phenomena for long-life and high-energy all-solid-state batteries." *ACS Appl. Mater. Interfaces*, **11**, 43138 (2019).
67. F. Strauss, L. de Biasi, A.-Y. Kim, J. Hertle, S. Schweidler, J. Janek, P. Hartmann, and T. Brezesinski, "Rational design of quasi-zero-strain NCM cathode materials for minimizing volume change effects in all-solid-state batteries." *ACS Materials Letters*, **2**, 84 (2020).
68. J. K. Eckhardt, P. J. Klar, J. Janek, and C. Heiliger, "Interplay of dynamic constriction and interface morphology between reversible metal anode and solid electrolyte in solid state batteries." *ACS Appl. Mater. Interfaces*, **14**, 35545 (2022).
69. R. Dugas, Y. Dupraz, E. Quemin, T. Koç, and J.-M. Tarascon, "Engineered three-electrode cells for improving solid state batteries." *J. Electrochem. Soc.*, **168**, 90508 (2021).
70. A. Ikezawa, G. Fukunishi, T. Okajima, F. Kitamura, K. Suzuki, M. Hirayama, R. Kanno, and H. Arai, "Performance of Li4Ti5O12-based reference electrode for the electrochemical analysis of all-solid-state lithium-ion batteries." *Electrochem. Commun.*, **116**, 106743 (2020).
71. R. Zhang, A. Kondrakov, J. Janek, and T. Brezesinski, "Timescale identification of electrochemical processes in all-solid-state batteries using an advanced three-electrode cell setup." *Energy Storage Mater.*, **75**, 104000 (2025).
72. C. D. Alt, S. Keuntje, I. L. Schneider, J. Westphal, P. Minnmann, J. K. Eckhardt, K. Peppler, and J. Janek, "In-Li counter electrodes in solid-state batteries—a comparative approach on kinetics, microstructure, and chemomechanics." *Adv. Energy Mater.*, **15**, 2404055 (2024).
73. S. Yanev, C. Heubner, K. Nikolowski, M. Partsch, H. Auer, and A. Michaelis, "Editors' Choice—Alleviating the kinetic limitations of the Li-In alloy anode in all-solid-state batteries." *J. Electrochem. Soc.*, **171**, 20512 (2024).
74. R. Zhang, A. Kondrakov, J. Janek, and T. Brezesinski, "Interfacial anode kinetics and its influence on cycling performance of sulfide solid-state batteries." *ACS Nano*, **20**, 1225 (2025).
75. P. Minnmann, L. Quillman, S. Burkhardt, F. H. Richter, and J. Janek, "Editors' Choice—Quantifying the impact of charge transport bottlenecks in composite cathodes of all-solid-state batteries." *J. Electrochem. Soc.*, **168**, 40537 (2021).
76. A. Bielefeld, D. A. Weber, and J. Janek, "Modeling effective ionic conductivity and binder influence in composite cathodes for all-solid-state batteries." *ACS Appl. Mater. Interfaces*, **12**, 12821 (2020).
77. A. Geslin, X. Le, D. Ganapathi, K. Moy, W. C. Chueh, and S. Onori, "Dynamic cycling enhances battery lifetime." *Nat. Energy*, **10**, 172 (2024).
78. M. Weiss et al., "Fast charging of lithium-ion batteries: A review of materials aspects." *Adv. Energy Mater.*, **11**, 2101126 (2021).

PART III

Conclusions and Outlook

8 Conclusions

This dissertation connects physico–electro-chemical understanding and process development in SSB research, focusing on microstructures and protective CAM coatings for composite cathodes. It highlights that process engineering, in the form of composite mixing and the systematic exploration of coating process parameters, is a decisive factor for reproducibility and reliable assessment of electrochemical performance in SSBs.

Coulometric titration comparison, a facile electrochemical in-situ method, was used and validated to quantify the CAM utilization, *i.e.*, the fraction of electrically connected CAM particles in the composite cathode. This microstructural property enables a detailed analysis of capacity losses, distinguishing between static losses, originating from electrochemically inactive CAM particles, and kinetic losses, which reduce the achievable capacity during cell operation. This differentiation allows for a more accurate and reliable evaluation of material performance, especially at early stages of SSB development. Without knowledge of the CAM utilization, capacity data, particularly when investigating new solid electrolytes, active materials, or coatings, is prone to misinterpretation.

Applying the coulometric titration comparison method to a representative model system comprising single-crystalline NCM82 as CAM, LPSCl as catholyte, and CNFs as conductive additive, it was demonstrated that the mixing process can induce significant scatter in the measured capacity values, even for identical materials. These variations arise from differences in CAM utilization caused by the mixing process, highlighting that electrochemical performance depends not only on intrinsic material or interfacial properties, but also on the underlying microstructure and ultimately on the processing, particularly the mixing strategy. The CAM utilization thus serves as a reliable microstructural descriptor to assess mixing quality and ensure reproducibility and comparability of electrochemical results.

The importance of the cathode composite mixing process was further addressed by investigating a scalable dry mixing approach based on mechanofusion. This process enables the tailored engineering of composite microstructures with improved interfacial contacts. In particular, a model coating system composed of LIC and CB was used to apply mixed conducting matrix coatings on single-crystalline NCM82. The influence of process

parameters on the morphology of the coatings was systematically studied experimentally and linked to process simulations. The electrochemical performance was found to be highly sensitive to the coating composition, revealing a trade-off between high static CAM utilization and fast kinetics, without further optimization. Overall, mechanofusion-derived mixed conducting matrix coatings represent a promising microstructural design concept, which is the direct result of advanced processing and provides a viable pathway toward the production of high-performing SSB cathodes.

Coatings were also investigated in the second part of this thesis, focusing on thin protective coatings to mitigate degradation between polycrystalline NCM85 and the sulfide catholyte LPSCl. As a model coating precursor, LPS was applied, and the coated particles were annealed to create an artificial CEI coating composed of oxygenated species. This study demonstrated the strong influence of individual process parameters, in this case the annealing temperature, on coating morphology, composition, and eventually overall cell performance. These findings underscore the necessity of moving beyond simple proof-of-principle coating studies toward more systematic investigations that account for a broader range of process parameters already at early stage of research. In this context, the importance of efficient and effective benchmarking methods becomes evident. To address this, a practical and time-efficient benchmarking approach is proposed, combining an XPS-based pre-characterization and electrochemical evaluation with a focus on impedance evolution during short-term aging. This aims at accelerating the reliable identification and optimization of promising coating strategies.

Overall, this dissertation hopefully advances the reproducible, reliable, and standardized testing and evaluation of SSB composite cathodes as well as protective CAM coatings. The methodologies and analytical approaches developed in this work are directly transferable to other material systems and battery chemistries. They lay the groundwork for a more systematic and comparable evaluation of composite cathodes and CAM coatings. By establishing robust tools and performance metrics, this work provides a scientific foundation that enables a deeper understanding of structure–performance relationships and accelerates the knowledge-driven development of high-performance SSB cathodes and coatings across different TRLs — in both academic and industrial contexts.

9 Outlook

The knowledge developed in this thesis can be applied in future research at different levels, from fundamental understanding to processing strategies. The following paragraphs summarize potential directions, directly or indirectly derived from the work presented here.

Material Level Based on the concepts of Publications I and II, new material systems can be more reliably explored. This includes high-energy materials such as LNMO, which need to be paired with suitable SEs or coatings to prevent interfacial degradation. The search for novel coating materials should extend beyond proof-of-concept studies to include exploration across a wider process parameter space, supported by rapid benchmarking methods as proposed in Publication IV and V. In this context, CAM doping strategies established in conventional LIBs[203] can be revisited to determine their relevance and effectiveness for SSBs. Moreover, cathode material blends, which are emerging in the field of LIBs[242,243], could be systematically evaluated for possible beneficial effects, *e.g.*, on the chemo-mechanics[197].

Fundamental and Mechanistic Level The roles and mechanisms of aging and self-discharge in SSBs are still poorly understood despite their critical importance, especially for stationary storage applications. Future systematic and quantitative studies should evaluate how coatings and SE properties influence these effects, as initially addressed in Publication V. Thereby, different protocols for formation cycles may have a significant impact on interface chemistry and stability. Understanding and tailoring these formation cycles could enable the controlled formation of beneficial interphase layers.

EIS might allow a complete characterization of cathode composites regarding mixing quality, microstructure, and interfacial properties. While Publications I and II of this thesis quantified static capacity losses in terms of CAM utilization, the work of Minnmann *et al.*[93] already quantified charge transport through composites. The remaining challenge is quantifying the interfacial contact quality. Recently, Kawaguchi *et al.*[25] reported that EIS can be used to quantify the CAM|SE interfacial contact. Combining all three approaches could allow a detailed and holistic assessment of cathode composites.

General open research questions remain regarding the impedance spectra of composite cathodes. So far, no generalized, universally applicable, and accepted impedance model exists. The use of distribution of relaxation times (DRT) analysis has recently become popular, but the fundamentals for SSBs are not yet fully understood.[226,244] Impedance modeling could clarify whether, and to what extent, SSB full cells and cathode composites can be accurately analyzed via impedance, given their complex three-dimensional structure, to avoid overfitting and misinterpretation.

Processing Level From a processing perspective, the scalable mechanofusion-derived mixed conducting matrix coating approach warrants further investigation. First, a highly conductive sulfide SE and CNFs as an electron conductive additive should be tested as coating components. Therefore, a suitable composition of the matrix and optimized process parameters need to be found. Once established, a binder must be successfully incorporated for manufacturing dry electrodes.[7,8,245] These electrodes should then be tested in pouch cells under realistic conditions, including low stack pressure, to assess industrial viability.

Final Remarks Apart from material and process innovations, bringing SSBs closer to commercialization requires better collaboration, reporting, and standardization. Improved collaboration between fundamental science, engineering, and industry is desired to account for the interdisciplinary challenges of SSBs. Combining the experience, equipment, expertise, and perspective of different groups can create synergies. Transparent and detailed reporting is another crucial aspect.[34,221,222] This includes experimental details but also the reporting of negative results, such as coating process conditions that did not lead to improvements. The lack of standardization is probably the most important but also most challenging issue. It is questionable whether establishing standardized testing methods for mechanical properties[96] or application-realistic electrochemical testing protocols is realistic in the SSB field. Even for LIBs, there is currently no worldwide standardized electrochemical testing program.[220]

Although financial and competitive pressures pose barriers to the above-mentioned aspects, especially in a rapidly growing market, improving reproducibility and comparability is crucial for true advancements in SSBs.

Bibliography

[1] Schill, W.-P., "Electricity Storage and the Renewable Energy Transition," *Joule* **2020**, *4*, 2059–2064, doi: 10.1016/j.joule.2020.07.022.

[2] Winter, M.; Brodd, R. J., "What are batteries, fuel cells, and supercapacitors?" *Chemical Reviews* **2004**, *104*, 4245–4269, doi: 10.1021/cr020730k.

[3] Goodenough, J. B.; Park, K.-S., "The Li-ion rechargeable battery: a perspective," *Journal of the American Chemical Society* **2013**, *135*, 1167–1176, doi: 10.1021/ja3091438.

[4] Blomgren, G. E., "The Development and Future of Lithium Ion Batteries," *Journal of The Electrochemical Society* **2017**, *164*, A5019–A5025, doi: 10.1149/2.0251701jes.

[5] Winter, M.; Barnett, B.; Xu, K., "Before Li Ion Batteries," *Chemical Reviews* **2018**, *118*, 11433–11456, doi: 10.1021/acs.chemrev.8b00422.

[6] Frith, J. T.; Lacey, M. J.; Ulissi, U., "A non-academic perspective on the future of lithium-based batteries," *Nature Communications* **2023**, *14*, 420, doi: 10.1038/s41467-023-35933-2.

[7] Schumm, B. et al., "Dry Battery Electrode Technology: From Early Concepts to Industrial Applications," *Advanced Energy Materials* **2025**, 2406011, doi: 10.1002/aenm.202406011.

[8] Lu, Y. et al., "Dry electrode technology, the rising star in solid-state battery industrialization," *Matter* **2022**, *5*, 876–898, doi: 10.1016/j.matt.2022.01.011.

[9] Janek, J.; Zeier, W. G., "A solid future for battery development," *Nature Energy* **2016**, *1*, 16141, doi: 10.1038/nenergy.2016.141.

[10] Wang, R. et al., "Lithium metal anodes: Present and future," *Journal of Energy Chemistry* **2020**, *48*, 145–159, doi: 10.1016/j.jechem.2019.12.024.

[11] Yu, X. et al., "Battery Safety: From Lithium-Ion to Solid-State Batteries," *Engineering* **2023**, *21*, 9–14, doi: 10.1016/j.eng.2022.06.022.

[12] Bates, A. M. et al., "Are solid-state batteries safer than lithium-ion batteries?" *Joule* **2022**, *6*, 742–755, doi: 10.1016/j.joule.2022.02.007.

[13] Jetybayeva, A. et al., "Critical review on recently developed lithium and non-lithium anode-based solid-state lithium-ion batteries," *Journal of Power Sources* **2023**, *566*, 232914, doi: 10.1016/j.jpowsour.2023.232914.

[14] Sun, Y.-K., "Promising All-Solid-State Batteries for Future Electric Vehicles," *ACS Energy Letters* **2020**, *5*, 3221–3223, doi: 10.1021/acsenergylett.0c01977.

[15] Greenwood, M. et al., "The Battery Component Readiness Level (BC-RL) framework: A technology-specific development framework," *Journal of Power Sources Advances* **2022**, *14*, 100089, doi: 10.1016/j.powera.2022.100089.

[16] Janek, J.; Zeier, W. G., "Challenges in speeding up solid-state battery development," *Nature Energy* **2023**, *8*, 230–240, doi: 10.1038/s41560-023-01208-9.

[17] Krauskopf, T. et al., "Physicochemical Concepts of the Lithium Metal Anode in Solid-State Batteries," *Chemical Reviews* **2020**, *120*, 7745–7794, doi: 10.1021/acs.chemrev.0c00431.

[18] Burton, M. et al., "Techno-economic assessment of thin lithium metal anodes for solid-state batteries," *Nature Energy* **2025**, *10*, 135–147, doi: 10.1038/s41560-024-01676-7.

[19] Randau, S. et al., "Benchmarking the performance of all-solid-state lithium batteries," *Nature Energy* **2020**, *5*, 259–270, doi: 10.1038/s41560-020-0565-1.

[20] Minnmann, P. et al., "Designing Cathodes and Cathode Active Materials for Solid–State Batteries," *Advanced Energy Materials* **2022**, *12*, 2201425, doi: 10.1002/aenm.202201425.

[21] Ren, D. et al., "Challenges and opportunities of practical sulfide-based all-solid-state batteries," *eTransportation* **2023**, *18*, 100272, doi: 10.1016/j.etran.2023.100272.

[22] Bielefeld, A.; Weber, D. A.; Janek, J., "Microstructural Modeling of Composite Cathodes for All-Solid-State Batteries," *Journal of Physical Chemistry C* **2019**, *123*, 1626–1634, doi: 10.1021/acs.jpcc.8b11043.

[23] Kim, J. et al., "High–Performance All–Solid–State Batteries Enabled by Intimate Interfacial Contact Between the Cathode and Sulfide–Based Solid Electrolytes," *Advanced Functional Materials* **2023**, *33*, 2211355, doi: 10.1002/adfm.202211355.

[24] Koerver, R. et al., "Capacity Fade in Solid-State Batteries: Interphase Formation and Chemomechanical Processes in Nickel-Rich Layered Oxide Cathodes and Lithium Thiophosphate Solid Electrolytes," *Chemistry of Materials* **2017**, *29*, 5574–5582, doi: 10.1021/acs.chemmater.7b00931.

[25] Kawaguchi, S. et al., "Quantifying the interfacial contact of active material–solid electrolyte interfaces in all-solid-state lithium-ion batteries," *Journal of Colloid and Interface Science* **2025**, *696*, 137878, doi: 10.1016/j.jcis.2025.137878.

[26] Lou, S. et al., "Interface Issues and Challenges in All-Solid-State Batteries: Lithium, Sodium, and Beyond," *Advanced Materials* **2021**, *33*, 2000721, doi: 10.1002/adma.202000721.

[27] Banerjee, A. et al., "Interfaces and Interphases in All-Solid-State Batteries with Inorganic Solid Electrolytes," doi: 10.1021/acs.chemrev.0c00101.

[28] Kim, K. J. et al., "Solid–State Li–Metal Batteries: Challenges and Horizons of Oxide and Sulfide Solid Electrolytes and Their Interfaces," *Advanced Energy Materials* **2021**, *11*, 2002689, doi: 10.1002/aenm.202002689.

[29] Bielefeld, A.; Weber, D. A.; Janek, J., "Modeling Effective Ionic Conductivity and Binder Influence in Composite Cathodes for All-Solid-State Batteries," *ACS Applied Materials and Interfaces* **2020**, *12*, 12821–12833, doi: 10.1021/acsami.9b22788.

[30] Frankenberg, F. et al., "Investigating the production of all-solid-state battery composite cathodes by numerical simulation of the stressing conditions in a high-intensity mixer," *Powder Technology* **2024**, *435*, 119403, doi: 10.1016/j.powtec.2024.119403.

[31] Fernandez-Diaz, L. et al., "Mixing methods for solid state electrodes: Techniques, fundamentals, recent advances, and perspectives," *Chemical Engineering Journal* **2023**, *464*, 142469, doi: 10.1016/j.cej.2023.142469.

[32] Culver, S. P. et al., "On the Functionality of Coatings for Cathode Active Materials in Thiophosphate–Based All–Solid–State Batteries," *Advanced Energy Materials* **2019**, *9*, 1900626, doi: 10.1002/aenm.201900626.

[33] Morchhale, A. et al., "Coating materials and processes for cathodes in sulfide-based all solid-state batteries," *Current Opinion in Electrochemistry* **2023**, *39*, 101251, doi: 10.1016/j.coelec.2023.101251.

[34] Puls, S. et al., "Benchmarking the reproducibility of all-solid-state battery cell performance," *Nature Energy* **2024**, *9*, 1310–1320, doi: 10.1038/s41560-024-01634-3.

[35] Johansson, P. et al., "Ten Ways to Fool the Masses When Presenting Battery Research**," *Batteries & Supercaps* **2021**, *4*, 1785–1788, doi: 10.1002/batt.202100154.

[36] Sen, S.; Richter, F. H., "Typology of Battery Cells – From Liquid to Solid Electrolytes," *Advanced Science* **2023**, *10*, doi: 10.1002/advs.202303985.

[37] Zhou, G. et al., "Quasi-solid electrolytes with tailored lithium solvation for fast-charging lithium metal batteries," *Cell Reports Physical Science* **2022**, *3*, 100722, doi: 10.1016/j.xcrp.2021.100722.

[38] Li, J. et al., "Recent applications of ionic liquids in quasi-solid-state lithium metal batteries," *Green Chemical Engineering* **2021**, *2*, 253–265, doi: 10.1016/J.GCE.2021.03.001.

[39] Hwang, J. et al., "Pseudo-solid-state electrolytes utilizing the ionic liquid family for rechargeable batteries," *Energy & Environmental Science* **2021**, *14*, 5834–5863, doi: 10.1039/D1EE02567H.

[40] Huo, H.; Janek, J., "Solid-state batteries: from 'all-solid' to 'almost-solid'," *National Science Review* **2023**, *10*, 1–3, doi: 10.1093/nsr/nwad098.

[41] Woolley, H. M.; Vargas-Barbosa, N. M., "Hybrid solid electrolyte-liquid electrolyte systems for (almost) solid-state batteries: Why, how, and where to?" *Journal of Materials Chemistry A* **2023**, 1083–1097, doi: 10.1039/D2TA02179J.

[42] Lee, H. et al., "Hybrid Liquid–Solid Composite Electrolytes for Sulfide–Based Solid–State Batteries: Advantages and Limitation," *Advanced Functional Materials* **2023**, *33*, 2305373, doi: 10.1002/adfm.202305373.

[43] Xin, C. et al., "Conductive gel composite cathodes with high mass loading of active oxides for high-performance solid-state lithium metal batteries," *Solid State Ionics* **2020**, *345*, 115196, doi: 10.1016/j.ssi.2019.115196.

[44] Rana, M. et al., "Toward Achieving High Areal Capacity in Silicon-Based Solid-State Battery Anodes: What Influences the Rate-Performance?" *ACS Energy Letters* **2023**, *8*, 3196–3203, doi: 10.1021/acsenergylett.3c00722.

[45] Kimura, Y. et al., "Coating layer design principles considering lithium chemical potential distribution within solid electrolytes of solid-state batteries," *Communications Materials* **2024**, *5*, 1–13, doi: 10.1038/s43246-024-00578-1.

[46] Chen, S. et al., "Sulfide solid electrolytes for all-solid-state lithium batteries: Structure, conductivity, stability and application," *Energy Storage Materials* **2018**, *14*, 58–74, doi: 10.1016/j.ensm.2018.02.020.

[47] Reddy, M. V. et al., "Sulfide and Oxide Inorganic Solid Electrolytes for All-Solid-State Li Batteries: A Review," *Nanomaterials* **2020**, *10*, 1606, doi: 10.3390/nano10081606.

[48] Jiang, P. et al., "Solid–State Li Ion Batteries with Oxide Solid Electrolytes: Progress and Perspective," *Energy Technology* **2023**, *11*, 2201288, doi: 10.1002/ente.202201288.

[49] Wang, Q. et al., "New advances in solid-state electrolytes: from halides to oxyhalides," *Inorganic Chemistry Frontiers* **2024**, *11*, 5810–5832, doi: 10.1039/D4QI01306A.

[50] Tao, B. et al., "Halide solid-state electrolytes for all-solid-state batteries: structural design, synthesis, environmental stability, interface optimization and challenges," *Chemical science* **2023**, *14*, 8693–8722, doi: 10.1039/D3SC02093B.

[51] Dahbi, M. et al., "Comparative study of EC/DMC LiTFSI and $LiPF_6$ electrolytes for electrochemical storage," *Journal of Power Sources* **2011**, *196*, 9743–9750, doi: 10.1016/j.jpowsour.2011.07.071.

[52] Fong, K. D. et al., "Ion Transport and the True Transference Number in Nonaqueous Polyelectrolyte Solutions for Lithium Ion Batteries," *ACS central science* **2019**, *5*, 1250–1260, doi: 10.1021/acscentsci.9b00406.

[53] Kamaya, N. et al., "A lithium superionic conductor," *Nature Materials* **2011**, *10*, 682–686, doi: 10.1038/nmat3066.

[54] Kato, Y. et al., "High-power all-solid-state batteries using sulfide superionic conductors," *Nature Energy 2022* **2016**, *1*, 1–7, doi: 10.1038/nenergy.2016.30.

[55] Kato, Y.; Hori, S.; Kanno, R., "$Li_{10}GeP_2S_{12}$ –Type Superionic Conductors: Synthesis, Structure, and Ionic Transportation," *Advanced Energy Materials* **2020**, *10*, 2002153, doi: 10.1002/aenm.202002153.

[56] Lee, Y. et al., "Lithium Argyrodite Sulfide Electrolytes with High Ionic Conductivity and Air Stability for All-Solid-State Li-Ion Batteries," *ACS Energy Letters* **2022**, *7*, 171–179, doi: 10.1021/acsenergylett.1c02428.

[57] Li, Y. et al., "A lithium superionic conductor for millimeter-thick battery electrode," *American Association for the Advancement of Science* **2023**.

[58] Lin, J. et al., "Synthetic Tailoring of Ionic Conductivity in Multicationic Substituted, High-Entropy Lithium Argyrodite Solid Electrolytes," *Small* **2023**, *20*, 2306832, doi: 10.1002/smll.202306832.

[59] Lin, J. et al., "Tuning Ion Mobility in Lithium Argyrodite Solid Electrolytes via Entropy Engineering," *Angewandte Chemie International Edition* **2024**, *63*, e202404874, doi: 10.1002/anie.202404874.

[60] Tanaka, Y. et al., "New Oxyhalide Solid Electrolytes with High Lithium Ionic Conductivity >10 mS cm^{-1} for All-Solid-State Batteries," *Angewandte Chemie International Edition* **2023**, *62*, e202217581, doi: 10.1002/anie.202217581.

[61] Bielefeld, A. et al., "Influence of Lithium Ion Kinetics, Particle Morphology and Voids on the Electrochemical Performance of Composite Cathodes for All-Solid-State Batteries," *Journal of The Electrochemical Society* **2022**, *169*, 020539, doi: 10.1149/1945-7111/ac50df.

[62] Kang, S.; Kim, M.; Min, K., "Discovery of Superionic Solid-State Electrolyte for Li-Ion Batteries via Machine Learning," *Journal of Physical Chemistry C* **2023**, *127*, 19335–19343, doi: 10.1021/acs.jpcc.3c02908.

[63] Lotsch, B. V.; Maier, J., "Relevance of solid electrolytes for lithium-based batteries: A realistic view," *Journal of Electroceramics* **2017**, *38*, 128–141, doi: 10.1007/s10832-017-0091-0.

[64] Alt, C. D. et al., "In–Li Counter Electrodes in Solid–State Batteries – A Comparative Approach on Kinetics, Microstructure, and Chemomechanics," *Advanced Energy Materials* **2024**, *15*, 2404055, doi: 10.1002/aenm.202404055.

[65] Ohno, S. et al., "Linking Solid Electrolyte Degradation to Charge Carrier Transport in the Thiophosphate–Based Composite Cathode toward Solid–State Lithium–Sulfur Batteries," *Advanced Functional Materials* **2021**, *31*, 2010620, doi: 10.1002/adfm.202010620.

[66] Quemin, E. et al., "Decoupling Parasitic Reactions at the Positive Electrode Interfaces in Argyrodite-Based Systems," *ACS Applied Materials and Interfaces* **2022**, *14*, 49284–49294, doi: 10.1021/acsami.2c13150.

[67] Teo, J. H. et al., "The interplay between (electro)chemical and (chemo)mechanical effects in the cycling performance of thiophosphate-based solid-state batteries," *Materials Futures* **2022**, *1*, 015102, doi: 10.1088/2752-5724/ac3897.

[68] Roitzheim, C. et al., "All-Solid-State Li Batteries with NCM–Garnet-Based Composite Cathodes: The Impact of NCM Composition on Material Compatibility," *ACS Applied Energy Materials* **2022**, *5*, 6913–6926, doi: 10.1021/acsaem.2c00533.

[69] Nikodimos, Y. et al., "Chemical stability of sulfide solid-state electrolytes: stability toward humid air and compatibility with solvents and binders," *Energy & Environmental Science* **2022**, *15*, 991–1033, doi: 10.1039/d1ee03032a.

[70] Hatz, A.-K. et al., "Chemical Stability and Ionic Conductivity of LGPS-Type Solid Electrolyte Tetra-Li_7SiPS_8 after Solvent Treatment," *ACS Applied Energy Materials* **2021**, *4*, 9932–9943, doi: 10.1021/acsaem.1c01917.

[71] Chen, Y.-T. et al., "Investigating dry room compatibility of sulfide solid-state electrolytes for scalable manufacturing," *Journal of Materials Chemistry A* **2022**, *10*, 7155–7164, doi: 10.1039/D1TA09846B.

[72] Batzer, M. et al., "Current Status of Formulations and Scalable Processes for Producing Sulfidic Solid–State Batteries," *Batteries & Supercaps* **2022**, *5*, e202200328, doi: 10.1002/batt.202200328.

[73] Zhou, R. et al., "Boosting Ionic Conductivity and Air Stability in Bromide–Rich Thioarsenate Argyrodite Solid Electrolytes," *Advanced Functional Materials* **2025**, *35*, 2420971, doi: 10.1002/adfm.202420971.

[74] Park, D. et al., "Theoretical Design of Lithium Chloride Superionic Conductors for All-Solid-State High-Voltage Lithium-Ion Batteries," *ACS Applied Materials and Interfaces* **2020**, *12*, 34806–34814, doi: 10.1021/acsami.0c07003.

[75] Xiao, Y. et al., "Computational Screening of Cathode Coatings for Solid-State Batteries," *Joule* **2019**, *3*, 1252–1275, doi: 10.1016/J.JOULE.2019.02.006.

[76] Chun, G. H.; Shim, J. H.; Yu, S., "Computational Investigation of the Interfacial Stability of Lithium Chloride Solid Electrolytes in All-Solid-State Lithium Batteries," *ACS Applied Materials and Interfaces* **2022**, *14*, 1241–1248, doi: 10.1021/acsami.1c22104.

[77] Walther, F. et al., "Influence of Carbon Additives on the Decomposition Pathways in Cathodes of Lithium Thiophosphate-Based All-Solid-State Batteries," *Chemistry of Materials* **2020**, *32*, 6123–6136, doi: 10.1021/acs.chemmater.0c01825.

[78] Kim, W. et al., "Aging Property of Halide Solid Electrolyte at the Cathode Interface," *Advanced Materials* **2023**, *35*, e2301631, doi: 10.1002/adma.202301631.

[79] Dewald, G. F. et al., "Experimental Assessment of the Practical Oxidative Stability of Lithium Thiophosphate Solid Electrolytes," *Chemistry of Materials* **2019**, *31*, 8328–8337, doi: 10.1021/acs.chemmater.9b01550.

[80] Boulineau, S. et al., "Mechanochemical synthesis of Li-argyrodite Li_6PS_5X (X=Cl, Br, I) as sulfur-based solid electrolytes for all solid state batteries application," *Solid State Ionics* **2012**, *221*, 1–5, doi: 10.1016/j.ssi.2012.06.008.

[81] Schwietert, T. K.; Vasileiadis, A.; Wagemaker, M., "First-Principles Prediction of the Electrochemical Stability and Reaction Mechanisms of Solid-State Electrolytes," *JACS Au* **2021**, *1*, 1488–1496, doi: 10.1021/jacsau.1c00228.

[82] Schwietert, T. K. et al., "Clarifying the relationship between redox activity and electrochemical stability in solid electrolytes," *Nature Materials* **2020**, *19*, 428–435, doi: 10.1038/s41563-019-0576-0.

[83] Riegger, L. M. et al., "Lithium-Metal Anode Instability of the Superionic Halide Solid Electrolytes and the Implications for Solid-State Batteries," *Angewandte Chemie International Edition* **2021**, *60*, 6718–6723, doi: 10.1002/anie.202015238.

[84] Li, W. et al., "Systematic safety evaluation of quasi-solid-state lithium batteries: a case study," *Energy & Environmental Science* **2023**, *16*, 5444–5453, doi: 10.1039/D3EE03073C.

[85] Kim, T. et al., "Thermal Runaway Behavior of Li_6PS_5Cl Solid Electrolytes for $LiNi_{0.8}Co_{0.1}Mn_{0.1}O_2$ and $LiFePO_4$ in All-Solid-State Batteries," *Chemistry of Materials* **2022**, *34*, 9159–9171, doi: 10.1021/acs.chemmater.2c02106.

[86] Muramatsu, H. et al., "Structural change of Li_2S–P_2S_5 sulfide solid electrolytes in the atmosphere," *Solid State Ionics* **2011**, *182*, 116–119, doi: 10.1016/j.ssi.2010.10.013.

[87] Dai, T. et al., "Inorganic glass electrolytes with polymer-like viscoelasticity," *Nature Energy* **2023**, *8*, 1221–1228, doi: 10.1038/s41560-023-01356-y.

[88] Nair, J. R. et al., "Lithium Metal Polymer Electrolyte Batteries: Opportunities and Challenges," *The Electrochemical Society Interface* **2019**, *28*, 55–61, doi: 10.1149/2.F05192if.

[89] Lu, X. et al., "Polymer–Based Solid–State Electrolytes for High–Energy–Density Lithium–Ion Batteries – Review," *Advanced Energy Materials* **2023**, *13*, 2301746, doi: 10.1002/aenm.202301746.

[90] Demuth, T. et al., "Influence of the sintering temperature on LLZO-NCM cathode composites for solid-state batteries studied by transmission electron microscopy," *Matter* **2023**, *6*, 2324–2339, doi: 10.1016/j.matt.2023.04.022.

[91] Singer, C. et al., "Insights Into Scalable Technologies and Process Chains for Sulfide–Based Solid–State Battery Production," *Batteries & Supercaps* **2024**, *7*, e202400142, doi: 10.1002/batt.202400142.

[92] Riegger, L. M. et al., "Evolution of the Interphase between Argyrodite-Based Solid Electrolytes and the Lithium Metal Anode-The Kinetics of Solid Electrolyte Interphase Growth," *Chemistry of Materials* **2023**, *35*, 5091–5099, doi: 10.1021/acs.chemmater.3c00676.

[93] Minnmann, P. et al., "Editors' Choice—Quantifying the Impact of Charge Transport Bottlenecks in Composite Cathodes of All-Solid-State Batteries," *Journal of The Electrochemical Society* **2021**, *168*, 040537, doi: 10.1149/1945-7111/abf8d7.

[94] Merola, L. et al., "Evaluation of Oxide|Sulfide Heteroionic Interface Stability for Developing Solid-State Batteries with a Lithium-Metal Electrode: The Case of LLZO|Li_6PS_5Cl and LLZO|$Li_7P_3S_{11}$," *ACS Applied Materials and Interfaces* **2024**, *16*, 54847–54863, doi: 10.1021/acsami.4c11597.

[95] Schmaltz, T. et al., "A Roadmap for Solid–State Batteries," *Advanced Energy Materials* **2023**, *13*, 2301886, doi: 10.1002/aenm.202301886.

[96] Hao, S. et al., "Intrinsic Mechanical Parameters and their Characterization in Solid–State Lithium Batteries," *Advanced Energy Materials* **2025**, *15*, 2404384, doi: 10.1002/aenm.202404384.

[97] Yu, S. et al., "Elastic Properties of the Solid Electrolyte $Li_7La_3Zr_2O_{12}$ (LLZO)," *Chemistry of Materials* **2016**, *28*, 197–206, doi: 10.1021/acs.chemmater.5b03854.

[98] McGrogan, F. P. et al., "Compliant Yet Brittle Mechanical Behavior of Li_2S–P_2S_5 Lithium–Ion–Conducting Solid Electrolyte," *Advanced Energy Materials* **2017**, *7*, 1602011, doi: 10.1002/aenm.201602011.

[99] Swallow, J. G. et al., "Effect of Electrochemical Charging on Elastoplastic Properties and Fracture Toughness of Li_XCoO_2," *Journal of The Electrochemical Society* **2014**, *161*, F3084–F3090, doi: 10.1149/2.0141411jes.

[100] Ni, J. E. et al., "Room temperature elastic moduli and Vickers hardness of hot-pressed LLZO cubic garnet," *Journal of Materials Science* **2012**, *47*, 7978–7985, doi: 10.1007/s10853-012-6687-5.

[101] Wolfenstine, J. et al., "Mechanical behavior of Li-ion-conducting crystalline oxide-based solid electrolytes: a brief review," *Ionics* **2018**, *24*, 1271–1276, doi: 10.1007/s11581-017-2314-4.

[102] Sakuda, A. et al., "Evaluation of elastic modulus of Li_2S–P_2S_5 glassy solid electrolyte by ultrasonic sound velocity measurement and compression test," *Journal of the Ceramic Society of Japan* **2013**, *121*, 946–949, doi: 10.2109/jcersj2.121.946.

[103] Sakuda, A.; Hayashi, A.; Tatsumisago, M., "Sulfide solid electrolyte with favorable mechanical property for all-solid-state lithium battery," *Scientific Reports* **2013**, *3*, 2261, doi: 10.1038/srep02261.

[104] Kato, A. et al., "Mechanical Properties of Li_2S–P_2S_5 Glasses with Lithium Halides and Application in All-Solid-State Batteries," *ACS Applied Energy Materials* **2018**, *1*, 1002–1007, doi: 10.1021/acsaem.7b00140.

[105] Wang, Z. Q. et al., "Elastic Properties of New Solid State Electrolyte Material $Li_{10}GeP_2S_{12}$: A Study from First-Principles Calculations," *International Journal of Electrochemical Science* **2014**, *9*, 562–568, doi: 10.1016/S1452-3981(23)07739-8.

[106] Deng, Z. et al., "Elastic Properties of Alkali Superionic Conductor Electrolytes from First Principles Calculations," *Journal of The Electrochemical Society* **2016**, *163*, A67–A74, doi: 10.1149/2.0061602jes.

[107] Kim, K. et al., "Material Design Strategy for Halide Solid Electrolytes Li_3MX_6 (X = Cl, Br, and I) for All-Solid-State High-Voltage Li-Ion Batteries," *Chemistry of Materials* **2021**, *33*, 3669–3677, doi: 10.1021/acs.chemmater.1c00555.

[108] Sangrós Giménez, C. et al., "Structural and mechanical characterization of lithium-ion battery electrodes via DEM simulations," *Advanced Powder Technology* **2018**, *29*, 2312–2321, doi: 10.1016/j.apt.2018.05.014.

[109] Park, S. H. et al., "Chemo-Mechanical Behavior and Stability of High-Loading Cathodes in Solid-State Batteries," *ACS Nano* **2025**, doi: 10.1021/acsnano.5c04431.

[110] Li, X. et al., "Water–Mediated Synthesis of a Superionic Halide Solid Electrolyte," *Angewandte Chemie* **2019**, *131*, 16579–16584, doi: 10.1002/ange.201909805.

[111] Wu, J. et al., "Lithium/Sulfide All-Solid-State Batteries using Sulfide Electrolytes," *Advanced Materials* **2021**, *33*, e2000751, doi: 10.1002/adma.202000751.

[112] Wang, C. et al., "A universal wet-chemistry synthesis of solid-state halide electrolytes for all-solid-state lithium-metal batteries," *Science Advances* **2021**, *7*.

[113] Batzer, M. et al., "Systematic evaluation of materials and recipe for scalable processing of sulfide-based solid-state batteries," *Materials Today Communications* **2022**, *30*, 103189, doi: 10.1016/j.mtcomm.2022.103189.

[114] Schlem, R. et al., "Energy Storage Materials for Solid–State Batteries: Design by Mechanochemistry," *Advanced Energy Materials* **2021**, *11*, 2101022, doi: 10.1002/aenm.202101022.

[115] Wang, K. et al., "A cost-effective and humidity-tolerant chloride solid electrolyte for lithium batteries," *Nature Communications* **2021**, *12*, 4410, doi: 10.1038/s41467-021-24697-2.

[116] Kwak, H. et al., "New Cost–Effective Halide Solid Electrolytes for All–Solid–State Batteries: Mechanochemically Prepared Fe^{3+} –Substituted Li_2ZrCl_6," *Advanced Energy Materials* **2021**, *11*, 2003190, doi: 10.1002/aenm.202003190.

[117] Wu, Z.-Z. et al., "Low-cost synthesis of high-purity Li_2S for sulfide solid state electrolytes enabled by polyvinyl alcohol," *Journal of Central South University* **2024**, *31*, 4449–4459, doi: 10.1007/s11771-024-5824-z.

[118] Wei, Y. et al., "Low-cost preparation and purification of Li_2S for sulfide solid electrolytes," *Journal of Energy Storage* **2024**, *103*, 114180, doi: 10.1016/j.est.2024.114180.

[119] Huang, W.-Z. et al., "Anode–Free Solid–State Lithium Batteries: A Review," *Advanced Energy Materials* **2022**, *12*, doi: 10.1002/aenm.202201044.

[120] Wang, C. et al., "The influence of pressure on lithium dealloying in solid-state and liquid electrolyte batteries," *Nature Materials* **2025**, *24*, 907–916, doi: 10.1038/s41563-025-02198-7.

[121] Lewis, J. A. et al., "The promise of alloy anodes for solid-state batteries," *Joule* **2022**, *6*, 1418–1430, doi: 10.1016/j.joule.2022.05.016.

[122] Huo, H.; Janek, J., "Silicon as Emerging Anode in Solid-State Batteries," *ACS Energy Letters* **2022**, *7*, 4005–4016, doi: 10.1021/acsenergylett.2c01950.

[123] Yanev, S. et al., "Editors' Choice—Alleviating the Kinetic Limitations of the Li-In Alloy Anode in All-Solid-State Batteries," *Journal of The Electrochemical Society* **2024**, *171*, 020512, doi: 10.1149/1945-7111/ad2594.

[124] Aspinall, J. et al., "Effect of Microstructure on the Cycling Behavior of Li–In Alloy Anodes for Solid-State Batteries," *ACS Energy Letters* **2024**, *9*, 578–585, doi: 10.1021/acsenergylett.3c02274.

[125] Santhosha, A. L. et al., "The Indium− Lithium Electrode in Solid-State Lithium-Ion Batteries: Phase Formation, Redox Potentials, and Interface Stability," *Batteries & Supercaps* **2019**, *2*, 524–529, doi: 10.1002/BATT.201800149.

[126] Noh, S. et al., "Importance of mixing protocol for enhanced performance of composite cathodes in all-solid-state batteries using sulfide solid electrolyte," *Journal of Electroceramics* **2018**, *40*, 293–299, doi: 10.1007/s10832-018-0129-y.

[127] Zhang, W. et al., "Interfacial Processes and Influence of Composite Cathode Microstructure Controlling the Performance of All-Solid-State Lithium Batteries," *ACS applied materials & interfaces* **2017**, *9*, 17835–17845, doi: 10.1021/acsami.7b01137.

[128] Cronk, A. et al., "Overcoming the Interfacial Challenges of $LiFePO_4$ in Inorganic All-Solid-State Batteries," *ACS Energy Letters* **2023**, *8*, 827–835, doi: 10.1021/acsenergylett.2c02138.

[129] Tsai, B.-Y. et al., "Microscopic Study of Solid–Solid Interfacial Reactions in All-Solid-State Batteries," *Journal of Physical Chemistry C* **2023**, *127*, 14336–14343, doi: 10.1021/acs.jpcc.3c03045.

[130] Lee, D. et al., "Interphase Stabilization of $LiNi_{0.5}Mn_{1.5}O_4$ Cathode for 5 V-Class All-Solid-State Batteries," *Small* **2024**, *20*, e2306053, doi: 10.1002/smll.202306053.

[131] Jang, J. et al., "Enabling a Co-Free, High-Voltage $LiNi_{0.5}Mn_{1.5}O_4$ Cathode in All-Solid-State Batteries with a Halide Electrolyte," *ACS Energy Letters* **2022**, *7*, 2531–2539, doi: 10.1021/acsenergylett.2c01397.

[132] Lee, H. J. et al., "$LiNi_{0.5}Mn_{1.5}O_4$ Cathode Microstructure for All-Solid-State Batteries," *Nano letters* **2022**, *22*, 7477–7483, doi: 10.1021/acs.nanolett.2c02426.

[133] Lim, G. et al., "Regulating Dynamic Electrochemical Interface of $LiNi_{0.5}Mn_{1.5}O_4$ Spinel Cathode for Realizing Simultaneous Mn and Ni Redox in Rechargeable Lithium Batteries," *Advanced Energy Materials* **2022**, *12*, 2202049, doi: 10.1002/aenm.202202049.

[134] Zhang, R. et al., "Transition-metal interdiffusion and solid electrolyte poisoning in all-solid-state batteries revealed by cryo-TEM," *Chemical Communications* **2023**, *59*, 4600–4603, doi: 10.1039/D3CC00516J.

[135] Payandeh, S. et al., "Single versus poly-crystalline layered oxide cathode materials for solid-state battery applications - a short review article," *Current Opinion in Electrochemistry* **2022**, *31*, 100877, doi: 10.1016/j.coelec.2021.100877.

[136] Han, Y. et al., "Single– or Poly–Crystalline Ni–Rich Layered Cathode, Sulfide or Halide Solid Electrolyte: Which Will be the Winners for All–Solid–State Batteries?" *Advanced Energy Materials* **2021**, *11*, 2100126, doi: 10.1002/aenm.202100126.

[137] Ruess, R. et al., "Single-Crystalline $LiNiO_2$ as High-Capacity Cathode Active Material for Solid-State Lithium-Ion Batteries," *Journal of The Electrochemical Society* **2023**, *170*, 020533, doi: 10.1149/1945-7111/acbc4f.

[138] Bianchini, M. et al., "There and Back Again-The Journey of $LiNiO_2$ as a Cathode Active Material," *Angewandte Chemie International Edition* **2019**, *58*, 10434–10458, doi: 10.1002/anie.201812472.

[139] Chang, L. et al., "A review on nickel-rich nickel-cobalt-manganese ternary cathode materials $LiNi_{0.6}Co_{0.2}Mn_{0.2}O_2$ for lithium-ion batteries: performance enhancement by modification," *Materials Horizons* **2023**, *10*, 4776–4826, doi: 10.1039/D3MH01151H.

[140] Noh, H.-J. et al., "Comparison of the structural and electrochemical properties of layered $Li[Ni_xCo_yMn_z]O_2$ (x = 1/3, 0.5, 0.6, 0.7, 0.8 and 0.85) cathode material for lithium-ion batteries," *Journal of Power Sources* **2013**, *233*, 121–130, doi: 10.1016/j.jpowsour.2013.01.063.

[141] Radin, M. D. et al., "Narrowing the Gap between Theoretical and Practical Capacities in Li–Ion Layered Oxide Cathode Materials," *Advanced Energy Materials* **2017**, *7*, 1602888, doi: 10.1002/aenm.201602888.

[142] Li, H. et al., "Updating the Structure and Electrochemistry of Li_xNiO_2 for $0 \leq x \leq 1$," *Journal of The Electrochemical Society* **2018**, *165*, A2985–A2993, doi: 10.1149/2.0381813jes.

[143] Märker, K. et al., "Evolution of Structure and Lithium Dynamics in $LiNi_{0.8}Mn_{0.1}Co_{0.1}O_2$ (NMC811) Cathodes during Electrochemical Cycling," *Chemistry of Materials* **2019**, *31*, 2545–2554, doi: 10.1021/acs.chemmater.9b00140.

[144] Biasi, L. de et al., "Between Scylla and Charybdis: Balancing Among Structural Stability and Energy Density of Layered NCM Cathode Materials for Advanced Lithium-Ion Batteries," *Journal of Physical Chemistry C* **2017**, *121*, 26163–26171, doi: 10.1021/acs.jpcc.7b06363.

[145] Kondrakov, A. O. et al., "Charge-Transfer-Induced Lattice Collapse in Ni-Rich NCM Cathode Materials during Delithiation," *Journal of Physical Chemistry C* **2017**, *121*, 24381–24388, doi: 10.1021/acs.jpcc.7b06598.

[146] Lim, J.-M. et al., "Intrinsic Origins of Crack Generation in Ni-rich $LiNi_{0.8}Mn_{0.1}Co_{0.1}O_2$ Layered Oxide Cathode Material," *Scientific reports* **2017**, *7*, 39669, doi: 10.1038/srep39669.

[147] Laubach, S. et al., "Changes in the crystal and electronic structure of $LiCoO_2$ and $LiNiO_2$ upon Li intercalation and de-intercalation," *Physical chemistry chemical physics* **2009**, *11*, 3278–3289, doi: 10.1039/B901200A.

[148] Zeng, Z. et al., "Composite cathode for all-solid-state lithium batteries: Progress and perspective," *Materials Today Physics* **2023**, *32*, 101009, doi: 10.1016/j.mtphys.2023.101009.

[149] Randau, S. et al., "On the Additive Microstructure in Composite Cathodes and Alumina-Coated Carbon Microwires for Improved All-Solid-State Batteries," *Chemistry of Materials* **2021**, *33*, 1380–1393, doi: 10.1021/acs.chemmater.0c04454.

[150] Kissel, M. et al., "Quantifying the Impact of Cathode Composite Mixing Quality on Active Mass Utilization and Reproducibility of Solid–State Battery Cells," *Advanced Energy Materials* **2025**, *15*, doi: 10.1002/aenm.202405405.

[151] Shi, T. et al., "High Active Material Loading in All–Solid–State Battery Electrode via Particle Size Optimization," *Advanced Energy Materials* **2020**, *10*, 1902881, doi: 10.1002/aenm.201902881.

[152] Laue, V. et al., "Modeling the Influence of Mixing Strategies on Microstructural Properties of All–Solid–State Electrodes," *Energy Technology* **2020**, *8*, 1801049, doi: 10.1002/ente.201801049.

[153] Kaiser, N. et al., "Ion transport limitations in all-solid-state lithium battery electrodes containing a sulfide-based electrolyte," *Journal of Power Sources* **2018**, *396*, 175–181, doi: 10.1016/j.jpowsour.2018.05.095.

[154] Hayakawa, E. et al., "Characterization of solid-electrolyte/active-material composite particles with different surface morphologies for all-solid-state batteries," *Advanced Powder Technology* **2022**, *33*, doi: 10.1016/j.apt.2022.103470.

[155] Schlautmann, E. et al., "Impact of the Solid Electrolyte Particle Size Distribution in Sulfide–Based Solid–State Battery Composites," *Advanced Energy Materials* **2023**, *13*, 2302309, doi: 10.1002/aenm.202302309.

[156] König, C. et al., "Mitigating the Ion Transport Tortuosity in Composite Cathodes of All-Solid-State Batteries by Wet Milling of the Solid Electrolyte Particles," *ACS Applied Energy Materials* **2023**, *6*, 9356–9362, doi: 10.1021/acsaem.3c01242.

[157] Hendriks, T. A. et al., "Balancing Partial Ionic and Electronic Transport for Optimized Cathode Utilization of High–Voltage $LiMn_2O_4/Li_3InCl_6$ Solid–State Batteries," *Batteries & Supercaps* **2023**, *6*, e202200544, doi: 10.1002/batt.202200544.

[158] Woolley, H. M. et al., "Toward High-Capacity Li–S Solid-State Batteries: The Role of Partial Ionic Transport in the Catholyte," *ACS Energy Letters* **2024**, *11*, 3547–3556, doi: 10.1021/acsenergylett.4c01444.

[159] Minnmann, P. et al., "Editors' Choice—Visualizing the Impact of the Composite Cathode Microstructure and Porosity on Solid-State Battery Performance," *Journal of The Electrochemical Society* **2024**, *171*, 060514, doi: 10.1149/1945-7111/ad510e.

[160] Naik, K. G.; Vishnugopi, B. S.; Mukherjee, P. P., "Kinetics or Transport: Whither Goes the Solid-State Battery Cathode?" *ACS Applied Materials and Interfaces* **2022**, *14*, 29754–29765, doi: 10.1021/acsami.2c04962.

[161] Ruess, R. et al., "Influence of NCM Particle Cracking on Kinetics of Lithium-Ion Batteries with Liquid or Solid Electrolyte," *Journal of The Electrochemical Society* **2020**, *167*, 100532, doi: 10.1149/1945-7111/ab9a2c.

[162] Kim, D. H. et al., "Infiltration of Solution-Processable Solid Electrolytes into Conventional Li-Ion-Battery Electrodes for All-Solid-State Li-Ion Batteries," *Nano letters* **2017**, *17*, 3013–3020, doi: 10.1021/acs.nanolett.7b00330.

[163] Kim, M.-J. et al., "Facile fabrication of solution-processed solid-electrolytes for high-energy-density all-solid-state-batteries by enhanced interfacial contact," *Scientific Reports* **2020**, *10*, 11923, doi: 10.1038/s41598-020-68885-4.

[164] Wang, C. et al., "Interface-assisted in-situ growth of halide electrolytes eliminating interfacial challenges of all-inorganic solid-state batteries," *Nano Energy* **2020**, *76*, 105015, doi: 10.1016/j.nanoen.2020.105015.

[165] Zhang, J. et al., "Microstructure engineering of solid-state composite cathode via solvent-assisted processing," *Joule* **2021**, *5*, 1845–1859, doi: 10.1016/j.joule.2021.05.017.

[166] Kawaguchi, T.; Nakamura, H.; Watano, S., "Dry coating of electrode particle with model particle of sulfide solid electrolytes for all-solid-state secondary battery," *Powder Technology* **2018**, *323*, 581–587, doi: 10.1016/j.powtec.2016.03.055.

[167] Kawaguchi, T.; Nakamura, H.; Watano, S., "Parametric study of dry coating process of electrode particle with model material of sulfide solid electrolytes for all-solid-state battery," *Powder Technology* **2017**, *305*, 241–249, doi: 10.1016/j.powtec.2016.09.085.

[168] Hayakawa, E. et al., "Dry mixing of cathode composite powder for all-solid-state batteries using a high-shear mixer," *Advanced Powder Technology* **2022**, *33*, 103705, doi: 10.1016/j.apt.2022.103705.

[169] Burmeister, C. F. et al., "Characterization of Stressing Conditions in a High Energy Ball Mill by Discrete Element Simulations," *Processes* **2022**, *10*, 692, doi: 10.3390/pr10040692.

[170] Burmeister, C. et al., "Dry grinding in planetary ball mills: Evaluation of a stressing model," *Advanced Powder Technology* **2018**, *29*, 191–201, doi: 10.1016/j.apt.2017.11.001.

[171] Kwade, A., "A Stressing Model for the Description and Optimization of Grinding Processes," *Chemical Engineering & Technology* **2003**, *26*, 199–205, doi: 10.1002/ceat.200390029.

[172] Gol, A. de et al., "Electro–Chemo–Mechanical Degradation in Solid–State Batteries: A Review of Microscale and Multiphysics Modeling," *Advanced Energy Materials* **2024**, 2403255, doi: 10.1002/aenm.202403255.

[173] Hertle, J. et al., "Benchmarking of Coatings for Cathode Active Materials in Solid-State Batteries Using Surface Analysis and Reference Electrodes," *ACS Applied Materials and Interfaces* **2024**, *16*, 9400–9413, doi: 10.1021/acsami.3c15723.

[174] Mangani, L. R.; Villevieille, C., "Mechanical vs. chemical stability of sulphide-based solid-state batteries. Which one is the biggest challenge to tackle? Overview of solid-state batteries and hybrid solid state batteries," *Journal of Materials Chemistry A* **2020**, *8*, 10150–10167, doi: 10.1039/D0TA02984J.

[175] Koerver, R. et al., "Redox-active cathode interphases in solid-state batteries," *Journal of Materials Chemistry A* **2017**, *5*, 22750–22760, doi: 10.1039/C7TA07641J.

[176] Walther, F. et al., "Visualization of the Interfacial Decomposition of Composite Cathodes in Argyrodite-Based All-Solid-State Batteries Using Time-of-Flight Secondary-Ion Mass Spectrometry," *Chemistry of Materials* **2019**, *31*, 3745–3755, doi: 10.1021/acs.chemmater.9b00770.

[177] Wang, S. et al., "Lithium Argyrodite as Solid Electrolyte and Cathode Precursor for Solid–State Batteries with Long Cycle Life," *Advanced Energy Materials* **2021**, *11*, 2101370, doi: 10.1002/aenm.202101370.

[178] Auvergniot, J. et al., "Redox activity of argyrodite Li_6PS_5Cl electrolyte in all-solid-state Li-ion battery: An XPS study," *Solid State Ionics* **2017**, *300*, 78–85, doi: 10.1016/j.ssi.2016.11.029.

[179] Kaeli, E. et al., "Decoupling first-cycle capacity loss mechanisms in sulfide solid-state batteries," *Energy & Environmental Science* **2025**, *18*, 1452–1463, doi: 10.1039/D4EE04908J.

[180] Kobayashi, S. et al., "Atomic-Scale Observations of Oxygen Release Degradation in Sulfide-Based All-Solid-State Batteries with Layered Oxide Cathodes," *ACS Applied Materials and Interfaces* **2022**, *14*, 39459–39466, doi: 10.1021/acsami.2c06950.

[181] Jung, R. et al., "Oxygen Release and Its Effect on the Cycling Stability of $LiNi_xMn_yCo_zO_2$ (NMC) Cathode Materials for Li-Ion Batteries," *Journal of The Electrochemical Society* **2017**, *164*, A1361–A1377, doi: 10.1149/2.0021707jes.

[182] Zhang, H. et al., "Oxygen Loss in Layered Oxide Cathodes for Li-Ion Batteries: Mechanisms, Effects, and Mitigation," *Chemical Reviews* **2022**, *122*, 5641–5681, doi: 10.1021/acs.chemrev.1c00327.

[183] Auvergniot, J. et al., "Interface Stability of Argyrodite Li_6PS_5Cl toward $LiCoO_2$, $LiNi_{1/3}Co_{1/3}Mn_{1/3}O_2$, and $LiMn_2O_4$ in Bulk All-Solid-State Batteries," *Chemistry of Materials* **2017**, *29*, 3883–3890, doi: 10.1021/acs.chemmater.6b04990.

[184] Homma, K. et al., "Optimization of a Heterogeneous Ternary Li_3PO_4–Li_3BO_3–Li_2SO_4 Mixture for Li-Ion Conductivity by Machine Learning," *Journal of Physical Chemistry C* **2020**, *124*, 12865–12870, doi: 10.1021/acs.jpcc.9b11654.

[185] Zuo, T.-T. et al., "Impact of the Chlorination of Lithium Argyrodites on the Electrolyte/Cathode Interface in Solid-State Batteries," *Angewandte Chemie International Edition* **2023**, *62*, e202213228, doi: 10.1002/anie.202213228.

[186] Zuo, T.-T. et al., "A mechanistic investigation of the $Li_{10}GeP_2S_{12}$ | $LiNi_{1-x-y}Co_xMn_yO_2$ interface stability in all-solid-state lithium batteries," *Nature Communications* **2021**, *12*, 1–10, doi: 10.1038/s41467-021-26895-4.

[187] Morino, Y., "Degradation rate at the Solid–Solid interface of sulfide-based solid Electrolyte–Cathode active material," *Journal of Power Sources* **2022**, *541*, 231672, doi: 10.1016/j.jpowsour.2022.231672.

[188] Li, X. et al., "Unravelling the Chemistry and Microstructure Evolution of a Cathodic Interface in Sulfide-Based All-Solid-State Li-Ion Batteries," *ACS Energy Letters* **2019**, *4*, 2480–2488, doi: 10.1021/acsenergylett.9b01676.

[189] Joshi, T. et al., "Effects of Dissolved Transition Metals on the Electrochemical Performance and SEI Growth in Lithium-Ion Batteries," *Journal of The Electrochemical Society* **2014**, *161*, A1915–A1921, doi: 10.1149/2.0861412jes.

[190] Sakuda, A.; Hayashi, A.; Tatsumisago, M., "Interfacial Observation between $LiCoO_2$ Electrode and Li_2S–P_2S_5 Solid Electrolytes of All-Solid-State Lithium Secondary Batteries Using Transmission Electron Microscopy," *Chemistry of Materials* **2010**, *22*, 949–956, doi: 10.1021/cm901819c.

[191] Walther, F. et al., "The Working Principle of a Li_2CO_3/$LiNbO_3$ Coating on NCM for Thiophosphate-Based All-Solid-State Batteries," *Chemistry of Materials* **2021**, *33*, 2110–2125, doi: 10.1021/acs.chemmater.0c04660.

[192] Lin, F. et al., "Surface reconstruction and chemical evolution of stoichiometric layered cathode materials for lithium-ion batteries," *Nature Communications* **2014**, *5*, 3529, doi: 10.1038/ncomms4529.

[193] Ryu, H.-H. et al., "Capacity Fading Mechanisms in Ni-Rich Single-Crystal NCM Cathodes," *ACS Energy Letters* **2021**, *6*, 2726–2734, doi: 10.1021/acsenergylett.1c01089.

[194] R. Hausbrand et al., "Fundamental degradation mechanisms of layered oxide Li-ion battery cathode materials: Methodology, insights and novel approaches," *Materials Science and Engineering B: Solid-State Materials for Advanced Technology* **2015**, *192*, 3–25, doi: 10.1016/j.mseb.2014.11.014.

[195] Kim, J. et al., "A facile approach to form an artificial CEI layer induced by residual Li compounds on $LiNi_{0.9}Co_{0.05}Mn_{0.05}O_2$ and Li_6PS_5Cl for all-solid-state batteries," *eTransportation* **2024**, *19*, 100306, doi: 10.1016/j.etran.2023.100306.

[196] Strauss, F. et al., "Gas Evolution in Lithium-Ion Batteries: Solid versus Liquid Electrolyte," *ACS Applied Materials and Interfaces* **2020**, *12*, 20462–20468, doi: 10.1021/acsami.0c02872.

[197] Koerver, R. et al., "Chemo-mechanical expansion of lithium electrode materials – on the route to mechanically optimized all-solid-state batteries," *Energy & Environmental Science* **2018**, *11*, 2142–2158, doi: 10.1039/C8EE00907D.

[198] Strauss, F. et al., "Rational Design of Quasi-Zero-Strain NCM Cathode Materials for Minimizing Volume Change Effects in All-Solid-State Batteries," *ACS Materials Letters* **2020**, *2*, 84–88, doi: 10.1021/acsmaterialslett.9b00441.

[199] Trevisanello, E. et al., "Polycrystalline and Single Crystalline NCM Cathode Materials—Quantifying Particle Cracking, Active Surface Area, and Lithium Diffusion," *Advanced Energy Materials* **2021**, *11*, 2003400, doi: 10.1002/aenm.202003400.

[200] Conforto, G. et al., "Editors' Choice—Quantification of the Impact of Chemo-Mechanical Degradation on the Performance and Cycling Stability of NCM-Based Cathodes in Solid-State Li-Ion Batteries," *Journal of The Electrochemical Society* **2021**, *168*, 070546, doi: 10.1149/1945-7111/ac13d2.

[201] Shi, B.-X. et al., "Mitigating Contact Loss in Li_6PS_5Cl–Based Solid–State Batteries Using a Thin Cationic Polymer Coating on NCM," *Advanced Energy Materials* **2023**, *13*, 2300310, doi: 10.1002/aenm.202300310.

[202] Jeon, H. et al., "Tailoring shape and exposed crystal facet of single-crystal layered-oxide cathode particles for all-solid-state batteries," *Chemical Engineering Journal* **2022**, *445*, 136828, doi: 10.1016/j.cej.2022.136828.

[203] Ahaliabadeh, Z. et al., "Extensive comparison of doping and coating strategies for Ni-rich positive electrode materials," *Journal of Power Sources* **2022**, *540*, 231633, doi: 10.1016/j.jpowsour.2022.231633.

[204] Liu, A. et al., "Investigating the Effects of Magnesium Doping in Various Ni-Rich Positive Electrode Materials for Lithium Ion Batteries," *Journal of The Electrochemical Society* **2019**, *166*, A4025–A4033, doi: 10.1149/2.1101915jes.

[205] Nakamura, T. et al., "Guidelines for All-Solid-State Battery Design and Electrode Buffer Layers Based on Chemical Potential Profile Calculation," *ACS Applied Materials and Interfaces* **2019**, *11*, 19968–19976, doi: 10.1021/acsami.9b03053.

[206] Zhang, R. et al., "Conformal Li_2HfO_3/HfO_2 Nanoparticle Coatings on Layered Ni-Rich Oxide Cathodes for Stabilizing Interfaces in All-Solid-State Batteries," *Chemistry of Materials* **2023**, *35*, 6835–6844, doi: 10.1021/acs.chemmater.3c01116.

[207] Payandeh, S. et al., "Tailoring the $LiNbO_3$ coating of Ni-rich cathode materials for stable and high-performance all-solid-state batteries," *Nano Research Energy* **2022**, *1*, e9120016, doi: 10.26599/NRE.2022.9120016.

[208] Shi, B.-X. et al., "Lithiated polymer coating for interface stabilization in Li_6PS_5Cl-based solid-state batteries with high-nickel NCM," *Journal of Materials Chemistry A* **2025**, *13*, 2600–2614, doi: 10.1039/D4TA07265K.

[209] Jin, F. et al., "Elucidating the Impact of Li_3InCl_6-Coated $LiNi_{0.8}Co_{0.15}Al_{0.05}O_2$ on the Electro-Chemo-Mechanics of Li_6PS_5Cl-Based Solid-State Batteries," *Chemistry of Materials* **2024**, *36*, 6017–6026, doi: 10.1021/acs.chemmater.4c00515.

[210] Strauss, F. et al., "On the role of surface carbonate species in determining the cycling performance of all-solid-state batteries," *Materials Futures* **2022**, *1*, 023501, doi: 10.1088/2752-5724/ac5b7d.

[211] Aktekin, B. et al., "The Formation of Residual Lithium Compounds on Ni–Rich NCM Oxides: Their Impact on the Electrochemical Performance of Sulfide–Based ASSBs," *Advanced Functional Materials* **2024**, 2313252, doi: 10.1002/adfm.202313252.

[212] Kim, A.-Y. et al., "Stabilizing Effect of a Hybrid Surface Coating on a Ni-Rich NCM Cathode Material in All-Solid-State Batteries," *Chemistry of Materials* **2019**, *31*, 9664–9672, doi: 10.1021/acs.chemmater.9b02947.

[213] Bong, W. S. K. et al., "Effect of thickness and uniformity of $LiNbO_3$-coated layer on $LiNi_{0.5}Co_{0.2}Mn_{0.3}O_2$ cathode material on enhancement of cycle performance of full-cell sulfide-based all-solid-state batteries," *Journal of Power Sources* **2023**, *577*, 233259, doi: 10.1016/j.jpowsour.2023.233259.

[214] Kissel, M. et al., "Engineering the Artificial Cathode-Electrolyte Interphase Coating for Solid-State Batteries via Tailored Annealing," *Chemistry of Materials* **2025**, *37*, doi: 10.1021/acs.chemmater.4c03086.

[215] Wu, E. A. et al., "A Facile, Dry-Processed Lithium Borate-Based Cathode Coating for Improved All-Solid-State Battery Performance," *Journal of The Electrochemical Society* **2020**, *167*, 130516, doi: 10.1149/1945-7111/abb8b3.

[216] Kitsche, D. et al., "Atomic Layer Deposition Derived Zirconia Coatings on Ni-Rich Cathodes in Solid-State Batteries: Correlation Between Surface Constitution and Cycling Performance," *Small Science* **2023**, *3*, 2200073, doi: 10.1002/smsc.202200073.

[217] Xiangsi Liu et al., "Electrochemo-Mechanical Effects on Structural Integrity of Ni-Rich Cathodes with Different Microstructures in All Solid-State Batteries," *Advanced Energy Materials* **2021**, *11*, 2003583, doi: 10.1002/aenm.202003583.

[218] Wu, D. et al., "The State of Reliable Characterization and Testing of Solid-State Batteries," *ACS Energy Letters* **2025**, 2617–2630, doi: 10.1021/acsenergylett.5c00923.

[219] Doux, J.-M. et al., "Stack Pressure Considerations for Room–Temperature All–Solid–State Lithium Metal Batteries," *Advanced Energy Materials* **2020**, *10*, 1903253, doi: 10.1002/aenm.201903253.

[220] Sanderson, K., "Battery researchers strive for standardization," *Nature* **2025**, *639*, S25–S27, doi: 10.1038/d41586-025-00745-5.

[221] Vargas-Barbosa, N. M., "My cell is better than yours," *Nature Nanotechnology* **2024**, *19*, 419–420, doi: 10.1038/s41565-024-01607-3.

[222] Villevieille, C., "The challenge of studying interfaces in battery materials," *Nature nanotechnology* **2025**, *20*, 2–5, doi: 10.1038/s41565-024-01836-6.

[223] Drnec, J.; Lyonnard, S., "Battery research needs more reliable, representative and reproducible synchrotron characterizations," *Nature nanotechnology* **2025**, *20*, 584–587, doi: 10.1038/s41565-025-01921-4.

[224] Hertle, J. et al., "Miniaturization of Reference Electrodes for Solid-State Lithium-Ion Batteries," *Journal of The Electrochemical Society* **2023**, *170*, 040519, doi: 10.1149/1945-7111/accb6f.

[225] Quemin, E. et al., "An Advanced Cell for Measuring In Situ Electronic Conductivity Evolutions in All–Solid–State Battery Composites," *Advanced Energy Materials* **2023**, *13*, 2301105, doi: 10.1002/aenm.202301105.

[226] Zhang, R. et al., "Timescale identification of electrochemical processes in all-solid-state batteries using an advanced three-electrode cell setup," *Energy Storage Materials* **2025**, *75*, 104000, doi: 10.1016/j.ensm.2025.104000.

[227] Ikezawa, A. et al., "Performance of $Li_4Ti_5O_{12}$-based reference electrode for the electrochemical analysis of all-solid-state lithium-ion batteries," *Electrochemistry Communications* **2020**, *116*, 106743, doi: 10.1016/j.elecom.2020.106743.

[228] Chen, Y.-.-T. et al., "Enabling Uniform and Accurate Control of Cycling Pressure for All–Solid–State Batteries," *Advanced Energy Materials* **2024**, *14*, 2304327, doi: 10.1002/aenm.202304327.

[229] Kostopoulos, E. D.; Spyropoulos, G. C.; Kaldellis, J. K., "Real-world study for the optimal charging of electric vehicles," *Energy Reports* **2020**, *6*, 418–426, doi: 10.1016/j.egyr.2019.12.008.

[230] Geslin, A. et al., "Dynamic cycling enhances battery lifetime," *Nature Energy* **2024**, 1–9, doi: 10.1038/s41560-024-01675-8.

[231] Pohlmann, S., "Metrics and methods for moving from research to innovation in energy storage," *Nature Communications* **2022**, *13*, 1538, doi: 10.1038/s41467-022-29257-w.

[232] Wu, J. et al., "Reducing the thickness of solid-state electrolyte membranes for high-energy lithium batteries," *Energy & Environmental Science* **2021**, *14*, 12–36, doi: 10.1039/D0EE02241A.

[233] Nam, Y. J. et al., "Bendable and thin sulfide solid electrolyte film: a new electrolyte opportunity for free-standing and stackable high-energy all-solid-state lithium-ion batteries," *Nano letters* **2015**, *15*, 3317–3323, doi: 10.1021/acs.nanolett.5b00538.

[234] Scurtu, R.-G. et al., "From small batteries to big claims," *Nature nanotechnology* **2025**, 1–7, doi: 10.1038/s41565-025-01906-3.

[235] Masias, A.; Marcicki, J.; Paxton, W. A., "Opportunities and Challenges of Lithium Ion Batteries in Automotive Applications," *ACS Energy Letters* **2021**, *6*, 621–630, doi: 10.1021/acsenergylett.0c02584.

[236] Oh, D. Y. et al., "Slurry-Fabricable Li^+-Conductive Polymeric Binders for Practical All-Solid-State Lithium-Ion Batteries Enabled by Solvate Ionic Liquids," *Advanced Energy Materials* **2019**, *9*, 1802927, doi: 10.1002/aenm.201802927.

[237] Oh, D. Y. et al., "Tactical hybrids of Li^+-conductive dry polymer electrolytes with sulfide solid electrolytes: Toward practical all-solid-state batteries with wider temperature operability," *Materials Today* **2022**, *53*, 7–15, doi: 10.1016/j.mattod.2021.01.006.

[238] Kim, K. T. et al., "Tailoring Slurries Using Cosolvents and Li Salt Targeting Practical All–Solid–State Batteries Employing Sulfide Solid Electrolytes," *Advanced Energy Materials* **2021**, *11*, 2003766, doi: 10.1002/aenm.202003766.

[239] Bartsch, T. et al., "Indirect state-of-charge determination of all-solid-state battery cells by X-ray diffraction," *Chemical Communications* **2019**, *55*, 11223–11226, doi: 10.1039/C9CC04453A.

[240] Hua, Z. C. et al., "Novel nanoparticle mixing approach for the production of solid-state battery hetero-agglomerates in vibrated fluidized beds," *Powder Technology* **2025**, *458*, 120906, doi: 10.1016/j.powtec.2025.120906.

[241] Zuo, T.-T. et al., "Formation of an Artificial Cathode–Electrolyte Interphase to Suppress Interfacial Degradation of Ni-Rich Cathode Active Material with Sulfide Electrolytes for Solid-State Batteries," *ACS Energy Letters* **2023**, *8*, 1322–1329, doi: 10.1021/acsenergylett.2c02835.

[242] Lee, S. et al., "Cost–Effective Layered Oxide – Olivine Blend Cathodes for High–Rate Pulse Power Lithium–Ion Batteries," *Advanced Energy Materials* **2025**, *15*, 2403002, doi: 10.1002/aenm.202403002.

[243] Kang, M. et al., "Unlocking the Potential of Internal Li-ion transfer in Ni-Rich Cathodes Blended with $LiFePO_4$ to Address First Cycle Irreversible Capacity Loss and Degradation," *Energy & Environmental Science* **2025**, doi: 10.1039/D5EE00404G.

[244] Plank, C. et al., "A review on the distribution of relaxation times analysis: A powerful tool for process identification of electrochemical systems," *Journal of Power Sources* **2024**, *594*, 233845, doi: 10.1016/j.jpowsour.2023.233845.

[245] Jin, W. et al., "Advancements in Dry Electrode Technologies: Towards Sustainable and Efficient Battery Manufacturing," *ChemElectroChem* **2024**, *11*, e202400288, doi: 10.1002/celc.202400288.

PART IV

Appendices

A Contributions

A.1. List of Publications

[1] Maximilian Kissel, Finn Frankenberg, Thomas Demuth, Anton Lai, Niklas Laser, Daniel Wagner, Ahmed Eisa, Peter Michalowski, Kerstin Volz, Arno Kwade, Jürgen Janek. Mechanofusion-derived cathode composite microstructures for solid-state batteries: A scalable mixed conducting matrix coating approach. *Nat Commun*, 2026, 17, 3215, DOI: https://doi.org/10.1038/s41467-026-71305-2

[2] Maximilian Kissel, Felix Schnaubelt, Jill Kessler-Kühn, Sebastian L. Benz, Anton Lai, Philip Minnmann, Holger Schneider, Jürgen Janek. Toward Efficient Benchmarking of new CAM Coatings. *J. Electrochem. Soc.*, 2026, 173, 070501, DOI:https://doi.org/10.1149/1945-7111/ae55d2

[3] Kilian Vettori, Maximilian Kissel, Daniel Wagner, Steffen Schröder, Jürgen Janek. Quantifying Static Capacity Losses in Solid-State Battery Composites via Coulometric Titration Comparison. *Chem. Commun.*, 2026, 62, 5241, DOI: https://doi.org/10.1039/D5CC07213A

[4] Finn Frankenberg, Carina A. Heck, Maximilian Kissel, Martin A. Lange, Vasiliki Faka, Alexander Diener, Philipp Haase, Peter Michalowski, Wolfgang G. Zeier, Jürgen Janek, and Arno Kwade, Tailoring Composite Microstructure through Milling for Dry-Processed Sulfide-Based Solid-State Battery Cathodes, *Small*, 2025, https://doi.org/10.1002/smll.202507279

[5] Zhi Cheng Hua, Finn Frankenberg, Maximilian Kissel, Jürgen Janek, Arno Kwade, Stefan Heinrich, Novel nanoparticle mixing approach for the production of solid-state battery hetero-agglomerates in vibrated fluidized beds, *Powder Technology*, 2025, 428, 120906, DOI: https://doi.org/10.1016/j.powtec.2025.120906

[6] Maximilian Kissel, Marie Schosland, Julia Töws, Daizy Kalita, Yannik Schneider, Jill Kessler-Kühn, Steffen Schröder, Johannes Schubert, Finn Frankenberg, Arno Kwade, Anja Bielefeld, Felix H. Richter, Jürgen Janek, Quantifying the Impact of Cathode Composite Mixing Quality on Active Mass Utilization and Reproducibility of Solid-State Battery Cells. *Adv. Energy Mater.*, 2025, 2405405, DOI: https://doi.org/10.1002/aenm.202405405.

[7] Maximilian Kissel, Felix Walther, Jonas Hertle, Thomas Demuth, Ruizhuo Zhang, Philipp Brüner, Torsten Brezesinski, Kerstin Volz, Jürgen Janek, Engineering the Artificial Cathode-Electrolyte Interphase Coating for Solid-State Batteries via Tailored Annealing. *Chem. Mater.*, 2025, 37, 6, 2192–2203, DOI: https://doi.org/10.1021/acs.chemmater.4c03086.

[8] Finn Frankenberg, Maximilian Kissel, Christine Friederike Burmeister, Mark Lippke, Jürgen Janek, Arno Kwade, Investigating the production of all-solid-state battery composite cathodes by numerical simulation of the stressing conditions in a high-intensity mixer, *Powder Technology*, 2024, 435, 119403, DOI: https://doi.org/10.1016/j.powtec.2024.119403

[9] Maximilian Kissel, Lukas Porz, Till Frömling, Atsutomo Nakamura, Jürgen Rödel, Marin Alexe, Enhanced Photoconductivity at Dislocations in $SrTiO_3$. *Adv. Mater.*, 2022, 34, 2203032, DOI: https://doi.org/10.1002/adma.202203032.

A.2. List of Conference Contributions

2025 "International Congress on Particle Technology (PARTEC)" in Nuremberg, Germany (September 2025) – Oral Presentation: *Particle Processing in Solid-State Battery Cathode Development: A Physico-Chemical Perspective*

"MRS Spring" (April 2025) in Seattle, USA – Oral Presentation: *Quantifying the Mixing Quality of Composite Cathodes and its Implications for Reproducibility and Comparability of Solid-State Battery Cells*

2024 "International Meeting on Lithium Batteries" in Hongkong (June 2024) – Poster Presentation: *Assessing the Potential of the Artificial Cathode/Electrolyte Interphase Formation with Sulfide Solid Electrolytes on Ni-rich Cathode Active Materials as Protective Coating Concept*

"Advanced Battery Power" in Aachen, Germany (April 2024) – Poster Presentation: *Tuning the Artificial Cathode/Electrolyte Interphase Formation as Coating for Cathode Active Materials in Solid-State Batteries*

2023 "International Congress on Particle Technology (PARTEC)" in Nuremberg, Germany (September 2023) – Poster Presentation: *Challenges and opportunities of dry-processed heteroaggregates for all-solid-state Li-ion batteries*

B Supporting Information for Publications

B.1. Supporting Information for Publication I

Supplementary Information for

Quantifying Static Capacity Losses in Solid-State Battery Composites via Coulometric Titration Comparison

Kilian Vettori[a†*], *Maximilian Kissel*[a†], *Daniel Wagner*[a], *Steffen Schröder*[b] *and Jürgen Janek*[a*]

[a]Institute of Physical Chemistry & Center for Materials Research (ZfM/LaMa), Justus Liebig University Giessen, Heinrich-Buff-Ring 17, 35392 Giessen, Germany.

[b]Institute of Experimental Physics I & Center for Materials Research (ZfM/LaMa), Justus Liebig-University Giessen, Heinrich-Buff-Ring 16, 35392 Giessen, Germany

[†] These authors contributed equally.

Table of Contents

1. Experimental details

For all experiments, single crystalline $LiNi_{0.82}Co_{0.11}Mn_{0.07}$ (MSE Supplies LLC, Tucson, AZ, USA) was used as cathode active material (CAM). This material was further used in solid state battery cells (SSB) and liquid electrolyte battery cells (LIB). Cell assembly and storage were done in an argon-filled glovebox, with oxygen residues of $p(O_2)/p < 1.0$ ppm and water residues of $p(H_2O)/p < 1.0$ ppm.

1.1. SSB assembly

The composites were mixed in a mini vibrating mill (Pulverisette 23 from Fritsch GmbH, Idar-Oberstein, Germany) using 6 ZrO_2 balls with 5 mm diameter at 30 Hz for 15 minutes. Commercially available Li_6PS_5Cl (Argyrodite-CSMP from Posco JK Solid Solution, South Korea) was used as catholyte without further modification. The composites had different mass ratios, while the total mass of 200 mg was kept constant. For certain composites, carbon nanofibers (product number 719781 from Sigma-Aldrich, Sainz Louis, MO, USA) were used as conductive additive.

For the electrochemical half cells, an in-house made cell casing was used, and the assembly followed a standardized protocol: First, 80 mg of Li_6PS_5Cl (NEI Corporation, Somerset, NJ, USA) were filled in the mold and pressed by hand. 15 mg of the prepared cathode composite were evenly distributed on top of the separator and pressed by hand. The cell was afterwards pressed uniaxially at 375 MPa for 3 min. Then, as anode, an indium foil (Alfa Aesar, 99.99%, 9 mm diameter, 100 µm thickness) and a lithium foil (China Energy Lithium, 6 mm diameter, 100 µm thickness) were placed on the bottom side of the separator.

1.2. LIB Assembly

For the preparation of LIB cathodes, a conventional tape-casting method was employed within Ar atmosphere. The slurry comprised a mixture of NCM, carbon, and binder at a weight ratio of 94:3:3, using N-methyl-2-pyrrolidone (NMP) as solvent and was cast onto aluminum foil. The materials used were NMP (Sigma-Aldrich Chemie GmbH, Steinheim, Germany), SuperP carbon (MSE Supplies LLC, Tucson, USA), and PVDF (Arkema France, Colombes Cedex, France) as binder.

Resulting cathodes had 12 mm diameter and were pressed at 200 MPa. Within the experiments different loadings from ~5-10 mg/cm^2 were used. Currents/C-rates were calculated based on a practical capacity of 200 mAh/g, resulting in areal capacities of ~1-2 mAh/cm^2. Low cathode loadings are desired for CTC as explained in the main text. For CTC, simple two-electrode setups are sufficient, if the anode potential is constant. Thus, coin cells were assembled from a lithium chip (MSE Supplies LLC, Tucson, USA) with a diameter of 14 mm and a thickness of 600 µm and a glass fiber (GF/D – Whatman, Global Life sciences solutions USA LLC, Marlborough, USA) and a Celgard® 2325 separator (Celgard LLC, Charlotte, North Carolina, USA) and the cathode. As LE, 70 µl of LP57 (EC:EMC 3:7 (wt) + 1 M LiPF6) (BASF SE, Ludwigshafen, Germany) was used.

1.3. Electrochemical protocols

For electrochemical testing a BCS-805 Battery Cycling System (Bio-Logic, Seyssinet-Pariset, France) was used. To obtain the LIB coulometric titration curve, two formation cycles with 0.1C were applied between 3.0 and 4.3 V. Then pulses were applied with either 0.1C for 10 min or 0.05C for 20 min with 2 h relaxation.

For CTC of the SSBs, the half cells were tested under a stack pressure of about 80 MPa at 25°C. After an initial OCV period of 6h, the half cells were subjected to a formation cycle at 0.05C. Then the cells were charged at 0.05C to 3.1/3.2/3.3/3.4/3.5 V *vs* In-InLi, each time followed by at least 8 h of OCV relaxation. As a last step, they were charged to 3.53 V *vs* In-InLi, held at this potential for 12 h as preparation for XRD.

The required time of titration measurements can in principle be shortened with a minimum limit for the potential change during relaxation dV/dt. This might be valuable to minimize effects of self discharge, *e.g.* for unstable electrolytes. It has to be noted that the application of such limits was not employed here, as the SE showed great stability and the dV/dt limits showed to be sensitive to fluctuations especially at the end of relaxations where dV/dt < ΔV from voltage noise.

1.4. XRD measurement and refinement

X-ray diffraction was conducted using an Empyrean 2 powder diffractometer (Malvern Panalytical) with a Cu source in reflection mode. The SSB pellets were extracted from the cell housing and measured in a dome containing Ar atmosphere. Topas software was used for

Rietveld refinement and a LaB_6 standard measurement was used to obtain the instrumental resolution functions. Due to height deviations of the pellets, a variable zero-error function was used for the different measurements. This height deviation is an explanation for the slight shift in peak position between the pristine sample and the inactive mass phase of the composites. Please refer to SI section S4 for discussion of measurements.

2. Discussion of Assumptions and Errors during CTC

This chapter deals with uncertainties within the applied CTC procedure. First, the assumption of completely connected active material in LIBs is tested, then the important errors of the titration curve of the LIB reference are discussed in detail. Finally, the errors entering the CTC formulas are quantitatively estimated.

2.1. Assumption of complete connection of CAM in LIBs

To test this, we have applied a slow 0.05C charge up to 5.0 V to a pristine cathode. The total observed charge after an included hold at 5.0 V reveals a capacity above the theoretical one (indicated by grey dashed line in Fig S1).

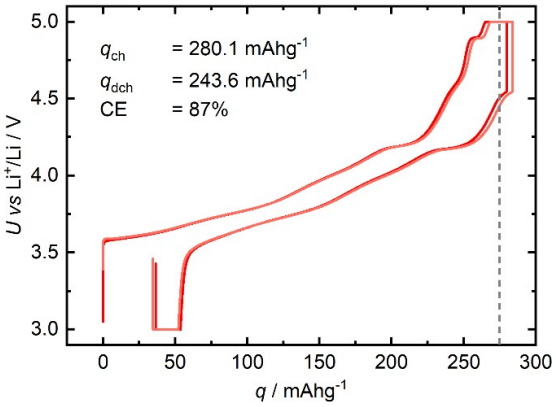

Fig S1: Dis-/charge curve of first cycle (0.05C + 4 h hold at 5 V and 24 h hold at 3 V) for two half cells (LIB). The observed specific capacity q exceeds the theoretical capacity indicated by the grey dashed line.

The observed charge certainly also contains contributions of parasitic currents and self-discharge which are difficult to quantify. Nevertheless, we believe the assumption of complete connection is justified as complete delithiation is kinetically hindered but capacities close to theoretical capacity are observed. Furthermore, the reference measurement could also have active mass utilizations below 100%, then all other measurements would show utilizations based on this reference. Thus, also a comparison among different SSB cells could be meaningful.

2.2. Suitable materials for CTC

In principle, CTC is suitable for all insertion materials that show potential evolution in near-equilibrium conditions when the stochiometry of the inserted species is varied. This applies to many active materials in various battery chemistries, most prominently layered oxides from the NCM family or $LiCoO_2$ (LCO)[1] which show solid solution behaviour over wide composition ranges.

As mentioned in the main text, the comparison of titration curves is more complicated for materials exhibiting extended voltage plateaus, where changes in stoichiometry lead to minimal variation in potential. This behavior, characteristic of two-phase reactions and staging phenomena, limits the sensitivity of voltage-based analyses to incremental composition changes. This is the case for $LiFePO_4$ (LFP)[2], $Li_4Ti_5O_{12}$ (LTO)[3] or $Na_3V_2(PO_4)_3$ (NVP)[4] exhibiting large 2-phase regions or hard carbon (HC)[5] anodes for Na-ion batteries, where a large voltage plateau due to Na insertion into nanoporous regions is observed. For such materials, suitable voltage windows (extending over the voltage plateaus) have to be chosen so that an evaluation with CTC becomes meaningful.

For conversion-type materials, voltage hysteresis, multi-electron processes, and structural rearrangements further decouple voltage response from stoichiometry,[6] as *e.g.* observed for lithium reaction with transition metal oxides such as CoO/Co_3O_4 or Fe_2O_3.

2.3. Error estimation for titration curves

For a coulometric titration curve the relaxed potentials after titration, *i.e.*, constant current steps, are measured and plotted against the obtained charge. The error handling of such titration curves

has not been done in detail in literature to the best of our knowledge but is very relevant especially for CTC. Hence, the following sections discuss uncertainties of coulometric titration during charging of NCM. Here, we present our approach, available as python script to be reused by other researchers and give multiple suggestions on how to improve the procedure further.

2.3.1. Discussion on potential uncertainties

For the titration curve equilibrated potentials (OCP) are recorded. These should be possibly free from contributions of other electrodes (best is 3-electrode setup). Here, we discuss several influences on the potential. First, ongoing lithiation of the CAM, changing the equilibrium potential and SoC (self-discharge), *e.g.* due to degradation of Li-containing compounds, in the following denoted by I_{sd}. Second, incomplete relaxation, meaning that a lithium concentration gradient from the CAM particle surfaces to particle centers leads to a diffusion controlled potential change. Additionally, we account for the instrument error of the potentiostat.

2.3.1.1. Instrument error

Instrument errors can be considered small since modern potentiostats measure currents and potentials with very high precision. For instance, the used BCS-805 Battery Cycling System (Bio-Logic, Seyssinet-Pariset, France) measures potentials with an accuracy of at least $\pm$ 0.01% of the measured value $\pm$ 0.3 mV and currents with an accuracy of 0.05% $\pm$ 0.015% of the current range.[7] With an average voltage $\bar{U} \approx 3.7\ V$ one calculates:

$$\delta U_{instr} = \pm\ 0.01\%\ U \pm 0.3\ mV \approx 0.7\ mV\ (for\ \bar{U} = 3.7\ V) \qquad (1)$$

2.3.1.2. Incomplete relaxation and self-discharge

To gain an understanding of relaxation during titration, we have plotted dU/dt of an exemplary LIB titration curve at the end of relaxation steps over OCP in Fig S2. Fig S2a reveals that dU/dt is very dependent on the evaluation time. Even when the last 600 s of 2 h of relaxation (grey datapoints) are linearly fitted, all dU/dt values are below zero and during discharge above zero, indicating not completely equilibrated concentration gradients. Fig S2b shows interpolated and

smoothed dU/dt over OCP curves for charge and discharge, corresponding to the blue datapoints in Fig S2a. The orange curve is their average.

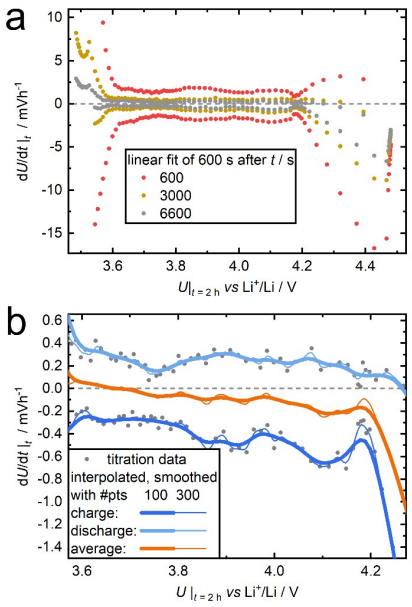

Fig S2: a) Change in potential in time dU/dt after various evaluation times during relaxation in a LIB. Positive values are from discharge, negative from charge. Deviation from zero indicates ongoing changes in lithium concentration at the particle surfaces. b) interpolated and smoothed dU/dt curves and their average (orange curve). Thick lines show interpolation with 100 datapoints and thin lines with 300.

The final dU/dt after charge contains a contribution from incomplete relaxation $\frac{\partial U}{\partial t}^{relax}$ and from self-discharge $\frac{\partial U}{\partial t}^{sd}$, both with negative signs (opposite sign of $\frac{\partial U}{\partial t}^{relax}$ for discharge). Calculating the average between dU/dt after charge and discharge (for the same potential/SoC) allows to separate $\frac{\partial U}{\partial t}^{sd}$ (Eq 2). The value can be used to calculate $\frac{\partial U}{\partial t}^{relax}$ according to Eq 3.

$$\frac{\partial U}{\partial t}^{sd} \approx \left(\frac{\partial U}{\partial t}\bigg|_{end\ of\ charge} + \frac{\partial U}{\partial t}\bigg|_{end\ of\ discharge}\right)/2 \tag{2}$$

$$\frac{\partial U}{\partial t}^{relax} \approx \frac{\partial U}{\partial t}\bigg|_{end\ of\ charge} - \frac{\partial U}{\partial t}^{sd} \tag{3}$$

For calculation of a self-discharge current, which also affects the measured charge during coulometric titration, please refer to SI section 2.2.2.2. The following equations show how U errors are calculated from both dU/dt contributions.

$$\delta U_{sd} \approx \frac{\partial U}{\partial t}^{sd} \cdot t_{relax} \tag{4}$$

$$\delta U_{relax} \approx \frac{\partial U}{\partial t}^{relax} \cdot t_{relax} \cdot f_{relax} \tag{5}$$

Here, we multiplied the potential change from self-discharge with the relaxation time t_{relax} to estimate the influence of self discharge after one titration step (Eq 4). $\frac{\partial U}{\partial t}^{relax}$ is multiplied with time t_{relax} which is scaled by an arbitrary factor f_{relax}, *e.g.* 2 (Eq 5). This factor assumes that the ongoing (linear) relaxation would need more time to equilibrate. For our well relaxed potential curves this appears reasonable but if the electrode of interest suffers from slow kinetics or the aim is to save time, then other more sophisticated extrapolations for the relaxed potentials are required.

To summarize: For the titration curve we used a symmetric statistical error due to the instrument δU_{instr} and a negative-only contribution due incomplete relaxation δU_{relax} and a positive-only

contribution δU_{sd} due to self-discharge. Care must be taken as these contributions depend on the sign of I_{pol}.

2.3.2. Discussion on charge uncertainties

This leads us to the estimation of charge uncertainties. If galvanostatic steps with identical current I_{pol} and time t_{pol} after initial charge Q_0 are applied, then the charge Q steps between datapoints are actually constant but still contain errors. These errors are in fact cumulative as also the total charge Q is the sum of all titration steps. The charge of step *i* can be expressed by Eq 6.

$$Q_i = Q_0 + \sum_1^i t_{pol} \cdot I_{pol} \tag{6}$$

This charge, as already mentioned, actually contains contributions from Faradaic efficiencies $FE \neq 1$ and self discharge current I_{sd} as shown in Eq 7.

$$Q_i = Q_0 + \sum_1^i t_{pol} \cdot I_{pol} \cdot FE - (t_{pol} + t_{relax}) \cdot I_{sd} \tag{7}$$

We suggest here an approach, where these additional contributions are estimated and summarized within errors of the actual charge Q. For our experiments we decided to assume $FE = 1$, as we believe we captured most of parasitic currents by I_{sd}. The important quantities are then Q_0, I_{pol} and I_{sd}.

2.3.2.1. Uncertainty of I_{pol}

The uncertainty of I_{pol} is given by the instrument error of the potentiostat[7] and results in an error in measured charge Q. For our titration settings ($I_{pol} = 52.5\ \mu A, I_{range} = 1\ mA, t_{pol} = 20\ min$) the errors can be calculated:

$$\delta I_{instr} = \pm\, 0.05\%\; I_{pol} \pm 0.015\%\; I_{range} \approx 0.18\ \mu A \tag{8}$$

$$\delta Q_{instr} = \delta I_{instr} \cdot t_{pol} \;\approx\; 0.06\ \mu Ah \tag{9}$$

2.3.2.2. Self-discharge current I_{sd}

Based on Fig S2 one can estimate I_{sd}. This represents a slightly modified version for a quantification of I_{sd} compared to common approaches which are well described in numerous publications.[8,9] There, much longer relaxation times are used and thus dU/dt is assumed to be only due to I_{sd}. Here, we chose an approach utilizing the potential fading $\frac{\partial U}{\partial t}^{sd}$ due to self-discharge and the slope of the titration curve itself.

$$I_{sd}(U) \approx \frac{\partial U}{\partial t}^{sd}\Big|_U \cdot \frac{\partial q}{\partial U}\Big|_U \cdot m_{CAM} \tag{10}$$

With this equation, I_{sd} is estimated as shown in Fig S3. For our procedure, we allowed only 0 > $\frac{\partial U}{\partial t}^{sd}$ > $\frac{\partial U}{\partial t}^{sd,max}$, with $\frac{\partial U}{\partial t}^{sd,max}$ being evaluated at 4.1 V to be 0.2 µV/s. At this potential the H2-H3 transformation and the according peak in dq/dU curves lead to large uncertainty and these high potentials are to be avoided for CTC. Further we estimate an average $\bar{I}_{sd}$ during the time of formation $t_{formation}$ in order to determine the initial Q error from I_{sd} simply via $\Delta Q_{sd,formation} = t_{formation} \cdot \bar{I}_{sd}$.

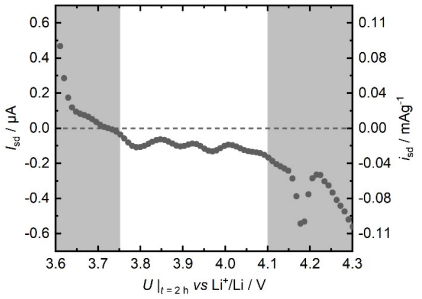

Fig S3: Self discharge current I_{sd} over potential as determined from Equation 10. Right axis shows i_{sd}, which is normalized to the mass of active material via $i_{sd} = I_{sd}/m_{CAM}$.

2.3.3. Mass uncertainty

The mass error is the most important factor when calculating $q = Q/m$. First, the effect of different cathode loadings in the LIB is discussed. Here, a higher cathode loading of the LIB can lead to more kinetic hindrance, and thus, errors in the reference titration curve. To show that the LIB reference used for CTC was unaffected from influence of loading, we performed coulometric titration on cathodes with varying loading as shown in Fig S4a.

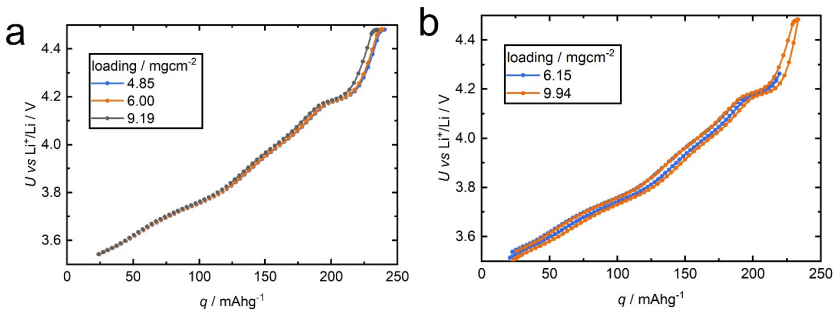

Fig S4: Titration curve (CAM in LIB) details. a) negligible effect of increasing cathode loadings below 4.2 V. b) Unexpected offset of titration curve between charge and discharge.

Here, the titration curves of the 6.00 mg/cm^2 cathode shows complete overlap with the 4.85 mg/cm^2 cathode. At 9.19 mg/cm^2 we observe a slight offset from the other curves, especially above 4.2 V. These potentials were avoided within the CTC protocol. The offset itself could be caused by incomplete relaxation but also by to static CAM loss, when CAM particles are no longer well connected within thick electrodes. As discussed in the main text, one deals with a tradeoff between high accuracy during weighing with increased loadings but more severe kinetic effects when concentration gradients within the cathode appear.

We also performed coulometric titration for charge and discharge and observed some hysteresis (Fig S4b), which deviates from the expected behavior of a characteristic titration curve. We believe this could be due to direction dependent phase transition behavior between the H2 and “quasi” H3 phase (seen in the orange curve) and due to lowered *FE* above 4.4 V when the cutoff potential is reached during polarization (orange and blue). In general, hysteresis behavior,

as *e.g.* during de-/lithiation of silicon, requires more sophisticated approaches. In our study, we chose to use titration curves during charge, as they show good overlap.

Regarding the mass error itself, we typically consider a weighing error of ≈ 0.1 mg if weighed masses are low. To understand the mass error during titration better, we used an experimental approach. Here, we explain the deviation of specific charges of N cells (with mass m_j and total charge Q_j at a given potential, here 4.15 V) from an average value $\bar{q}$ only by a mass error.

$$\delta m \approx \frac{1}{N}\sum_{j=1}^{N}\frac{Q_j}{\bar{q}} - m_j \tag{11}$$

For 6 tested cells we obtained δm ≈ 0.09 mg. With low loadings of ≈ 4 mg this corresponds to 2.3%.

2.3.4. Resulting uncertainties for titration curve

Based on the discussions above we included the following errors (Table 1) for the display of the titration curve of the LIB reference. Some of the errors are handled separately by the python script since this allows us to cancel errors for calculating ΔQ between two potentials. (see SI section 2.3)

Table 1: List of error contributions to titration curves (LIB)

error	type	sign
δU_{instr}	statistic	$\pm$
δU_{relax}	systematic	$-$ (for charge)
δU_{sd}	systematic	$+$ (for charge)
δQ_{instr}	statistic, cumulative	$\pm$
δQ_{sd}	systematic, cumulative	$-$
δm	statistic (systematic for q)	$\pm$

Since all q values of the titration curve are affected systematically, the listed uncertainties are added linearly. Here all charge contributions with same signs are simply added for $\delta Q_{\pm}$.

$$\Delta q_{\pm} \approx \frac{\delta Q_{\pm}}{m_{CAM}} + q \cdot \frac{\delta m}{m_{CAM}} \tag{12}$$

With this the following titration curve with error bands can be plotted in Fig S5.

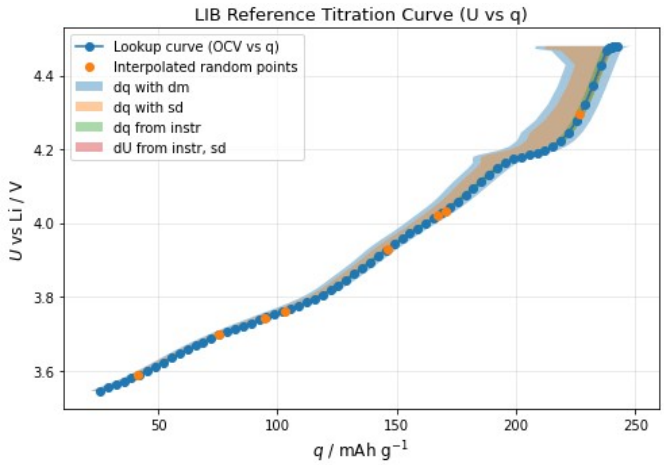

Fig S5: Resulting titration curve with error bands. This is also the output of the python script.

Here we see the inherent problem of cumulative errors for Q and the influence of mass error at higher specific charges. Especially at high SoC the influence of cumulative Q errors from self-discharge leads to large errors with negative sign. Also, potential plateaus as visible at around 4.2 V lead to increased uncertainty in q. This is expected as a slight change in potential corresponds to more charge if compared to steeper regions in the titration curve.

2.4. Errors of CTC

When applying CTC, a specific charge difference $^{\Delta q_{LIB}}$ between two potentials, $^{U_1 < U_2}$, is looked up from the titration curve shown in Fig S5. Since the q values share parts of their errors, these cancel out in the difference $^{\Delta q_{LIB}}$. In the following, the error propagation of the LIB reference titration curve and the "look-up" values of the SSB cell are discussed.

The active mass $^{m_{CAM.act}}$ of the SSB is calculated with Eq 13.

$$m_{CAM,act} = \frac{\Delta Q_{SSB}(U_1,U_2)}{\Delta q_{LIB}(U_1,U_2)} \qquad (13)$$

For our evaluation we estimated errors of $^{Q_{SSB}}$ and potentials from potentiostat accuracy and furthermore included a potential error with negative sign from incomplete relaxation again by

evaluating dU/dt at the end of relaxation periods. For δU_{relax} the relaxation time is scaled again by an arbitrary factor $f_{relax,SSB}$, in our case 1.63 (corresponding to additional 5 h of relaxation). We believe this captures the biggest error as slow kinetics pose the biggest challenge for SSBs. For calculating active mass utilization $\theta_{CAM,act}$ the weighing error enters as well.

The following table summarizes the errors for the SSB:

Table 2: Error contributions for SSB

error	type	sign
δU_{instr}	statistic	$\pm$
δU_{relax}	systematic	$^-$ (for charge)
δQ_{instr}	statistic, cumulative	$\pm$
δm	statistic (systematic for q)	$\pm$

For eq 13 we have to lookup $\Delta q_{LIB}(U_1,U_2)$ from the titration curve. Here the errors of $U_1$and U_2 and the errors of the titration curve have to be propagated. In the following the quantities belong to the LIB (reference) curve by default and are indicated by SSB otherwise:

For the calculation of $\Delta q_{LIB}(U_1,U_2)$ itself we need to compute:

$$\Delta q = \frac{Q(U_2) - Q(U_1)}{m_{CAM,LIB}} \tag{14}$$

Then we check the sensitivity to perturbations in potential by the derivative at $U_1$and U_2.

$$A = \frac{dQ}{dU}(U_2),\ B = -\frac{dQ}{dU}(U_1) \tag{15}$$

The resulting errors for Q from $U_1$and U_2 ($i = 1,2$) are then dependent on the SSB and LIB measurement. Since both can contain “deterministic” contributions, positive and negative error contributions are denoted by $\pm$ in the index:

$$\delta U_{i,\pm} = \delta U_{i,SSB,\pm} + \delta U_{i,\pm} \tag{16}$$

(17)

$$\delta Q_{U,\pm} = A \cdot \delta U_{2,\pm} + B \cdot \delta U_{1,\pm}$$

Now the Q errors can be calculated. These are composed of $^{\delta Q_{U,\pm}}$ and the shared, cumulative contributions $^{\delta Q_{sd}}$, $^{\delta Q_{instr}}$. The latter cancel partially as shown in eq 18,19.

$$\delta Q_{+} = \delta Q_{U,+} + \delta Q_{instr}(U_2) - \delta Q_{instr}(U_1) \quad (18)$$

$$\delta Q_{-} = \delta Q_{U,-} + \delta Q_{instr}(U_2) - \delta Q_{instr}(U_1) + \delta Q_{sd}(U_2) - \delta Q_{sd}(U_1) \quad (19)$$

Now we need to introduce the mass error (δm) to get from Q data to specific capacities.

$$\delta q_m = \Delta q \cdot \frac{\delta m}{m_{AM}} \quad (20)$$

The final uncertainties in q are then:

$$\delta q_{\pm} = \frac{\delta Q_{\pm}}{m_{AM}} + \delta q_m \quad (21)$$

With the resulting (asymmetric) errors of $^{\Delta q_{LIB}(U_1,U_2)}$ and the errors of $^{\Delta Q_{SSB}(U_1,U_2)}$, the resulting error of $^{m_{CAM,act}}$ can be easily calculated (all Q errors for SSB are combined in $^{\delta Q_{SSB}}$):

$$\delta m_{CAM,act,\pm} = \pm \frac{Q_{SSB} \pm \delta Q_{SSB}}{q_{LIB} \mp \delta q_{\pm}} \mp \frac{Q_{SSB}}{q_{LIB}} \quad (22)$$

Eq 23 gives then the propagated error for $^{\theta_{CAM,act}}$

$$\delta \theta_{CAM,act,\pm} = \pm \frac{m_{CAM,act} \pm \delta m_{CAM,act,\pm}}{m_{CAM,tot} \mp \delta m_{CAM,tot}} \mp \frac{m_{CAM,act}}{m_{CAM,tot}} \quad (23)$$

3. Application of CTC to different SSB cells

The following section deals with the application of CTC to various SSB cells. The data evaluation is done with the Python script provided on github.[10]

3.1. Conversion to LIB reference potential

It might be necessary to use a different anode or reference electrode potential within the SSB compared to the reference titration measurement in LE. For the SSB cells of this study a typical In-InLi anode instead of pure Li metal was used for stability reasons. If SSB and LIB have varying reference electrodes, then the recorded cell voltages have to be converted to the LIB reference potential. This is only meaningful if the used reference potential within the SSB (anode or reference electrode) is stable and known.[11]

E.g., for the In-InLi two phase voltage plateau (employed in this study) an offset of +620 mV *vs* Li^+/Li is applied.[12] The accuracy of the offset can be checked by comparing the voltage of plateaus in titration curves of the investigated CAM or with more effort in additional cells of the type: SSB anode| SE | LIB anode (if applicable). A CAM titration curve becomes immediately distorted if the (relaxed) anode potential is not stable over the course of titration. To ensure stability, capacitively oversized anodes might be helpful.

3.2. Multiple potential steps

One approach to crosscheck results for $m_{CAM,act}$ or $\theta_{CAM,act}$, is the application of the CTC method at multiple relaxation potentials. Fig S6 shows exemplary output of the used python script for “good” and “bad” SSB. This labeling indicates that different cathode compositions and preparation protocols were used, for which varying degrees of CAM utilization are expected. For “good” SSB a mixture of CAM:SE:CNF with ratio of 70:30:1 and for “bad” SSB a mixture of CAM:SE of 60:40 was used. For more experimental details check section S1.1.

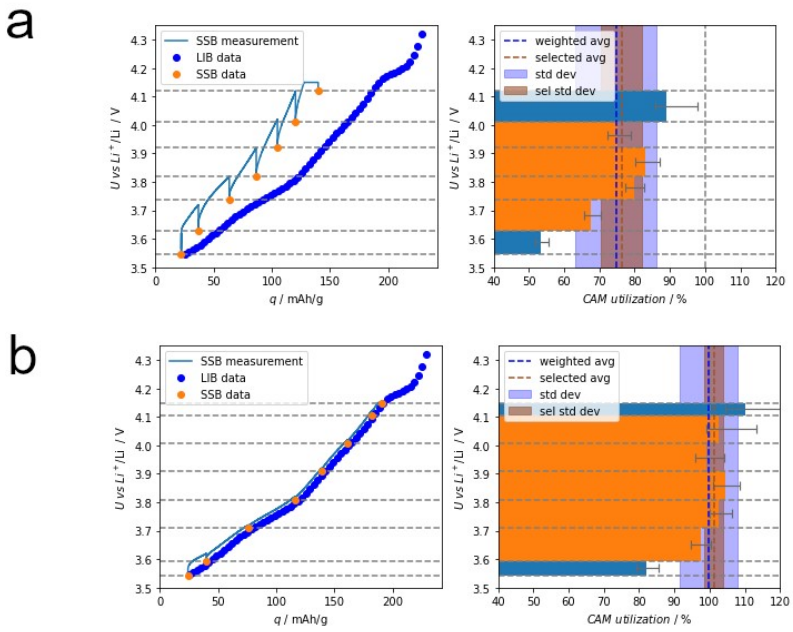

Fig S6: Result of Python script for CTC between different potential steps for a) "bad SSB" and b) "good SSB". Horizontal lines indicate voltage steps. In the right diagrams, each voltage step shows the corresponding $\theta_{CAM,act}$ result with error bars in grey. Averaged $\theta_{CAM,act}$ values are indicated via vertical dashed lines, standard deviations as transparent areas. A selected average is shown in orange/brown, for voltage steps with good kinetics.

For each potential step (indicated via horizontal lines) one result with uncertainty for $\theta_{CAM,act}$ can be calculated. Assuming constant $\theta_{CAM,act}$ during titration and fulfilled requirements for CTC (as discussed in the main text) means these $\theta_{CAM,act}$ can be averaged. The average and standard deviation for the exemplary "good" and "bad" SSB are shown in Fig S6 (right side) as dashed blue line and transparent blue. Additionally, we have incorporated the functionality in the python code to select a voltage window for a "selected" average. This can be useful to avoid voltage regions with bad kinetics (as for the presented SSBs at high and low potentials/SoC) or where side reactions are expected (*e.g.* if the SE in a given system shows reversible capacity). The

respective result is indicated as orange/brown in Fig S6, which is also the value given in the main text.

3.3. Various composite mixtures

We have tried different compositions to obtain a low CAM utilization in SSB composites and applied CTC to them. While the cells showed bad performance even during 0.05C cycling, CTC revealed that the capacity losses are mainly due to kinetics.

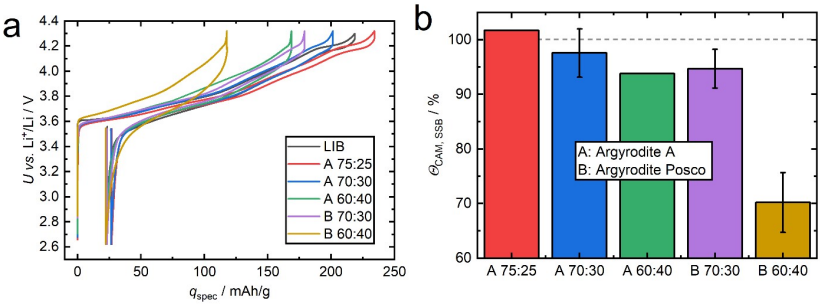

Fig S7: a) Performance during 1st charge of various SSB compositions. *A* and *B* refer to different Li_6PS_5Cl catholyte batches from different suppliers. b) Static CAM utilizations measured via CTC. Error bars here represent standard deviation of the average from multiple cells.

4. XRD measurements

Fig S8 shows complete diffractograms of pristine composite use for two good and bad SSBs each.

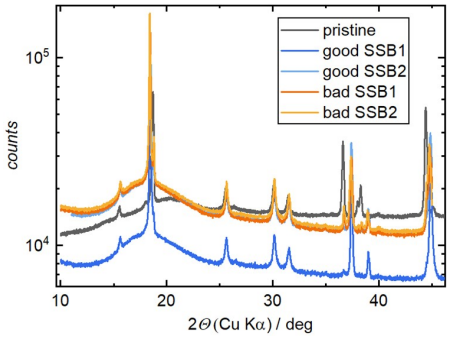

Fig S8: Complete diffractograms of composite pellets

To investigate the reflex shifting of NCM82 during delithiation, we conducted *in situ* XRD measurements using a Malvern Panalytical Empyrean 3 diffractometer equipped with a Molybdenum (Mo) source. The measurements were performed in transmission mode on a LIB in a pouch cell configuration, where no inactive material was expected. Two angle regions of interest are shown in Fig S9.

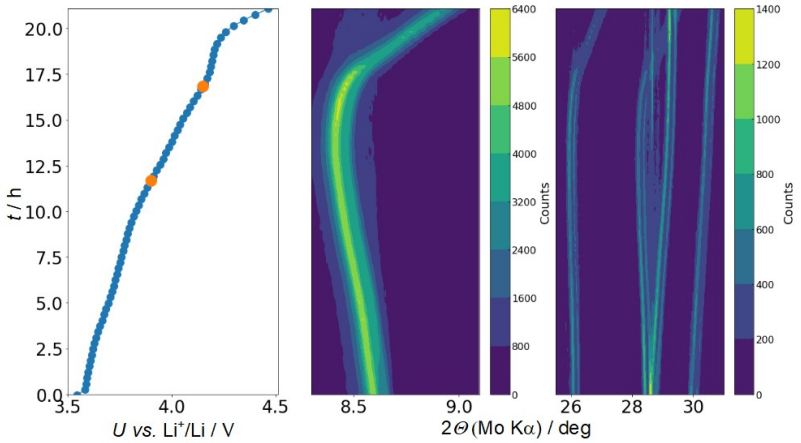

Fig S9: In-situ XRD measurement on LIB in pouch cell.

5. SSB performance normalized to $m_{CAM,act}$

With CTC it is possible to differentiate between static and kinetic capacity losses in SSBs.[13] For the two tested cells (good SSB and bad SSB) the 1st charges were normalized to the determined actual mass (meaning no static capacity losses). The remaining capacity loss is defined as "kinetic", shown as red in Fig S10.

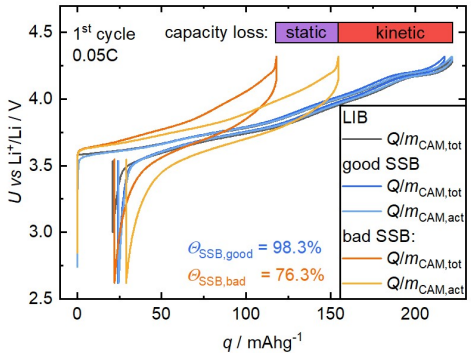

Fig S10: Schematic showing static and kinetic capacity losses. 1st cycle charge curves for SSBs are scaled by their actual mass of CAM (determined via CTC) and capacity losses for the "bad SSB" are indicated with purple and red.

6. Kinetic effects during LIB charging

To showcase how kinetic effects lead to a deviation of the charge curve from the titration curve, we have performed a rate test on the LIB. Fig S11 shows mainly increasing overpotentials but especially in regions of kinetic hindrance (low and high potentials) more complex behavior is observed.

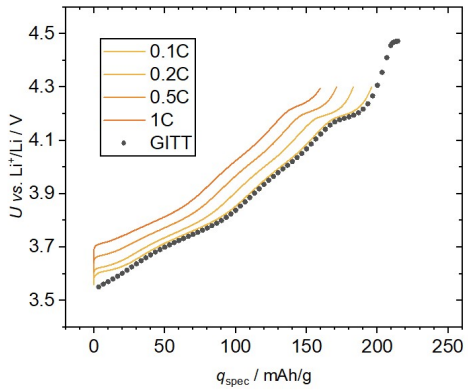

Fig S11: Kinetic effects on charge curve of LIB at different C-rates.

References

1 K. Mizushima, P. C. Jones, P. J. Wiseman and J. B. Goodenough, *Materials Research Bulletin*, 1980, **15**, 783–789.

2 A. K. Padhi, K. S. Nanjundaswamy and J. B. Goodenough, *J. Electrochem. Soc.*, 1997, **144**, 1188–1194.

3 T. Ohzuku, A. Ueda and N. Yamamoto, *J. Electrochem. Soc.*, 1995, **142**, 1431–1435.

4 G. Li, D. Jiang, H. Wang, X. Lan, H. Zhong and Y. Jiang, *Journal of Power Sources*, 2014, **265**, 325–334.

5 D. A. Stevens and J. R. Dahn, *Journal of The Electrochemical Society*, 2000, **147**, 1271.

6 J. Cabana, L. Monconduit, D. Larcher and M. R. Palacín, *Advanced Materials*, 2010, **22**, E170-92.

7 BioLogic, https://my.biologic.net/products/bcs-800-superseded/, (accessed 8 December 2025).

8 T. Roth, L. Streck, A. Graule, P. Niehoff and A. Jossen, *J. Electrochem. Soc.*, 2023, **170**, 20502.

9 L. Streck, T. Roth, P. Keil, B. Strehle, S. Ludmann and A. Jossen, *J. Electrochem. Soc.*, 2023, **170**, 40520.

10 Kilian Vettori, *CTC-data-analysis*, Zenodo. DOI: 10.5281/zenodo.17967963.

11 R. Zhang, A. Kondrakov, J. Janek and T. Brezesinski, *ACS Nano*, 2025. DOI: 10.1021/acsnano.5c17276.

12 A. L. Santhosha, Lukas Medenbach, Johannes R. Buchheim and Philipp Adelhelm, *Batteries & Supercaps*, 2019, **2**, 524–529.

13 M. Kissel, M. Schosland, J. Töws, D. Kalita, Y. Schneider, J. Kessler-Kühn, S. Schröder, J. Schubert, F. Frankenberg, A. Kwade, A. Bielefeld, F. H. Richter and J. Janek, *Advanced Energy Materials*, 2025, **15**. DOI: 10.1002/aenm.202405405.

B.2. Supporting Information for Publication II

ADVANCED ENERGY MATERIALS

Supporting Information

for *Adv. Energy Mater.*, DOI 10.1002/aenm.202405405

Quantifying the Impact of Cathode Composite Mixing Quality on Active Mass Utilization and Reproducibility of Solid-State Battery Cells

*Maximilian Kissel, Marie Schosland, Julia Töws, Daizy Kalita, Yannik Schneider, Jill Kessler-Kühn, Steffen Schröder, Johannes Schubert, Finn Frankenberg, Arno Kwade, Anja Bielefeld, Felix H. Richter and Jürgen Janek**

Supporting Information for

Quantifying the Impact of Cathode Composite Mixing Quality

on Active Mass Utilization and Reproducibility of Solid-State Battery Cells

Maximilian Kissel[1,2], Marie Schosland[1,2], Julia Töws[1,2], Daizy Kalita[1,2], Yannik Schneider[1,2], Jill Kessler-Kühn[1,2], Steffen Schröder[1,2], Johannes Schubert[1,2], Finn Frankenberg[3], Arno Kwade[3], Anja Bielefeld[1,2], Felix H. Richter[1,2], Jürgen Janek[1,2]*

[1]Institute of Physical Chemistry, Justus-Liebig-University Giessen,
Heinrich-Buff-Ring 17, 35392 Giessen, Germany.

[2]Center for Materials Research (ZfM/LaMa), Justus-Liebig-University Giessen,
Heinrich-Buff-Ring 16, 35392 Giessen, Germany.

[3]Institute for Particle Technology, Volkmaroder Straße 5, Braunschweig, 38104, Germany

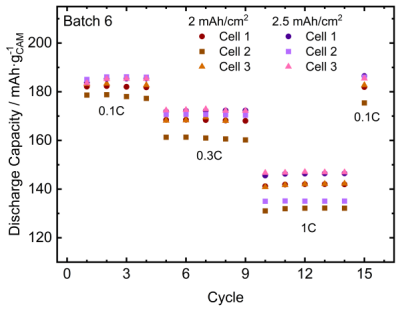

***Figure S1**. Influence of cathode loading on the achievable capacities. The specific capacities are referred to the total CAM mass. The same composite batch has been used (batch 6).*

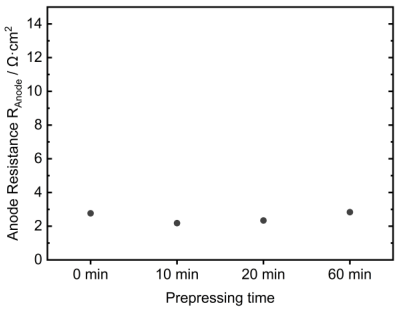

***Figure S2**. Influence of prepressing the cell for different times on the anode contribution to the resistance. The prepressing time has no influence.*

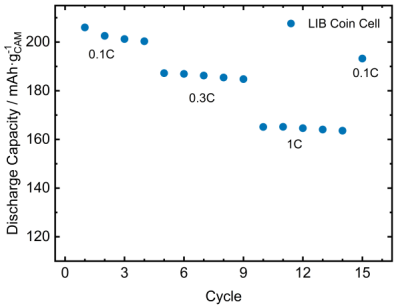

***Figure S3**. Specific discharge capacities obtained for a liquid cell during the benchmarking.*

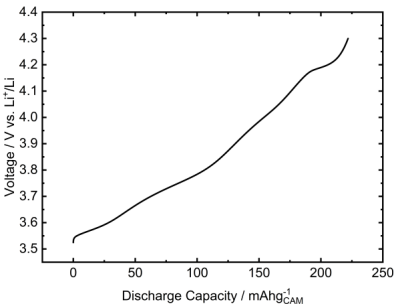

***Figure S4**. Quasi-OCP curve (0.02C) of a lithium-ion battery cell with the same CAM taken as reference for active mass determination.*

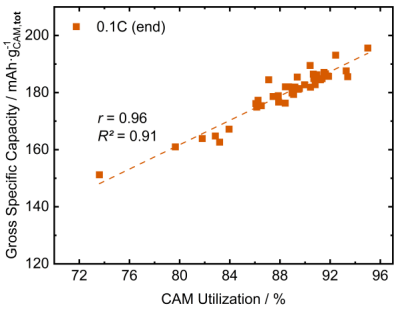

***Figure S5**. Correlation plot between the gross specific capacity measured at the end of the benchmarking program and CAM utilization.*

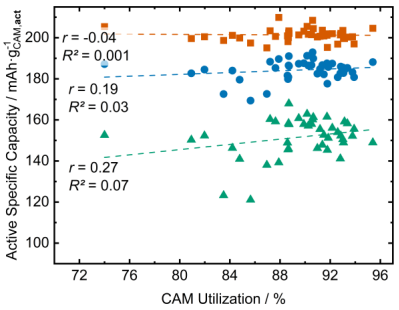

***Figure S6**. Linear regression results for the CAM utilization and active specific capacities at different C-rates.*

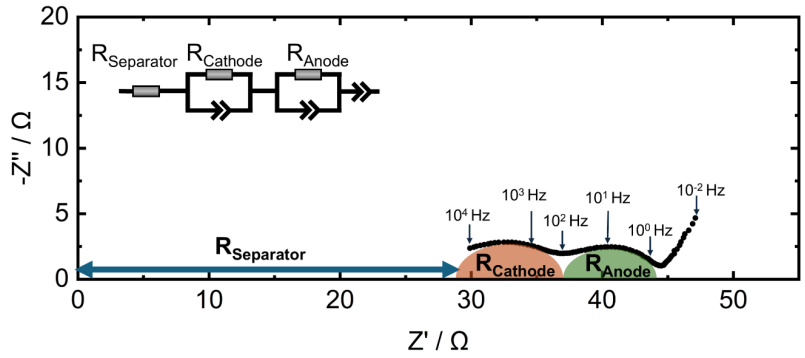

Figure S7. *Exemplary Nyquist plot recorded at 3.1 V vs. In/InLi and corresponding equivalent circuit for the impedance fitting. Black circles represent the measured data which were recorded in a frequency range from 10 kHz to 10 mHz. The colored semicircles for the cathode- and anode-related contributions, $R_{Cathode}$ and R_{Anode}, represent a guide-to-the-eye.*

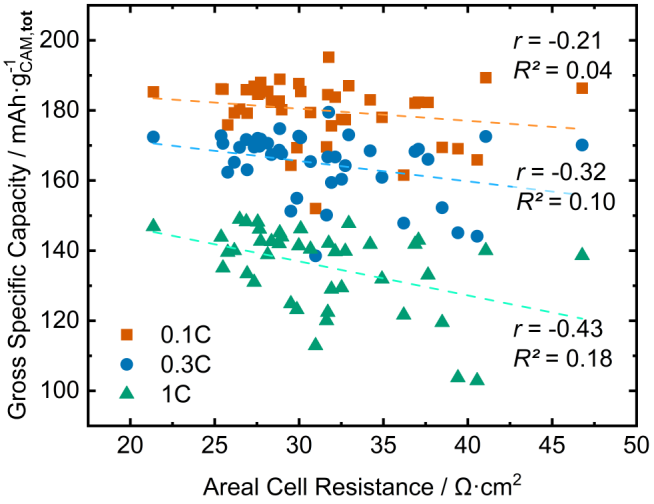

Figure S8. *Correlation plot between the gross specific discharge capacities and the areal full cell resistance extracted from the impedance at 3.1 V vs. In/InLi.*

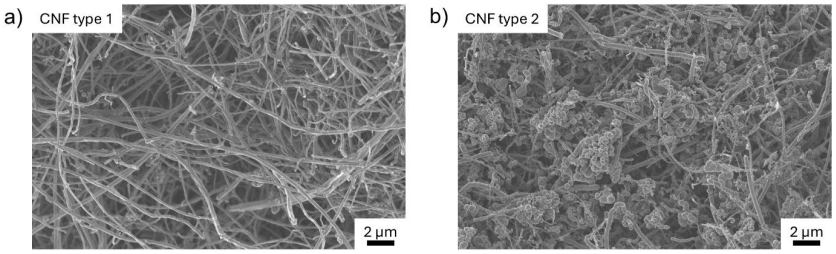

Figure S9. *SEM (GeminiSEM 560, Carl Zeiss Microscopy, Oberkochen, Germany) images of the two different CNF types. For CNF type 1 fibers are visible while microstructure of CNF type 2 is dominated by spherical and agglomerated entities and fibers appear to be disrupted.*

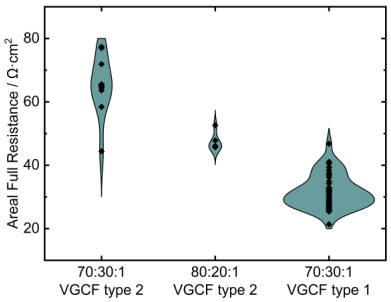

Figure S10. *Violin plots of the areal full cell resistances extracted from the impedance measured at 3.1 V vs. In/InLi for all tested cells of the three composite types.*

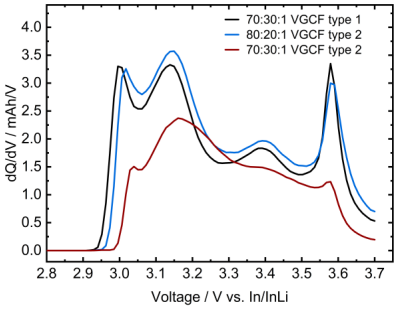

Figure S11. *Comparison of representative dQ/dV plots for the three different composite types.*

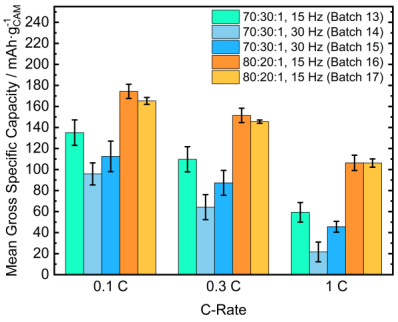

Figure S12. *Mean gross specific discharge capacities for different composite batches, calculated with respect to the total CAM mass in the cathode, all using CNF type 2. The standard deviations are calculated based on at least three cells that have been built.*

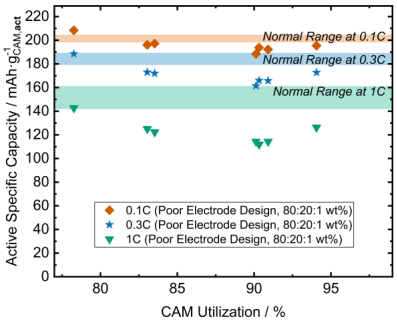

Figure S13. *Active specific capacities, versus CAM utilization for the composites using CNF type 2 (poor electrode design). The shaded areas indicate the mean values and standard deviations (normal range) of capacities achieved for cells with a good electron design using CNF type 1.*

S1: Insights into the parameter study for the mixing process in a mini vibrating mill

The mechanically mixed composites were mixed in a mini vibrating mill (Pulverisette 23, Fritsch GmbH, Idar-Oberstein, Germany). The parameters that can be varied during the mixing process are the vibration frequency, the mixing time, as well as the type and number of milling media.

We first investigated the influence of the frequency while keeping all other parameters constant, *i.e.*, the milling time was 30 minutes and ZrO_2 milling balls with 5 mm diameter were used. As can be seen in **Figure S14**, the capacities change the frequency while a frequency of 20 Hz leads to the highest capacities at all C-rates with the smallest variations. We emphasize that this is only valid for the given mixing time of 30 minutes. By shortening the milling time at higher frequencies to keep the stress number similar, also higher capacities might be achieved. However, depending on the frequency and, thus, stress energy also the motion of the balls and the distribution of the material within the mill might change. We assume that higher frequencies lead to partial degradation of the particles, mainly the solid electrolyte during mixing, resulting in the slightly weaker performance.

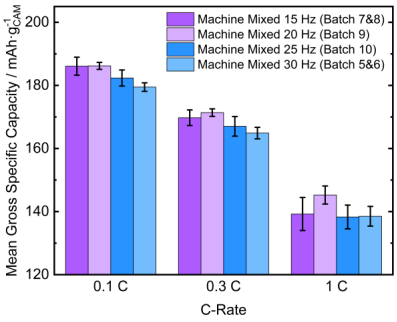

Figure S14. *Influence of the vibration frequency during milling on the achievable discharge capacities. The specific capacities are referred to the total CAM mass.*

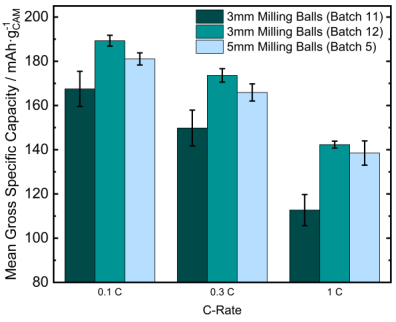

Figure S15. *Influence of the milling media size on the achievable discharge capacities. The specific capacities are referred to the total CAM mass.*

Regarding the milling media, we investigated the effect of using smaller ZrO_2 milling balls with 3 mm instead of 5 mm diameter. By default, 3 ZrO_2 milling balls with 5 mm diameter were used per 100 mg of cathode composite, *i.e.*, 9 milling balls for a typical batch of 300 mg. Although this is rather arbitrary, it results in a satisfactory reproducibility. However, the milling balls may be too large for the particles to be mixed which are in the size range of 0.5 to 3 µm. Therefore, we tested milling balls with a diameter of only 3 mm while keeping the total volume of the milling balls constant. Accordingly, 28 milling balls were used per 300 mg composite, which is a relatively impractical high number. As shown in **Figure S15**, we observed a significant worsening but, in another batch, also improvement of the performance. Possible reasons for the differences could be different types of caking, e.g. due to different milling ball surfaces (fresh from the supplier and used and cleaned dry/wet), or different filling of the milling jar. The results show that it is possible to improve the mixing quality by changing the milling media. At the same time, however, a detrimental effect on reproducibility cannot be excluded and remains to be further investigated. Obviously, optimization of a mixing process is a challenging task where little modifications can drastically impact the performance and reproducibility. Overall, optimizing the mixing process is extremely time consuming when using a try-and-error strategy and was not the goal of this work. In our case, three 5 mm ZrO_2 milling per 100 mg of cathode composite led to satisfying reproducibility.

B.3. Supporting Information for Publication III

Supplementary Information for

Mechanofusion-derived cathode composite microstructures with scalable mixed conducting matrix coatings for solid state batteries

Maximilian Kissel[1,†], Finn Frankenberg[2,†], Thomas Demuth[3], Anton Lai[1], Niklas Laser[2], Daniel Wagner[1], Ahmed Eisa[2], Peter Michalowski[2], Kerstin Volz[3], Arno Kwade[2,], Jürgen Janek[1,*]*

[1]Justus-Liebig-Universität Gießen, Institute of Physical Chemistry & Center for Materials Research, Heinrich-Buff-Ring 17, Gießen, 35392, Hesse, Germany

[2]Technische Universität Braunschweig, Institute for Particle Technology, Volkmaroder Straße 5, Braunschweig, 38104, Lower Saxony, Germany

[3]Materials Science Center (WZMW) and Department of Physics, Philipps-University Marburg, Marburg 35032, Hesse, Germany

*Corresponding authors:

E-mail: juergen.janek@pc.jlug.de; arno.kwade@tu-braunschweig.de

† These authors contributed equally to this work

Table S1. Overview about the exact weighing and the calculated mixed densities.

Type of Investigation	Nomenclature in manuscript	Composition (Mass in g)				Composition (Volume in cm³)				Mixed density / g cm⁻³
		NCM	LIC		∑	NCM	LIC		∑	ρ_{mix}
Coating Thickness Variation (**without** CB) Variation of coating content 1-20 wt.%	99:1:0	22.92	0.23		23.15	4.82	0.09		4.91	4.71
	98:2:0	22.49	0.46		22.95	4.73	0.18		4.91	4.67
	95:5:0	21.28	1.12		22.40	4.48	0.43		4.91	4.56
	90:10:0	19.35	2.15		21.50	4.07	0.83		4.90	4.38
	80:20:0	16	4		20.00	3.37	1.54		4.91	4.07
		NCM	LIC	CB	∑	NCM	LIC	CB	∑	ρ_{mix}
Coating Thickness Variation (**with** CB) Variation of coating content 1-20 wt.%	99:1:0.2	22.83	0.23	0.04	23.1	4.81	0.09	0.02	4.91	4.70
	98:2:0.3	22.32	0.46	0.07	22.85	4.7	0.18	0.04	4.91	4.65
	95:5:0.8	20.93	1.1	0.17	22.2	4.41	0.43	0.09	4.92	4.51
	90:10:1.5	18.76	2.08	0.32	21.17	3.95	0.8	0.16	4.92	4.3
	80:20:3	15.05	3.76	0.58	19.4	3.17	1.45	0.3	4.92	3.94
		NCM	LIC	CB	∑	NCM	LIC	CB	∑	ρ_{mix}
Process Parameter Variation	95:5:0.8	20.93	1.1	0.17	22.2	4.41	0.43	0.09	4.92	4.51
	80:20:3	15.05	3.76	0.58	19.4	3.17	1.45	0.3	4.92	3.94
		NCM	LIC	CB	∑	NCM	LIC	CB	∑	ρ_{mix}
Matrix Optimization CB content variation: 0-3 w.t%	80:20:0	16	4	0	20.00	3.37	1.54	0	4.91	4.07
	80:20:0.2	15.93	3.98	0.04	19.95	3.35	1.54	0.02	4.91	4.06
	80:20:0.5	15.84	3.96	0.1	19.9	3.33	1.53	0.05	4.91	4.05
	80:20:1	15.68	3.92	0.2	19.8	3.3	1.51	0.1	4.92	4.03
	80:20:2	15.35	3.84	0.39	19.58	3.23	1.48	0.2	4.91	3.99
	80:20:3	15.05	3.76	0.58	19.4	3.17	1.45	0.3	4.92	3.94

Supplementary Note 1 - Particle Size Distributions via particleOS.ai

The SEM Image Analysis Tool, part of the particleOS.ai platform developed at the Institute for Particle Technology at Technical University Braunschweig, enables quantitative characterization of scanning electron microscope images through AI-driven segmentation and morphological analysis. Meta's Segment Anything Model (SAM) provides precise particle boundary delineation through two operational modes: automatic segmentation for batch processing of multiple particles, and manual selection mode for targeted analysis of specific regions of interest. The workflow consists of image upload, scale calibration, and mode selection, followed by automated segmentation and Morphological analysis.

The system generates number-based (q_0) particle size distributions by calculating equivalent circle diameter ($\sqrt{(4\times Area/\pi)}$). Users can analyze multiple SEM images of the same sample and automatically generate averaged distributions for improved statistical robustness.

Morphological characterization includes calculation of key shape metrics, particularly circularity ($4\pi \times \text{Area}/\text{Perimeter}^2$) and aspect ratio (maximum Feret diameter/minimum Feret diameter). Circularity quantifies how closely a particle resembles a perfect circle (value of 1.0), while aspect ratio identifies elongated particles. Additional parameters including convexity, solidity, and equivalent diameter are also calculated. These metrics enable classification into distinct morphological categories and provide quantitative data on shape heterogeneity.

This implementation improves upon previous approaches [1] by leveraging SAM's zero-shot capabilities with customized filtering algorithms. As demonstrated in the manual mode analysis above, this eliminates the need for specialized training datasets while improving the processing of complex, overlapping particle arrangements that are challenging for conventional segmentation methods.

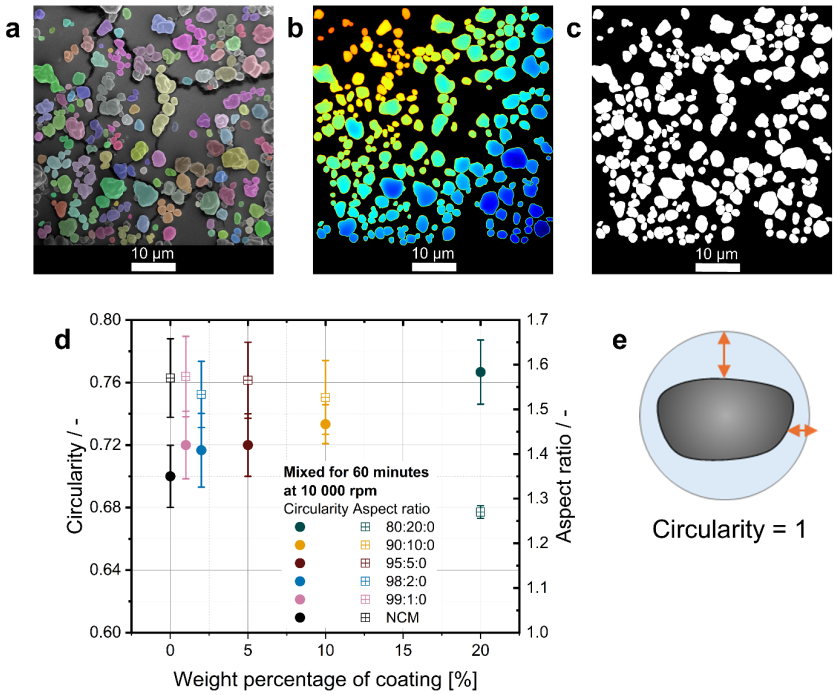

Figure S1. *Exemplary result from the in-house particleOS.ai tool, which was used for analyzing the coating based on SEM images.* ***a*** *Example of a segmented SEM image of the 80:20:0 composition, accompanied by the corresponding depth map* ***b*** *and binary image* ***c****. In addition to the PSD, particle shape descriptors such as circularity and aspect ratio were determined with the particleOS.ai tool, as illustrated in* ***d*** *for different coating compositions. Error bars represent the standard deviation of n = 3 segmented SEM images.* ***e*** *Simplified sketch illustrating that a high circularity value means that the NCM particle is covered by a differently thick coating layer given the non-spherical shape of the NCM particle.*

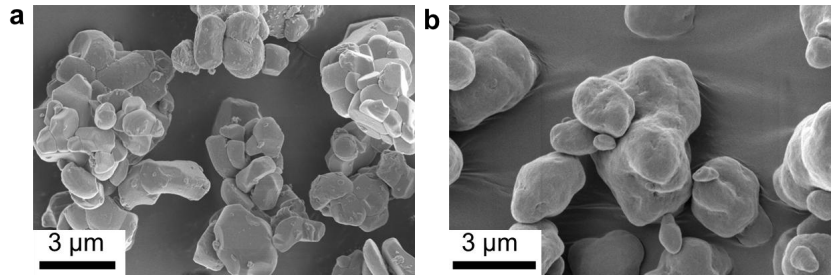

Figure S2. *SEM images of the* ***a*** *pristine NCM and* ***b*** *LIC-coated NCM (80:20:0).*

Supplementary Note 2 – Calculation of the theoretical coating thickness

The theoretical coating thickness was calculated using the raw material densities, the mixed density of the coated material, and geometric considerations. As a first step, the average mass and volume of one NCM particle was approximated based on the median particle diameter of 2.05 µm obtained from the q_0 PSD.

$$V_{\mathrm{NCM}} = \frac{4}{3}\pi \cdot R_{\mathrm{NCM}}^3$$

$$m_{NCM} = V_{\mathrm{NCM}} \cdot \rho_{\mathrm{NCM}}$$

Based on the material compositions and weight fractions, and assuming a uniform coating on each particle, the coating volume per individual NCM particle was calculated. For samples without CB, a coating density of 2.59 g cm^{-3} was used corresponding to the density of pure LIC. For samples containing CB, a reduced coating density of 2.48 g cm^{-3} was applied, calculated from the fixed volume ratio between CB and LIC (20:80 vol.%).

$$V_{\mathrm{coating}} = \frac{m_{\mathrm{coating}}}{\rho_{\mathrm{coating}}} = \frac{wt.\%_{\mathrm{coating}} \cdot m_{\mathrm{NCM}}}{\rho_{\mathrm{coating}}}$$

Based on geometric considerations and using the radius of the NCM particles, the coating thickness can be approximated mathematically. Therefore, the coating volume is derived geometrically as follows:

$$V_{\mathrm{coating}} = \frac{4}{3} \cdot \pi \cdot \left(R_{\mathrm{total}}^3 - R_{\mathrm{NCM}}^3\right)$$

$$V_{\mathrm{coating}} = \frac{4}{3} \cdot \pi \cdot \left((s + R_{\mathrm{NCM}})^3 - R_{\mathrm{NCM}}^3\right)$$

By rearranging this equation for the coating thickness s and substituting the coating volume derived from the volume ratios, the theoretical coating thickness can be calculated.

$$s = \sqrt[3]{\frac{V_{coating} \cdot 3}{\pi \cdot 4} + R_{NCM}^3} - R_{NCM}$$

The resulting thickness values are depicted in Figure S3:

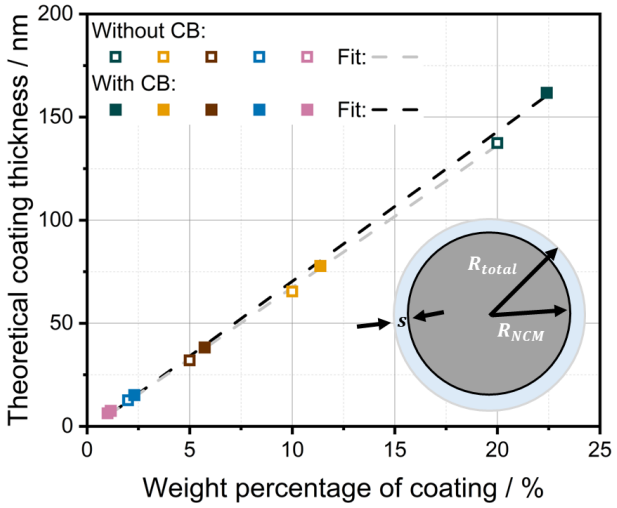

Figure S3. *Theoretical coating thickness depending on coating content. The coating thickness was estimated based on the d_{50} value of 2.05 µm (q_0 distribution of NCM) and the corresponding weight ratio of the coating material. The calculation assumes spherical NCM particles, uniform coating of each particle and the absence of porosity within the coating layer.*

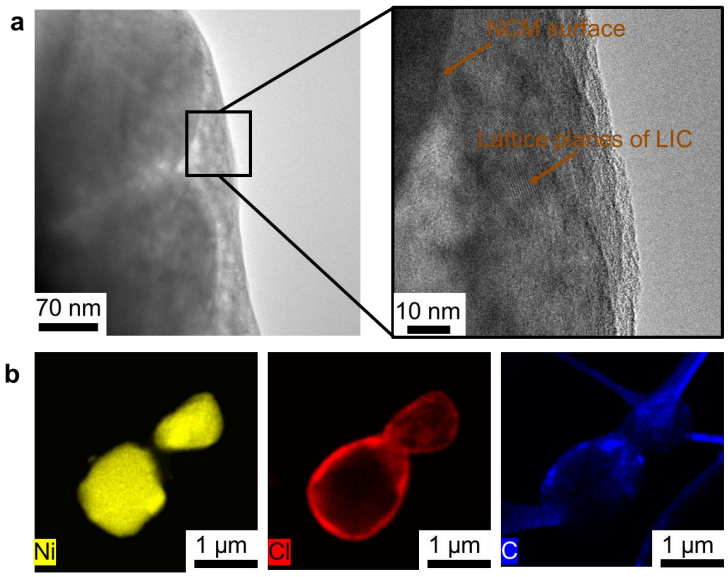

Figure S4. ***a*** *HR-TEM images and* ***b*** *STEM-EDX maps of building blocks with 80:20:1 composition.*

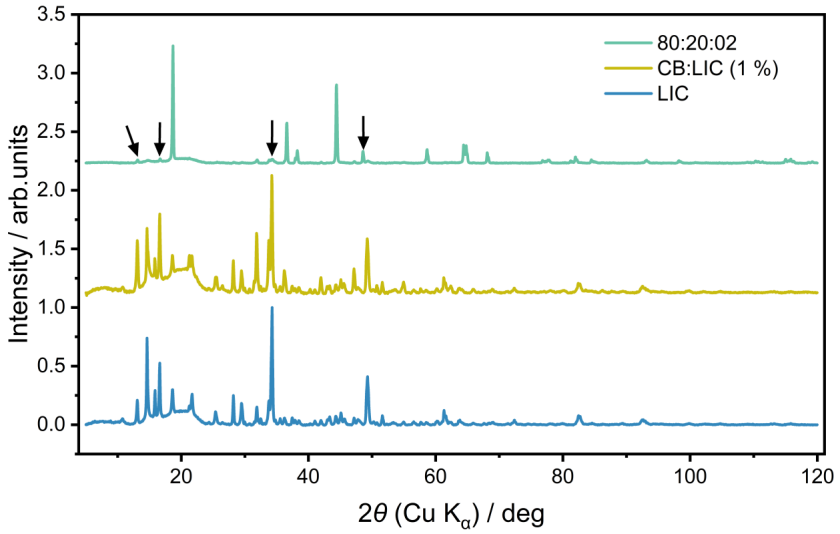

Figure S5. *X-ray diffractograms obtained in reflection geometry of pristine LIC, CB-LIC premix and NCM-LIC-CB composite revealing the presence of LIC in the premix as well as in the composite.*

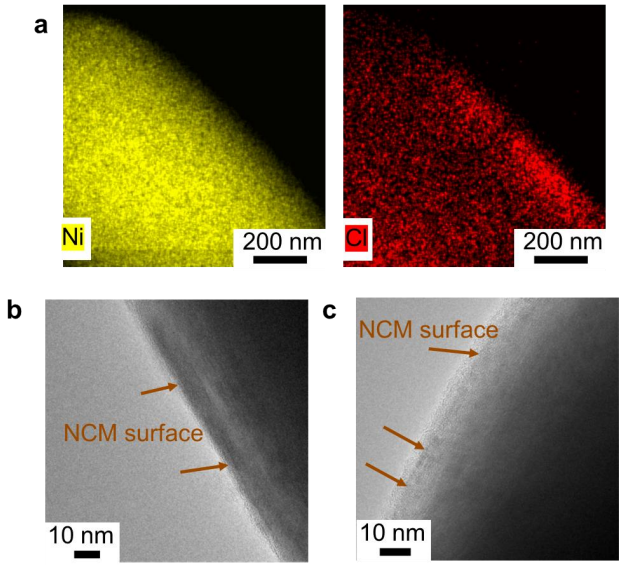

Figure S6. ***a*** *STEM-EDX maps and* ***b,c*** *HR-TEM images of coated particles with composition 99:1:0.*

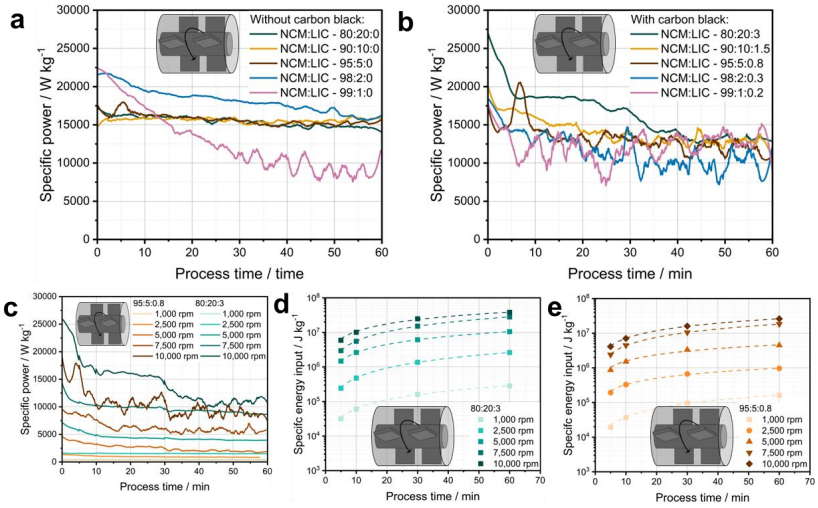

Figure S 7. *Specific power for different compositions* ***a*** *with CB and* ***b*** *without CB.* ***c*** *Specific power recorded for compositions 95:5:0.8 and 80:20:3 depending on the rotational speed. Specific energy input calculated from the recorded power data for the mixing of the compositions* ***d*** *95:5:0.8 and* ***e*** *80:20:3.*

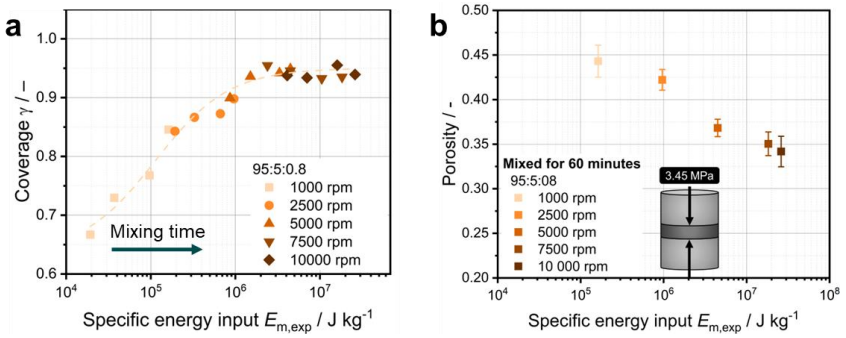

Figure S8. *Evolution of* ***a*** *coverage and* ***b*** *porosity as function of specific energy input during high-intensity mixing. Error bars represent the standard deviation of n = 3 measurements.*

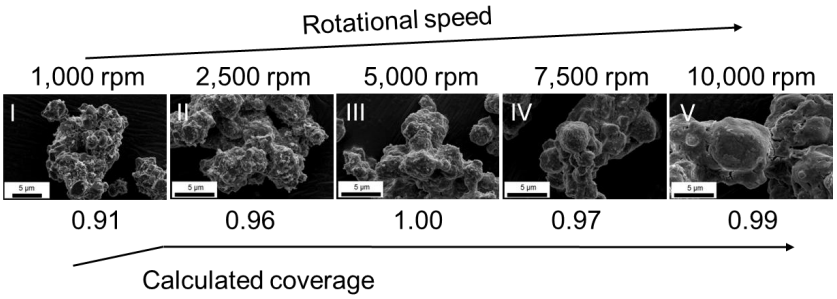

***Figure S9**. Calculated coverage values and corresponding SEM images for building blocks with composition 80:20:3 mixed at different rotational speeds.*

Supplementary Note 3 – Calibration and calculation of the coarse grain density

The particle density used in the simulation was calculated to 2.417 g cm^{-3}, based on the measured bulk density of the 80:20:3 powder mixture (1.450 g cm^{-3}), as well as the true material density of the 80:20:3 composition, which is 3.944 g cm^{-3}. Here an internal coarse-grain porosity of 0.39 is assumed.

The simulation was further validated by plotting the coverage as a function of the experimental and simulated specific energy input, fitting both datasets, and calculating the relative error between the resulting curves (cf. Supplementary Figure S11). The maximum deviation was found to be maximum 2 %, demonstrating that the DEM simulation accurately captures the coating process on a macroscopic scale.

It should be noted that by employing the normalized parameters $\overline{SI}_{\mathrm{CG}}$ and $\overline{SN}_{\mathrm{p}}$, the coarse-graining of particles in the DEM simulation is effectively accounted for, as opposed to using the absolute values of the stressing energy $\overline{SE}_{\mathrm{CG}}$ and stress number SN_{CG}. In principle, the $\overline{SI}$ should remain constant when changing the particle size, as both the collision energy and the particle mass under impact stress scale with the cube of the particle diameter ($\overline{SI}_{\mathrm{CG}} = \frac{\overline{SE}_{\mathrm{CG}}}{m_{\mathrm{particle,CG}}} = \frac{\overline{SE}_0 \cdot f^3}{m_{\mathrm{particle},0} \cdot f^3}$). However, due to the narrow gap between the rotor and chamber wall, the $\overline{SE}_{\mathrm{CG}}$ may be slightly overestimated for the coarse-grained particles. If the scaling of $\overline{SE}_0$

exceeds f^3, this would lead to a minor overestimation of the stress intensity in the coarse-grained system. This is why it is denoted as $\overline{SI}_{CG}$ throughout this study. The mean stress number per particle should also be scale-invariant, as the stress frequency decreases approximately with the cube of the particle diameter [2], while the coarse-grained particle mass increases with the cube of the particle diameter.

Table S2. *Overview about the simulation parameters applied in this study. See Supplementary Note 3 for details on the particle density.*

Calibration parameters	**Particle – Particle**	**Particle – Wall**	
Static friction / -	0.46	0.45	
Dynamic friction / -	0.31	0.25	
Yield ratio / -	0.00756	0.0256	
Restitution coefficient / -	0.3	0.3	
Properties	**Particle**	**Wall (Rotor)**	**Wall (Chamber)**
Density / g·cm^{-3}	2.417*	4.510	7.850
Young's modulus / GPa	0.228	120	200
Poisson ratio / -	0.3	0.3	0.3

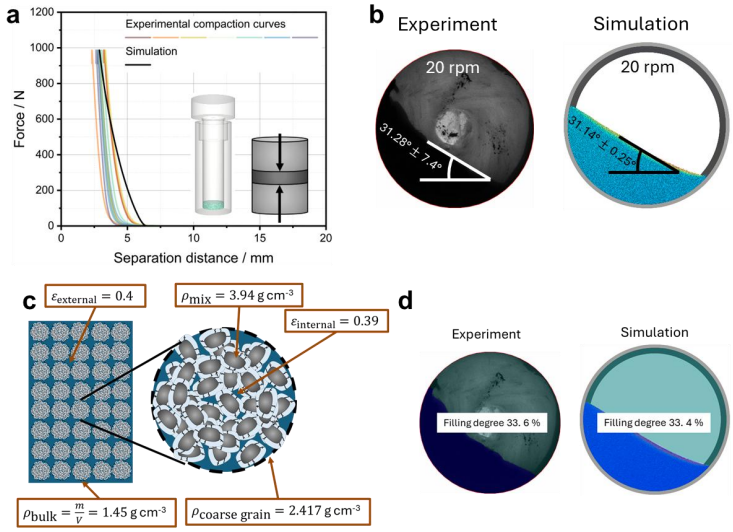

Figure S10. *Calibration procedure of the DEM simulation with* ***a*** *compaction test simulation and experiment,* ***b*** *dynamic angle of repose simulation and experiment,* ***c*** *illustration of how the coarse-grain density was calculated and* ***d*** *comparison of the filling degree between simulation and experiment, thereby confirming the coarse-grain density.*

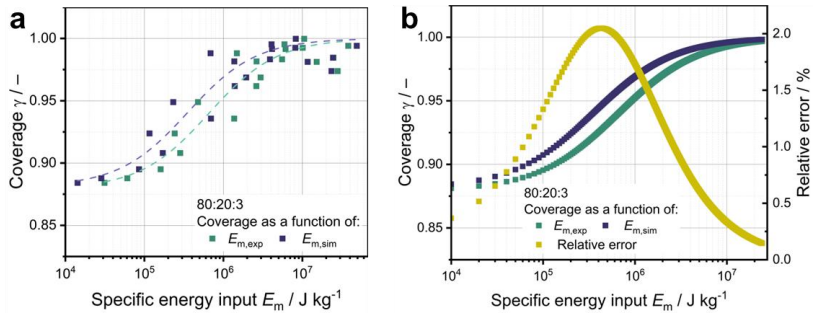

Figure S11. a *Coverage as a function of the experimental and simulated specific energy input and their fit functions and* ***b*** *fit functions from the coverage and the corresponding relative error.*

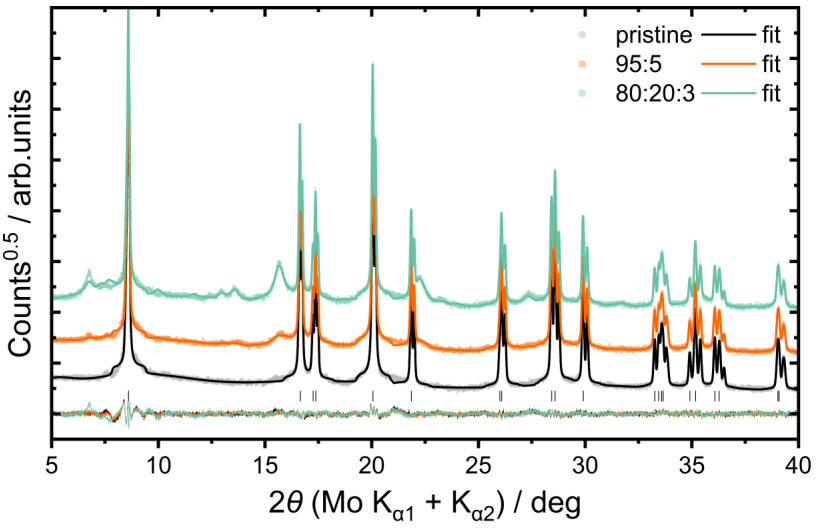

Figure S12. *X-ray diffractograms obtained in transmission geometry of pristine NCM and two LIC-coated NCM samples with a thin (95:5) and a thick (80:20:3) coating.*

Table S3. *Lattice parameters, lattice strain, and mass ratios out of Rietveld refinement of three exemplary samples.*

Sample	a / Å	c / Å	Lattice strain / %	NCM / wt.%	LIC / wt.%
Pristine	2.895739	14.304153	0.037	100	-
95:5:0	2.895918	14.304236	0.05	92	8
80:20:3	2.895848	14.303675	0.045	79	21

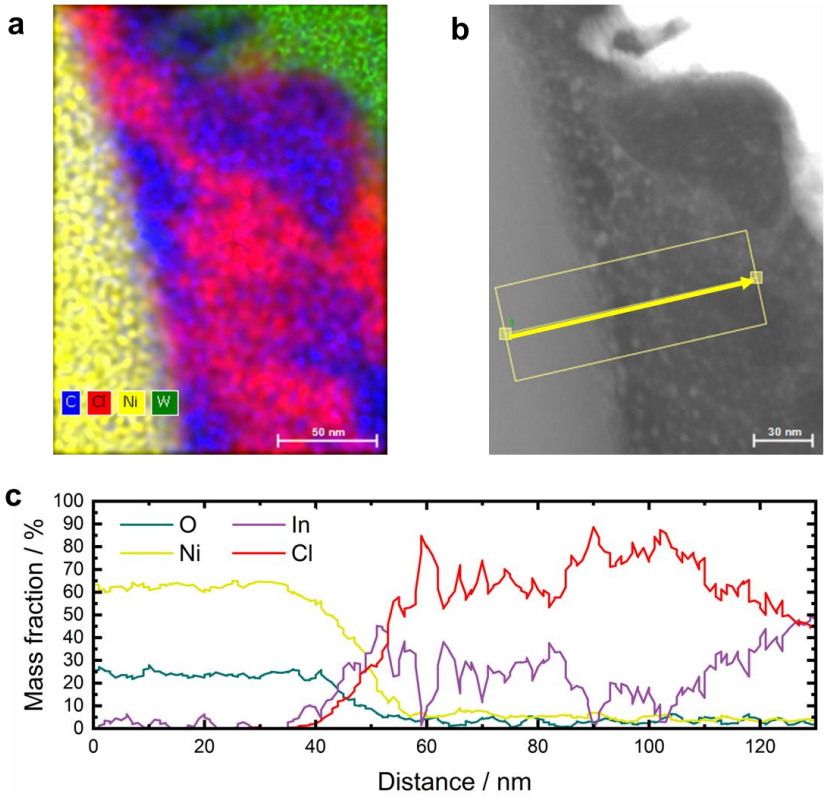

Figure S 13. *STEM-EDX line scan.* ***a*** *Elemental map,* ***b*** *line scan direction and* ***c*** *measured mass fraction versus distance curve. Due to the NCM surface being slightly slanted, both materials overlap a bit in this region. However, no sign of element diffusion beyond this overlapping area of approximately 10-15 nm width was detected.*

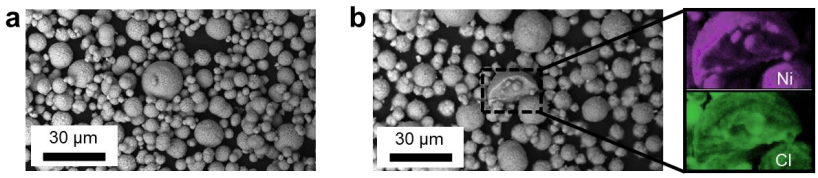

Figure S* 14.** *SEM images of* ***a *polycrystalline NCM raw material and* ***b*** *polycrystals after processing at 10,000 rpm for 60 min with 20 wt.% LIC.*

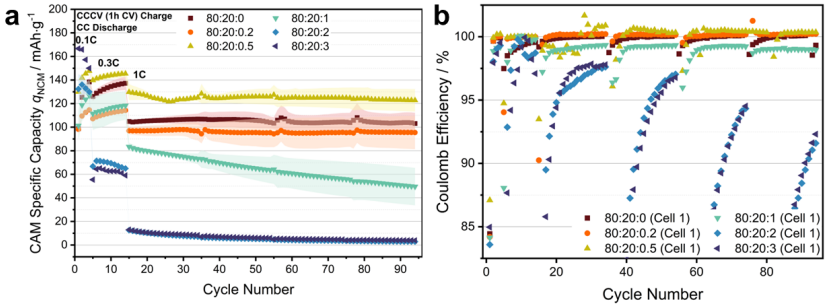

Figure S 15. *Cycling performance depending on the cathode composition.* ***a*** *CAM-specific capacity (using the total nominal CAM mass in the cathode) versus cycle number when cycled in CCCV mode at 25°C under 80 MPa stack pressure (1C ≈ 200 mA/g ≈ 3 mA/cm²). Error bars represent the standard deviation of n = 2 cells.* ***b*** *Corresponding Coulomb efficiencies (CEs) versus cycle number. See Supplementary Note 4 for additional comments.*

Supplementary Note 4 – Periodicity in Coulomb efficiency

In Figure S15a fluctuations in the capacities are observed every 20 cycles during 1C CCCV cycling. Furthermore, a periodicity in Coulomb efficiencies (CEs) over 20 cycles at 1C is observed in Figure S15b, most obvious for compositions 80:20:2 and 80:20:3. Thereby a characteristic drop in CE is observed followed by a gradual recovery over the subsequent cycles.

Both phenomena are directly related to the determination of the CAM utilization every 20 cycles. This step, referred to as the check-up cycle in the following, involves slower charging and discharging as well as extended equilibration periods (see Methods section). As a result, it

deviates significantly from the monotonic high C-rate CCCV cycling, leading to periodic fluctuations in both capacities and CEs. Importantly, this step alters the lithium inventory within the CAM, increasing its lithium content at the beginning of each 20-cycle sequence. In the first cycle after the check-up, this 'excess' lithium inventory is exploited, leading to higher extracted charge. During subsequent discharging, the same amount of lithium must be reinserted to maintain a high CE. However, for compositions such as 80:20:2, kinetic limitations dominate, resulting in incomplete re-lithiation and thus a temporary CE reduction. Over the following cycles, the CAM remains less lithiated than at the beginning, which reduces the kinetic asymmetry between discharge and charge and leads to a gradual recovery of CE.

For the 80:20:0.5 composition, CEs above 100% are observed over several cycles, which at first glance appears unphysical. However, the CE in the first cycle of each 20-cycle block is clearly below 100%. In the subsequent cycles, the remaining Li sites are progressively refilled, resulting in apparent CEs > 100%. When the total charge and discharge capacities of all 20 cycles are considered together, the cumulative CE remains below 100% (99.32 % for the 80:20:0.5 cell), which is physically reasonable.

Overall, the extended rest period during the check-up cycle allows the system to equilibrate, resulting in an asymmetric kinetic response between discharge and charge. This imbalance is reinforced immediately after the check-up cycle.

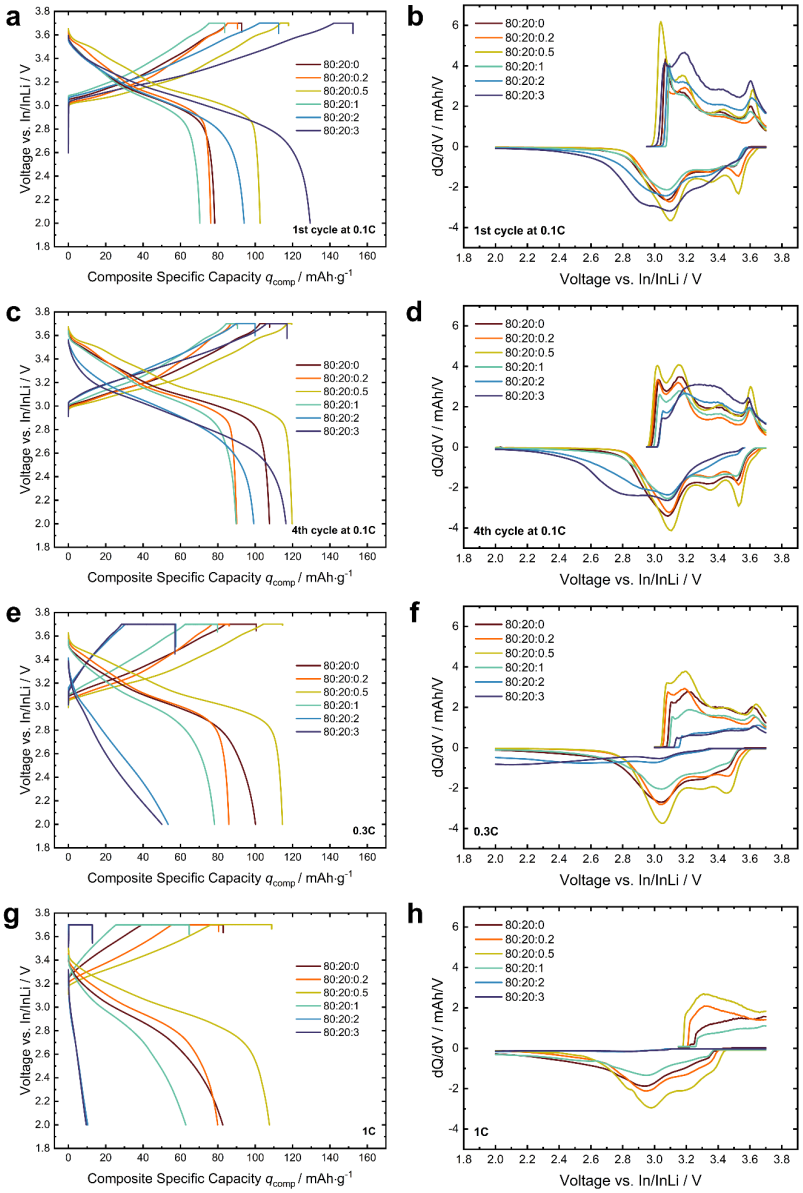

Figure S 16. *Full voltage curves and differential charge plot of all investigated compositions for the* ***a,b*** *initial cycle at 0.1C,* ***c,d*** *the last cycle at 0.1C,* ***e,f*** *a representative cycle at 0.3C and* ***g,h*** *a representative cycle at 1C (1C ≈ 200 mA/g ≈ 3 mA/cm²).*

Table S4. *Electrochemical data for all compositions: Initial charge capacities $Q_{0,\text{charge}}$ of the CC and CV step, initial discharge capacities $Q_{0,\text{discharge}}$ (all referred to the total composite mass), initial Coulomb efficiency and capacity retention over 80 cycles at 1C in CCCV mode.*

Composition	$Q_{0,\text{charge}}$ (CC) $\text{mAh}\cdot\text{g}^{-1}$	$Q_{0,\text{charge}}$ (CV) $\text{mAh}\cdot\text{g}^{-1}$	$Q_{0,\text{discharge}}$ (CC) $\text{mAh}\cdot\text{g}^{-1}$	ICE %	Capacity retention %
80:20:0	85.3	7.5	78.3	84.4	91.7
80:20:0.2	85.2	5.3	76.2	84.2	108.5
80:20:0.5	113.0	4.8	102.6	87.1	96.7
80:20:1	75.4	8.3	70.4	84.1	81.8
80:20:2	102.1	10.5	94.1	83.6	21.8
80:20:3	142.0	10.3	129.4	85.0	30.1

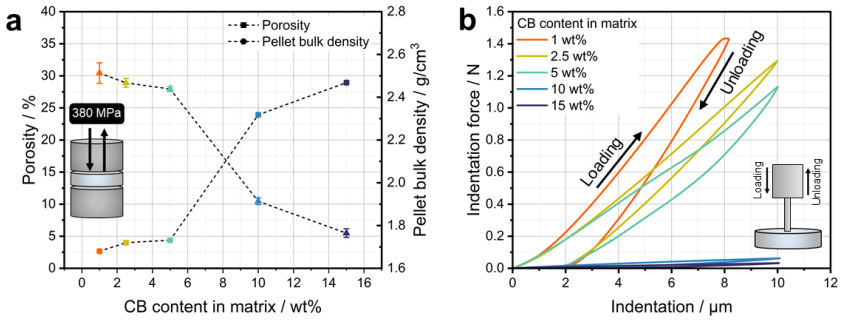

Figure S17. *Investigation of the mechanical properties of the CB-LIC premix.* ***a*** *Porosity and bulk density of pellets prepared from the CB-LIC premix compacted at 380 MPa. Error bars represent the standard deviation of n = 24 indentations.* ***b*** *Nanoindentation measurements performed on the pellets shown in a. Each force–indentation curve represents the average of 25 individual indents.*

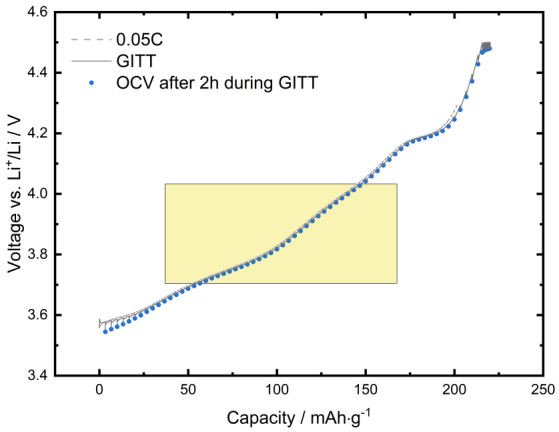

Figure S18. *Comparison between the voltage versus capacity profile obtained from galvanostatic charging at 0.05C and from galvanostatic intermittent titration technique (GITT) for a LIB reference cell. The relaxed OCV after 2h during GITT are displayed as blue data points. The curves significantly overlap, especially in the yellow voltage region, which was used for the CAM utilization determination. The low C-rate charging profile is thus considered as quasi-OCP and used to quantify the CAM utilization in the SSB cells.*

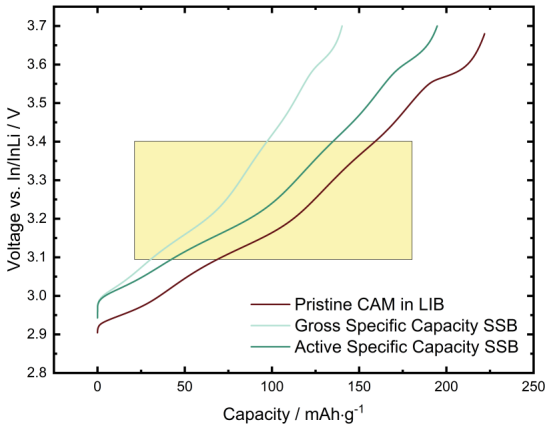

Figure S19. *Comparison of Voltage-Capacity curves for the LIB reference cell and the SSB cell. For the SSB cell, the gross specific capacity, referred to the total mass of CAM in the cathode, and the active specific capacity, referred only to the active fraction of CAM in the cathode are displayed. No significant differences between the voltage curves of the LIB and the SSB, especially in the yellow voltage region, which was used for the CAM utilization determination, are observed. The visible shift is due to kinetic effects since the SSB was cycled at 0.1C while the LIB was cycled a 0.02C.*

Supplementary References

[1] J. Bals, K. Loza, P. Epple, T. Kircher and M. Epple, "Deep learning for automated size and shape analysis of nanoparticles in scanning electron microscopy," RSC Advances, 2023, 13, 2795-2802.

[2] M. Sakai, M. Abe, Y. Shigeto, S. Mizutani, H. Takahashi, A. Viré, J. Percival, J. Xiang, C. Pain, "Verification and validation of a coarse grain model of the DEM in a bubbling fluidized bed," Chemical Engineering Journal, 2014, 244, 33-43.

B.4. Supporting Information for Publication IV

Supplementary Information for

Engineering the Artificial Cathode-Electrolyte Interphase Coating for Solid-State Batteries via Tailored Annealing

Maximilian Kissel[1,2], Felix Walther[1,2], Jonas Hertle[1,2], Thomas Demuth[3], Ruizhuo Zhang[4], Philipp Brüner[5], Torsten Brezesinski[4], Kerstin Volz[3], and Jürgen Janek[1,2,4]*

[1]Institute of Physical Chemistry, Justus Liebig University Giessen, Heinrich-Buff-Ring 17, 35392 Giessen, Germany.

[2]Center for Materials Research (ZfM/LaMa), Justus Liebig University Giessen, Heinrich-Buff-Ring 16, 35392 Giessen, Germany.

[3]Materials Science Center (WZMW) and Department of Physics, Philipps-University Marburg, 35032 Marburg, Germany.

[4]Battery and Electrochemistry Laboratory (BELLA), Institute of Nanotechnology, Karlsruhe Institute of Technology (KIT), Kaiserstr. 12, 76131 Karlsruhe, Germany.

[5]IONTOF GmbH, Heisenbergstr. 15, 48149 Münster, Germany.

*corresponding author: juergen.janek@pc.jlug.de

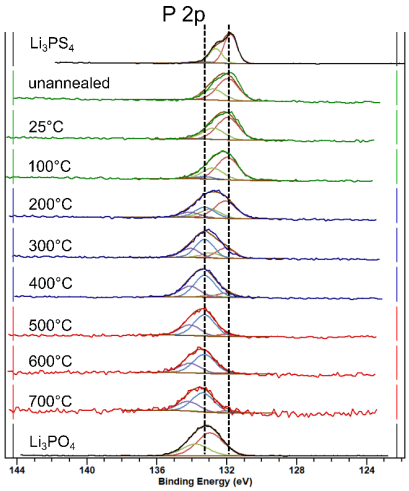

Figure S1: XP detail spectra of the P 2p signal for Li_3PS_4-coated NCM85 annealed at different temperatures. The increasing signal intensity of the peak at higher binding energies indicates a gradual increase of oxidized phosphor from Li_3PS_4 to Li_3PO_4 with increasing annealing temperature.

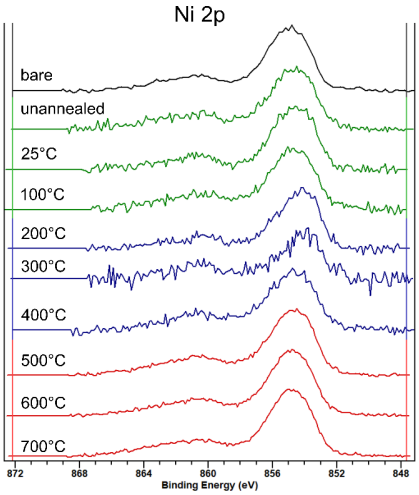

Figure S2: XP detail spectra of the Ni 2p signal after background subtraction. Signals with good peak-to-noise ratio indicate that the NCM particles are not fully covered with the SE-coating which is the case for low and high annealing temperatures. The intensity is the lowest for the sample annealed at 300°C as seen in the noisy signal indicating a high coverage of the NCM particles.

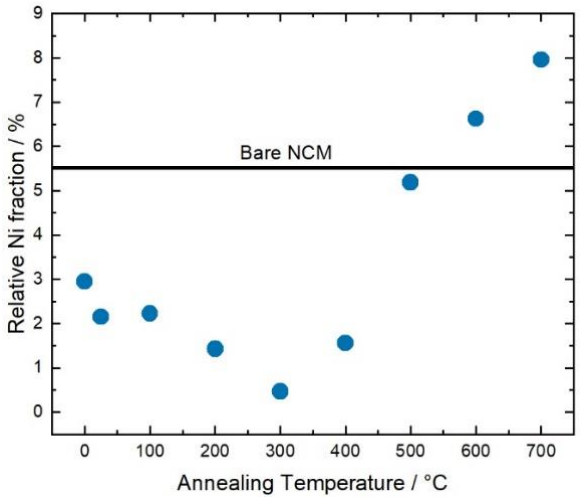

Figure S3: Relative Ni fraction calculated by evaluating the relative intensity of the Ni-region (**Figure S3**) for Li_3PS_4 coated NCM85 samples annealed at different temperatures (hereby 0 °C means unannealed). The relative Ni fraction is a measure for the coating coverage which is high when the measurable Ni fraction is low.

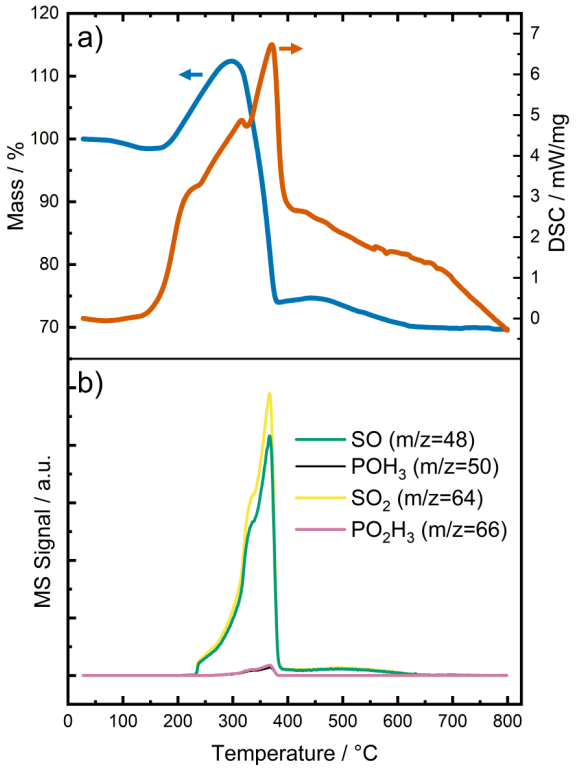

Figure S4: a) Thermogravimetric analysis (TGA) coupled with b) mass spectrometry (MS) of the coating precursor Li_3PS_4. An oxidation reaction is visible between 300 and 400 °C accompanied by a mass loss and concurrent release of gaseous SO_x and PO_xH_y species.

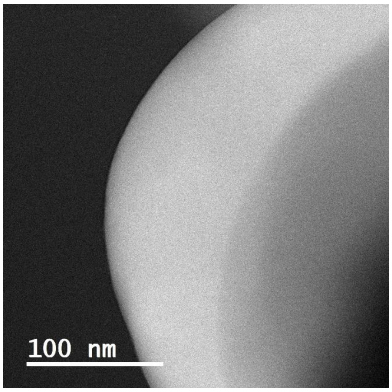

Figure S5: LAADF-STEM image of the uncoated NCM85 showing no coating layer.

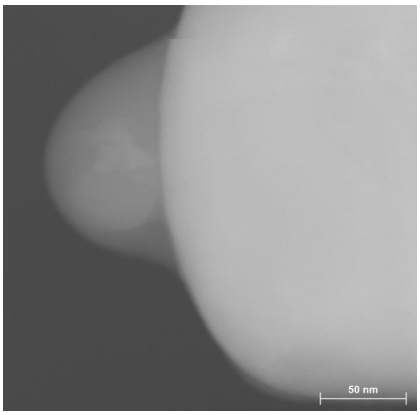

Figure S6: LAADF-STEM image of Li_3PS_4-coated NCM85 annealed at 100 °C possessing a large coating particle on the surface.

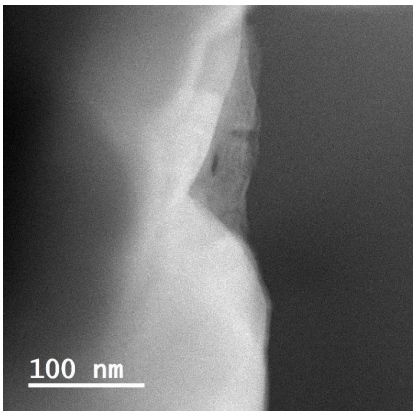

Figure S7: LAADF-STEM image of Li_3PS_4-coated NCM85 annealed at 100 °C showing accumulation of coating material in notches.

S1: Effect of annealing time and atmosphere

As discussed, the SE coating only shows a superior performance if the coating morphology and composition are appropriately tuned during the annealing process. This defines the two aims of annealing: a high coating coverage and a full oxidation of the solid electrolyte. The highest coverage was found for an annealing temperature of 300 °C, while at higher annealing temperatures the coating tended to evaporate. On the other hand, a fully oxidized coating layer required a temperature of more than 300 °C. We further investigated the annealing process by varying the annealing time and changing the annealing atmosphere from synthetic air to pure oxygen. The goal was to obtain a coating for which both the coverage and oxidation are as high as possible. After annealing, the samples were analyzed with XPS to (semi-)quantify these parameters.

The coverage was calculated according to Equation 1 and is depicted in **Figure S8a**. The coverage for samples annealed at 300 °C is found to be almost independent of the annealing time. The coverage obtained for the sample annealing in pure O_2 compared to annealing in synthetic air is systematically shifted towards higher values. In contrast, the samples annealed at 400 °C show a decrease in coverage with increasing annealing time in addition to the already lower coverage after annealing for 1 h.

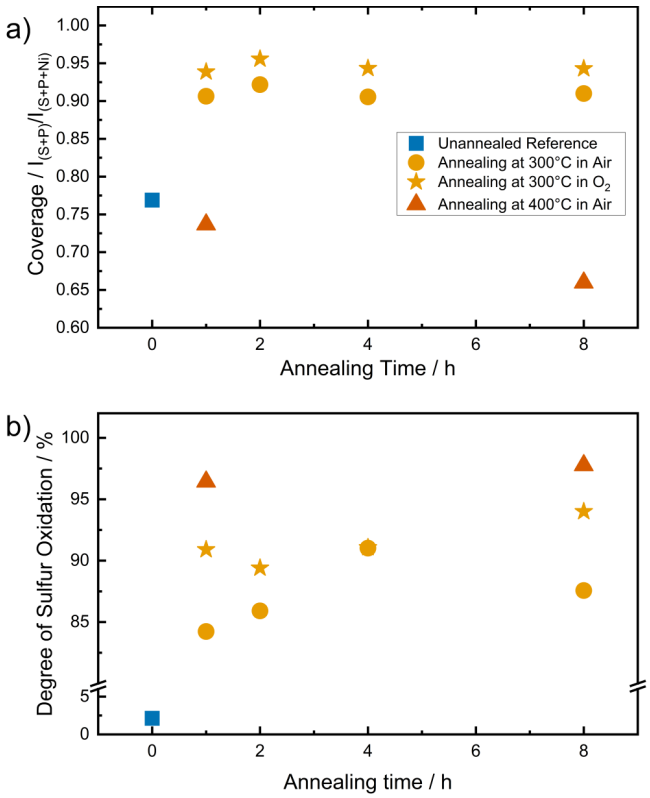

Figure S8. Influence of annealing time, temperature and atmosphere on the a) coating coverage and b) degree of oxidation of the coating for Li_3PS_4-coated NCM85. Both parameters are derived from XPS measurements.

The degree of oxidation was approximated by quantitatively evaluating the S 2p signal. As already seen in Figure 1, the signal shows two well separated regions at around 161 eV (pristine Li_3PS_4) and 170 eV (oxidized Li_3PS_4, *i.e.*, Li_2SO_4). To obtain the degree of sulfur oxidation depicted in **Figure S8b**, the intensity of the region around 170 eV was compared to the intensity

sum of both regions. The oxidation degree is the highest after the annealing at 400 °C and remains unchanged with respect to the annealing time. As expected for the samples annealed at 300 °C, the degree of sulfur oxidation is lower, but seems to increase with annealing time. Especially when annealing in pure oxygen, a higher degree of oxidation was found compared to the sample annealed in synthetic air. Thus, a higher oxygen partial pressure during annealing can be used to reduce the time for complete oxidation at lower temperatures. Overall, the coating morphology and composition was shown to be sensitive to different annealing conditions. This allows to tune the coating properties by a tailored annealing process which significantly impacts the overall coating performance with respect to electrochemical properties and interfacial degradation products.

B.5. Supporting Information for Publication V

Supplementary Information for

Toward efficient development and reliable benchmarking of novel CAM coatings for solid state batteries

Maximilian Kissel[*1,2], Felix Schnaubelt[1,2], Jill Kessler-Kühn[1,2], Sebastian L. Benz[1,2], Anton Lai[1,2], Philip Minnmann[3], Holger Schneider[4] and Jürgen Janek*[*1,2]*

[1]Institute of Physical Chemistry, Justus Liebig University Giessen, Heinrich-Buff-Ring 17, 35392 Giessen, Germany

[2]Center for Materials Research (ZfM/LaMa), Justus Liebig University Giessen, Heinrich-Buff-Ring 16, 35392 Giessen, Germany

[3]HTE GmbH, 69123 Heidelberg, Germany

[4]BASF SE, 67056 Ludwigshafen, Germany

AUTHOR INFORMATION

Corresponding Authors

maximilian.kissel@pc.jlug.de; juergen.janek@pc.jlug.de

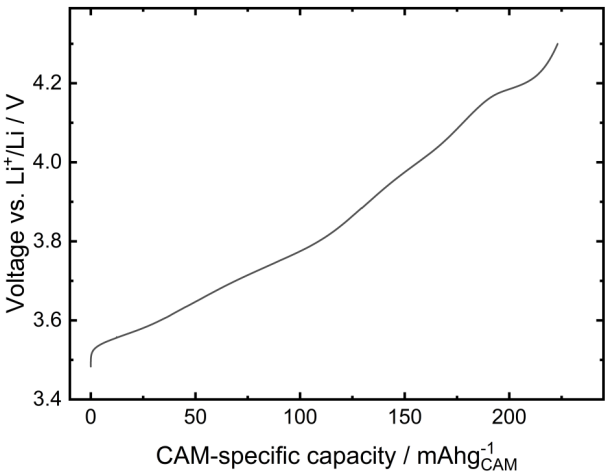

Figure S1: Quasi-OCP curve (0.02C) of a lithium-ion battery cell with the same base CAM (NCM85) taken as reference for CAM utilization calculation.

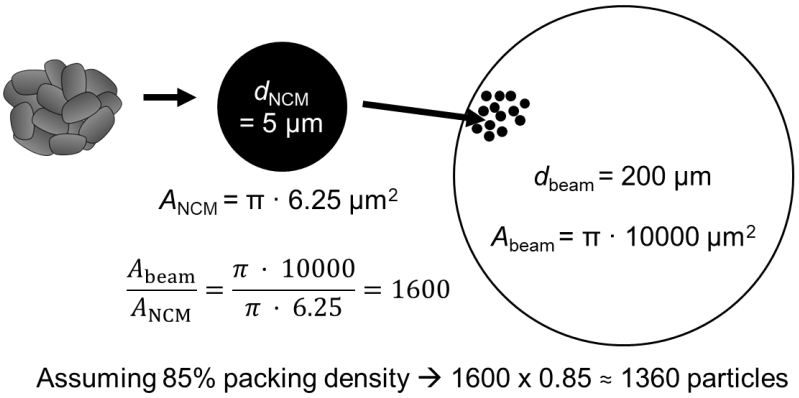

Figure S2: Sketch and estimation of the number of NCM particles probed during an XPS measurement.

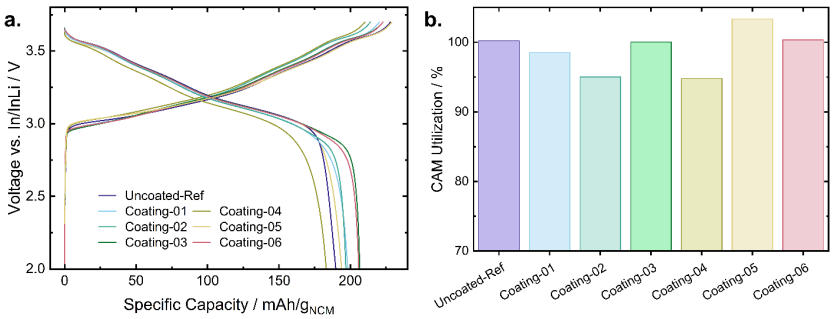

Figure S3: a) Initial voltage profiles of the cells. The total mass of NCM was used for the specific capacity calculation. b) Estimated CAM utilization for different coatings.

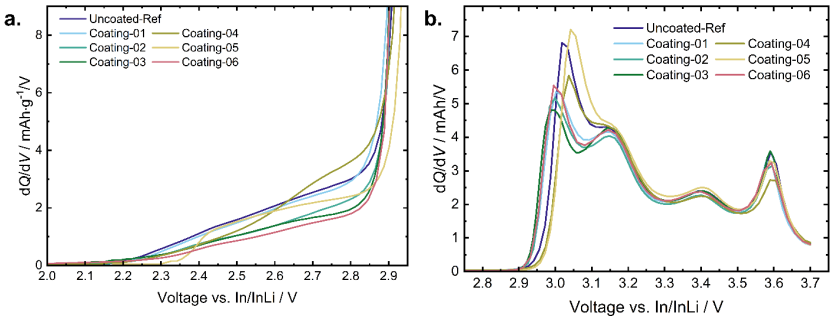

Figure S4: a) Enlarged differential capacity plot of the first cycle revealing slightly different degrees of electrochemical degradation below 3 V vs. In/InLi. b) Full differential capacity plots for the first galvanostatic charging cycle at 0.05 C.

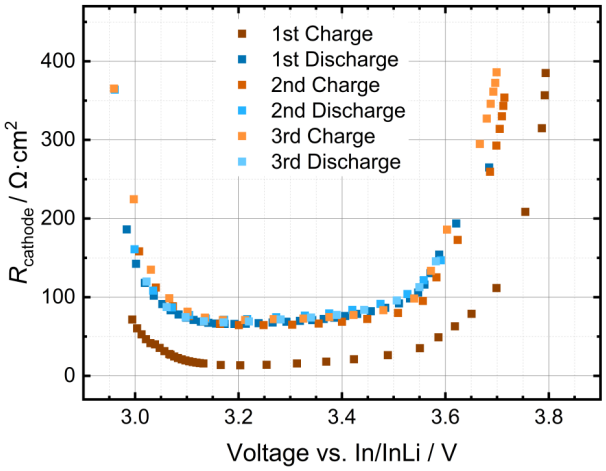

Figure S5: Fitted cathode contribution to the impedance, $R_{cathode}$, versus SoC reflecting the characteristic U-shaped curve with increasing resistance at low and high SoC. The data was acquired for cells with *Uncoated-Ref* as CAM.

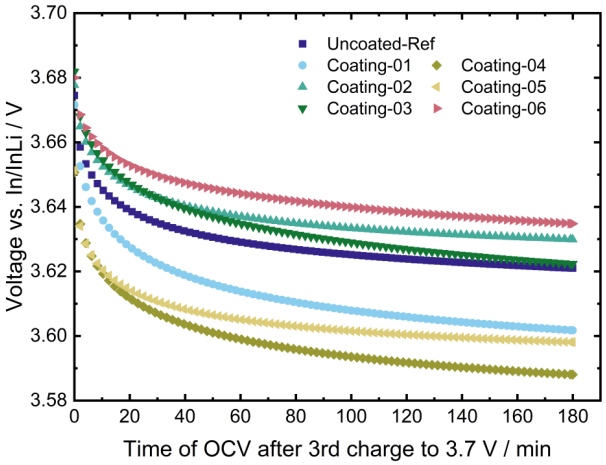

Figure S6: OCV relaxation during 3h after galvanostatic charge at 0.1C to 3.7 V vs. In/InLi.

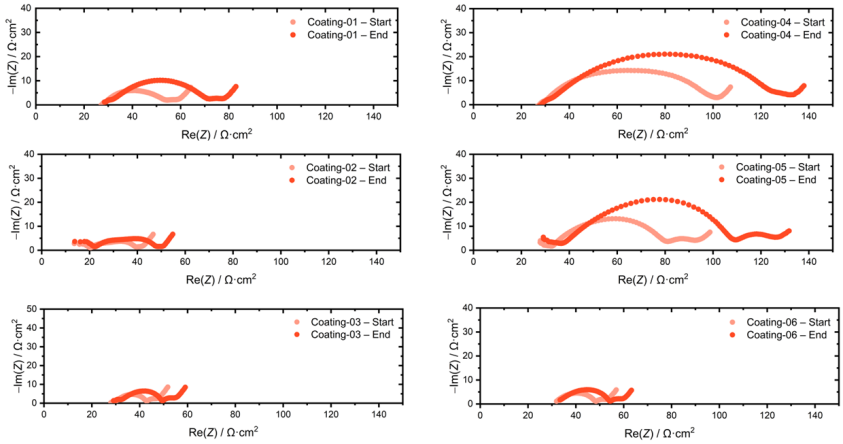

Figure S7: Impedance spectra for the half cells with differently coated CAMs recorded at 3.1 V vs. In/InLi at the start and end of the benchmarking program.

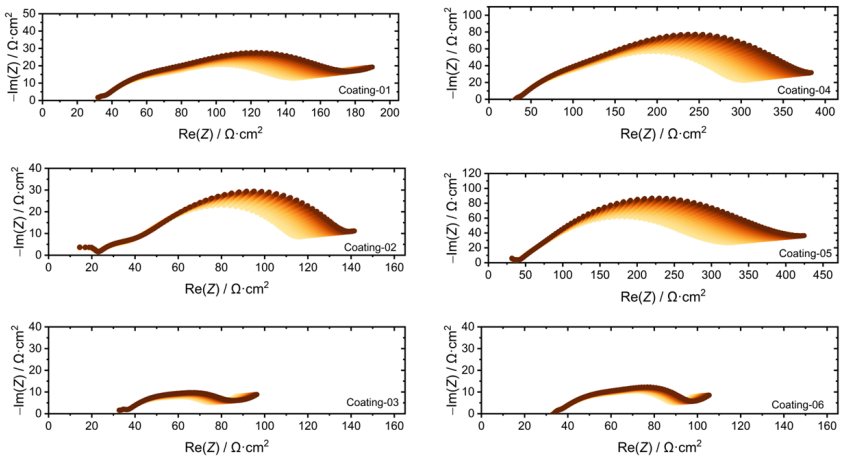

Figure S8: Evolution of the impedance spectra for the half cells with differently coated CAMs during 10h hold at 3.7 V vs. In/InLi.

Table S1: Resistance value R_{cathode} obtained from fitting the spectra shown in Figure S7 and S8 as well as slope of the linear fit for all samples.

Sample	R_{cathode} (@3.1V) (start) / Ω·cm²	R_{cathode} (@3.1V) (end) / Ω·cm²	R_{cathode} (@3.7V) (start) / Ω·cm²	R_{cathode} (@3.7V) (end) / Ω·cm²	Slope during hold at 3.7V / Ω·cm²·h$^{-0.5}$
Uncoated-Ref	22.0	37.0	105.0	146.2	14.6
Coating-01	27.5	41.2	114.2	147.1	12.1
Coating-02	19.4	26.8	96.3	120.2	8.9
Coating-03	13.3	17.6	44.5	53.6	3.2
Coating-04	71.4	98.7	269.5	353.6	30.1
Coating-05	49.5	72.6	296.6	415.7	40.8
Coating-06	17.5	21.9	55.4	64.1	3.0

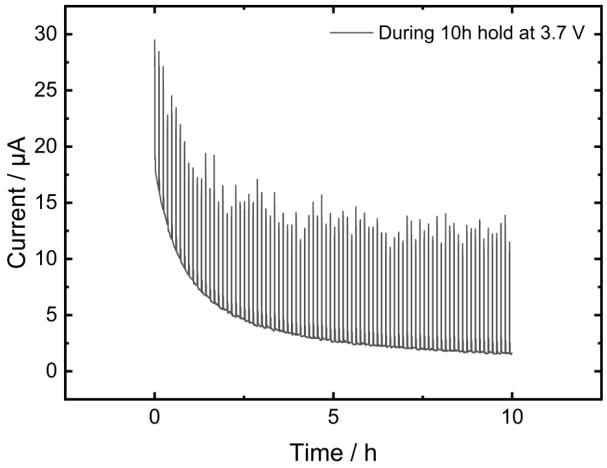

Figure S9: Measured current during impedance measurement for *Uncoated-Ref*. The current decreases from about 15 µA to approximately 1.5 µA during the 10h measurement.

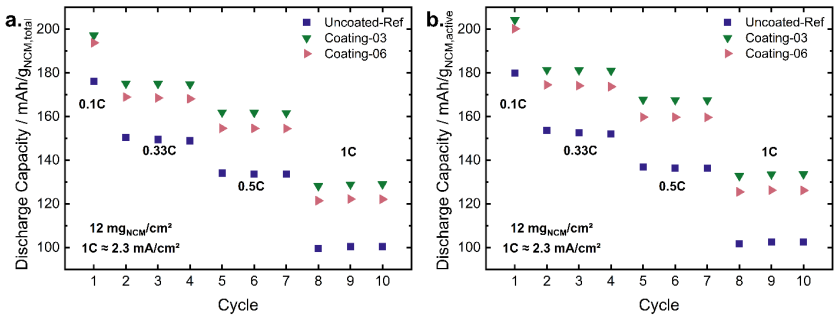

Figure S10: Rate capability at 25°C of *Uncoated-Ref*, *Coating-03* and *Coating-06*, represented as a) gross specific capacity (charge per total mass of NCM) and b) active specific capacity (charge per electrochemically active mass of NCM). The two coatings perform similar and significantly better than the bare reference.

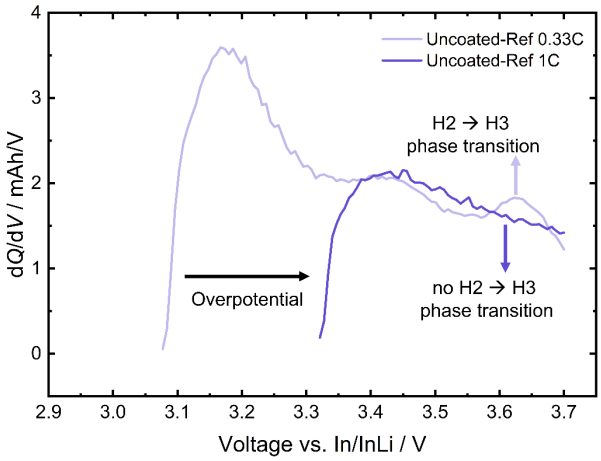

Figure S11: Differential capacity plots for *Uncoated-Ref* at 0.33C and 1C. While the H2→H3 phase transition is visible at 0.33C, it vanishes when charging with 1C due to the higher overpotential.

Table S2: Comparison of short-term testing and long-term cycling.

Characteristic	**Short-term Cycling**	**Long-Term Cycling**
Duration	∼1 week	weeks — months
Goal	efficient screening	final validation
Focus	CAM—SE interface	cell performance
Reproducibility	higher (standardizable)	lower (cell-to-cell variation)
Accessible coating parameter space	broad	narrow
Feedback loop	short	long
Error sources	limited	many
Degradation mechanism	controlled: CAM—SE interface at high SoC	variable: complex overlap
Parameter/Metric		
ICE[a]	✓	✓
Initial capacities[a]	✓	✓
CAM Utilization	✓	✓, if sequence included
Overpotential evolution	✗, limited cycles	✓, many cycles
Impedance analysis	✓, more easily accessible	✗, not easily accessible
Chemo-mechanical degradation	✗, only initial	✓, should be quantified

[a] ICE and Initial capacities depend on multiple factors beyond the coating in both short- and long-term tests, whereby short-term provides relatively more coating-specific insight.

C Acknowledgements

Während meines Studiums an der TU Darmstadt hätte ich nie gedacht, dass ich einmal *in Gießen* promovieren würde. Rückblickend kann ich sagen, dass dies eine der besten Entscheidungen war, die ich treffen konnte — vor allem wegen der Menschen, denen ich im Folgenden danken möchte:

Mein erster großer Dank geht an Prof. Jürgen Janek, dass er mich als externen MaWi mit wenig speziellem Vorwissen ohne zu Zögern als Doktorand herzlich aufgenommen hat. Den stets menschlichen Umgang, die Hilfsbereitschaft und Erreichbarkeit, die Möglichkeit zur Teilnahme an (inter)nationalen Konferenzen sowie die Unterstützung während meines Auslandsaufenthalts in Südkorea weiß ich besonders zu schätzen.

Bei Prof. Arno Kwade möchte ich mich für die Übernahme des Zweitgutachtens und die gute Zusammenarbeit im gemeinsamen DFG Projekt bedanken. Für das Mitwirken in der Prüfungskommission danke ich Prof. Anja Henß und Prof. Matthias Elm.

Danke an Dr. Felix Richter und Dr. Janis Eckhardt für das hilfreiche Korrekturlesen der Thesis. Danke auch an alle anderen, die mir im Laufe der Zeit wertvolles Feedback zu Manuskripten, Postern oder Präsentationen gegeben haben.

Ich möchte Dr. Felix Walther und Dr. Jonas Hertle für den Halt danken, den sie mir im ersten Jahr im Rahmen des BASF-Projekts gegeben haben — ich konnte dabei viel für die weiteren Jahre lernen. Danke auch an Dr. Holger Schneider von der BASF für die immer angenehme Zusammenarbeit im Projekt.

Danke an Dr. Philip Minnmann für hilfreiche Tipps vor allem in meiner Anfangszeit.

Danke an die Kollegen aus dem DFG SPP2289, dass ich die Ingenieursperspektive kennenlernen durfte. Insbesondere möchte ich Finn Frankenberg von der TU Braunschweig für die hervorragende Zusammenarbeit im gemeinsamen Projekt und die vielen Heteroaggregate danken.

Großen Dank geht an meine HiWis Jens Birschel, Joshua Neuweger, Marie Schosland und Anton Lai für das Bauen und Reinigen von etlichen Presszellen mit verschiedenen Kathodenkompositen oder Coatings. Zudem danke ich Anika Siebert, Mark Ulherr und Steffen Paul für ihre Vertiefungsarbeiten an Themen, die es leider nie in ein Paper geschafft haben — trotzdem konnte ich daraus viel mitnehmen.

Danke an die komplette Arbeitsgruppe für die konstruktive Arbeitsatmosphäre — ich bin sehr froh, dass man sich bei uns immer gegenseitig hilft und unterstützt. Auch die gemeinsame Zeit und die Aktivitäten abseits der Arbeit im Institut habe ich genossen. Danke an alle Kollegen und Freunde in der AG Janek, insbesondere an Konrad Münch, Florian Rink, Yannik Schneider, Steffen Schröder, Bing-Xuan Shi, Johannes Schubert, Max Wacha, Timo Weintraut.

Meiner Freundin Helena möchte ich für das Korrekturlesen meiner Thesis, ihr Verständnis während stressiger Phasen und die Möglichkeit Energie zu tanken danken. Mein letzter großer Dank geht an meine Eltern, die immer für mich da sind und mich bedingungslos unterstützen. Auch wenn sie wahrscheinlich nicht verstehen, was ich mit Batterien genau mache, sind sie sich sicher, dass ich es gut mache.♡